# Bolaamphiphilic Rylene Bisimides: Thermodynamics of Self-assembly and Stimuli-responsive Properties in Water

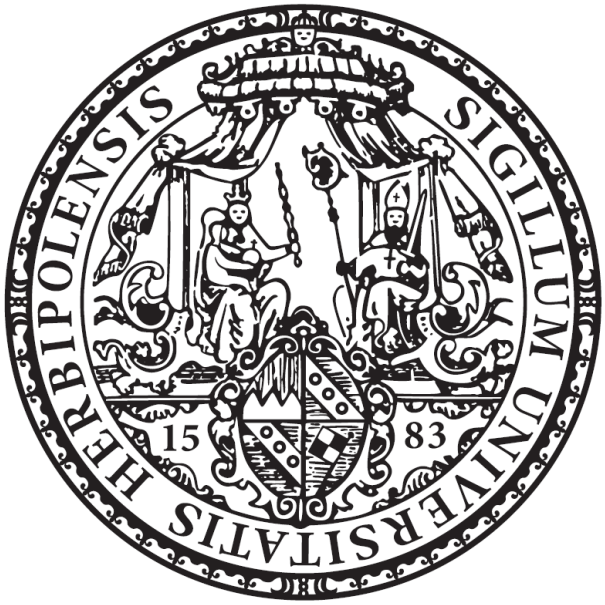


Dissertation zur Erlangung des

naturwissenschaftlichen Doktorgrades

der Julius-Maximilians-Universität Würzburg

vorgelegt von

Pradeep Peethambaran Nair Syamala

aus Trivandrum, Indien

Würzburg 2020

Eingereicht bei der Fakultät für Chemie und Pharmazie am:

17 Juli 2020

Gutachter der schriftlichen Arbeit:

1. Gutachter: Prof. Dr. Frank Würthner

2. Gutachter: Prof. Dr. Ingo Fischer

Prüfer des öffentlichen Promotionskolloquiums:

1. Prüfer: Prof. Dr. Frank Würthner

2. Prüfer: Prof. Dr. Ingo Fischer

3. Prüfer:  Prof. Dr. Matthias Lehmann

Datum des öffentlichen Promotionskolloquiums:

08 Oktober 2020

Doktorurkunde ausgehändigt am:

_____

*For Ammoomma*

## List of Abbreviations

| | |
|---|---|
| 1D/2D/3D | one dimensional/ two dimensional/ three dimensional |
| a.u. | arbitrary unit |
| ACN | acetonitrile |
| ADP | adenosine diphosphate |
| AFM | atomic force microscopy |
| AMP | adenosine monophosphate |
| Ar | aryl |
| ATP | adenosine triphosphate |
| BSA | bovine serum albumin |
| BTA | benzene-1,3,5-tricarboxamide |
| CAC | critical aggregation concentration |
| CB*n* | cucurbit[*n*]urils |
| CD | circular dichroism |
| COSMO | conductor-like screening model |
| COSY | correlation spectroscopy |
| DAN | 1,5-dialkoxynaphthalene |
| DBO | 2,3-diazabicyclo[2.2.2]oct-2-ene |
| DCM | dichloromethane |
| DEAD | diethyl azodicarboxylate |
| DFT | density functional theory |
| DLS | dynamic light scattering |
| DMF | dimethylformamide |
| DNA | deoxyribonucleic acid |
| DSC | differential scanning calorimetry |

| | |
|---|---|
| e.g. | for example (Latin: *exempli gratia*) |
| eqn. | equation |
| ESI | electrospray ionization |
| Et | ethyl |
| *et al.* | and others (Latin: *et alia*) |
| etc. | and so forth (Latin: *et cetera*) |
| FRET | Förster/ fluorescence resonance energy transfer |
| FT-IR | Fourier-transform infrared |
| GPC | gel permeation chromatography |
| GROMOS | Groningen molecular simulation |
| HBC | hexabenzocoronene |
| HCA | human carbonic anhydrase |
| HRMS | high-resolution mass spectrometry |
| *i. e.* | which means (Latin: *id est*) |
| ITC | isothermal titration calorimetry |
| LCST | lower critical solution temperature |
| LCW | Lum-Chandler-Week |
| LEFR | linear free energy relationship |
| MD | molecular dynamics |
| Me | methyl |
| MeOH | methanol |
| MUP | major urinary protein |
| NBI | naphthalene bisimide |
| NICS | nucleus-independent chemical shift |
| nm | nanometer |
| NMR | nuclear magnetic resonance |

| | |
|---|---|
| NOE | nuclear Overhauser effect |
| OD | optical density |
| OEG | oligo ethylene glycol |
| PBI | perylene bisimide |
| PEG | polyethylene glycol |
| PNiPAm | poly-N-isopropyl acrylamide |
| Pr | propylene |
| QM/MM | quantum mechanics/molecular mechanics |
| ROESY | rotating-frame nuclear Overhauser effect correlation spectroscopy |
| RT | room temperature |
| SSDU | supramolecular structure-directing unit |
| ST | swallow-tail |
| TEM | transmission electron microscopy |
| THF | tetrahydrofuran |
| TLC | thin-layer chromatography |
| TOF | time of flight |
| UV-vis | ultraviolet-visible |
| vdW | van der Waals |
| *via* | by means of (Latin) |
| *viz.* | namely (Latin: *videlicet*) |
| VT | variable temperature |
| $\alpha$-CD | $\alpha$-cyclodextrin |

# Table of Contents

# Chapter 1

# Introduction and Aim of the Thesis

The ubiquitous role of water in all life forms makes research on amphiphilic molecules an alluring topic that surpasses the boundaries of physics, chemistry, and biology. This 'universal solvent' is quintessential for numerous biochemical reactions, both as a substrate and media. The molecular construction of water, composed of infinite hydrogen-bonded networks in the bulk state with localized and structured clustering,[1] leads to many interesting properties.[2, 3] Among these, one of the most prevalent is the enhanced association of non-polar units in water, commonly referred to as hydrophobic effect.[4]

As early as 1773, Benjamin Franklin has published first experiments in the direction of hydrophobic effect, where he investigated the 'wave-calming effect' by dropping oil into a pond at Clapham Common.[5] Later, Rayleigh attributed this phenomenon to the monolayer formation of oil on the water surface.[6] In 1891, Traube noticed that amphiphilic molecules have a higher tendency to be deposited at the air-water interface than in the solution, due to the lesser affinity between organic components and water.[7] Pockel,[8] Langmuir[9] and Blodget[10] pioneered the quantitative experiments on oil films on the water surface, which led Gorter and Grendel to discover the 'bilayer' formation of lipids from red blood cells by Langmuir trough experiments in 1925.[11] Despite many such advancements documenting the unusual behavior of hydrocarbons in water, hydrophobic effect in its stature known today was popularized by Walter Kauzmann in the 1950s, as the driving force for the quaternary structure formation of proteins.[12] Today the segregation of oil and water has grown from an everyday observation to a scientific phenomenon which wheels cleaning industry to the complexities of the biological world, including protein-ligand binding, assembly of membrane components to lipid bilayers, folding of proteins with a hydrophobic interior, stacking of nucleotides in the DNA, enzyme-catalyzed recognition and signaling etc.[13-15]

In the last two decades, self-assembly has taken the central stage in supramolecular chemistry to emulate nature's strategy of synthesizing complex arrays by the organization of molecular building blocks. Water, as a solvent in this regard, is not only attractive as the matrix of life but also due to the strong aggregation of non-polar molecules in this medium.

As a result, such architectures can be achieved at dilute conditions as hydrophobic effect results in large binding constants.[16] Generally, the construction of the building blocks is realized by introducing water-soluble ionic/non-ionic functionalities to the parent non-polar unit like a π-core or alkyl chains. Using this strategy, countless examples of nanostructures in water have been achieved for benzene tricarboxamides,[17-20] naphthalene[21-23] and perylene bisimides,[16, 24, 25] *p*-oligophenylenes,[26-28] *p*-oligophenylenevinylenes,[29-31] oligophenyleneethinylenes,[32, 33] triphenylenes,[34, 35] hexabenzocoronenes,[36-38] squaraines,[39-42] squaramides,[43, 44] etc.

Despite the fact that life is the antithesis of equilibrium and several recent advances in kinetic considerations,[45-47] thermodynamic approach still remains the overarching method for designing functional architectures by artificial molecules, both in aqueous and organic media. In this regard, several mathematical models (isodesmic,[48, 49] cooperative,[50, 51] and anti-cooperative[52, 53]) have been proposed, which shed light on the mechanism of 1D supramolecular polymerization.[54] However, the complex interplay of enthalpy and entropy in the change in standard Gibbs free energy of self-assembly is mostly overlooked, presumably because optimization of association has focused on energetic contributions by modulation of non-covalent interactions.[55] However, many seminal works by Whitesides and Klebe have noted that both enthalpy and entropy dominated profiles are observed for ligand binding to a protein, which is accessible by minor changes in the ligand structure.[14, 56-58] Recently, Tezcan and coworkers have shown that the entropy-driven free-energy landscape of a cysteine functionalized protein (L-rhamnulose-1-phosphate aldolase) is dictated by solvent reorganization and can be tuned by perturbing protein-protein and protein-solvent interactions.[59] Exploring such a mastery of enthalpy and entropy for artificial self-assembled systems can yield enticing materials that respond differently to a temperature stimulus.

Symmetrical π-conjugated systems are ideal model compounds to obtain fundamental thermodynamic insights, as they result in one-dimensional assembly with less complexities and can be easily accessed with conventional synthetic methods.[60, 61] Rylene bisimides, especially their naphthalene[62] and perylene[63] homologs, are attractive in this regard as their aggregation can be traced by easily detectable spectral changes resulting from the excitonic coupling of dyes and the two equivalent planar surfaces exhibit identical binding on both sites.[45] In our group, we have previously identified that bolaamphiphilic perylene bisimides (PBI) with water-soluble oligo ethylene glycol (OEG) head groups, self-assemble quite

strongly in water ($K > 10^8$ $M^{-1}$) due to hydrophobic effect[64] leading to numerous nanostructures in aqueous media.[65-67] Recently, Daniel Görl serendipitously came across the unique temperature dependence of their self-assembly, where the propensity of aggregation is enhanced at higher temperatures.[60, 68] This is markedly different from the majority of π-conjugated molecules which associate with cooling, due to enthalpic favorability arising from the non-covalent bond formation. ITC dilution experiment in water has proven the endothermic nature of its self-assembly despite the large π-π interactions which direct the association of these extended π-scaffolds. However, this PBI derivative aggregated too strongly in water impeding insights into the thermodynamic components operating its self-assembly.

Following up on this groundwork, one of the principal aims of the current thesis was to obtain a quantitative picture of the aforementioned entropically driven self-assembly and to elucidate the structural parameters that dictate the enthalpy and entropy of its association. To surpass the limitation set by the larger π-core of perylene bisimides, we synthesized their smaller naphthalene bisimide (NBI) homologs, which are known to aggregate less strongly (Figure 1.1a) and investigated different parameters pertaining to their self-assembly (Figure 1.1b).

While both entropically and enthalpically favored aggregation has been observed for OEG appended π-systems, an understanding of this differential thermodynamic behavior remains elusive. This fundamental question was addressed in the next part of this thesis, where structural insights into the bifurcated thermal response were probed for both PBI and NBI derivatives in water.

Finally, to extend the potential of these molecules as 'smart materials,' we explored the thermoresponsive behavior of OEG appended PBIs associated with the Lower Critical Solution Temperature (LCST) phenomenon. The role of hydrophobic and hydrophilic components of head groups in determining the phase transition temperature was studied in detail and was explained based on the structural arrangement of monomers within the self-assembled structure.

**Chapter 2** outlines previous work that has been carried out in regard to driving forces for the association and host-guest interactions in water along with thermodynamic and morphological features of π-amphiphile self-assembly. Furthermore, analytical techniques

and associated mathematical models used to extract binding constant, as well as the enthalpy and entropy of self-assembly is also covered.

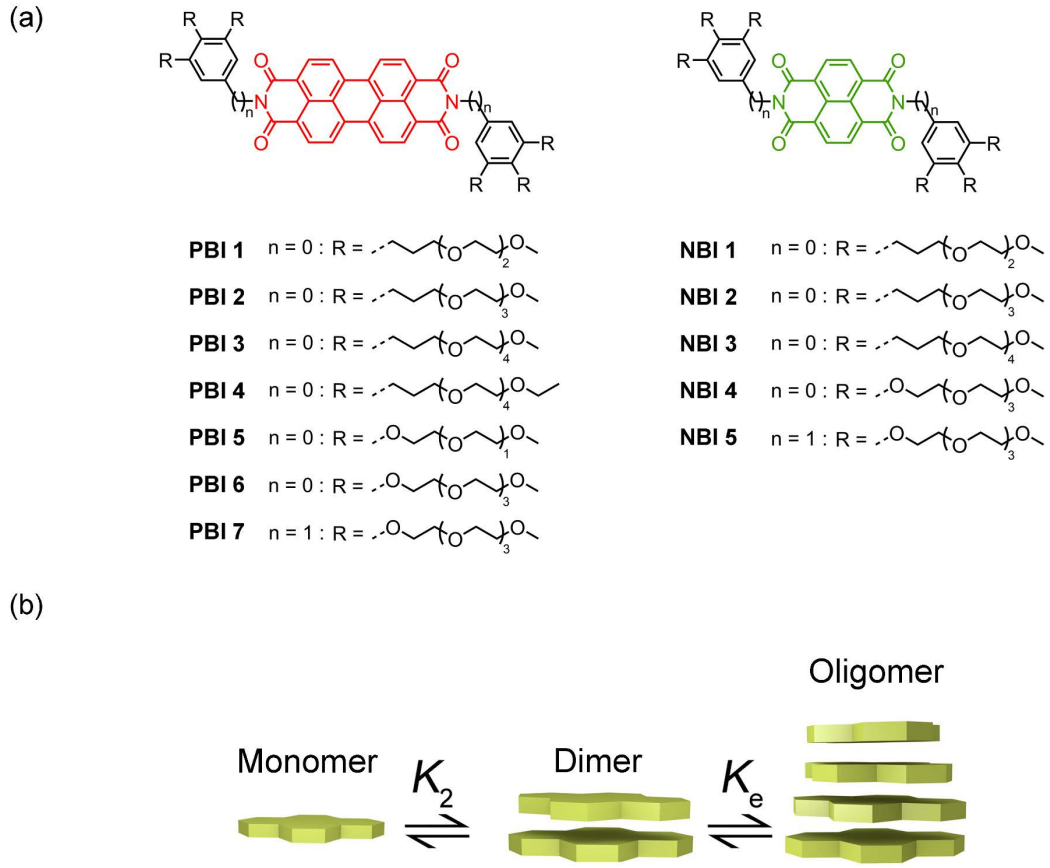


**Figure 1.1**: (a) Chemical structures of bolaamphiphilic PBIs and NBIs described in this thesis. (b) Schematic representation showing the self-assembly of NBI monomer into dimer and oligomer.

**Chapter 3-6** discusses the results of this thesis in detail. After a brief overview of synthetic routes adopted to obtain respective perylene and naphthalene bisimide bolaamphiphiles (**Chapter 3**), self-assembly studies of **NBI 1-3** are discussed in **Chapter 4**. In-depth UV-vis and ITC experiments are carried out to explore the consequences of OEG side chains on the entropically driven self-assembly in water. Furthermore, MD simulations and 2D NMR measurements are performed to rationalize the conformation of side chains and their role in orchestrating specific binding tendencies within these molecules. **Chapter 5** provides a *de novo* design strategy to realize thermodynamic bias for both PBI and NBI derivatives (**PBI 6**, **7** and **NBI 4**, **5**). The thermodynamic analysis is carried out *via* spectroscopic and calorimetric methods along with elucidation of the origin of this bifurcated response using 2D NMR and PM7 calculations. Finally, in **Chapter 6**, structural

parameters that dictate LCST associated phase separation for PBI derivatives (**PBI 1**-**6**) are investigated to realize a control over their thermoresponsiveness in water.

**Chapter 7** and **Chapter 8** summarizes the results of this thesis in English and German, respectively.

**Chapter 9** documents the experimental part of this thesis with detailed synthetic procedures for literature unknown compounds as well as materials and methods used.

In **Chapter 10**, the appendix for the Chapters 4,5 and 6 are presented.

# Chapter 2

# State of the Art

## 2.1 Driving forces for self-assembly and binding in water

### 2.1.1 Hydrophobic contributions

There are very few topics in chemistry that are as widely discussed and equally controversial as the hydrophobic effect. Nearly seven decades after Frank and Evans proposed the 'iceberg' model for water around non-polar solutes,[69] we are yet to reach a common consensus in this issue, and many accepted theories are proven and disproven each year. The following section covers a general picture of hydrophobic contributions to the association, which are frequently cited, keeping in mind that several experimental and theoretical studies have been reported contradicting even these 'commonly accepted' models.

The unique and anomalous properties of water can be traced to its structure and H-bonding capabilities in the bulk state. The $H_2O$ molecule possesses a permanent dipole moment (1.85 D) and is a strong hydrogen bond donor ($\alpha = 1.17$) and a moderate hydrogen bond acceptor ($\beta = 0.47$) according to Kamlet-Taft scale.[70] There are more than 40 models that have been proposed for the water molecule in which the charge distribution around oxygen and hydrogen atoms are defined.[71] While none of these models can describe the properties of water in all the three states, many models like TIP5P where partial charges are distributed on tetrahedral arms, has been able to successfully account for the density maximum at 4 °C and the dielectric constant of the liquid water (Figure 2.1).[72]

In solid state, the water molecules are tetrahedrally coordinated with highly directional O−H···O bonds. However, in the liquid state, the hydrogen bonds are transient with a lifetime of 0.8-0.9 ps and an average coordination number of 3.6.[73] The inherent H-bond network in liquid water is often debated and is described as 'flickering clusters'[55, 74] to account for the ring and chain-like structures (with two hydrogen bonds) rather than the expected cages (with four hydrogen bonds), as revealed by subfemtosecond experiments.[75] Nevertheless, the proton hopping in liquid water (Grotthus mechanism) points towards the

existence of a cooperative H-bond network[3], which, as we see in the following section, dictates the unusual association of nonpolar solutes in this solvent.

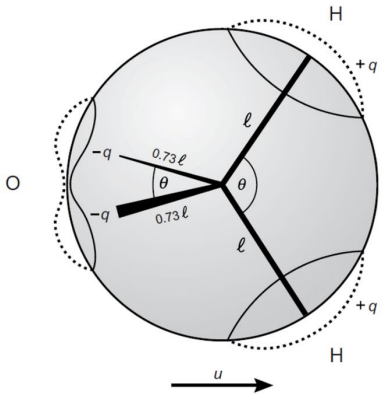


**Figure 2.1**: TIP5P model for water. $q$ = 0.24$e$, $l$ = 0.096 nm, $\theta$ = 104.5° and $\varphi$ = 109.5°. Adapted from reference[3], Copyright (2010), with permission from Elsevier.

The orientation of water molecules around a non-polar solute is heavily dependent on its size, shape as well as exogenous factors like temperature and pressure. When a solute is introduced into liquid water, the solvent molecules have to reorient themselves to accommodate this molecule. This process is termed as 'hydrophobic hydration' or 'hydrophobic solvation.'[3] If the solute is small enough, this can be achieved without sacrificing any H-bonds; however, the directionality, as well as the disorder of O−H···O bonds, are lost in this process which results in an entropic unfavorability (Figure 2.2a). For example, the dissolution of gaseous methane is accompanied by the standard free energy of solvation, $\Delta G^0$, of 25.5 kJ mol$^{-1}$ of which the enthalpic component ($\Delta H^0$) constitutes −13.8 kJ mol$^{-1}$ and the entropic component ($-T\Delta S^0$) 39.3 kJ mol$^{-1}$.[76] (The earlier approaches of calculating the standard free energy of transfer from the liquid state to water were criticized by Ben-Naim, and currently, the accepted practice is to consider the gas-water transfer).[77-79] In 1945, Frank and Evans in their classic paper stated that "when a rare gas atom or a non-polar molecule dissolves in water at room temperature it modifies the water structure in the direction of greater 'crystallinity'-the water, so to speak, builds a microscopic iceberg around it".[69] The substantiate entropic penalty and subsequent poor solubility observed for hydrocarbon dissolution was attributed to this structuring of water molecules. While earlier evidence for such an ordering came from the crystal structures of gas hydrates,[80] neutron scattering experiments by Soper and Finney on methane and other hydrocarbons in aqueous solution revealed that the strength, as well as the ordering of H-bonds around a non-polar solute, is not different from bulk.[81, 82]

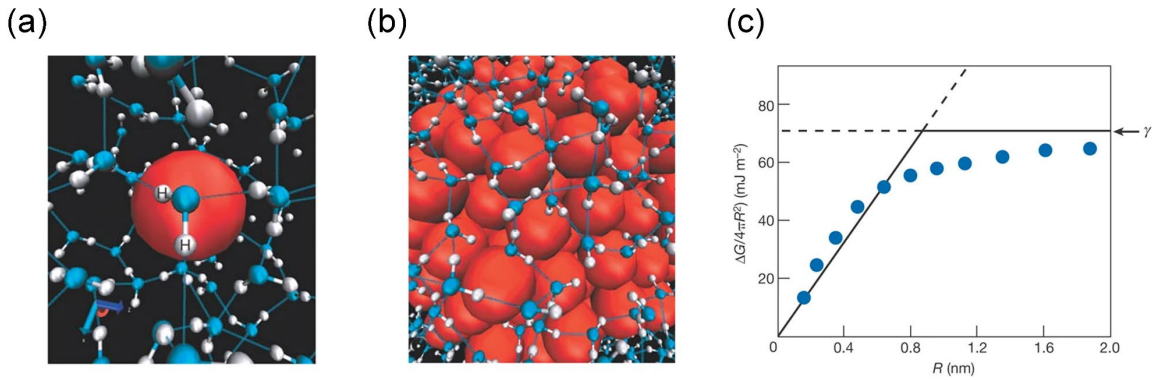


**Figure 2.2**: The arrangement of water molecules around a (a) small non-polar solute (equivalent to one methane molecule, size < 1 nm) and (b) large non-polar solute (equivalent to 135 methane molecules, size > 1 nm). (c) Solvation free energy for a spherical cavity with respect to its cavity radius showing the crossover behavior. Adapted by permission from Springer Nature: reference[4], copyright 2005.

Indeed, such inclusion of an apolar solute with accompanying negative entropy of transfer is not desirable considering the narcissistic nature of water where its network with other water molecules is more favored. This leads to the clustering of the solute where the interfaces with water are reduced compared to their individual hydrated counterparts. This process is termed as 'hydrophobic interaction' and accounts for the higher tendency of non-polar solutes to aggregate in water compared to free space. An elegant way to experimentally probe this effect was suggested by Ben-Naim on the basis of two interacting methane molecules in water.[76, 83] Since the force field produced by two methane molecules in close proximity is the same as that of an ethane molecule, the hydration shell of an individual ethane molecule in water is equivalent to that of two methane molecules clustered together. Hence, the Gibbs energy involved in the hydrophobic interaction, $\Delta G^{\mathrm{HI}}$ can be expressed as:

$$\Delta G^{\mathrm{HI}} = \Delta\mu^{0}_{\mathrm{ethane}} - 2\Delta\mu^{0}_{methane} \qquad (2.1)$$

where $\Delta\mu^{0}_{ethane}$ and $\Delta\mu^{0}_{methane}$ are the standard chemical potential of gaseous ethane and gaseous methane hydration, respectively.

In 1959, Walter Kauzmann popularized the concept of hydrophobic interactions by extending it as the major driving force for the folding of proteins[12] and later Tanford for the self-assembly of amphiphiles.[84] It should be noted that 'hydrophobic interactions' does not refer to any type of fundamental interactions like H-bonding or van der Waal's interactions, but is rather a secondary effect of the aforesaid forces.[55] The terms such as 'hydrophobic bond,' first proposed by Kauzmann[12] and perpetuated in the literature

afterward, or 'hydrophobic forces' are clearly wrong and should be abstained from using. In recent literature, the use of 'water-mediated interactions' is widely adopted to avoid this confusion.[85] The hydrophobic hydration and the resultant hydrophobic interactions are collectively referred to as 'hydrophobic effect.'

While small solutes like methane can be easily accommodated into the water by reducing the volume of configuration space available for H-bonding, it is no longer possible that the H-bonding can go around the solute as it becomes larger (Figure 2.2b).[4] Already in the early 70's Jencks and Stillinger recognized that a large hydrophobic surface perturbs the H-bonding of water molecules and can lead to an enthalpy dominated hydrophobic interaction.[86, 87] Departing from the 'iceberg model,' Chandler and coworkers explained the hydrophobic interactions at different length scales by comparing the solvation of an apolar solute to the formation of a cavity/void in the bulk water and the corresponding interfacial cost associated with it (known as Lum-Chandler-Week (LCW) theory).[4, 88] Here, the free energy of hydration of a cavity with radius '*R*' is given as:

$$\Delta G \approx 4\pi R^2 \gamma \tag{2.2}$$

where $\gamma$ is the liquid-vapor surface tension.

For small solutes, the hydration free energy at standard condition scales with the volume of the solute, whereas for a large solute, it scales with surface area (Figure 2.2c). The crossover behavior arises at 1 nm since, after this radius, an interface is formed, which is equivalent to the liquid-vapor surface tension ($\gamma$) and a microscopic dewetting is observed. The aggregation of such dewetted large solutes is enthalpically favorable since water molecules at the interface can form more H-bonds in the bulk.

Raman scattering measurements on linear alcohols have shown that the hydration shells around smaller solutes (<1 nm) is more ordered with enhanced H-bonding network, whereas after the crossover regime they are replaced by a disordered solvation shell with weaker H-bonding in comparison to bulk water.[89] A similar length scale dependence was also observed for hydrophobic polymers with aromatic monomers of different sizes *via* single-molecule force spectroscopy, in line with the theoretical predictions for microscopic dewetting mentioned above.[90]

However, studies on benzene dimerization using recently developed mean-field QM/MM method-DFT-CES have questioned this length scale dependence suggested by the LCW theory.[91] This *ab initio* method can describe the experimental hydration free energies

accurately as well as can dissect the enthalpy and entropy of hydrophobic association using a two-phase thermodynamic model. Benzene, which has a length along the molecular axis less than 1 nm, should self-assemble in an entropically driven fashion. However, at equilibrium binding distance, this entropic stabilization is compensated by the enthalpic cost of initiating the dewetting transition. As a result, the overall solute pair-interaction is driven by the enthalpically favorable electrostatic and dispersion interactions associated with the π-π stacking and not the expulsion of the hydration shell. Furthermore, the nature of interface proposed in the LCW theory, as well as the use of van der Waals-like approach appropriate only for simple Lennard-Jones fluids, has been severely criticized.[92]

The entropically favorable hydrophobic interaction associated with small solutes is often referred to as 'classical hydrophobic effect' whereas the enthalpically favored association as 'non-classical hydrophobic effect.' However, such bifurcation of hydrophobic effect originates from the studies on idealized hydrophobic surfaces (often modeled as ellipsoid plates) and not on conventional amphiphilic systems which contain both hydrophobic and hydrophilic parts. As a result, naming the hydrophobic effect based on the overall experimental thermodynamic signature is erroneous and misleading. For example, perylene bisimides have a length along its long molecular axis of 2.1 nm and should self-assemble in a 'non-classical' fashion as reported recently for an anionic di(glycyl) derivative.[93] However, Görl and Würthner have reported entropically driven self-assembly of a perylene bisimide derivative which has been attributed to the release of H-bonded water molecules from the side chains.[68] Here the overall thermodynamic fingerprint arises from multiple non-covalent interactions and not from a hydrophobic component alone. Additionally, this thermodynamic signature is highly dependent on exogenous factors like temperature. For example, entropically driven hydration of smaller alkanes which are negative at ambient conditions are shifted to positive at higher temperatures, attributed to the weakening of H-bonds (Figure 2.3a).[85, 94] Similarly, many protein folding processes are accompanied by a specific temperature where the enthalpy or entropy change associated is zero ($T_h$ and $T_s$ respectively) and reverses its sign afterwards (Figure 2.3b).[95] Hence the process can be driven by one of the parameters up to a temperature and by another one afterwards. Recently, Cremer *et al.* recommended the usage 'hydrophobic effect with an enthalpy/entropy dominated profile' instead of the terminology-classical/non-classical hydrophobic effect.[55]

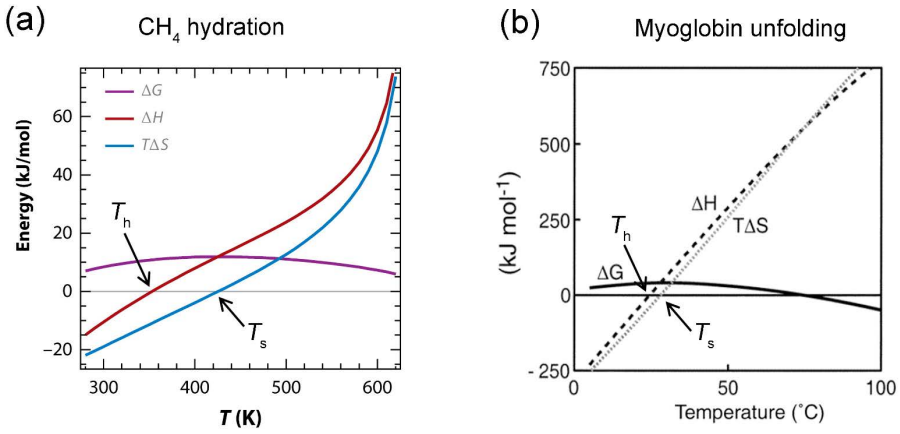


**Figure 2.3**: Temperature dependence for (a) experimental hydration thermodynamics of methane. Republished with permission of Annual Reviews, Inc., from reference[85]; permission conveyed through Copyright Clearance Center, Inc. and (b) protein (myoglobin) unfolding. Adapted with permission from reference[95]. Copyright 2002 American Chemical Society.

The popularity of hydrophobic effect is often attributed to its implications in biological processes like protein folding, the formation of lipid bilayers, the base pairing of DNA, recognition of ligands by proteins etc.[84] While most of these processes are driven by the synergetic effect of multiple factors including steric constraints, H-bonds, electrostatic interactions, etc., it has been proposed that the hydrophobic effect contributes nearly three quarter to it.[13] Initial insights into their influence on biomolecular processes were inspired by the identical temperature dependence of protein unfolding and transfer of small molecules to water.[95] Later, it was also extended for ligand binding in the active site of a protein. The classical 'protein-centric' view of biomolecular recognition was motivated by the 'lock-and-key' principle, where the size complementarity of the active site and ligand dictates the association. However, several pioneering studies on human carbonic anhydrase (HCA) by Whitesides have shown that the hydrophobic effect in protein-ligand binding depends on the nature of water molecules at active sites as well as around the ligand, which led to a 'water-centric' view, widely accepted today (Figure 2.4).[13, 96-98] Theoretical studies on the binding of alcohols with major urinary protein (MUP) using explicit solvation model also confirms this view.[99] Hence, designing a ligand with favorable association should rely on how effective it is able to displace the hydration shell in the binding pocket, rather than the interactions between protein and ligand itself.

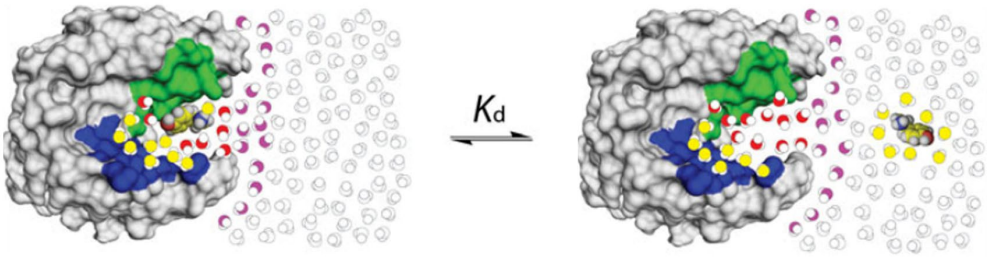


**Figure 2.4**: 'Water-centric' view of ligand binding. The water molecules are shaded based on their thermodynamic characteristics relative to the bulk water. The white water molecules have the same free energy as of bulk, yellow have less favorable entropy than bulk, whereas red represents those with less favorable enthalpy than bulk. Purple water molecules reside at polar regions of proteins and are more stable than bulk water. The green and blue color of protein surface represent hydrophobic and polar regions respectively. Reprinted by permission from Springer Nature: reference[13], copyright 2014.

Despite its popularity, the views on the hydrophobic effect are plagued by many contradicting theories. It should be noted that the very word 'hydro*phobic*' is disputable as there are no repulsive interactions between water and apolar solutes, but rather significant attractive interactions aided by van der Waals forces.[3, 85] As Gibb *et al.* pointed out in a recent review, "the most honest statement about the hydrophobic effect is that we are far from fully understanding it."[70]

### 2.1.2 High-energy water

Already in the early 1990s, Diedrich and coworkers identified very high enthalpic favorability for the association of aromatic hydrocarbons with water-soluble cyclophanes, in contrast to the entropically driven nature associated with the conventional hydrophobic effect.[100] While the release of cavity water leading to the exothermic nature for such host-guest binding has been theoretically postulated earlier,[101, 102] quantitative exploration of this effect was first conducted by Biedermann and De Simone *et al.* on their investigations of the binding studies on cucurbit[*n*]urils (**1-4**, CB*n* with *n*=5-8) (Figure 2.5).[103]

The affinity of CB*n* with organic guests are very high (*K* up to $10^{17}$ $M^{-1}$), in comparison to most of the synthetic macrocycles and surpassing one of the strongest natural non-covalent interaction pair, biotin-avidin complex.[104] This binding affinity with neutral organic residues is highly dependent on the cavity size of the cucurbituril, with CB7 possessing an intermediate cavity size showing the highest affinity. MD simulations conducted to explore the hydration of these CB*n* series showed significant differences in the number as well as H-bonding capacity of water inside these hydrophobic cavities (Figure 2.5c). Since the

entropic gain of filling water molecules cannot compensate for the enthalpic cost of breaking the hydrogen bonds, host cavities with a radius less than 1 nm are essentially 'dry.'[105, 106] This is the case for the smallest CB*n* derivative with five glycoluril units, CB5. However, with an increase in cavity size, it is more favorable to fill it with water molecules, albeit the energetic cost, as "nature abhors a vacuum." However, water-water interactions in these CB*n* cavities are impaired compared to those in bulk due to the lesser H-bonding network as well as a less favorable potential energy of water molecules inside the cavity. These energetically frustrated water molecules are called 'high-energy' water (Figure 2.5b). It is precisely the release of this high-energy water molecules which drive the guest binding with high affinities for cucurbiturils in water. The total energy of high-energy water increases with cavity size since the absolute number of water molecules increases. On the other hand, the energy of individual water molecules decreases with cavity size as more stable H-bonded networks can be formed. For example, MD simulations indicate that the H-bonding network in the largest CB*n* homolog CB8, is structurally similar to the bulk phase. To scale this effect for a variety of hosts, it is imperative to introduce a parameter '*Z*' to reflect the effect of high-energy water[107], which is expressed as:

$$Z = N(3.62 - m) \qquad (2.3)$$

where '*N*' is the total number of water molecules inside the cavity, 3.62 is the average coordination number for liquid water and '*m*' is the average H-bonding count per water molecule within the cavity.

The higher binding tendency of CB7 ($Z$=8.7) in comparison to CB6 ($Z$=6.3) and CB8 ($Z$=7.3) can be associated with the intermediate cavity size, which favors maximum contribution from the high-energy water. Isothermal titration calorimetry with a series of neutral guests with the aforementioned hosts suggests a very high enthalpic gain upon binding (up to $\Delta H = -75$ kJ mol$^{-1}$ for the binding of CB7 and 2,3-diazabicyclo[2.2.2]oct-2-ene (DBO)), which results from new H-bond formation of these energetically frustrated water molecules when they are released into the bulk.[103]

Apart from the cavity size, the chemical functionality of the cavity also plays a crucial role in determining the effectiveness of high energy water. The presence of functionalities that act as a H-bond donor or acceptor can affect the energy of water molecules within the cavity. For example, $\alpha$-cyclodextrin ($\alpha$-CD) and CB6 have similar cavity dimensions as well as the number of cavity water molecules.[107] However, the binding affinity of 1-butanol

with CB6 ($K$=1200 $M^{-1}$) is higher than in $\alpha$-CD ($K$=80 $M^{-1}$) and is enthalpically more favored. ($\Delta H$ [CB6] = −30.3 kJ $mol^{-1}$ < $\Delta H$ [$\alpha$-CD] = −11.6 kJ $mol^{-1}$).[108, 109] This can be explained based on a more significant effect of high-energy water for CB6 ($Z$ = 6.3) than for $\alpha$-CD ($Z$ = 3.1) based on MD simulations.[107] The cavity water cluster in $\alpha$-CD is more stabilized due to the inward-facing oxygen lone pairs by H-bonding. As a result, the exothermic driving force, as well as the binding affinity, is decreased for the latter. Traditional design concepts that focus on size complementarity inspired by the 'lock and key' principle should be reevaluated for systems in water to accommodate for this influence on the cavity water strength.

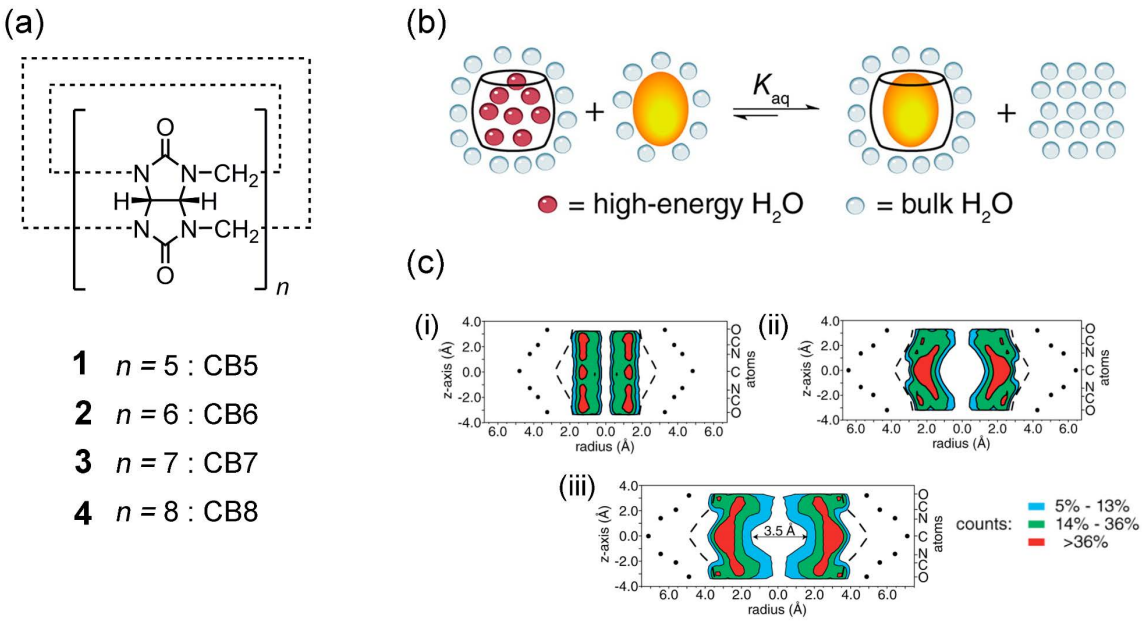


**Figure 2.5**: (a) Chemical structures of CB5 to CB8 (**1**-**4**). (b) Schematic diagram showing the release of high energy water molecules upon binding with guests. (c) Distribution of cavity water molecules in CB6 (i), CB7 (ii), and CB8 (iii). Dots represent the location of CB atoms, and the dashed line shows the corresponding inner vdW surface. Adapted with permission from reference[103]. Copyright 2012 American Chemical Society.

Finally, the shape of the host molecule also plays a vital role in the optimal formation of high-energy water inside the cavity (Figure 2.6).[107] Generally, a concave and a deep cavity is a prerequisite since they can effectively screen the H-bonding of cavity water with that of bulk. This is the case for a wide variety of molecular barrels, cups, and some molecular tweezers. Flat structures, as in the case for numerous π-conjugated chromophores, cannot screen the surface water from that of bulk and hence are ineffective for the generation of high-energy water.

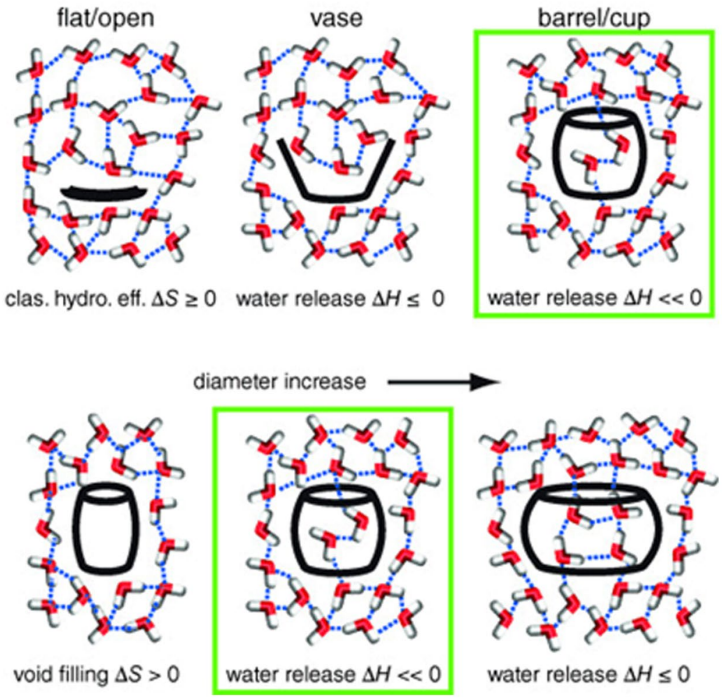


**Figure 2.6**: Influence of the geometry on the configuration of high-energy water molecules and resultant changes in thermodynamics upon binding with a guest. Reproduced with permission from reference[107]. Copyright 2014 Wiley-VCH Verlag GmbH & Co. KGaA, Weinheim.

Extending the concept of high-energy water from artificial receptors to biopolymers like proteins or DNA is not straightforward as the latter contain various functional groups that can stabilize the water molecules at the active site. Whitesides *et al.* have identified that the water displaced from the active site of human carbonic anhydrase (HCA) is the predominant determinant of thermodynamic fingerprint for the binding of various benzothiazole sulfonamide ligands.[57] Similarly, Klebe and coworkers attribute the enthalpically favorable binding of thermolysin with a series of hydrophobic ligands to the release of conformationally restricted water molecules.[14] The development of new computational tools like WaterMap[110] and Szmap[111] are able to dissect the thermodynamic properties in terms of water-structure and might be vital for our understanding of high-energy water in terms of drug-designing and protein folding.

While the influence of high-energy water has been identified for a wide variety of artificial hosts in guest binding, its influence on directing self-assembly has been mostly overlooked. Indeed, flat π-conjugated amphiphiles, which constitute the lion's share of aggregation studies, do not harbor any energetically frustrated water molecules since they can directly form H-bonds with the bulk water. However, it has been identified that naphthalene based tweezer **5** and anthracene based clip **6** undergo dimerization in water with high binding

constants ($K$ (**5**) = 22.8×10$^5$ M$^{-1}$, $K$ (**6**) = 1.6×10$^5$ M$^{-1}$) and high enthalpic favorability ($\Delta H$ (**5**) = −20.9 kcal mol$^{-1}$, $\Delta H$ (**6**) = −13.8 kcal mol$^{-1}$) estimated with van't Hoff plots (Figure 2.7a, c).[112] Recent water box simulations on their core structures have shown the presence of high-energy water despite the lack of a closed cavity.[107] Hence, it can be assumed that the enthalpically favorable dimerization is driven by the release of these high-energy water molecules (Figure 2.7b). As non-planar π-conjugated structures consisting of warped[113] or bowl shape[114, 115] are recently gathering attention; it would be interesting to explore the influence of cavity water molecules in directing their self-assembly.

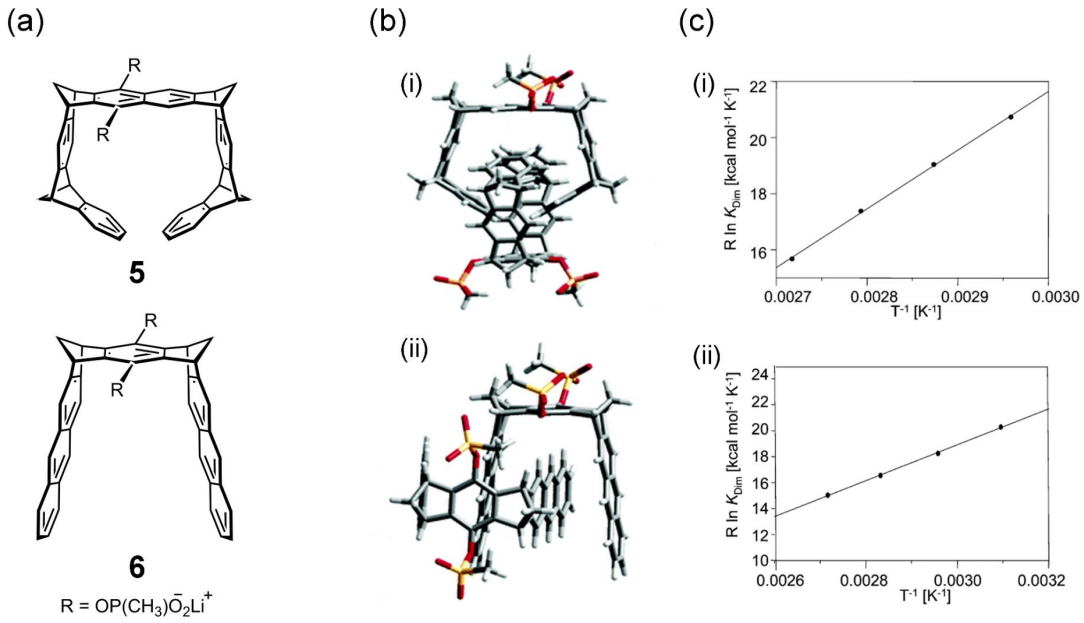


**Figure 2.7**: (a) Chemical structures of tweezer **5** and clip **6**. (b) Force-field calculation of dimer structures of **5** (i) and **6** (ii). (c) Van't Hoff plots for the self-assembly of **5** (i) and **6** (ii) in $D_2O$ showing enthalpically driven association. Adapted with permission from reference[112]. Copyright 2006 American Chemical Society.

Similar to hydrophobic effect, the role of high-energy water in directing exothermic binding is also not devoid of criticisms. Ben-Amotz proposed that any contributions arising from the water-reorganization enthalpy are compensated by water-reorganization entropy and, as a result, has no contribution towards overall free energy change.[85] This is because the chemical potential of all water molecules in an equilibrium solution is the same. While the enthalpy and entropy of cavity water and bulk water may differ, their free energies cannot, and as a result, there is no free energy driving force for host-guest binding. However, Kinoshita *et al.* argued that the chemical potentials are dependent on the inter solute distance (provided they are not far apart) and hence can induce binding, even in the absence of direct water-solute interactions.[116]

### 2.1.3 Dispersive interactions

Dispersion forces originate from the interactions between charge fluctuations in the electron distributions of atoms[117, 118], and constitute the third most crucial contribution towards van der Waals force.[119] They direct many important phenomena such as protein folding, wetting, adsorption, physical properties of gases, liquids etc.[3] *Ab initio* calculations have shown that dispersion interactions play a significant role in supramolecular complex formation and incorporating corresponding corrections can increase the accuracy of theoretical predictions.[120, 121] However, molecular balance experiments for both alkyl and aromatic stacking have revealed that in solution, these forces are attenuated by solvent molecules and hence have smaller influence compared to *in vacuo*.[122, 123]

While dispersion interactions may be hampered in solution, it can still be a major driving force for binding in water compared to organic solvents. This is attributed to the low bulk polarizability of water ($\alpha$=1.57Å$^3$) compared to organic solvents, and hence it competes less with dispersion interactions.[15] Despite this, the role of such forces has been largely overlooked in aqueous supramolecular chemistry barring a few exceptions, presumably due to the overshadowing of hydrophobic effect. Iverson *et al.* investigated the stacking of electron-poor 1,4,5,8-naphthalene bisimide (NBI) derivative **7** and electron-rich 1,5-dialkoxynaphthalene (DAN) **8** in solvents of different polarities and computed the association constants using $^1$H NMR experiments (Scheme 2.1).[124] Surprisingly, the trend in association constants is in line with the bulk polarizability of solvents, indicating the role of dispersion forces in directing aromatic stacking. While the very high binding constant in water can be attributed to solvophobic effects as the authors suggest, it might be supplemented by dispersion interactions. A similar observation was also noted by Würthner and coworkers for the self-assembly of a bolaamphiphilic perylene bisimide derivative, where an increase in association constants can be found with a decrease in bulk polarizability of the solvent.[64]

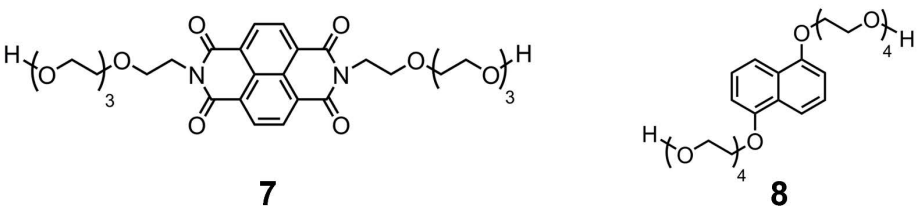

**7** **8**

**Scheme 2.1**: Chemical structures of electron-poor NBI derivative **7** and electron-rich DAN derivative **8**.

While the above examples indicate the possible contribution of dispersion in stacking, the successful differentiation of these forces from solvophobic contributions was first carried out by Schneider and coworkers.[125, 126] They investigated the association of water-soluble porphyrin **9** with a variety of guest molecules containing different functionalities (Scheme 2.2). The contributions of alkyl groups were observed to be minimal (~1-2 kJ mol$^{-1}$ per $CH_2$ group), whereas a single nitro group, irrespective if it is in an aliphatic or aromatic fragment, contributes nearly 5 kJ mol$^{-1}$ to the overall association. This indicates the smaller role of hydrophobic effect in driving the association in comparison to dispersion interactions. The increase in binding strength with increasing polarizability, for example, within halogens and in molecules with $sp^2$ character, shows that it is indeed the dispersion interactions that predominantly drives the association. In another example, authors studied the binding of a related porphyrin derivative, **10** with heteroarenes and found that the association strength depends on the contact size as well as the polarizability of substituents, and not on their hydrophobicity or the location of electronegative atoms (*i.e.*, electrostatic contributions), which is also in line with dispersive contributions.[127]

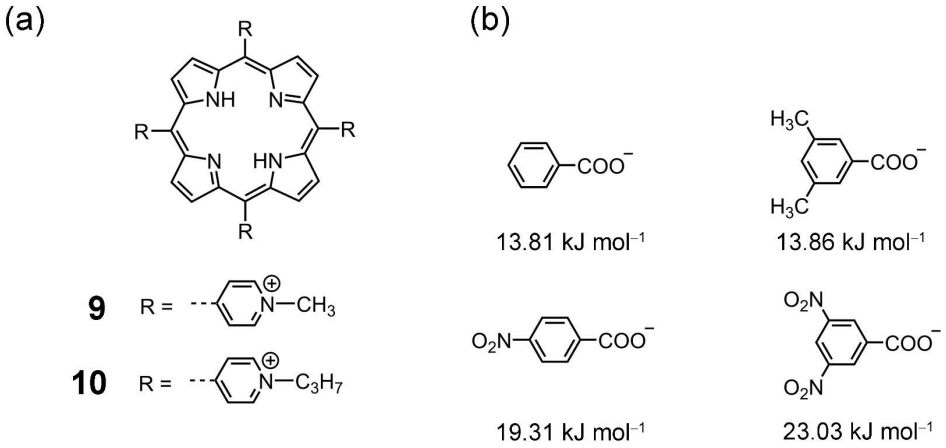


**Scheme 2.2**: (a) Chemical structures of porphyrin derivatives (**9** and **10**) and (b) some guest molecules with the corresponding free energy change of binding (with **9**). Data taken from reference[125].

Recently, Biedermann and Nau *et al.* investigated the binding of noble gases with cucurbituril derivative, CB5 (**1**) by $^1$H NMR displacement measurements, and dissected the dispersion and cavitation energies which direct the association (Figure 2.8).[128] At first, the authors estimated the binding free energies in the gas phase using the Born-Haber cycle along with dispersion-corrected density functional theory and concluded that dispersion forces indeed drive the association in the gaseous state (Figure 2.8b). However, in water, the energetic cost of forming a vacuum associated with the hydration of noble gases also

comes into play along with the former. Surprisingly, the dispersive interactions are disfavored since the polarizability of the CB5 cavity is less than that of bulk water. Hence, the driving force in aqueous media solely comes from the cavitation energy, which is smaller inside the host for noble gases than in the bulk. The net free energy of binding is therefore the sum of unfavorable dispersion energies and favorable cavitation energies, which matches well with theoretical predictions (Figure 2.8c). While this study signifies the counteracting dispersion forces in binding, the authors themselves point out that CB5 is an exception rather than the norm, since most other macrocyclic hosts have larger polarizable cavities where the role of cavitation energies becomes less. This exceptional study hence advocates for the explicit consideration of dispersion forces in host-guest binding in water.

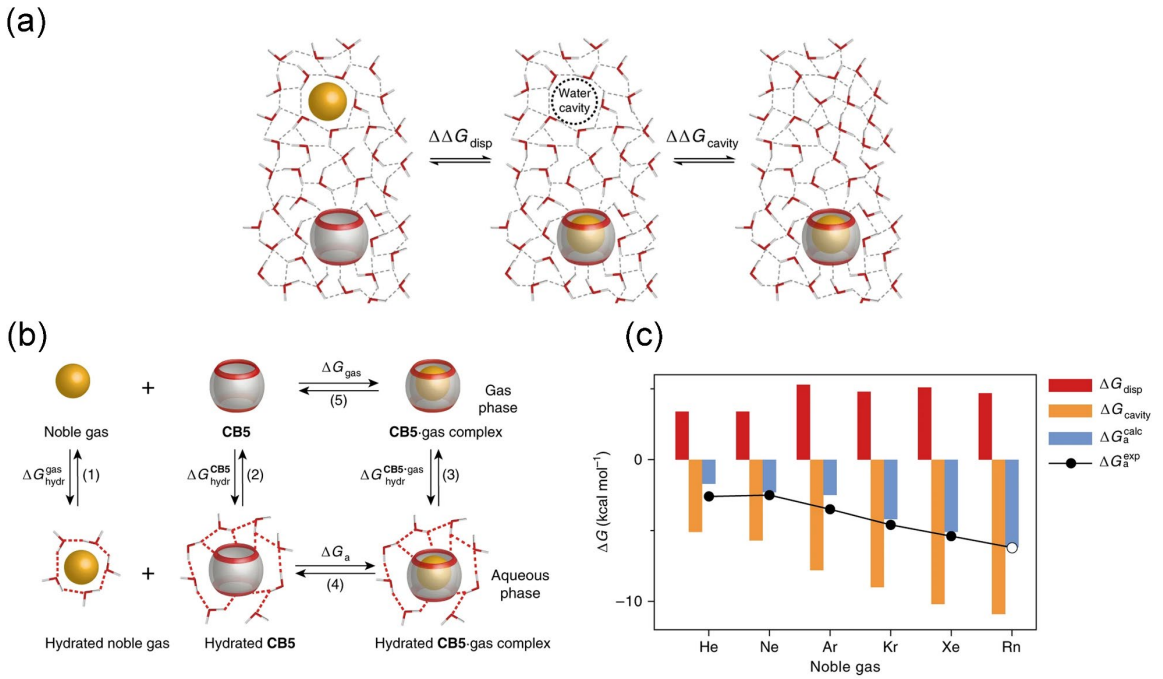


**Figure 2.8**: Schematic diagram showing the (a) binding of a noble gas with CB5 in water with the recovery of cavitation free energy and (b) association in gaseous and aqueous phases with related free energy changes. (c) Contributions of dispersion and cavitation free energies to the overall association free energy of different noble gases. Reprinted by permission from Springer Nature: reference[128], copyright 2018.

The dispersive interactions also play a significant role in stabilizing biological structures. For example, inhibition of serine protease factor by phenyl acetamide derivatives with halogen substituents is dependent on the polarizability of halogen atoms.[129] Similarly, the thermal unfolding of a $\beta$-hairpin peptide is dictated by the dispersive interactions between the N-terminal phenylalanine and halogen substituents on the opposing phenyl ring.[130] The

enthalpic driving force of its folding is correlated with the polarizability of halogen atoms and is attributed to dispersive forces along with halogen-π interactions.[126] Sulphur-arene interactions with polarizable sulfur groups like −SH and −SMe commonly found in proteins is also associated with dispersive forces. For example, −SMe group of methionine is often found adjacent to tryptophan attributing to sulfur-arene interactions[131], which contributes nearly 2-5 kJ $mol^{-1}$ for the protein stability.[132] It has even been suggested that the primary driving force for double helix formation in DNA is stacking interactions and not the widely popular hydrogen bond between nucleotides.[15, 125, 133] The replacement of A-T base pairs with non-hydrogen bonding stacking units have found to have the same stability as a native DNA by melting temperature measurements.[134] While such claims should be thoroughly inspected to include the contributions from electrostatic, hydrophobic and other interactions, it is indisputable that the dispersive forces play a non-trivial role in directing the self-assembly and binding, especially in aqueous media.

### 2.1.4 Other interactions (H-bonds, metal-ligand etc.)

Apart from the aforementioned driving forces which dictate association in water, other non-covalent interactions like H-bonding or metal-ligand interactions can also be used for this purpose. However, since most of these forces compete with water, necessary design principles are required either to screen them from the solvent or multiple binding motifs have to be combined to achieve substantiate association.[135] For example, H-bonds are widely used for self-assembly in organic media due to their directionality and complementarity. However, in protic solvents like water, they are largely attenuated. Meijer *et al.* have shown that by creating a hydrophobic microenvironment, H-bonds can be shielded in water and can hence drive self-assembly (see section 2.2.1).[136-138]

While relatively less explored, coordination bond between a metal and an organic ligand is also attractive to generate supramolecular structures in water, and are more stable than H-bonded assemblies. Fujita and coworkers have reported several palladium(II) based systems in aqueous media which constitute a wide range of geometries.[139] Nitschke reported a water-soluble tetrahedral cage by the interaction of Fe(II) and a pyridine derivative which was used for the encapsulation of white phosphorous and render it air-stable.[140]

In nature, electrostatic interactions between charged species play a major role in determining the activity of enzymes and proteins.[141] Here, the microenvironment at the

active site is stabilized by the expulsion of water molecules. Such a strategy is often hard to adopt for small artificial assemblies since most of the interacting sites are exposed to the high dielectric medium of water and hence compete with ion-pair formation.[142] Nevertheless, Reinhoudt exploited amidinium-carboxylate interactions distributed on two calix[4]arenes (**11** and **12**) to generate one of the first water-soluble capsules (Figure 2.9).[143] ITC studies revealed surprisingly high association constant for the exothermic complex formation ($K = 3.3\times10^4$ $M^{-1}$) in borate buffered water with a positive entropy change, which the authors attribute to the release of solvent molecules. The self-complementary assembly of zwitterionic peptides, especially dipeptides with hydrophobic residues, also utilizes ion-pair formation to yield microporous crystalline materials.[142] Often, combining multiple weak forces is a prerequisite to generate such robust assemblies in water.

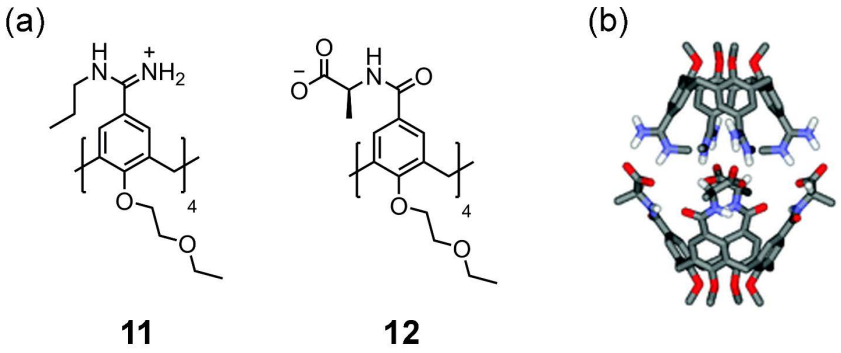


**Figure 2.9**: (a) Chemical structures of oppositely charged calix[4]arene half-spheres (**11** and **12**) and (b) the capsule formed by the ion-pair interaction of **11** and **12** (glycol chains and apolar/achiral hydrogen atoms omitted for clarity). Reproduced from reference[142] with permission from The Royal Society of Chemistry.

## 2.2 Self-assembly of π-amphiphiles in water

### 2.2.1 Smaller π-scaffolds

While smaller π-amphiphiles possessing benzene or its heterocyclic derivative cores can aggregate in water by virtue of hydrophobic effect, in general, such assemblies are quite weak to yield stable supramolecular polymers. Hence, it is quintessential to supplement the stacking of hydrophobic units with a secondary interaction like H-bonding. However, unlike most organic solvents, water strongly competes with this interaction, and an appropriate microenvironment has to be created to shield it from the bulk medium.

Meijer *et al.* pioneered mechanistic investigations of supramolecular polymerization utilizing a model compound, benzene-1,3,5-tricarboxamides (BTAs), decorated with H-bonding amide groups at 1,3,5 positions of a benzene ring. Generally, they form robust

one-dimensional assembly by three-fold α-helical type intermolecular H-bonding in alkane solvents in a cooperative fashion.[19, 144, 145] However, obtaining such stable assemblies in aqueous media facilitated by H-bonding is only possible when they are shielded with an aliphatic spacer. For example, BTA derivatives **13** and **14** appended with solubilizing oligo ethylene glycol chains are linked to the amide moiety by chiral and achiral aliphatic spacers (Figure 2.10a).[137] Both molecules self-assemble in water into micrometer long narrow fibrillar aggregates, as revealed by TEM measurements (Figure 2.10b). However, no discernible aggregation in water was observed for the BTA derivative **15**, where the side arms are connected directly to the H-bond donor.[145] The length of the spacer used for shielding also proved to be critical, as a decyl spacer instead of the dodecyl spacer (as in **13**) does not stabilize intermolecular amide-amide interactions and fails to generate high-aspect-ratio polymers as in the former case.[138] The introduction of homochirality in **14** by stereogenic methyl in the alkyl spacer does not perturb the supramolecular structure as both **13** and **14** form fibers with comparable dimensions. However, it increases the internal order as well as the persistence of H-bonding within the fibers, which in turn reduces the monomer exchange rate in comparison to the achiral derivative, **13**.[146]

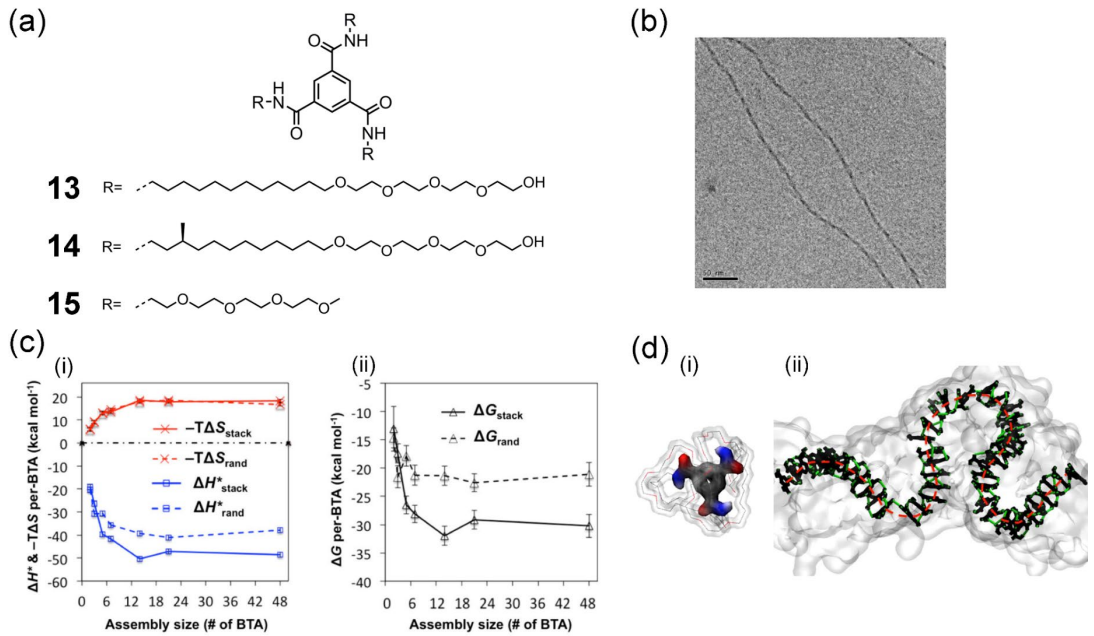


**Figure 2.10**: (a) Chemical structures of BTA derivatives **13-15**. (b) Cryo-TEM image of **13** in water showing long fibrillar aggregates. Reproduced from reference[137] with permission from The Royal Society of Chemistry. (c) Enthalpy and entropy changes (i) and free energy change (ii) per BTA assembly, where the solid lines represent ordered stacks and dashed lines denote disordered aggregates. (d) Equilibrated structure of BTA monomer (i) and a stack of 48 BTA units (ii) showing folding of side chains (primary folding) and folding of the fiber itself (secondary folding). Adapted with permission from reference[147]. Copyright 2016 American Chemical Society.

While the mechanistic aspects of BTA self-assembly in organic media are well established, experimental probe into their aggregation in water is hindered by their robust assembly, which is resistant to depolymerization. Hence, the interplay of hydrophobicity and H-bonding in stabilizing such BTA stacks was investigated by all-atom MD simulations by Pavan *et al*.[147] It was observed that the stability of **13** stacking is maintained only after a persistent length of ~14 BTA monomers, after which the favorable enthalpy and unfavorable entropy of self-assembly attain convergent values, suggesting cooperativity (Figure 2.10c). Furthermore, during the MD regime, the oligo ethylene side chains undergo folding (primary folding) to screen the BTA core from the bulk water, and the fibers themselves undergo further folding (secondary folding) to additionally reduce the exposed hydrophobic surfaces (Figure 2.10d). The major contribution towards enthalpic stabilization of higher-ordered aggregates originates from the electrostatic interactions arising from the H-bonding, which contributes ~ −3.4 kcal $mol^{-1}$ per BTA to the overall free energy. However, different from the trifold H-bonding observed for BTA assembly in organic solvents, here, the average BTA-BTA H-bonds are limited to 2 due to the competition with water as well as structural defects. While the presence of H-bonds is not indispensable for the formation of such fibrous structures in water (the analog of **13** with non H-bonding ester also forms one-dimensional fibers), it serves as a linchpin for the stability and persistence of supramolecular polymers formed by BTA association.

Instead of the oligo ethylene glycol substituted $C_3$-symmetrical derivatives mentioned above, charged metal chelate complexes can be appended on the periphery to control the structure of aggregates as well as the self-assembly mechanism in water. In **16**, the BTA core is extended with a fluorinated L-phenylalanine and an aminobenzoate spacer to facilitate the hydrophobic environment for H-bonds, whereas water solubility, as well as ionic character, is imparted by the hydrophilic metal chelate complexes (Figure 2.11a).[17] While **16** is charge neutral, **17** and **18** contain one and two negative charges per arm respectively which impart Columbic frustration on the discotic assembly. Mechanistic investigations on their enthalpy-driven self-assembly have shown that **16** and **17** follow a cooperative mechanism, while **18** with the highest charge frustration on the periphery, aggregates in an anti-cooperative fashion. This is also manifested in the morphology of columnar stacks where elongated fibers with high aspect ratio were observed for **16**, whereas **18** self-assembles into discrete spherical particles (Figure 2.11b). The role of electrostatic repulsions in confining the aggregate growth in the case of **18** was confirmed

by aggregation studies at higher ionic strengths, where the cooperativity, as well as the rod-like structure, is restored due to electrostatic screening. Further studies have shown that the activation constant, and hence, the cooperativity is directly linked to the salt concentration of aqueous buffer which acts as an external feedback to control the discotic assembly.[148]

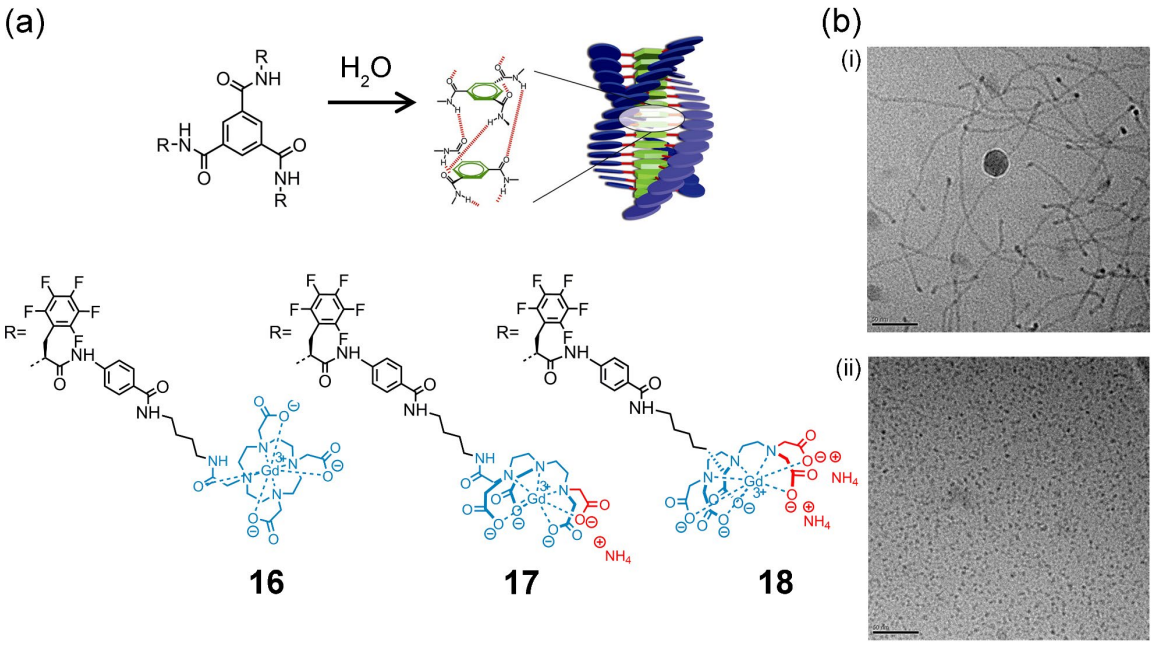


**Figure 2.11**: (a) Chemical structures of BTA derivatives **16**-**18** and schematic representation of the self-assembly in water by triple H-bonds. (b) Cryo-TEM image of **16** in the water showing long fibers (i) and of **18** showing spherical particles (ii). Adapted with permission from reference[17]. Copyright (2010) National Academy of Sciences, U.S.A.

One of the first examples for entropy-driven self-assembly for artificial systems was demonstrated by Fenniri *et al.* on the hierarchical assembly of heteroaromatic bicyclic base **19** conjugated with a crown ether periphery (Figure 2.12a).[149] The complementary donor-donor-acceptor and acceptor-acceptor-donor functionalities of the monomer result in intermolecular H-bonding to produce a rosette type macrocycle stabilized by 18 H-bonds (Figure 2.12b (i)). The hydrophobic nature of this supermacrocycle leads to a secondary organization into nanotubes with tunable pore size depending on the chemical functionality (Figure 2.12b (ii)). Temperature-dependent DLS and TEM studies have revealed that the latter process is driven by entropy, as an increase in the tube length was observed at higher temperatures (Figure 2.12c). While **19** self-assembles into a racemic mixture in its native state, the addition of chiral amino acid promoters which binds to the crown ether moiety can produce nanotubes with predefined helicities, where the degree of chiral induction depends on the chemical nature of amino acid.[150]

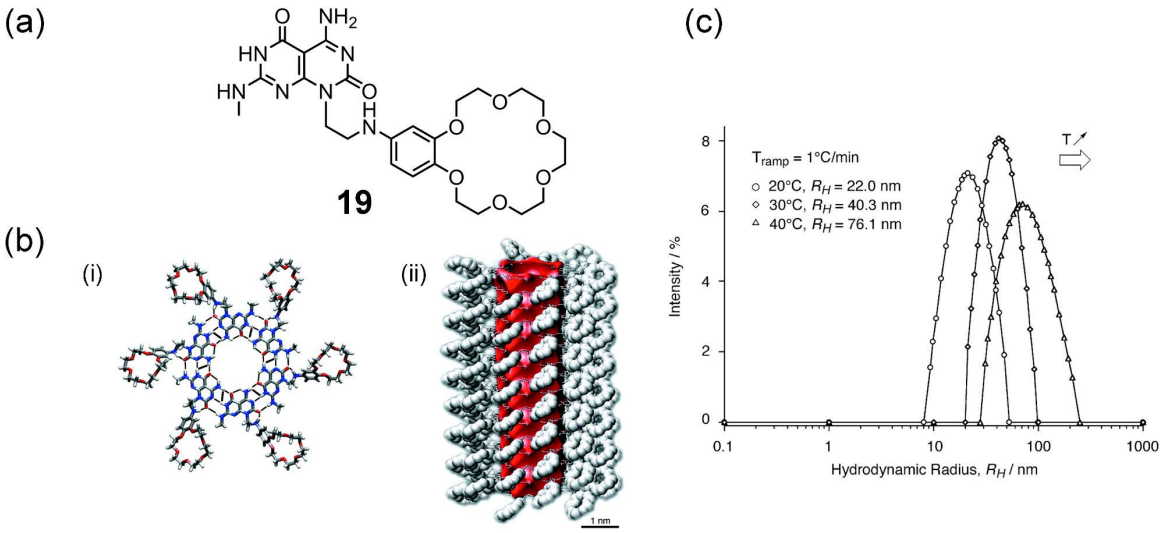


**Figure 2.12**: (a) Chemical structure of bicyclic base **19**. (b) Primary assembly of **19** into rosette macrocycle (i) and subsequent entropically driven assembly into helical nanotubes (ii). DLS profile of **19** in water at different temperatures. Adapted with permission from reference[149]. Copyright (2002) National Academy of Sciences, U.S.A.

In most of the above-mentioned examples, the role of H-bonding is well explored in terms of their consequences in mechanism as well as morphology. However, the influence of the aromatic core is often overlooked. Kieltyka and coworkers studied the aromatic interaction energies in the self-assembly of a bis(squaramide) bolaamphiphile, which aggregates into stiff micrometer-long fibrils in water.[151] The assembly of such derivatives generally occurs by the synergetic effect of H-bonding and π-π stacking. However, nucleus-independent chemical shift (NICS) calculations have shown that the aggregation is accompanied by an aromatic gain where the pentamer shows 30% more aromatic character than the monomer, enabled by the orbital overlap between squaramide units. The role of aromatic stabilization was further exemplified by the studies on an analogous bis(urea) based isostere, where the absence of such an aromatic gain leads to a higher critical aggregation concentration (CAC) and worm-like shorter nanostructures.

### 2.2.2 Naphthalene bisimides (NBIs)

Similar to their larger perylene bisimide counterparts (see section 2.2.3), naphthalene bisimides have also been employed widely to obtain insights into the self-assembly of π-amphiphiles. The design principles to render them water-soluble are similar to that of PBIs (*vide infra*), where hydrophilic side arms are appended on the imide positions.

Pioneering studies on NBI self-assembly, as well as its co-assembly with electron-rich systems, were conducted by Iverson and coworkers in the early 1990s. They synthesized

the first aromatic foldamer in water (termed 'aedamer') by alternate networking of 1,5-dialkoxynaphthalene (DAN) and 1,4,5,8- naphthalenetetracarboxylic bisimide (NBI), with peptide linkers that fold into pleated structures in water by donor-acceptor interactions.[152] Later investigations of aromatic stacking operating in such systems revealed pronounced hydrophobic effect in directing their association in water, which the authors ascribed on the solid-state geometry (face-centered for DAN: NBI, off-set stacking for NBI: NBI) and thus the hydrophobic area exposed to the bulk water.[124, 153] However, studies on an analogous NBI derivative has revealed that the packing is different in the crystalline state where the offset leads to a weak blue emission *versus* in water where strong green emission (aided by preassociated excimer formation) is observed, attributing to a more compact packing.[154]

NBIs can be rendered water-soluble by substitution of zwitterionic peptide residues at imide positions in contrast to the non-ionic oligo ethylene glycol chains widely used. Unlike the latter, which does not significantly perturb the fate of π-stacked aggregates, these charged units can determine the type, as well as properties of aggregates formed, as electrostatic repulsions, can destabilize specific packing arrangements. Unsymmetric NBI-peptide conjugates, **20** and **21** are equipped with a dilysine peptide backbone to drive the *β*-sheet formation and an NBI chromophore (at the *ε*-amino position) to drive π-π stacking (Figure 2.13a).[155] While **20** forms helical nanofibers, **21** self-assembles into twisted nanoribbons in water (Figure 2.13b). Here, the position of ammonium terminal of lysine efficiently sequesters the hydrophobic core and leads to the stacking of two *β*-sheet aggregates resulting in the ribbon-like morphology. If the charged carboxyl units of L-lysine are appended on both imide positions as in the case of symmetrical NBI derivative **22**, then it assembles first into nano-rings which stack atop each other to produce micrometer long nanotubes with a slip-stacked arrangement of chromophores (Figure 2.13c, d).[156] Here, the attractive electrostatic interactions are crucial for such hierarchical self-assembly, as no discernable nanostructures were observed for the corresponding methyl ester. Very recently, Ulijn and coworkers utilized this peptide dependent self-assembly to generate different target structures by *in situ* editing of imide substituents.[157] Bolaamphiphile **23** is substituted on both sides with *L*- and *D*- enantiomers of tyrosine methyl ester, which results in a *meso* structure with no net chirality (Figure 2.13a). By using an enzyme that preferentially catalyzes *L*-amino-acid terminus (α-chymotrypsin) for hydrolysis or amide formation, an enantio-specific internal delay can be generated. The incorporation of different amino acid amides to **23** with varying hydrophobic/hydrophilic

nature, pathway complexity can be created with consequences on the self-assembling structures as well as its chirality. This not only enables temporal control over the morphology of aggregates (2D-sheets→nanofibers→tubular structures), but also aids in the modulation of electrical conductance, which can be transiently tuned.

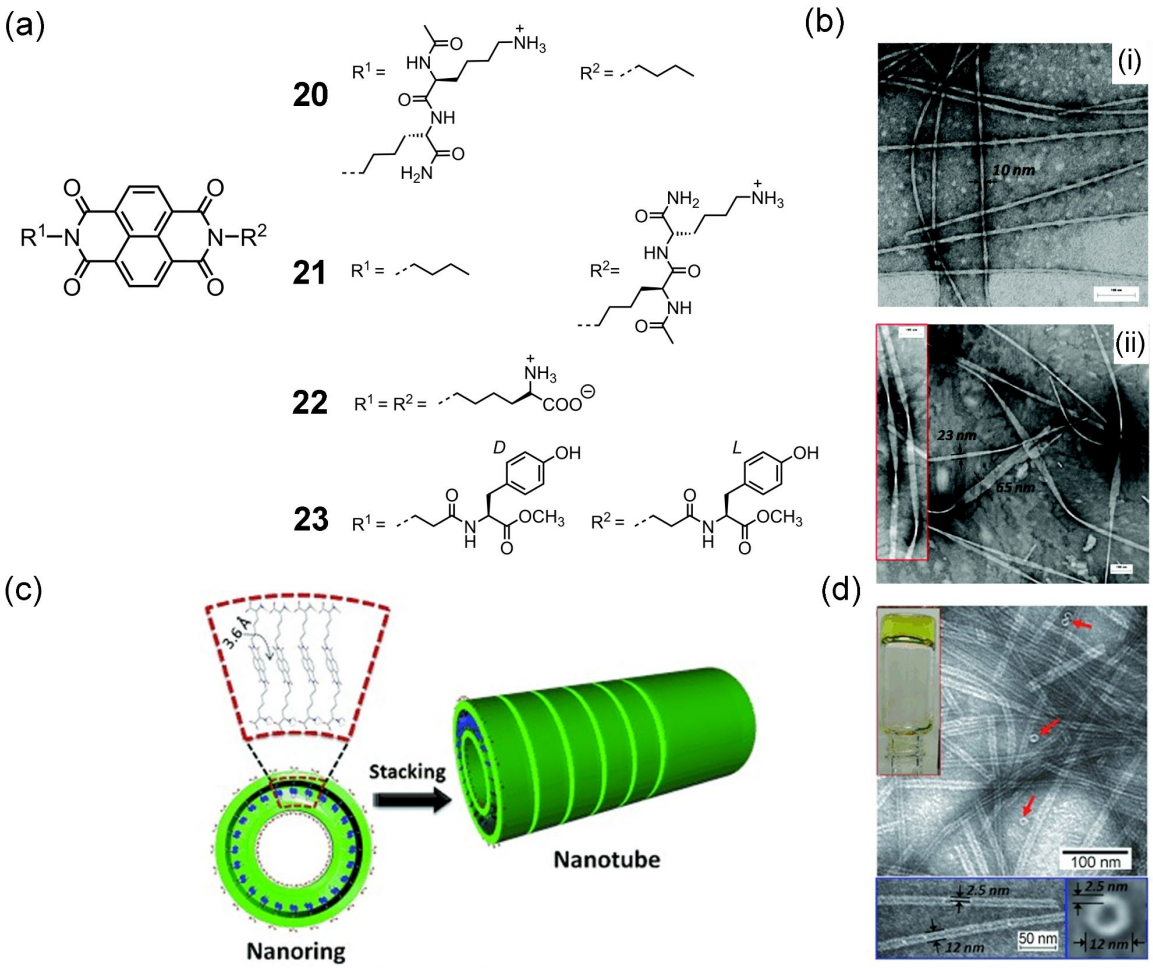


**Figure 2.13**: (a) Chemical structures of peptide conjugated NBI derivatives **20**-**23**. (b) TEM image of **20** showing nanofibers (i) and of **21** showing twisted nanoribbons (ii). Reprinted with permission from reference[155]. Copyright 2009 American Chemical Society. (c) Schematic representation of the self-assembly of **22,** resulting in nanorings and its further stacking to produce nanotubes. (d) TEM image of the nanotubes formed by **22**. Reproduced with permission from reference[156]. Copyright 2010 Wiley-VCH Verlag GmbH & Co. KGaA, Weinheim.

Akin to the peptide-functionalized NBIs, naphthalene bisimide amphiphiles substituted with dipicolylethylenediamine can use electrostatic interactions to modulate the self-assembly parameters by binding with biologically relevant guest molecules like adenosine phosphate. George *et al.* reported one of the first examples of guest induced chiral self-assembly for an NBI by the polymerization of achiral derivative **24**, triggered by the binding with adenine nucleotides (ATP, ADP or AMP) (Figure 2.14a, b). The handedness

of the helical polymer formed by the synergetic effect of π-π stacking and hydrophobic effect is determined by the type of binding nucleotide (*P* for **24**-ATP, *M* for **24**-AMP/ADP), which can be reversed by competitive binding of the guest (Figure 2.14c).[158] In a subsequent example, they used chiroptical signals associated with the aforementioned helical bias to probe mechanistic insights into enzymatic ATP hydrolysis (Figure 2.14d).[159] As this stereomutation is triggered by the consumption of ATP/ADP, it is possible to create a fuel-driven control over this conformational switching with tunable lifetime, rate as well as transient states within this transformation.[160, 161]

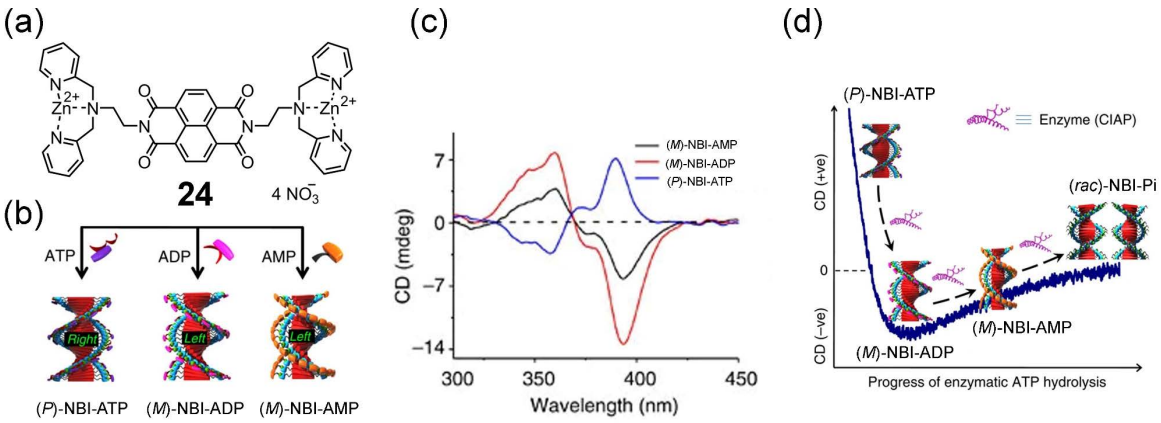


**Figure 2.14**: (a) Chemical structure of NBI derivative **24**. (b) Schematic diagram showing the helical assembly of **24** induced by binding with adenosine phosphates. (c) CD spectra of **24** upon binding with AMP, ADP, and ATP. (d) Chiroptical changes at different stages of enzymatic ATP hydrolysis. Adapted by permission from Springer Nature: reference[159], copyright 2014.

Ghosh *et al.* combined H-bonding along with π-π stacking of NBIs to generate diverse self-assembled structures in water which exhibit enticing properties. They synthesized an NBI bolaamphiphile **25** with hydrazide units sandwiched between the hydrophobic chromophore and the phenyl ring of hydrophilic wedges to facilitate H-bonding in water (Figure 2.15a).[162] FT-IR studies confirmed the presence of H-bonding in aqueous media, which along with the π-π stacking directs **25** to assemble in a vesicular structure. The addition of an electron-rich pyrene derivative to **25** leads to its intercalation by donor-acceptor interactions, which activates the fusion of vesicles and its eventual transformation into 1D fibers (Figure 2.15b,c). The intermolecular H-bonding seemed to be stabilizing such an intercalation as charge-transfer interactions between pyrene derivative and NBI chromophore were absent in a control molecule that lacks any H-bonding motif.[163]

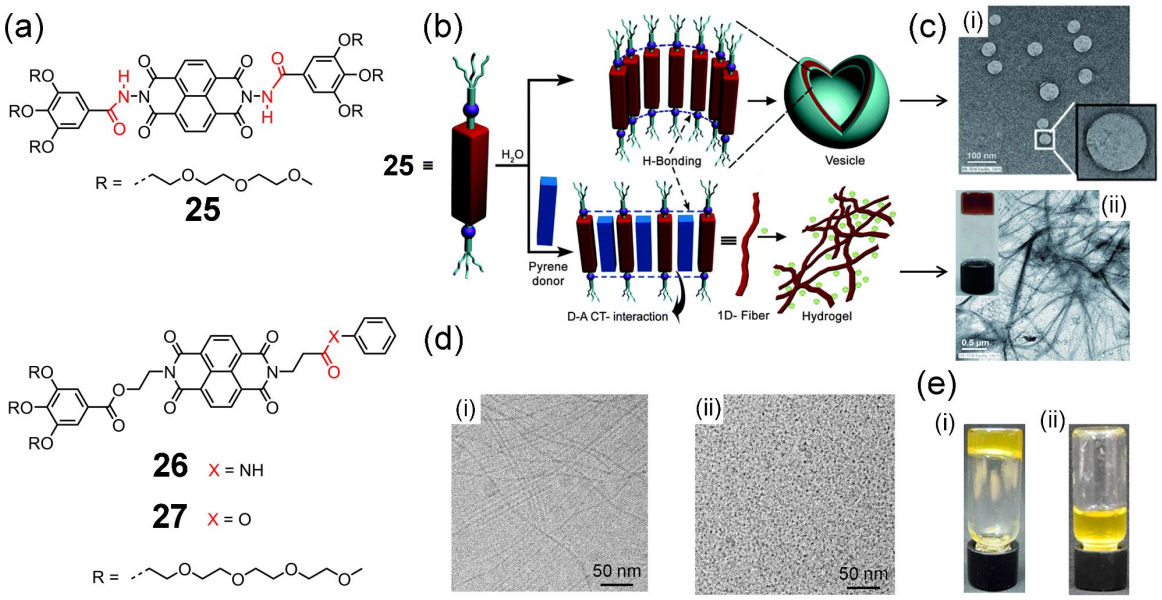


**Figure 2.15**: (a) Chemical structure of NBI derivatives **25**-**27**. (b) Schematic diagram showing the self-assembly of **25** forming vesicles and coassembly with a pyrene donor resulting in 1D-fiber and hydrogel. (c) TEM image of **25** showing vesicles (i) and **25**+pyrene gel showing networked fibers (ii). Adapted with permission from reference[162]. Copyright 2012 Wiley-VCH Verlag GmbH & Co. KGaA, Weinheim. (d) Cryo-TEM images of **26** (i) and **27** (ii) in $D_2O$. (e) The hydrogel formed by the H-bonding NBI derivative **26** (i) and sol formed by **27** (ii) in water. Adapted with permission from reference[22]. Copyright 2017 American Chemical Society.

The presence of such amide-amide H-bonding in a self-assembled structure can even surpass the packing parameters and decide the fate of the aggregate structures formed.[22] Amphiphilic NBIs **26** and **27** possess the same hydrophobic/hydrophilic balance and only differ by a single functional group at one of the imide positions (Figure 2.15a). While **27** with non H-bonding ester groups forms micelles as expected for such amphiphilic molecules, **26** with H-bond aiding amide groups self-assembles into one-dimensional fibers which at higher concentrations undergo gelation and finally transforms into crystals (Figure 2.15d,e). The rigidity of the H-bonding donor is also important as direct linking of NH to the NBI chromophore yields cylindrical micelles, whereas connecting it *via* an ethylene spacer leads to polymersomes.[23] The difference in the connectivity of the H-bonding motif can also determine emergent functions of aggregated structures, as shown for glucose decorated asymmetrical NBIs.[164] If the donor NH is directly linked to the imide nitrogen (*i.e.*, hydrazide) of the NBI chromophore, then the resulting cylindrical micelles shows superior multivalent binding to a lectin (Concanavalin A), in comparison to the vesicles formed from the derivative where NH is linked to the carbon atom of the phenyl group (*i.e.*, amide). This 'glycocluster effect' is linked to the adaptive nature of 1D fibers which can

adjust the conformation of peripheral ligands in comparison to the vesicles. In a control molecule which lacks any H-bonding motifs, no specific multivalent binding was observed.

Similar amphiphilic designs consisting of NBI core and the H-bonding donor as the supramolecular structure-directing unit (SSDU) can be extended to macromolecules by conjugating a protein or a covalent polymer at one of the imide positions (Figure 2.16a). Ghosh and coworkers investigated several of these polymer conjugates (**28**-**31**) and discovered that irrespective of the polymer backbone (ionic/non-ionic and backbone structure), the supramolecular structure is defined by the SSDU which instigates them to assemble first as spherical micelles in water which transforms into cylindrical micellar structure upon aging (Figure 2.16b, c).[23, 165] Furthermore, thermodynamic investigations into their aggregation by ITC dilution experiments revealed an entropically driven and enthalpically disfavored process, which the authors attribute to the release of water molecules from the hydrophilic units (Figure 2.16d). In a similar fashion, bovine serum albumin (BSA) was conjugated to the aforementioned SSDU consisting of π-stacking NBI core and H-bond forming hydrazide group, to yield NBI-BSA complex, **33** (Figure 2.16a).[166] Compared to the enthalpically favored aggregation of the control molecule **32**, which lacks a protein conjugation, **33** self-assembles in an enthalpically disfavored fashion into micellar nanoparticles. Co-assembly of **33** with another SSDU conjugate of poly-N-isopropyl acrylamide (PNiPAm) (**34**) suppresses the enzymatic activity of **33** above LCST, due to the coil-to-globule transition of PNiPAm and the subsequent blocking of the active sites of the protein.

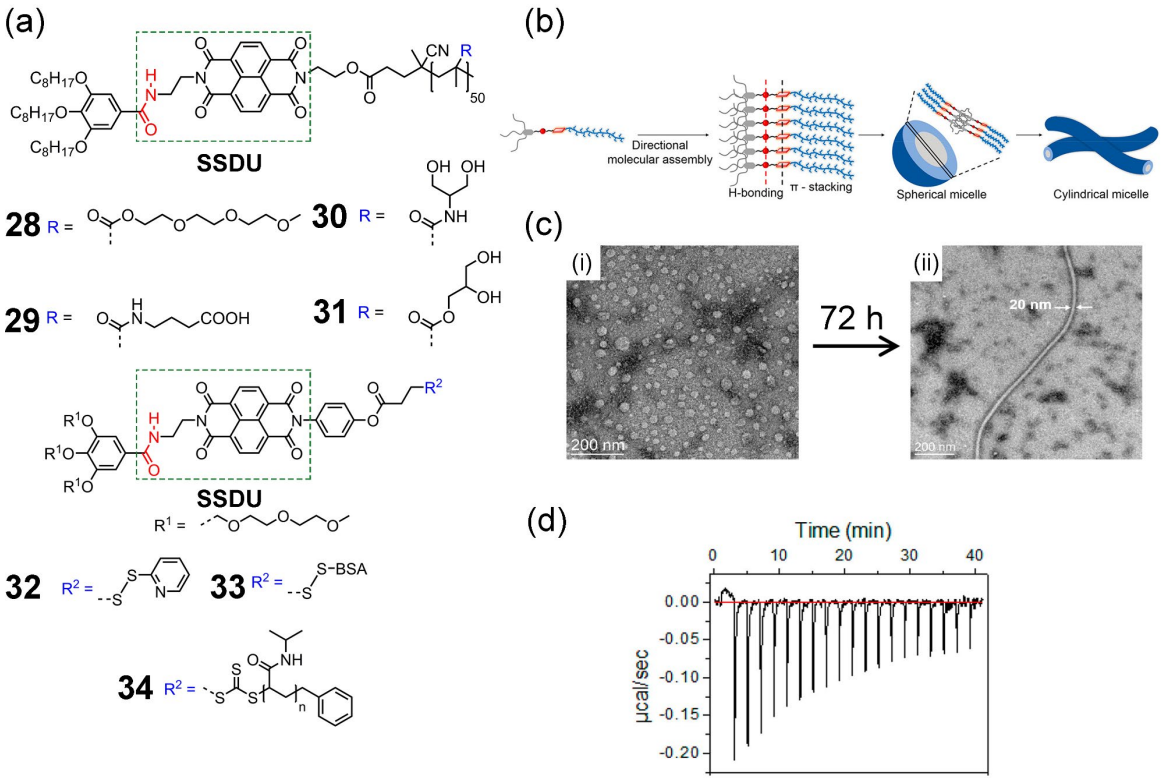


**Figure 2.16**: (a) Chemical structures of NBI derivatives **28**-**34**. (b) Schematic diagram showing the assembly of NBI-polymer conjugates **28**-**31**, first into spherical micelles and then to cylindrical micelles. (c) TEM images of **29** in water, freshly prepared (i) and after aging (ii). (d) The heat released upon ITC dilution experiments for **28** in water. Adapted with permission from reference[165]. Copyright 2018 American Chemical Society.

### 2.2.3 Perylene bisimides (PBIs)

Perylene bisimides constituting an electron-deficient π-core have emerged as the working horse for the development of supramolecular architectures with various functionalities, attributing to their unique optical, electronic and redox properties.[63] While much of the studies on their self-assembly are focussed on organic media, attempts have been made to render them water-soluble and generate different nanostructures.[16, 24]

Mechanistic understanding of their aqueous self-assembly was pioneered by Würthner and coworkers who mainly utilized bolaamphiphilic perylene bisimides with neutral oligo ethylene glycol or charged spermine chains as water-solubilizing units. They noticed the remarkable aggregation tendency of a PBI derivative, **35** appended with three oligo ethylene glycol chains at the 3,4,5-positions of a phenyl group, in water (Figure 2.17a).[64] Self-assembly studies of its association in polar solvents revealed face-to-face stacked H-type aggregates which showed a linear dependency of aggregation strength with increasing solvent polarity. Surprisingly, the association in water deviates from this linear free energy

relationship (LEFR), where even at nanomolar concentrations, a complete association was observed. The surprisingly high aggregation constant ($K > 10^8$ $M^{-1}$) and the disparity from other polar solvents were attributed to the contributions from the hydrophobic effect, in addition to the electrostatic and dispersion interactions of π-π stacking. Morphological investigations on its self-assembly in water revealed a hierarchical growth from nanorods (by columnar stacking of monomers) to nanoribbons (by side-by-side fusion of nanorods) which could be differentiated by electron microscopy as well as by fluorescence spectroscopy (Figure 2.17b, c).[67]

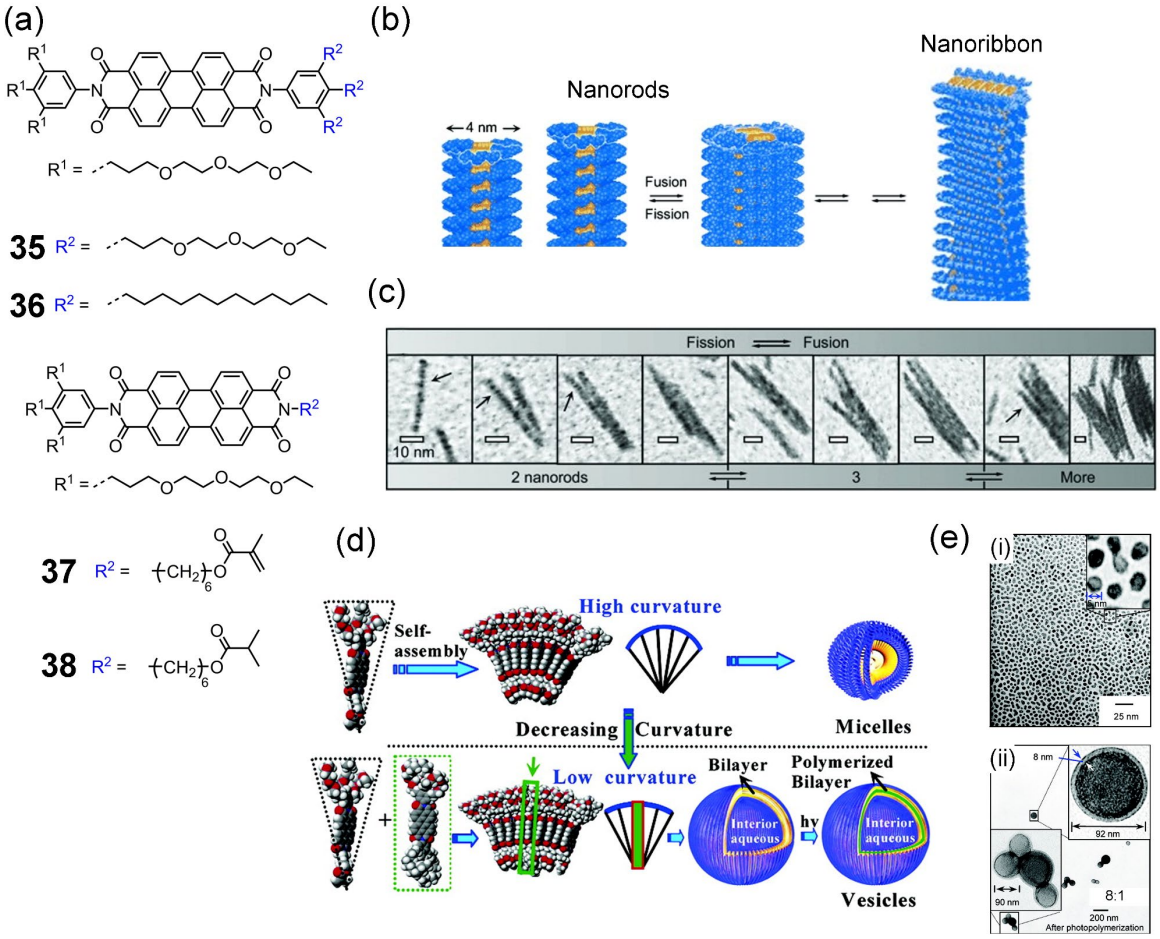


**Figure 2.17**: (a) Chemical structures of PBI derivatives **35-38**. (b) Schematic illustration of the hierarchical self-assembly of **35,** showing the fusion of nanorods into nanoribbons. (c) TEM images showing the fusion and fission of segmented nanorods of **35**. Adapted with permission from reference[67]. Copyright 2014 Wiley-VCH Verlag GmbH & Co. KGaA, Weinheim. (d) Schematic illustration showing the self-assembly of **37** into micelles (top) and the co-assembly of **36** and **37** into vesicles (bottom). (e) TEM images showing the micelles (i) formed by the assembly of **37** and vesicles (ii) formed by the co-assembly of **36** and **37** (after photopolymerization). Adapted with permission from reference[65]. Copyright 2007 American Chemical Society.

Already in 2007, Würthner and coworkers noted that the morphology of assemblies formed by amphiphilic PBIs in water is highly dependent on the curvature imparted by imide

substituents.[65] For instance, if one of the triethylene glycol brush is replaced by hydrophobic hexyl chain end-capped with methacryloyloxy (**37**) or isobutyryloxy units (**38**), spherical micelles are obtained instead of the columnar linear polymers mentioned above (Figure 2.17d, e). This is in accordance with the Israelachvili's packing parameter ($P_c$), which predicts micellar formation for $P_c < 1/3$. If the curvature is further decreased, e.g., by copolymerization with amphiphilic **36**, then vesicles with a wall thickness of 7-8 nm are formed, which can be stabilized by *in situ* photopolymerization. Due to the inherent electron-deficient nature of PBI scaffolds, the bilayer in such vesicles can act as an electron acceptor.[66] If they are loaded with an appropriate electron donor like 1,7-bis(1-methyl-pyrenyl)-1,4,7-triazaheptane, the fluorescence resonance energy transfer (FRET) between both can provide ultrasensitive pH information in an aqueous environment. This FRET process between an electron donor and acceptor can also be used to generate a white light emitting nano system in water, as demonstrated for the biscarbazole-loaded micelles of PBI **37**.[167]

A bit later, a unique entropically driven self-assembly of such bolaamphiphilic dyes in water was noted by the same authors.[68] Compared to previous examples, longer ethylene glycol chains (**PBI 3**) were used to impart more solubility in aqueous media and thus facilitate in-depth concentration and calorimetric studies (Figure 2.18a). The deviation from the monotonic increase of binding strength at higher water content confirms the contribution of the hydrophobic effect as observed for the shorter derivative, **35**. Surprisingly, temperature-dependent measurements revealed that aggregate formation is favored more at higher temperatures, signifying the effect of entropy in driving the self-assembly (Figure 2.18c (i)). ITC studies have revealed that this entropically driven association is even enthalpically disfavored, counterintuitive to the exothermic π-π stacking normally observed (Figure 2.18b (i)). This was attributed to the expulsion of water molecules upon aggregation from the hydrophilic OEG units, which countervails favorable enthalpic contribution from the stacking of chromophores. However, such an entropic contribution can be attenuated and reversed to a conventional enthalpy-driven assembly by the addition of a co-solvent like THF, which competes with water in the solvation of the molecules (Figure 2.18b (ii), c (ii)).

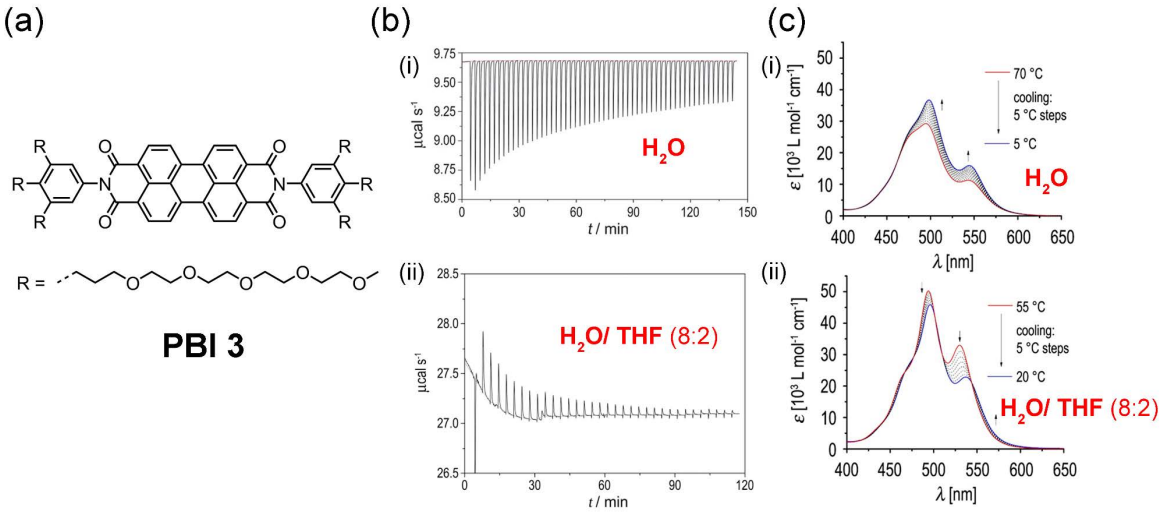


**Figure 2.18**: (a) Chemical structure of **PBI 3**. (b) ITC dilution studies of **PBI 3** showing (i) the exothermic disassembly (enthalpically disfavored self-assembly) in water and (ii) endothermic disassembly (enthalpically favored assembly) in water/THF (8:2) mixture. (c) Temperature-dependent UV-vis studies showing the entropically driven self-assembly of **PBI 3** in water (i) and enthalpically driven self-assembly in water/THF (8:2) mixture (ii). Adapted with permission from reference[68]. Copyright 2016 Wiley-VCH Verlag GmbH & Co. KGaA, Weinheim.

Yagai utilized this varied contribution of entropy and enthalpy dependent on solvent composition to generate distinct nanostructures in water for an alkyl tethered bis-PBI derivative appended with a swallow-tail OEG ($ST_{OEG}$) chain and a swallow-tail alkyl ($ST_{alkyl}$) chain (**39**) (Figure 2.19a).[168] In a THF/water mixture of equal proportion at 20 °C, the $ST_{OEG}$ chain is non-optimally hydrated, and the dyad molecule predominantly stacks in a columnar 1D-aggregate driven by the enthalpically favored π-π stacking along with an unstable kinetic intermediate, vesicles (Figure 2.19b). However, when the water content is increased to 90% or if the temperature is elevated, this vesicular aggregate is stabilized, suggesting the entropic contributions which dictate its association. When THF is added to this intermediate, the $ST_{OEG}$ units are again solvated by organic solvent and can produce the thermodynamic nanofibers. Applying a temperature gradient to the entropically stabilized vesicular aggregate can also yield other kinetic products like nanorings (under microflow) and nano-coils (in bulk conditions). Such complex interplay of entropy and enthalpy might be crucial in the formation of diverse kinetic nanostructures observed for other π-amphiphiles in aqueous media.

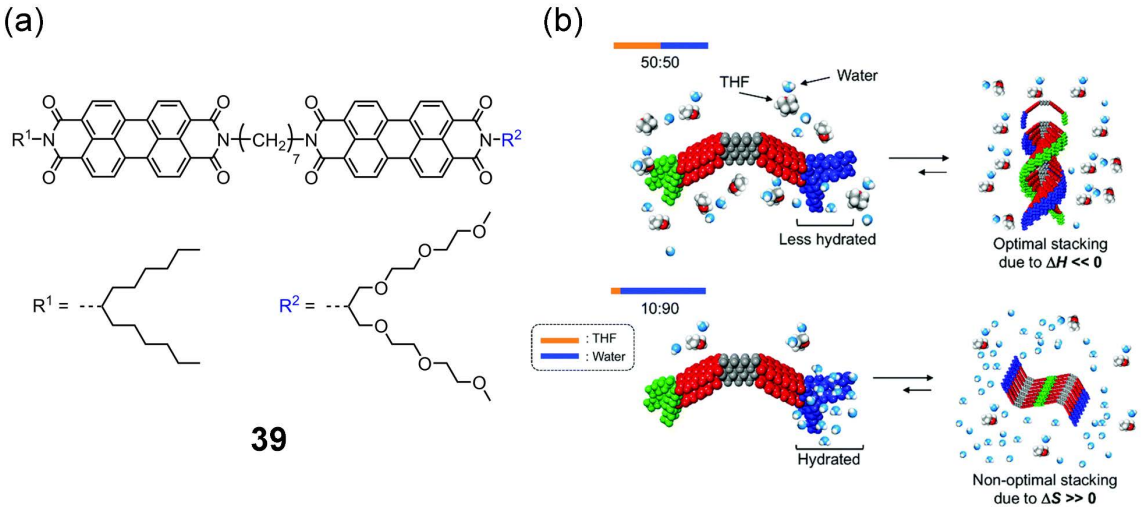


**Figure 2.19**: (a) Chemical structure of amphiphilic PBI derivative **39**. (b) Schematic illustration showing the contributions of enthalpy and entropy in the self-assembly of **39** in different THF/water mixtures due to the variation in solvation. Adapted from reference[168] with permission from The Royal Society of Chemistry.

In most of the aforementioned cases, the PBI molecules suffer from less solubility in pure water due to their strong aggregation tendency, which also affects desirable optical properties like luminescence, which is quenched due to a forbidden transition to the ground state in a co-facial packing. However, such disadvantages can be circumvented by introducing either bulkier dendrons of higher generation or ionic side chains at imide positions. Haag and Würthner noticed that the aggregation tendency of polyglycerol dendron appended PBIs is governed primarily by its generation (G).[169, 170] While derivatives with G1 dendron exists in the aggregated state due to less sterical shielding, third and fourth generation dendrons (G3 and G4) render them monomeric over a wide concentration range due to their bulkiness. This dendritic effect also leads to an increase in the fluorescence quantum yield from 33% (for G1) to nearly 100% (for G4) in water, by the suppression of π-π stacking. Introduction of charged side-chains like spermine can also hinder H-aggregation by means of electrostatic repulsion and thus enhance fluorescence quantum yields in water.[171]

In comparison to imide substituted PBI scaffolds, its bay-substituted counterparts are relatively less explored. However, such a core-distortion can result in variation of self-assembly mechanism as well as photophysical properties in water, similar to those observed in organic media.[172] For example, if sterically demanding aryloxy groups are attached to the 1,6,7,12 positions of the perylene core, aggregation into dimer is observed in contrast to the isodesmic growth into nanorod observed for bay-unsubstituted **35**.[173] If even bulkier

triethylene glycol dendrons are introduced at bay-position along with H-bond donors at imide position (**40**), it is possible to shift the aggregation from commonly observed co-facial arrangement to slip-stacked aggregates with J-type exciton coupling and superior luminescence characteristics (Figure 2.20a).[174] Such an amphiphile exhibits a weak excitonically coupled H-type intermediate at ambient conditions due to the hindered π-π stacking, which can be transformed into a stable H-bond driven J-aggregate in an entropically driven fashion by increasing the temperature (Figure 2.20b). At higher concentrations (5-40 wt%), these aggregates form hydrogels that exhibit thermoresponsive color change and fluorescence turn-on in a biologically relevant temperature window.

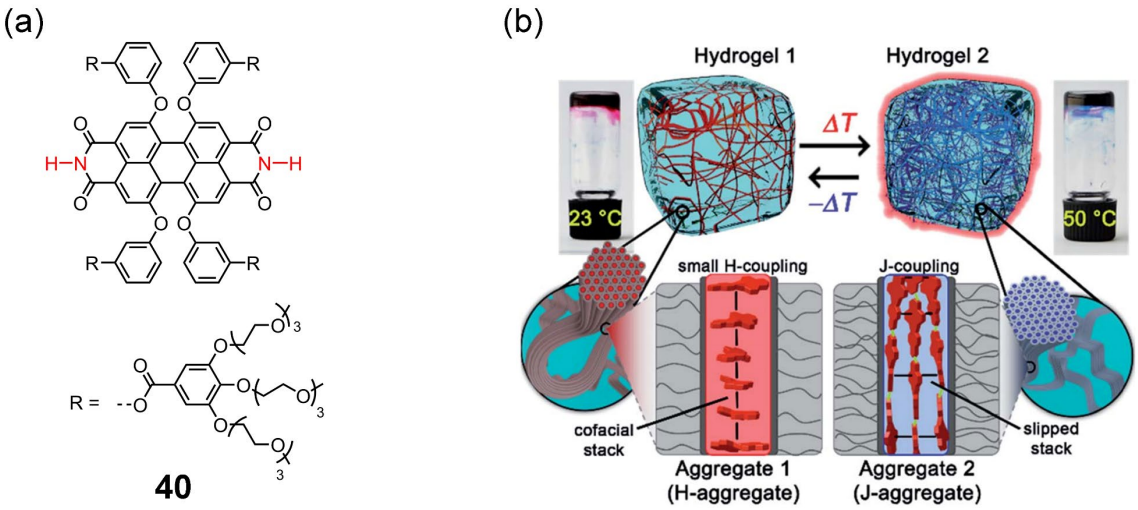


**Figure 2.20**: (a) Chemical structure of bay-substituted PBI derivative, **40**. (b) Schematic representation showing the temperature-induced changes in the hydrogel formed by **40** as well as the H- and J-type packing of monomers in each hydrogel. Adapted from reference[174] with permission from The Royal Society of Chemistry.

Rybtchinski used bay substitution on PBIs to generate extended hydrophobic scaffolds and thus more robust supramolecular polymers in water, by attaching either other PBI-chromophores or different non-polar units. Amphiphilic PBI **41** substituted with a perfluorooctyl chain on the core exhibited immense stability and unique self-assembly mechanism in comparison to the non-fluorinated derivative, **42** (Figure 2.21a).[175] Temperature-dependent studies revealed isodesmic self-assembly for **42** irrespective of the solvent composition, which results in the formation of small nanofibers. In contrast, the fluorinated analog **41** exhibits a cooperative mechanism at lower water contents yielding long aggregates, which transform at high water content resulting into tube-like fibers (Figure 2.21b). The lower estimate of the association constant of fluorinated derivative in pure water is very high (~$10^{15}$ $M^{-1}$) and three orders greater than that of the non-fluorinated

counterpart (~$10^{12}$ $M^{-1}$). Since the π-stacking of PBIs at higher water content follows an exponential trend,[68] the real binding constants might be much higher than those estimated from linear extrapolation. This high binding tendency, as well as solvent-composition dependent self-assembly mechanism, was attributed to the hydrophobicity as well as conformational rigidity of fluorocarbon chains.

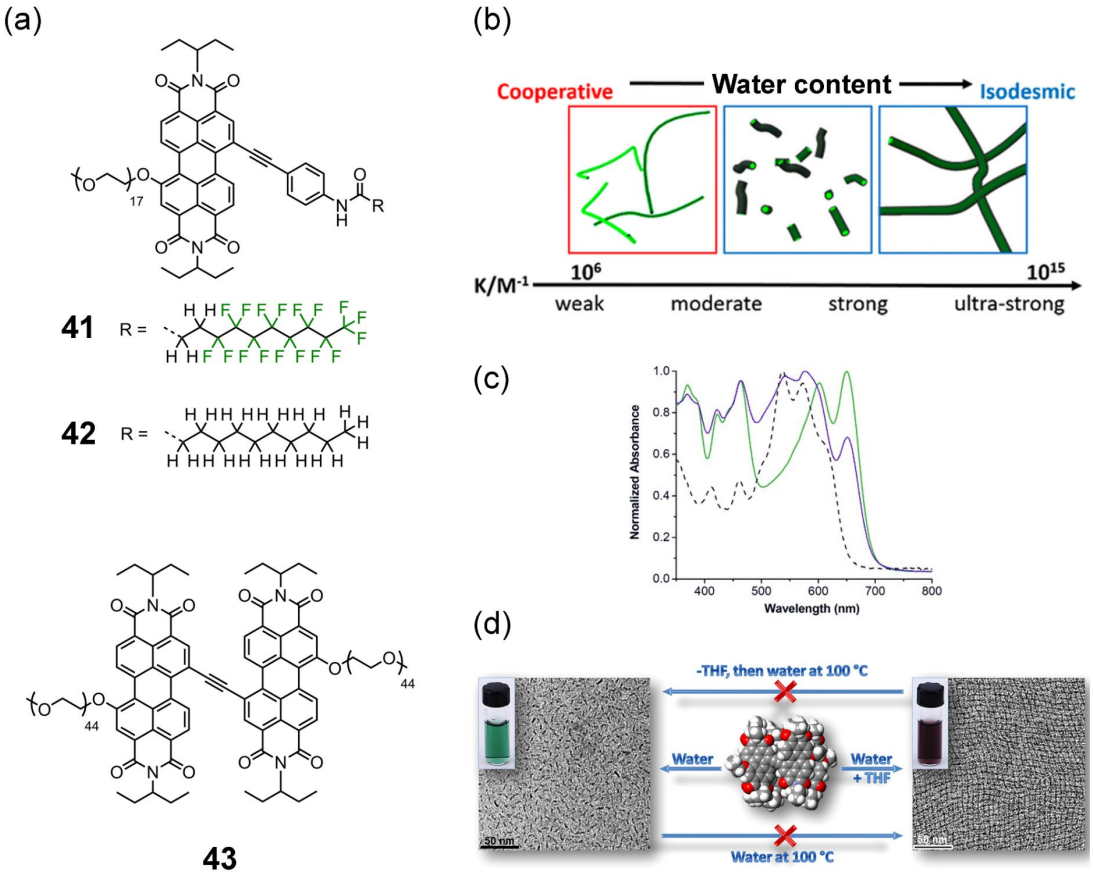


**Figure 2.21**: (a) Chemical structures of bay-substituted PBI derivatives, **41** and **42**, as well as the bis-PBI **43**. (b) Schematic illustration showing the self-assembly of fluorinated derivative **41** at varying water content. Adapted with permission from reference[175]. Copyright 2014 American Chemical Society. (c) Normalized UV-vis spectra of green aggregates (solid green line) and purple aggregates (solid purple line) of **43** in water along with the spectrum in THF (dashed black line). Adapted with permission from reference[176]. Copyright 2014 Wiley-VCH Verlag GmbH & Co. KGaA, Weinheim. (d) Cryo-TEM images of green and purple assemblies of bis-PBI **43** and photographs of their solution in water (insets). Adapted with permission from reference[177]. Copyright 2019 American Chemical Society.

Bis-PBI dyads tethered *via* the bay position were used by Rybtchinski to generate kinetic intermediates with diverse morphologies, triggered by co-solvent addition. PBI derivative, **43** with solubilizing glycol chains can form purple-colored assemblies (long aligned fibers) with predominant H-type coupling characteristics, and green assemblies (short nanorods) with J-type features (Figure 2.21c, d).[176] While the conversion from one assembly to

another requires attenuation of hydrophobic effect by means of a co-solvent, both of these polymorphs are stable in neat water for months and at high temperatures, signifying their deeply trapped state. EPR and femtosecond measurements revealed that these polymorphs show either electron or exciton transfer properties attributed to the difference in the overlap of the hydrophobic cores. Further investigations on the kinetics of this transformation indicated that it proceeds *via* a nucleation-growth mechanism with exceptionally high activation barriers (18.6 kcal $mol^{-1}$ for nucleation at 293 K).[178] The thermodynamic parameters extracted from Eyring plots indicated the significant contribution of negative activation entropy in the overall barrier, associated with hydration dynamics. A related bis-PBI derivative tethered through a bis(ethynyl)bipyridyl linker at bay position formed strong 3D-networked fibers in water and was used to fabricate ultrafiltration membranes for the separation of metal and semiconductor nanoparticles.[177, 179, 180]

### 2.2.4 Other π-systems

Hexabenzocoronene (HBC) is one of the largest π-systems which has been used to construct supramolecular polymers in water. Despite their appealing optoelectronic properties, the low solubility arising from the large π-core makes them less suitable compared to many of the aforementioned π-amphiphiles. Müllen and coworkers synthesized amphiphilic HBCs where the water solubility was introduced by non-ionic oligo ethylene glycol dendrons or ionic imidazolium groups, which aggregate as long columnar stacks in water.[36, 181] Aida has also reported similar HBCs with either uncharged oligo ethylene glycol chains (**44**)[37] or positively charged isothiouronium groups (**45**) (Figure 2.22a).[38] The morphology of assemblies formed by **44** is dependent on the solvent composition, where a mixture of water/THF (20% v/v) produces predominantly coiled nanotapes and pure THF yields nanotubes with a diameter one order of magnitude larger than single-walled carbon nanotubes (Figure 2.22b). The introduction of isothiouronium at one of the glycol chain terminals (**45**) imparts better solubility in water, where the positively charged surface pendants prevent bundling due to electrostatic repulsion, in comparison to their non-ionic counterpart (Figure 2.22d). The specific interactions between isothiouronium units and oxoanions were utilized to post-functionalize these nanotubes by treating with sodium poly(4-styrenesulfonate) or sodium anthraquinone-2-carboxylate (Figure 2.22c,d).

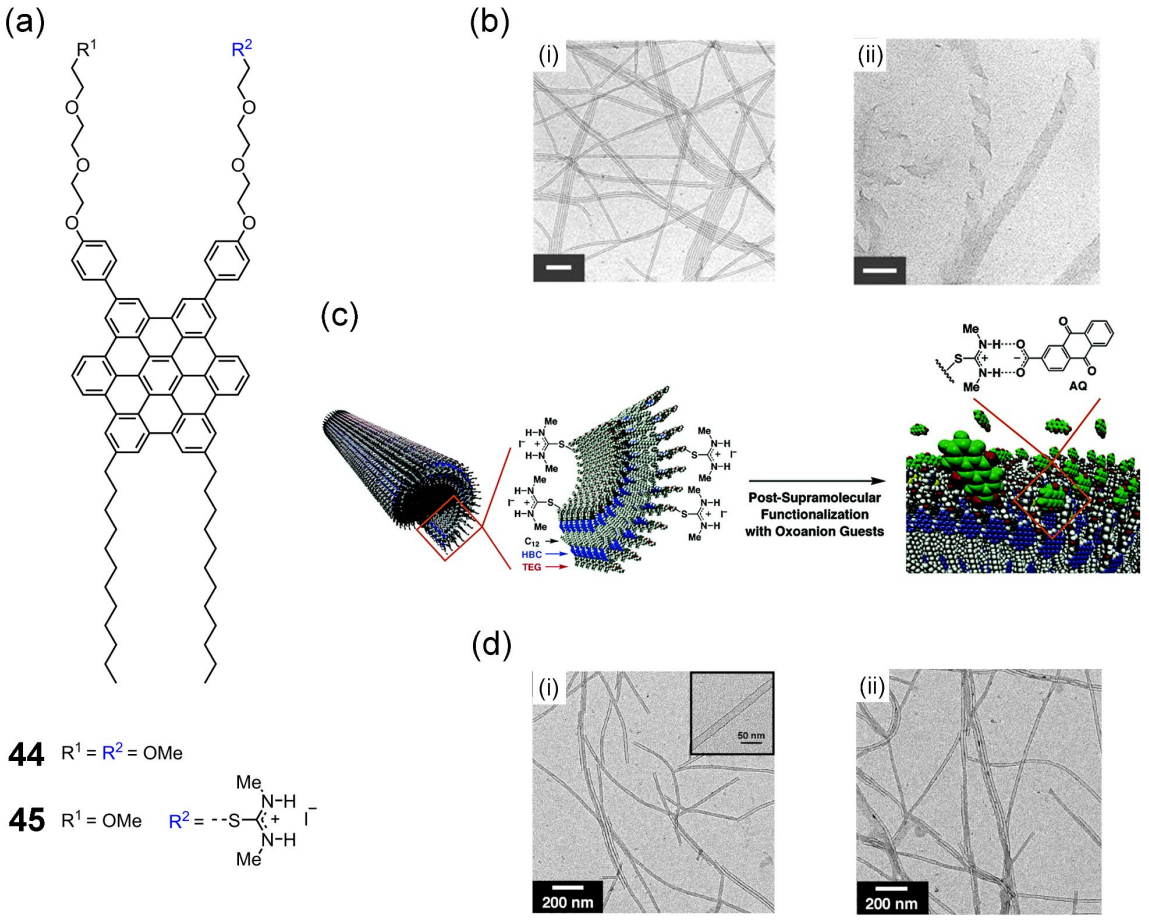


**Figure 2.22**: (a) Chemical structures of HBC derivatives **44** and **45**. (b) TEM images of **44** in THF (i) and THF/water mixture (ii). From reference[37]. Reprinted with permission from AAAS. (c) Schematic illustration of the bilayer nanotube formed by **45** and complexation with anthraquinone-2-carboxylate. (d) TEM images of **45** in water (i) and after post functionalization with anthraquinone-2-carboxylate (ii). Adapted with permission from reference[38]. Copyright 2007 American Chemical Society.

Different from the above examples where only one or two aromatic cores constitute the hydrophobic unit in a monomer, several small π-scaffolds can be tethered together to yield rod or 'V'-shaped amphiphiles. Lee and coworkers explored numerous *p*-oligophenylene derivatives appended with oligo ethylene glycol dendrons as stimuli-responsive materials, utilizing the lower critical solution temperature (LCST) based phase transition or coordination with metal ions. For example, they grafted hydrophilic oligo ethylene dendron and hydrophobic branched heptyl chains on a hepta(*p*-phenylene) rod (**46**), which self-assembles in a 2D-sheet like structure in water by the formation of a bilayer (Figure 2.23a, b).[182] Upon increasing the temperature above LCST, these sheets roll up into tubular scrolls in a reversible fashion (Figure 2.23b). This arises from the dehydration of oligo ethylene glycol chains, which result in an increased hydrophobicity and the subsequent effort to

reduce the solvent-exposed hydrophobic surface. By co-assembling, the above molecule with an analogous penta(*p*-phenylene) rod with only the OEG dendron (**47**), curvature can be induced in the packing, leading to the formation of toroidal structures (Figure 2.23c, d).[183] The hydrophobic interior of these motifs can be used to encapsulate $C_{60}$ fullerene, which triggers them to stack on top of each other and form 1D tubules. Introduction of carbohydrate (mannose) units in such rod-shaped amphiphiles at the OEG terminals can render them bioactive, which can regulate agglutination and propagation of specific bacterial cells[184] or promote T-cell activation (after binding with Concanavalin-A).[185]

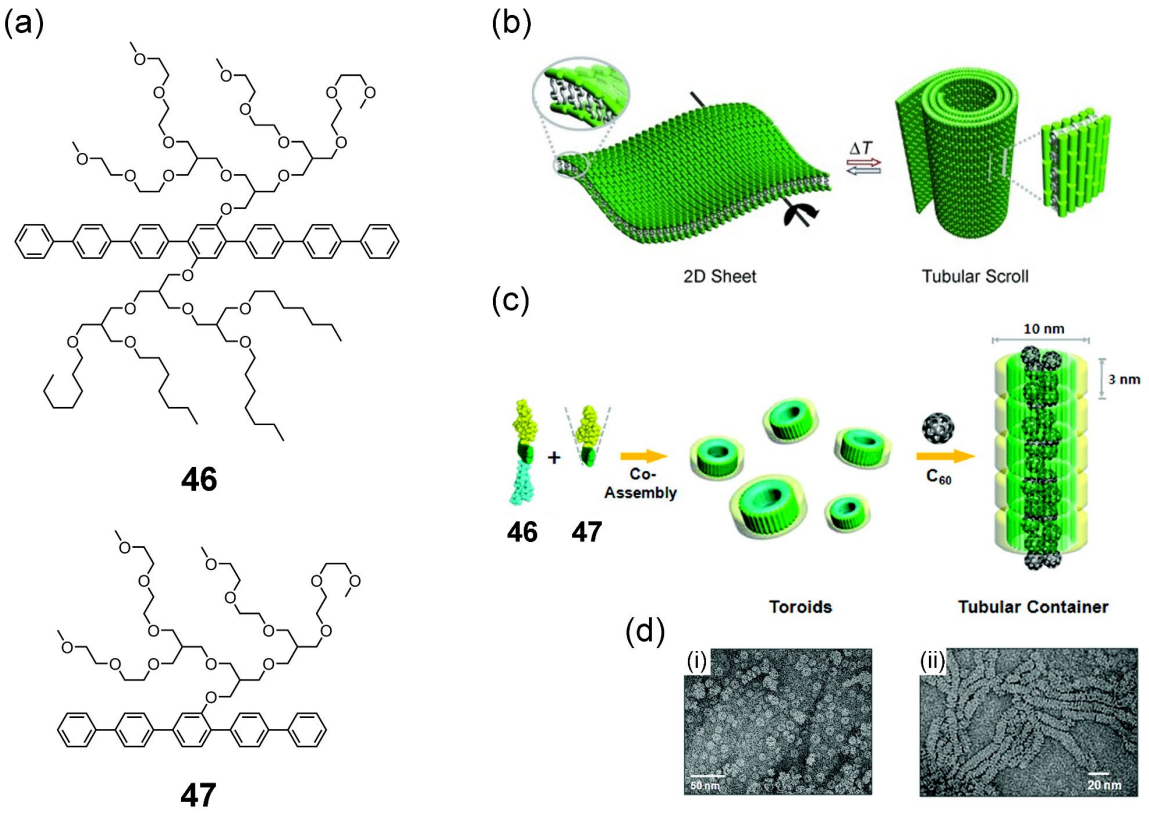


**Figure 2.23**: Chemical structures of rod-shaped *p*-oligophenylene derivatives **46** and **47**. (b) Schematic illustration showing the 2D sheet formed by **46** and its reversible scrolling induced by LCST. Adapted with permission from reference[182]. Copyright 2009 Wiley-VCH Verlag GmbH & Co. KGaA, Weinheim. (c) Schematic illustration showing the co-assembly of **46** with **47** forming toroids and its stacking upon the inclusion of $C_{60}$. (d) TEM images of toroids (i) and tubular stacks with $C_{60}$ (ii). Adapted with permission from reference[183]. Copyright 2009 American Chemical Society.

Tethering the *p*-oligophenylene units in a 'V'-shaped structure with an internal angle of 120° in contrast to the rod-shape mentioned above generates a new set of supramolecular structures in water. The bent oligophenylene derivative, **48**, where the aromatic *p*-oligophenylene units are linked at the *meta* positions of a benzene ring, forms helical tubules in water composed of hexameric macrocycle formed by the preliminary stacking of

monomer units (Figure 2.24a, b).[186] Upon addition of a hydrophobic silver salt (silver dodecyl sulfate), these structures dissociate into segmented tubules *via* encapsulation of guests into the hydrophobic cavity and the coordination interaction between Ag and nitrile groups (Figure 2.24b, c). While increasing the length of *meta* substituents alone does not perturb the morphology or the aggregate type (H-type), the introduction of a pyridine ring as the aromatic linker instead of benzene modulates the packing into a slip-stacked packing (**49**) (Figure 2.24a).[26] The formation of water clusters at the nitrogen atom of the pyridine group leads to this slipped arrangement of aromatic segments as confirmed by a red-shifted J-type absorption maximum and enhanced fluorescence with respect to the monomer, which results in the expansion of hexameric macrocycle. Thermal dehydration of water at OEG chains and pyridine nitrogen leads to the contraction of the internal cavity by nearly 50%, along with the packing arrangement shifting to a cofacial overlap (Figure 2.24d). This reversible thermally regulated pulsating motion of tubules, which is also accompanied by chirality inversion, can be utilized to encapsulate and release $C_{60}$ fullerene in a stimuli-responsive way. The guest encapsulation on such structures can also be used to control the cavity volume, without the assistance of temperature, as an analogous 'V'-shaped molecule inflates into tubules from collapsed fibers upon binding with hydrophobic *p*-phenylphenol.[187] If pyridine units are introduced at the terminal (of *p*-oligophenylene) instead of the 'valley' position as in the above cases, then they assemble in a zig-zag fashion to yield 2D-sheets.[188] Upon addition of Ag(I) ions, these sheets transform into chiral tubules by stacking of dimeric macrocycles due to the coordination of silver with pyridine units. This morphological conversion is reversible as the addition of a fluoride salt reinstates the sheet structure.

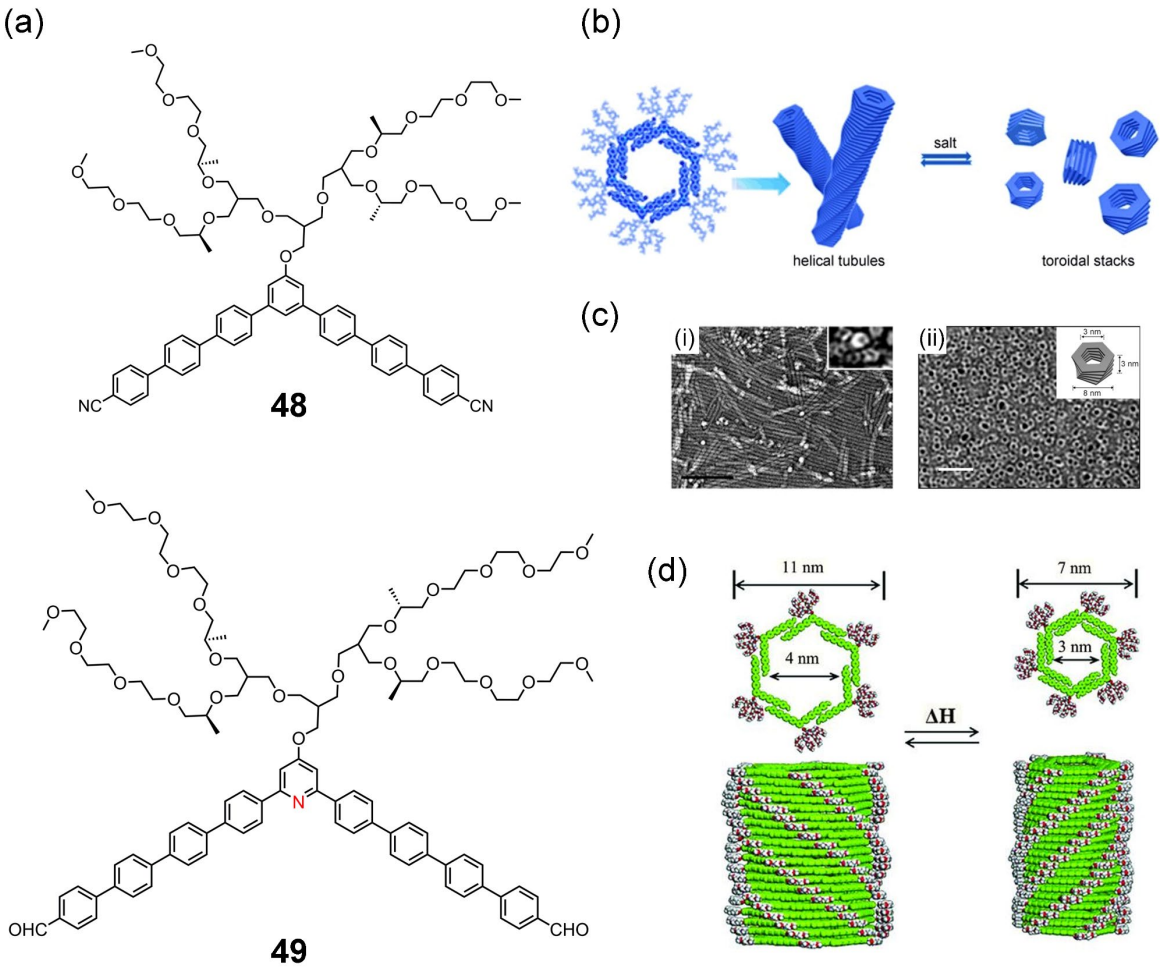


**Figure 2.24**: (a) Chemical structures of V-shaped *p*-oligophenylene derivatives **48** and **49**. (b) Schematic illustration of stacking of **48** macrocycles into tubules and salt-induced dissociation into toroids. (c) TEM-images of **48** before (i) and after the addition of silver salt (ii). Adapted with permission from reference[186]. Copyright 2010 Wiley-VCH Verlag GmbH & Co. KGaA, Weinheim. (d) Schematic diagram showing the expansion and contraction of **49** tubules with chirality inversion. From reference[26]. Reprinted with permission from AAAS.

## 2.3 Determination of thermodynamic parameters of self-assembly

The quantification of binding constants and related thermodynamic parameters is of utmost importance to understand the mechanism of aggregation as well as to tailor the properties of self-assembled structures.[189] In the following section, three main methods adopted for this purpose, namely spectroscopy, isothermal titration calorimetry, and differential scanning calorimetry, are explained. Since spectroscopic techniques are the most popular, mainly the thermodynamic models adopted, as well as the determination of assembly parameters by temperature-dependent techniques are described. For the less explored ITC and DSC, some illustrative examples are also provided for which the derivation of binding models and their successful application in aggregation studies are carried out.

### 2.3.1 Spectroscopic methods

Since the self-assembly of π-amphiphiles directly results in changes in their optical properties (due to the interaction between the π-clouds) and chemical environment (due to shielding/deshielding), spectroscopic techniques including UV-vis, circular dichroism (CD) and NMR are prime candidates to estimate the association constant.[45] The versatility of optical methods lies in the fact that they can be applied over a wide range of concentrations (UV-vis and CD). Generally, the changes in spectral parameters (denoted as '*Z*') like molar extinction coefficient ($\varepsilon$), chemical shift ($\delta$), etc. are tracked from monomer to aggregates as a function of concentration or temperature, to first determine the degree of aggregation, $\alpha_{agg}$.[50]

$$\alpha_{\mathrm{agg}} = \frac{Z(T,c) - Z_{\mathrm{mon}}}{Z_{\mathrm{agg}} - Z_{\mathrm{mon}}} \tag{2.4}$$

where $Z$ ($T$, $c$) is the physical property at a given temperature or concentration, $Z_{mon}$ is the spectral feature of the monomer, and $Z_{agg,}$ that of the aggregate.

By fitting $\alpha_{agg}$ to different thermodynamic models developed for one-dimensional self-assembly (*vide infra*), the corresponding mechanism, as well as association constant, can be determined.

One of the simplest models to describe the aggregation of cofacial π-stacked structures is the monomer-dimer model, where the equilibrium is exclusively between monomers and dimer aggregates.[48] The extension of stacking is limited either by sterical constraints[190] or electrostatic interaction of chromophores.[191] The dimerization constant, $K_D$ and the total concentration of molecules, $c_T$ in such a case can be defined as:

$$\alpha_{\mathrm{agg}} = \frac{4K_{\mathrm{D}}c_{\mathrm{T}}+1-\sqrt{8K_{\mathrm{D}}c_{\mathrm{T}}+1}}{4K_{\mathrm{D}}c_{\mathrm{T}}} \tag{2.5}$$

The fraction of aggregated π-surfaces in a dimer model can be expressed as:[48]

$$\alpha_{\mathrm{agg-\pi}} = 0.5\alpha_{\mathrm{agg}} \tag{2.6}$$

Thus, the maximum of $\alpha_{\mathrm{agg-\pi}}$ for dimer model is 0.5, whereas of $\alpha_{\mathrm{agg}}$ is 1.

Dimer model has been successfully applied to describe the aggregation of many dyes, including cyanine,[192] merocyanine,[191, 193] phthalocyanines,[194] perylene bisimides[53, 190, 195], etc. However, many recent findings have revealed that dimer formation found for several π-systems might be a special case of anti-cooperative aggregation, where the elongation

into higher aggregates was not observed due to the utilization of a limited concentration /temperature range or solvent choice.[53]

The formation of higher aggregates is more complex and is mainly described by three mathematical models: isodesmic, cooperative, and anti-cooperative.[48, 54] In the isodesmic model (also referred to as equal *K*), which is equivalent to step-growth polymerization of its covalent counterpart, each reversible step is accompanied by the same association constant and Gibbs free energy change. The absence of a critical concentration or critical temperature leads to their characteristic sigmoidal transition when the fraction of aggregated π-surfaces ($\alpha_{\mathrm{agg-\pi}}$) is plotted as a function of $Kc_{\mathrm{T}}$ (Figure 2.25, purple line). Generally, they are observed for systems with single non-covalent interactions, like π-π stacking, provided there is no sterical hindrance in association from other substituents. The concentration-dependent degree of aggregation in an isodesmic model can be calculated as:[48]

$$\alpha_{\mathrm{agg}} = 1 - \frac{2Kc_{\mathrm{T}}+1-\sqrt{4Kc_{\mathrm{T}}+1}}{2K^2c_{\mathrm{T}}^2} \tag{2.7}$$

where *K* is the binding constant, and $C_{\mathrm{T}}$ is the total concentration.

For isodesmic model, $\alpha_{\mathrm{agg-\pi}}$ can be determined using the following equation:[48]

$$\alpha_{\mathrm{agg-\pi}} = \frac{2Kc_{\mathrm{T}}+1-\sqrt{4Kc_{\mathrm{T}}+1}}{2Kc_{\mathrm{T}}} \tag{2.8}$$

At a constant concentration, isodesmic binding can also be tracked by varying the temperature, where the degree of aggregation shows a temperature dependency, which can be expressed as:[50]

$$\alpha_{\mathrm{agg}} \cong \frac{1}{1+exp\left[-0.908\Delta H\frac{T-T_m}{RT_m^2}\right]} \tag{2.9}$$

where Δ*H* is the molar enthalpy of self-assembly, *T* is the current temperature, $T_{\mathrm{m}}$ is the melting temperature (defined as the temperature at which $\alpha_{\mathrm{agg}}$=0.5), and *R* is the universal gas constant.

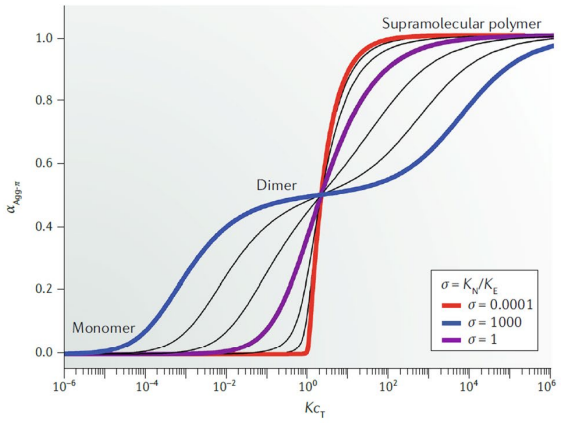


**Figure 2.25**: Plot of the degree of aggregated π-surfaces, $\alpha_{agg\text{-}\pi}$ against normalized concentration showing different association models (nucleus size is two). Reprinted by permission from Springer Nature: reference[45], copyright 2020.

Unlike the above case, if the polymerization occurs first by the formation of a nucleus with an association constant, $K_{N,}$ and then elongates with an association constant, $K_e$, it can be described by a nucleation-elongation model.[51] Such two-step processes can be defined based on the cooperativity factor, $\sigma = K_N / K_e$. If the nucleation which proceeds in a linear isodesmic manner is less favored than elongation, *i.e.*, $\sigma < 1$, then the process is referred to as cooperative polymerization (Figure 2.25, red line). Unlike an isodesmic process, where a gradual increase in the aggregated species occurs, cooperative mechanism follows a bimodal distribution of monomers and elongated polymers, once the nucleation conditions (critical concentration or temperature) is reached. Many molecules with a combination of π-π stacking and H-bonding displays this polymerization mechanism.[45]

If the nucleation is more favored than the elongation, *i.e.*, $\sigma > 1$, then such a process is termed as anti-cooperative (Figure 2.25, blue line). While this mechanism has been hugely overlooked in comparison to isodesmic and cooperative, many dipolar chromophores, which dimerize strongly by means of electrostatic interactions, can show a less favored elongation *via* π-π stacking.[196] Sterical constraints of side chains can also hinder the elongation as demonstrated for a perylene derivative by Bouteiller *et al.*[197]

Goldstein and Stryer developed a model to describe the concentration-dependent changes in the fraction of aggregates for nucleation-elongation processes which proceeds by the formation of a nucleus size '*s*'.[51, 52] Here, the dimensionless constant, $K_e c_T$ can be expressed in terms of monomer concentration, $c_1$ and total concentration $c_T$ as:

$$K_e c_T = \sum_{n-1}^{s} n\sigma^{n-1}(K_e c_1)^n + \sum_{n=s+1}^{\infty} n\sigma^{s-1}(K_e c_1)^n$$
$$= \frac{s(K_e c_1)^s \sigma^{s-1}}{1-K_e c_1} + \frac{(K_e c_1)^{s+1}\sigma^{s-1}}{(1-K_e c_1)^2} + \frac{K_e c_1(s(\sigma K_e c_1)^{s-1}-1)}{\sigma K_e c_1 - 1} - \frac{s(K_e c_1)^2\,((\sigma K_e c_1)^{s-1}-1)}{(\sigma K_e c_1 - 1)^2} \quad (2.10)$$

For the most prevalent nucleation process which affords a dimer nucleus, the above equation can be simplified into equation 2.11, which is commonly known as the $K_2$-$K$ model.[53]

$$K_e c_T = (1-\sigma)K_e c_1 + \frac{\sigma K_e c_1}{(1-K_e c_1)^2} \quad (2.11)$$

The $\alpha_{agg-\pi}$ for the non-isodesmic processes can be expressed using the following equation:[48]

$$\alpha_{agg-\pi} = \frac{\sigma K_e c_1^2}{(1-K_e c_1)^2(1-\sigma)c_1 + \sigma c_1} \quad (2.12)$$

The conventional $K_2$-$K$ model does not consider the distribution of monomers within the aggregates for the situation of anti-cooperative growth, where even number of molecules should prevail over odd number, due to the favored stacking into dimeric nuclei. Hence Würthner and coworkers modified this model to accommodate the distribution of monomers and applied it for the anti-cooperative aggregation of a PBI molecule that showed a preference for hydrogen-bonded dimeric units.[53]

Cooperative polymerization can also be evaluated with temperature-dependent measurements, which is more convenient and straightforward than concentration-dependent measurements.[50] For the elongation regime, the degree of aggregation with respect to temperature, $T$ can be defined on the basis of elongation temperature, $T_e$ as:[198, 199]

$$\alpha_{agg} = \alpha_{sat}\left(1 - \exp\left[\frac{-\Delta H_e}{RT_e^2}(T - T_e)\right]\right) \quad (2.13)$$

where $\alpha_{sat}$ is a parameter introduced to ensure that $\alpha_{agg}$ does not exceed unity, $\Delta H_e$ is the enthalpy change of elongation, and $R$ is the universal gas constant.

For the nucleation regime, the degree of aggregation is expressed as:

$$\alpha_{agg} = \sqrt[3]{K_a}\exp\left[\left(\frac{2}{3.\sqrt[3]{K_a}} - 1\right)\frac{\Delta H_e}{RT_e^2}(T - T_e)\right] \quad (2.14)$$

where $K_a$ is the equilibrium constant associated with the activation of inactive monomers into nuclei.

Along with the choice of appropriate mathematical models, experimental execution is also important to obtain reliable binding constants.[48] Thus, aggregation should be followed around a concentration of $1/K$, where $K$ is the association constant, and data should be acquired over a regime of at least two orders of magnitude. However, poor solubility, high optical density as well as limited sensitivity can hamper the variation of concentration in many cases.

#### 2.3.1.1 Temperature dependence of binding constants and derivation of thermodynamic parameters at standard conditions

While the application of thermodynamic models on concentration-dependent measurements yields association constants for the monomer-aggregate equilibrium, they do not directly provide any information about the enthalpy change or entropy change associated with the process. One of the most popular and accepted ways to obtain thermodynamic parameters of association is by using the dependence of association constants with respect to temperature using a van't Hoff equation.[119, 200]

The standard change in free energy of a system can be expressed by the Gibbs-Helmholtz equation as:

$$\Delta G^0 = \Delta H^0 - T\Delta S^0 \tag{2.15}$$

The free energy can also be expressed in terms of the association constant as:

$$\Delta G^0 = -RT \ln K_{ass} \tag{2.16}$$

By combining the above two equations,

$$\ln K_{ass} = -\frac{\Delta H^0}{RT} + \frac{\Delta S^0}{R} \tag{2.17}$$

The above equation provides a linear relationship of association constants with the inverse of temperature and can be used to make a van't Hoff plot with $\ln K_{ass}$ plotted on *x*-axis and $T^{-1}$ on *y*-axis. The slope of the line corresponds to $-\frac{\Delta H^0}{R}$ whereas the intercept of the fit gives $\frac{\Delta S^0}{R}$. From this, both standard enthalpy change, as well as standard entropy change for the association process, can be calculated.

Whilst being attractive due to its simplicity, van't Hoff's equation makes several incorrect assumptions. The linear relationship of association constants and temperature is not always kept. For example, the acid dissociation constant of acetic acid in aqueous solution first increases, passes through a maximum and then decreases.[201] For many association phenomena as well as host-guest complexations, it is shown that the linearity is kept only for a very small temperature range.[202] Furthermore, it is assumed that enthalpy, as well as entropy changes of association, is constant at all temperatures. A plethora of calorimetric measurements have proven that this is hardly true, and these parameters are indeed temperature dependent. The vast discrepancies observed between calorimetric enthalpies and van't Hoff enthalpies can probably be traced to these physically incorrect assumptions. Hence, it is essential to modify the equation to accommodate not only the non-linear behavior of binding constants with temperature, but also for the inevitable changes in enthalpy with temperature.

Clarke and Glew proposed one such modification where the isobaric temperature dependence of equilibrium constants is defined around a reference temperature, $\theta$.[203, 204] Generally, this corresponds to the temperature where standard thermodynamic functions are to be determined. This new method takes into account the heat capacity changes at constant pressure, $\Delta C_p$ by which temperature dependence of enthalpy can be described.

According to this, the relationship between association constant *K* and the temperature with standard thermodynamic parameters is given by a Taylor series:

$$\begin{aligned} R\ln K(T) = &-\frac{\Delta G(\theta)}{\theta} + \Delta H(\theta)\left[\frac{1}{\theta} - \frac{1}{T}\right] + \Delta C_p(\theta)\left[\left(\frac{\theta}{T}\right) - 1 + \ln\left(\frac{T}{\theta}\right)\right] + \\ &\frac{\theta}{2}\left(\frac{d\Delta C_p}{dT}\right)_\theta\left[\left(\frac{T}{\theta}\right) - \left(\frac{\theta}{T}\right) - 2\ln\left(\frac{T}{\theta}\right)\right] + \frac{\theta^2}{12}\left(\frac{d^2\Delta C_p}{dT^2}\right)_\theta\left[\left(\frac{T}{\theta}\right)^2 - \right. \\ &\left. 6\left(\frac{T}{\theta}\right) + 3 + 2\left(\frac{\theta}{T}\right) - 6\ln\left(\frac{T}{\theta}\right)\right] + \cdots \end{aligned} \tag{2.18}$$

For most practical purposes, the higher-order derivatives of $\Delta C_p$ can be neglected as heat-capacity remains temperature-independent for narrow temperature windows used for experimental studies. Then, the equation (2.18) upon rearranging becomes:

$$\ln K(T) = \ln K(\theta) + \frac{\Delta H(\theta)}{R}\left[\frac{1}{\theta} - \frac{1}{T}\right] + \frac{\Delta C_p(\theta)}{R}\left[\left(\frac{\theta}{T}\right) - 1 + \ln\left(\frac{T}{\theta}\right)\right] \tag{2.19}$$

The above equation can describe non-linear association constants and non-constant enthalpy changes of self-assembly by taking into consideration heat capacity changes, thus

providing a more accurate determination of thermodynamic parameters in comparison with van't Hoff equation.

### 2.3.2 Isothermal Titration Calorimetry (ITC)

One of the most efficient and convenient ways to obtain the thermodynamic parameters is by probing the heat signals associated with intermolecular association by isothermal titration calorimetry (ITC). Compared to conventional spectroscopic techniques, ITC offers several advantages: (i) the enthalpy, entropy, association constant as well as free energy can be determined in a single experiment, (ii) systems with higher association constants (up to $10^9\,M^{-1}$) can be studied, (iii) the enthalpy of an association process can be determined directly and (iv) is label-free and destruction-free.[202, 205-208]

An ITC instrument consists of a two-cell setup (sample cell and reference cell), which are enclosed in an adiabatic jacket and maintained at a thermal equilibrium (Figure 2.26a).[206] The reference cell is filled with pure solvent, whereas the sample cell is filled with a solution of one partner of the binding study (for host-guest interactions). An injection syringe, which is loaded with the other partner of the association process, is inserted co-axially to the sample cell. The paddle shape of the needle tip allows rapid mixing of components through the rotation of the syringe.[202]

When an aliquot of the binding partner is injected into the sample, the association event produces a heat effect that either increases or decreases the temperature in the sample cell. This temperature fluctuation initiates the feedback regulator to adjust the electrical power required to maintain both cells in an isothermal condition.[209] This generates a heat pulse (heat production over time), which is the primary signal observed in an ITC experiment (Figure 2.26b). The integration of this with respect to time is plotted against the molar ratio of host and guest, which provides the corresponding enthalpogram (Figure 2.26c). Fitting this isotherm to appropriate models, yields the enthalpy, $\Delta H$ as the step height, complexation stoichiometry, $n$ as the inflection point and association constant $K$, as the slope at the inflection point.[206]

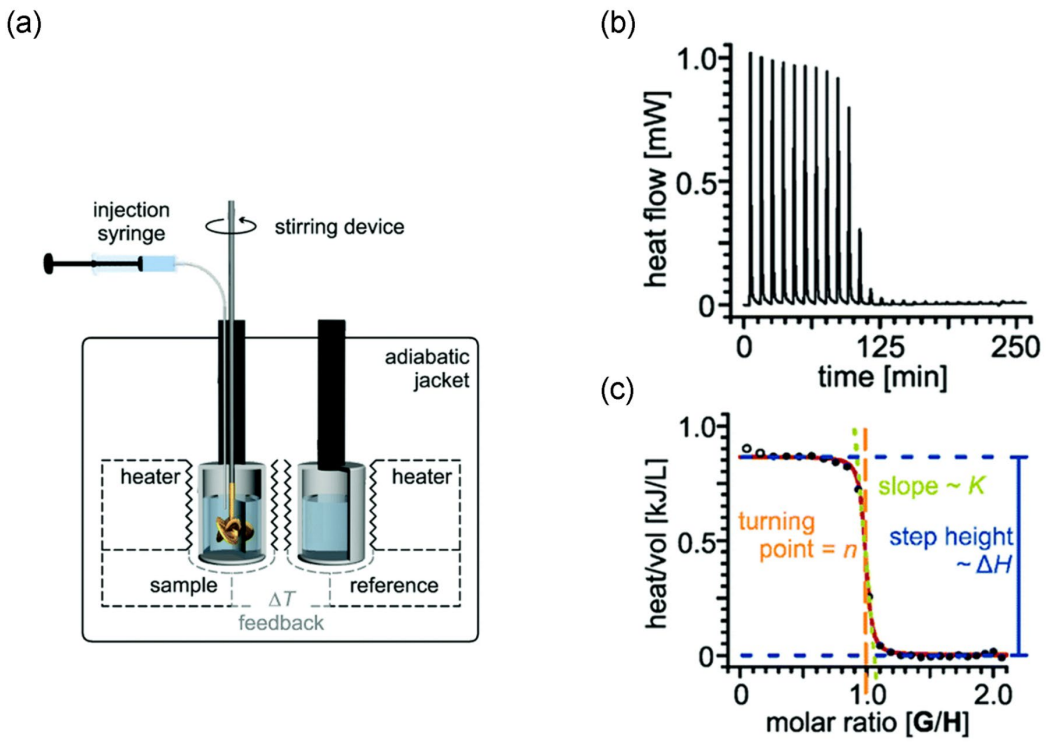


**Figure 2.26**: (a) Schematic diagram of an isothermal titration calorimeter, (b) Raw heat signals obtained in a titration experiment, and (c) the integrated heat signals plotted against the molar ratio which depicts the enthalpy ($\Delta H$), stoichiometry ($n$) and association constant ($K$). Reproduced from reference[206] with permission from The Royal Society of Chemistry.

The utilization of ITC to probe host-guest interactions, for both artificial and natural molecules, is widely studied and is covered in many excellent reviews.[202, 205, 210, 211] Hence, the following section will focus on the application of this technique on supramolecular polymerization processes, the principles which underlie its usage as well as examples where this has been successfully applied to derive the thermodynamic parameters of aggregation.

### 2.3.2.1 Isothermal Titration Calorimetry of Supramolecular Polymers

The advantages of ITC utilized to study host-guest interactions can also be extended to probe self-assembly, where the association of monomers into aggregates is followed by a heat signal. However, the standard ITC titration protocol cannot be applied for aggregation studies, and here we have to employ a dilution technique to track the association (dissociation) phenomenon.[212-214] In an ITC dilution experiment, a concentrated solution of aggregated compound taken in the syringe is injected into the sample cell containing pure solvent. The initial injections lead to the dissociation of the aggregate into monomers or partially aggregated species, which result in a heat pulse. Upon further injection, the concentration of the associated species increases in the cell, which saturates the heat signal.

The dilution enthalpogram resulting from the energetic profile of dissociation typically has a hyperbolic profile.[214] Only for highly cooperative systems, a sigmoidal type isotherm has been observed.

The initial utilization of the dilution technique has already been carried since the 1990s for self-assembled structures with finite-size, like micelles.[215-218] The isotherm, which generally resembles a 1:1 stoichiometry, is defined based on the pseudo-phase model or the mass action model, offered by the theory of micellization.[202] However, the first attempt to use this technique for supramolecular polymers (specifically one-dimensional aggregates) was made by Bouteiller and coworkers who developed a model to study the co-operative association of a bis-urea based polymer, **50** (Figure 2.27a).[212]

Boutellier *et al.* proposed that the heat exchange during the $i^{th}$ injection of an aggregate solution into a cell of pure solvent is:

$$\boldsymbol{Q_{obs}(i) = \Delta Q(i) + Q_{dil}} \tag{2.20}$$

where $\Delta Q\,(i)$ corresponds to the heat resulting from the dissociation of supramolecular polymer into shorter structures whereas $Q_{\text{dil}}$ corresponds to the mechanical heat of injection as well as heat of dilution of solutes.

The heat component arising from the disaggregation, $\Delta Q(i)$ can be expressed as:

$$\boldsymbol{\Delta Q(i) = Q(i) - Q(i-1) + \frac{\Delta V_i}{V_0}\left[\frac{Q(i)+Q(i-1)}{2}\right]} \tag{2.21}$$

where $Q\,(i)$ is the heat exchanged when a supramolecular polymer solution of volume $V_{\text{i}}$ and concentration $C_0^s$ is injected into the sample cell with pure solvent where its concentration is reduced to $C_0^c$ (the superscripts '*s*' and '*c*' corresponds to syringe and cell respectively). $\Delta V_i$ is the volume per injections for '*i*' injections and $V_0$ is the calorimetric cell volume.

By applying equations developed for a self-association process with two aggregation constants (dimerization constant $K_2$ and elongation constant $K$) and two aggregation enthalpies (dimerization enthalpy change $\Delta H_2$ and elongation enthalpy change $\Delta H$) derived from mass action law, where the concentration of polymer chains with a degree of aggregation, $\alpha_{\text{agg}}$, 0 = $C_0$, and 1 = $C_1$, the following expression can be derived for $Q\,(i)$.

$$Q(i) = -\Delta H K_2 K V_i \left\{\frac{(C_1^S)^3}{(1-KC_1^S)^2} - \frac{C_0^S[C_1^C(i)]^3}{C_0^C(i)[1-KC_1^C(i)]^2}\right\} - \Delta H_2 K_2 V_i \left\{\frac{(C_1^S)^2}{1-KC_1^S} - \frac{C_0^S[C_1^C(i)]^2}{C_0^C(i)[1-KC_1^C(i)]}\right\} \quad (2.22)$$

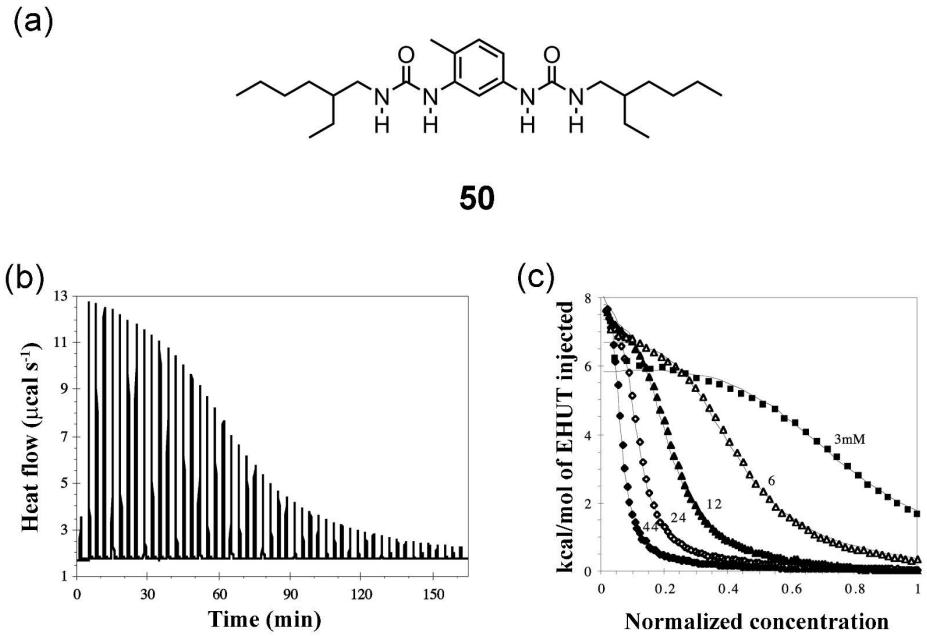


**Figure 2.27**: (a) Chemical structure of **50**, (b) Heat release per injection of aliquots of **50** (in $CDCl_3$) into pure $CDCl_3$ at 20 °C. (c) Enthalpograms at different concentrations of **50** plotted against concentration normalized by final cell concentration and fit according to the cooperative model. Adapted with permission from reference[212]. Copyright 2004 American Chemical Society.

Upon dilution of **50** into pure $CDCl_3$ in the cell, endothermic signals corresponding to the dissociation of H-bonds were observed, which constitute the major non-covalent bond involved in the self-assembly of **50** (Figure 2.27b). The enthalpograms obtained at different concentrations were fitted to a cooperative model described by the equations mentioned above, and the corresponding thermodynamic parameters were deduced (Figure 2.27c). These were in excellent agreement with the values obtained with FT-IR measurements, substantiating the validity of this new fitting protocol. Demonstrating the potential of the ITC dilution method, they further studied the polymerization of **50** in toluene, where previously self-assembly studies were not viable by FT-IR or NMR spectroscopy due to the high aggregation tendency in this solvent.

In another example, the authors extended the mass action laws to describe the competition of two supramolecular polymers in equilibrium of the same bis-urea derivate (**50**).[219] Depending on concentration and temperature, **50** exists as filaments or tubes in toluene.

Supplemented by differential scanning calorimetry (DSC), they were able to successfully define the enthalpograms of the ITC dilution experiment and derive binding constants and enthalpy changes of both these polymers. The length, as well as the proportion of these two self-assembled structures and the monomer species, were calculated successfully, which agree with the experimental phase diagram as well as to viscosity measurements.

The empirical nature of self-assembly models, including the aforementioned one, has been criticized because they do not take into account entropy changes with aggregate growth.[220] Addressing these limitations of conventional association models, Turcu and Mic proposed a DK (decreasing *K*) model on the grounds of statistical thermodynamics.[214] This takes into account the influence of aggregate size on association constant *K*, and concomitantly on Gibbs free energy, by considering the variation of entropy based on size dependence. The authors applied this model to investigate the association (dissociation) of Ciprofloxacin (**51**), a broad-spectrum antimicrobial antibiotic (Figure 2.28a). Upon dilution in water, **51** gave exothermic signals signifying that the self-assembly is endothermic or enthalpically favored (Figure 2.28c). Initial attempts to fit the isotherm with the native DK model was inadequate and did not agree well with the association constants measured from independent NMR experiments. Authors attributed this to the coexistence of two processes, the initial dimerization due to cation-π interactions and further elongation *via* π-π stacking (Figure 2.28b). The initial step does not create significant changes in the magnetic environment of studied nuclear spin and hence leads to the discrepancy with the ITC dilution experiment, which measures overall heat as cumulated contributions from all processes. Taking into consideration of these two competing events, the authors developed a new hybrid model where the initial dimerization is also considered and was able to successfully describe the isotherms from the ITC dilution experiment (Figure 2.28d).

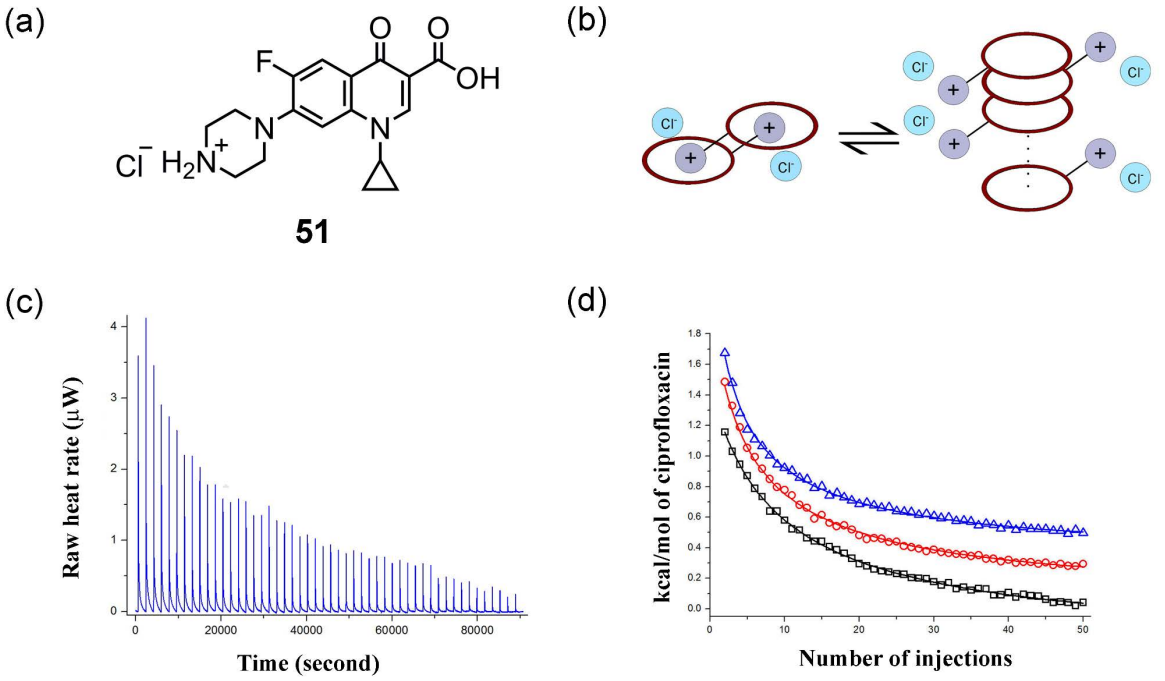


**Figure 2.28**: (a) Chemical structure of Ciprofloxacin, **51**. (b) Schematic diagram showing the dimer formation of **51** assisted by cation-π interactions and elongation by π-π interactions. (c) Heat release per injection of **51** into the water at 25 °C. (c) Enthalpograms at different concentrations of **51** and fit according to the hybrid-DK model. Adapted with permission from reference[214]. Copyright 2013 American Chemical Society.

In many biophysical studies, ITC has been successfully applied to investigate the thermodynamics of binding of ligands with a host like DNA. Since many such DNA grove binders are planar aromatic molecules, they can self-associate in water, which generates multiple coupled equilibria consisting of ligand self-association (dissociation) as well as DNA-ligand binding.[221] Generally, for simplicity, model-free ITC fits are used in such cases, which measure only a statistically meaningful $\Delta H$ and not the binding constants.[222] In order to address these problems, Buurma and Haq developed a mathematical model that can successfully describe calorimetric data representing multiple equilibria using a simulated annealing approach.[213] Using this, they investigated the aggregation as well as DNA binding of the bis-benzimidazole dye Hoechst 33258 (H33258). H33258 can bind to DNA oligonucleotides lacking cognate minor groove A-T sites. However, it can also undergo association at higher concentrations in a step-wise manner driven by π-π stacking. ITC dilution experiments revealed an enthalpy-driven self-assembly of the dye, which follows an isodesmic mechanism. The parameters obtained from these aggregation studies were further utilized to fit the complex binding equilibria of H33258 with different non-cognate DNA sequences, thus demonstrating the significance of this new method. Later, the authors utilized the model to successfully describe the binding of a thiazotropsin class

of dye with cognate DNA[223] and a tetraazaperopyrene with G-quadruplex[224] using ITC, where the aggregation of ligand leads to multiple equilibria.

Despite its myriad advantages and a plethora of models developed to describe self-assembly by ITC, this technique is still less versatile compared to conventional spectroscopic methods. Major bottlenecks in adapting ITC for self-assembly are poor heat signals, as well as an inability to cover a wider range of aggregated species in a single experiment.[225] These could inevitably create larger uncertainties in the binding constant as well as other thermodynamic parameters derived. Hence, it is advisable to use ITC dilution experiments in concordance with an independent method that can verify the estimated values quantitatively.

### 2.3.3 Differential Scanning Calorimetry (DSC)

DSC measures the heat capacity of a solution with respect to temperature. In modern power-compensated DSC's, the solution containing solute is placed on the sample cell, whereas an equal volume of pure solvent is placed on the reference cell.[226] The two cells are heated simultaneously in a quasi-adiabatic fashion, and the electrical power required to keep the temperature difference between two cells is measured. The apparent molar heat capacity (at constant pressure) is plotted against temperature to obtain a thermogram or thermal transition curve (Figure 2.29).

The difference between the molar heat capacities of initial and final states gives the change in molar heat capacity (at constant pressure) of the transition, $\Delta C_p$.[227] $T_m$ denotes the transition midpoint where 50% of the conversion from the initial state to final state occurs. Since the change in heat capacity is a temperature derivative of enthalpy change, the integration of a DSC thermogram provides the enthalpy change associated with the process.

$$\Delta H = \int_{T_1}^{T_2} \Delta C_p \tag{2.23}$$

The value thus derived is often termed as calorimetric enthalpy, $\Delta H^{\mathrm{cal}}$ and is a model-independent parameter that does not depend on the shape of the transition curve. The transition curve can also be analyzed by a van't Hoff equation to obtain van't Hoff enthalpy, $\Delta H^{\mathrm{vH}}$. The determination of van't Hoff enthalpy assumes an equilibrium state between only two states and is model dependent. If the ratio of calorimetric and van't Hoff enthalpies is 1, then the transition occurs *via* two states. A ratio of more than 1 indicates the presence of intermediate states, whereas a ratio of less than 1 denotes an irreversible process.

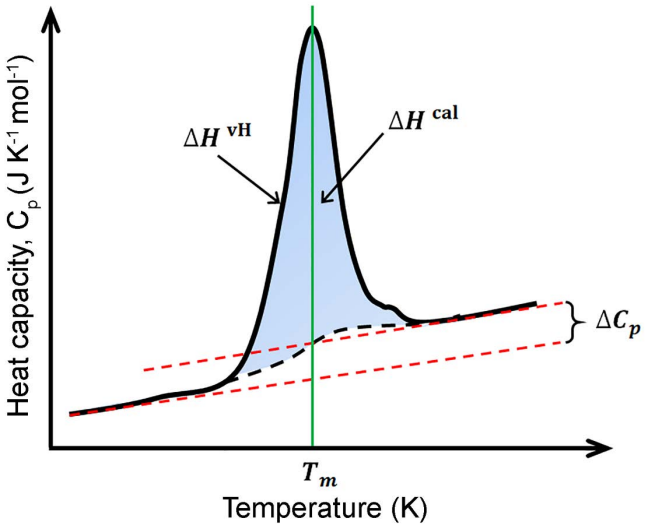


**Figure 2.29**: Representative DSC thermogram, where apparent heat capacity is plotted as a function of temperature.

While DSC has been utilized in the biophysical community[227] as well as for solid-state characterization[228], the application of this technique to self-assembly studies in solution state is scarce. Chiappisi *et al.* developed a new mass action model to describe the DSC curves of self-assembling systems and successfully applied it to study the micellization behavior of poly (ethylene oxide)-poly (propylene oxide) copolymers in water.[229] Here, an aggregation process with unimers and monodisperse micelles at equilibrium are considered, according to a closed-association model. The molar heat capacity obtained in a DSC thermogram in such a case is expressed as:

$$C_p(T) = -\frac{\partial \chi(T)}{\partial T}\left[\overline{\Delta H_m^0}(T^*) + \overline{\Delta C_{p_m}^{\ 0}}(T - T^*)\right] \tag{2.24}$$

where $\chi$ is the fraction of non-aggregated surfactant, $\overline{\Delta H_m^0}$ is the change in standard enthalpy of micellization at temperature, $T^*$ and $\overline{\Delta C_{p_m}^{\ 0}}$ is the change in heat capacity per mole for the aggregation process.

The fraction of non-aggregated surfactant, $\chi$ can be given as:

$$\frac{1-\chi(T)}{\chi(T)^{N(T)}} = N(T)c^{N(T)-1}\exp\left\{-\left[\frac{N(T)}{R}\left[\frac{\overline{\Delta G_m^0}(T^*)}{T^*} + \left(\overline{\Delta H_m^0}(T^*) - T^*\overline{\Delta C_{p_m}^{\ 0}}\right)\left(\frac{1}{T}-\frac{1}{T^*}\right) - \overline{\Delta C_{p_m}^{\ 0}}\ln\left(\frac{T}{T^*}\right)\right]\right]\right\} \quad (2.25)$$

where $N(T)$ is the aggregation number at temperature $T$, $c$ is the total concentration of surfactant, $R$ is the universal gas constant, and $\overline{\Delta G_m^0}$ is the change in standard free energy of micellation.

By fitting the above equation to the DSC thermograms for a series of surfactants, the authors were able to successfully derive thermodynamic parameters of micellization and studied the effect of aggregation numbers on the output of DSC experiments. Significantly, the calorimetric and van't Hoff enthalpies as well as the aggregation numbers derived matches with each other, and agrees with the light scattering experiments, confirming the validity of the model. Furthermore, modification of this model was also carried out to accommodate the polydispersity of the block copolymers used.

Bouteiller *et al.* utilized DSC to investigate the transition between two supramolecular structures, tubes, and filaments formed by the self-assembly of bis-urea derivative **50** in toluene.[219] While this conversion was indicated by an endothermic peak suggesting an enthalpic penalty; there was no significant difference in the molar heat capacity of tubes and filaments ($\Delta C_p = 0$). The transition temperatures determined for various concentrations match with the observations from ITC and FT-IR and is even able to fill the concentration gap in the data obtained by the above two measurements. Furthermore, the calorimetric enthalpy calculated at different concentrations matches with the ITC data obtained by a new mass-action model, under the assumption that enthalpic contributions from dimers are neglected compared to longer oligomers.

DSC can also be utilized to differentiate between isodesmic and cooperative polymerization.[50] Meijer *et al.* have shown that the transition at elongation temperature, $T_e$ for an oligo(*p*-phenylenevinylene) derivative is accompanied by a strong endotherm compared to the broad peak at the nucleating regime.[199]

Despite its information density, DSC is yet to receive appreciation among the supramolecular community as a useful technique to quantify the thermodynamic parameters. Especially, processes that follow a two-state equilibrium under thermodynamic

conditions can be characterized by DSC since the calorimetric enthalpy calculated directly without the help of any models can yield the enthalpy of aggregation. A bottleneck in many cases is the low signal to noise ratio of the heat pulse unless the enthalpy change of transformation is appreciably high. The potential of DSC to investigate structural transitions *via* cooperative processes might be interesting as they are usually accompanied by significant heat changes.

# Chapter 3

# Synthesis

## 3.1 Molecular design

In our effort to understand the self-assembly of π-conjugated molecules in water, we have adopted bolaamphiphilic rylene bisimides consisting of a hydrophobic core and water-soluble head groups (referred to as 'brushes') on both ends. The symmetrical design utilized in the current work ensures easier synthetic accessibility as well as less-complex self-assembly processes, which generally yields one-dimensional columnar aggregates.[60] As the hydrophobic cores, perylene and naphthalene bisimides were chosen (Figure 3.1). As the hydrophilic brush substituents at imide positions, we have employed a phenyl or benzyl ring substituted with oligo ethylene glycol chains at 3,4,5 positions. Based on their structure as well as the synthetic route adopted to obtain the respective amine, these brushes can be classified into three types (Type I, Type II, and Type III) (Figure 3.1). In Type I brushes, the oxygen atom of the ethylene glycol chain is connected to the phenyl ring *via* a propylene spacer. In Type II, this spacer is avoided, and the oxygen atoms are connected directly to the phenyl ring. Finally, in a Type III brush, the oligo ethylene glycol chains are directly linked to a benzyl ring instead of the phenyl ring used above.

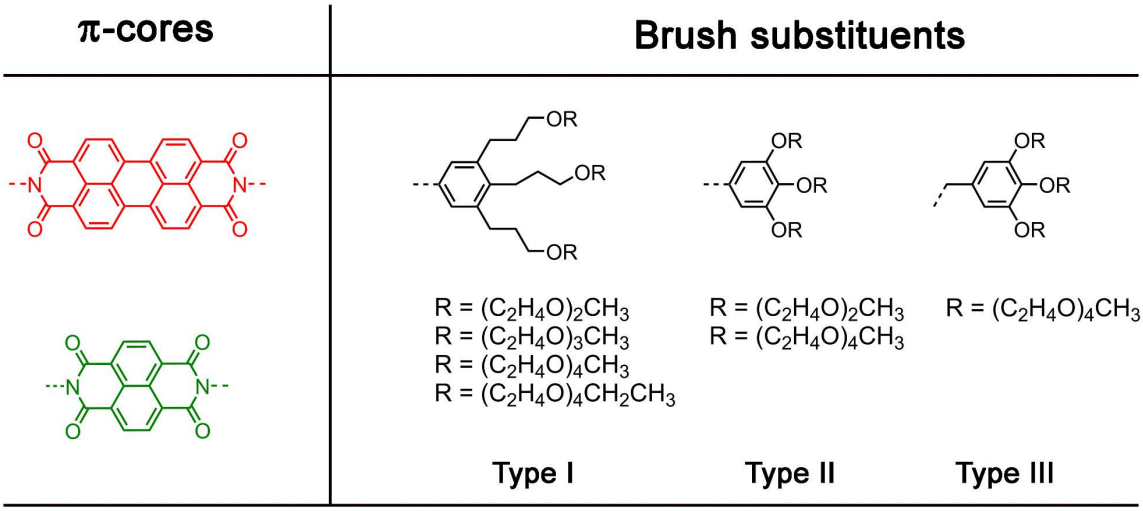


**Figure 3.1**: Chemical structures of π-cores and brush substituents used in this thesis.

## 3.2 Synthesis

### 3.2.1 Synthesis of brush substituents

For the synthesis of Type I brushes, a multi-step synthetic route was adopted akin to previous reports on analogous molecules (Scheme 3.1).[68, 230] Generally, this starts with the alkynation of a commercially available ethylene glycol monoalkyl ether using propargyl bromide.[231] When the glycol unit is not commercially available, the synthesis was carried out, starting from the mono benzyl derivative of the glycol chain. This was first treated with the tosylated glycol chain in the presence of sodium hydride to obtain a glycol fragment of the desired length. Finally, the benzyl protection was removed by reduction with $H_2$ in the presence of Pd/ C catalyst at room temperature and 1 atm pressure. The alkynated glycol unit was then coupled to 2-bromo-1,3-diiodo-5-nitrobenzene (obtained by iodination of 1-bromo-4-nitrobenzene)[232] in a two-step one-pot Sonagashira reaction with $NEt_3$ as the solvent. In the first step carried out at room temperature, the two I atoms are replaced by the alkynated glycol fragment to yield the di-substituted derivative as the major product. In the second step, the Br atom, being less reactive, is replaced by carrying out the reaction at a higher temperature (75 °C) for a short time (~1 hr). Since both disubstituted, as well as trisubstituted derivatives, decompose at elevated temperatures, it is crucial to stop the reaction when the predominant conversion has taken place. Unlike the previous reports, a one-pot approach was used in the current work where the isolation of intermediate (di-substituted derivative) was avoided. This resulted in an easier purification process *via* column chromatography. It should be noted that the utilization of tri-iodo substituted analog of **57** will result in a complex mixture with several decomposed products, which is rather difficult to purify by conventional chromatographic techniques.

In the next step, the trisubstituted nitro derivative, **58**, is reduced to its corresponding amine in an autoclave in the presence of $H_2$ and Pd/ C catalyst. The purity of catalyst as well as pressure (6-10 bar) and reaction time (~ 4 days) are crucial for the complete conversion and an easy purification process.

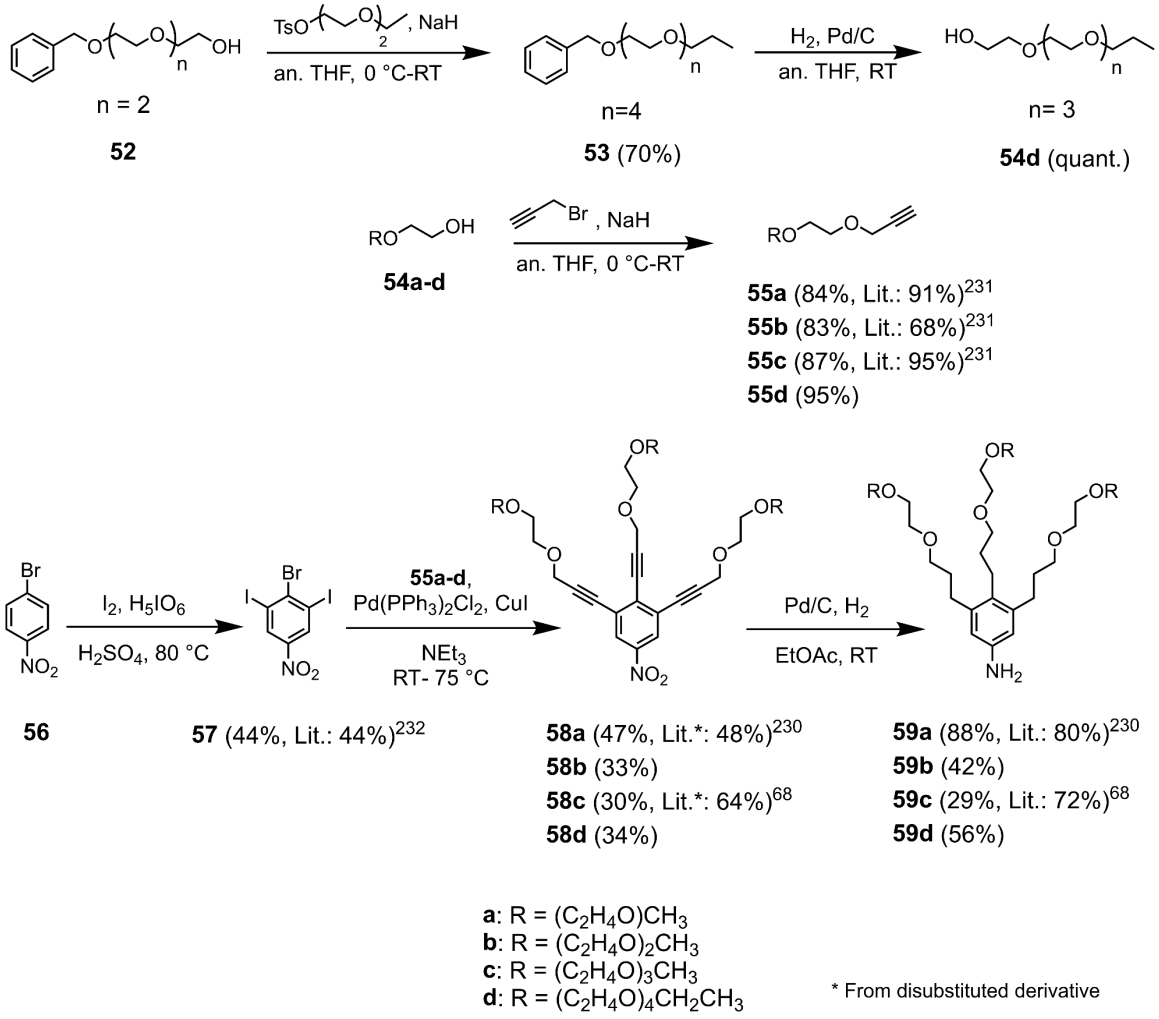


**Scheme 3.1**: Synthesis of amine derivatives of Type I brushes (**59a-d**).

Type II brushes, where the oxygen atom was directly attached to the phenyl ring, were synthesized either from commercially available methyl gallate (**60**) or pyrogallol (**64**) (Scheme 3.2). Starting from methyl gallate, glycol chains were appended by treating with corresponding tosylated monomethyl glycol in the presence of $K_2CO_3$ and KI.[233] In the subsequent step, the ester group was converted into an amide by treating with aqueous ammonia. Initial attempts to perform the reaction at room temperature gave poor yields. To surpass this, the reaction mixture was heated gently (to avoid base hydrolysis) for several days to obtain the desired product, **62** in moderate yield. This was further treated with $Br_2$ water in the presence of KOH (Hofmann's degradation reaction) to obtain the corresponding amine **63**.

The amino derivative of shorter Type II brush (**67**) has been previously reported[234] and was synthesized accordingly with slight modifications (Scheme 3.2). Unlike the reported procedure where pyrogallol was functionalized with the glycol chain in the presence of 18-

crown-6 and acetone, the reaction was carried out with $K_2CO_3$, KI, and ACN, which afforded better yields in considerably less time. In the next step, **65** was nitrated using silica gel treated with nitric acid ($SiO_2$**.**$HNO_3$) and nitric acid. The product was reduced with $H_2$ in the presence of Pd/ C catalyst at room temperature to afford the corresponding amine.

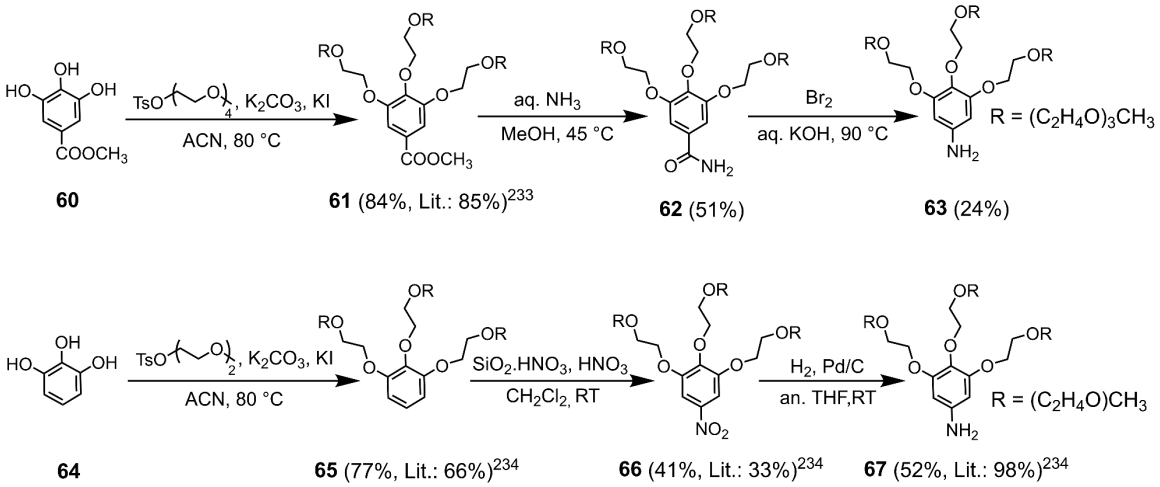


**Scheme 3.2**: Synthesis of amine derivatives of Type II brushes (**63** and **67**).

In a Type III brush, the glycol chains are attached to a benzyl ring, unlike the former two cases where the connectivity at 3,4,5 positions was on a phenyl ring. For this, methyl gallate was first treated with tosylated glycol in the presence of $K_2CO_3$ and KI in acetonitrile to obtain the corresponding glycol substituted ester (**61**) (Scheme 3.3). Subsequent reduction with $LiAlH_4$ afforded the benzyl alcohol derivative (**68**) in good yields.[233] The conversion of this to amine was achieved *via* Mitsunobu reaction by first treating with phthalimide in the presence of diethyl azodicarboxylate (DEAD) and triphenylphosphane ($PPh_3$) to obtain **69**, followed by the hydrazinolysis with hydrazine monohydrate.

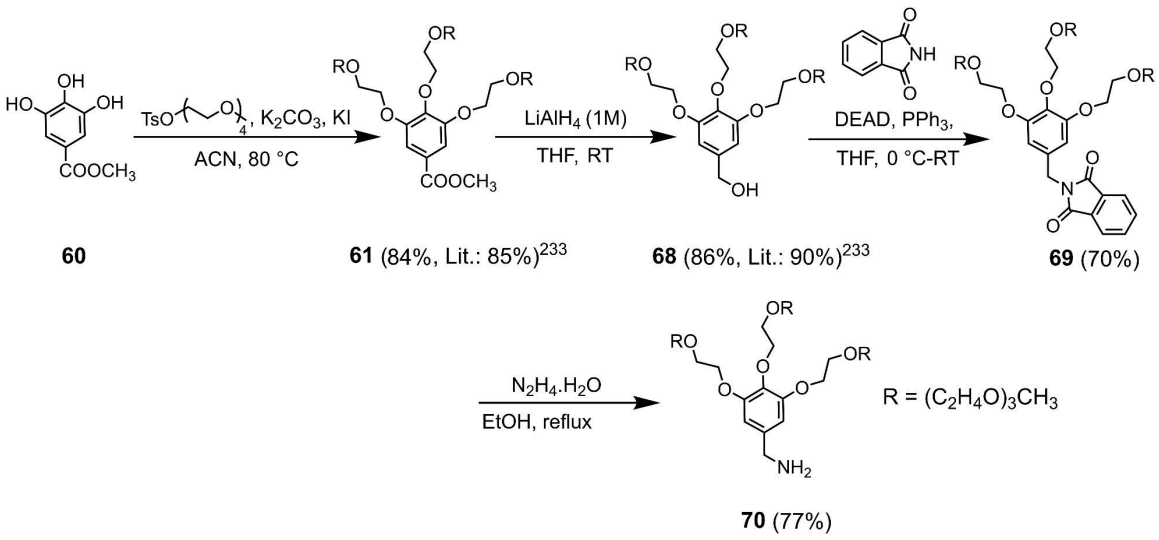


**Scheme 3.3**: Synthesis of amine derivative of Type III brush (**70**).

### 3.2.2 Synthesis of bolaamphiphilic perylene and naphthalene bisimides

The synthesis of symmetrical *N*,*N*' perylene derivatives was carried out by well-reported condensation reaction of corresponding amine and perylene-3, 4: 9, 10-tetracarboxylic acid bisanhydride (Scheme 3.4).[235] Imidazole was used as the solvent and anhydrous zinc acetate as a Lewis acid catalyst.

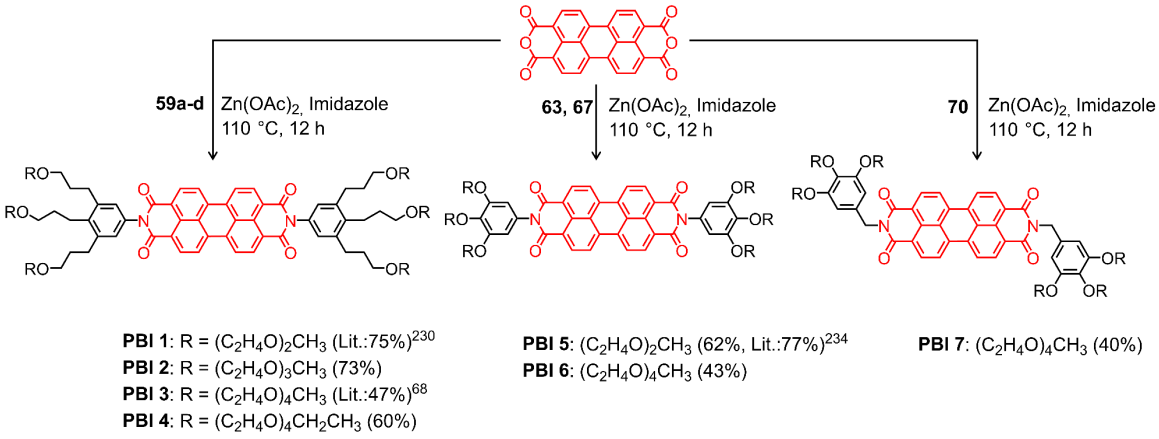


**Scheme 3.4**: Synthesis of bolaamphiphilic PBI derivatives, **PBI 1-7**.

The bolaamphiphilic NBI derivatives were synthesized by imidization reaction of 1,4,5,8-naphthalene tetracarboxylic acid bisanhydride and the respective amine derivative in either acetic acid or DMF as the solvent (Scheme 3.5). While DMF is a suitable solvent for such reactions, for Type I brushes, several byproducts corresponding to decomposed amine were observed, making the purification cumbersome. An acidic workup using HCl was not suited to remove these impurities. However, when performing the reaction in acetic acid, these

side products were not observed, albeit a considerable decrease of the reaction yield. Hence, for the imidization of Type I brushes, acetic acid was chosen as the solvent. For Type II & III brushes, such a decomposition of amines was not observed, and DMF could be used as the reaction medium. The purification of all final compounds was achieved by a combination of silica gel column chromatography and gel permeation chromatography.

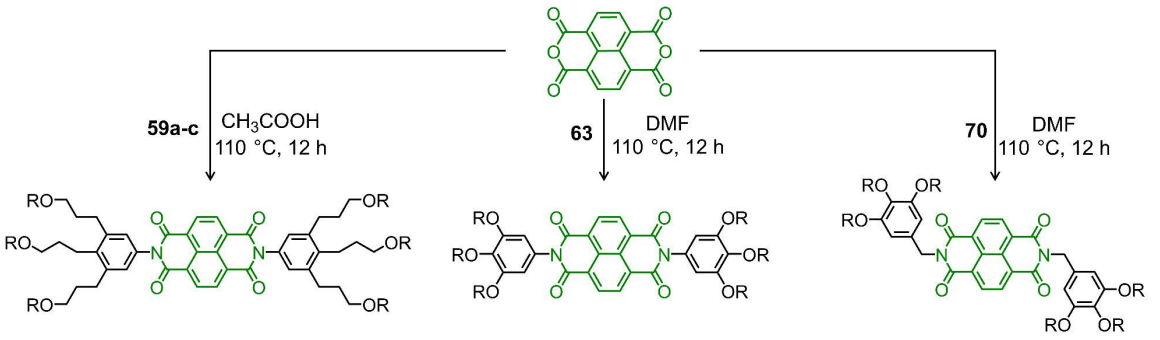


**NBI 1**: R = $(C_2H_4O)_2CH_3$ (35%)
**NBI 2**: R = $(C_2H_4O)_3CH_3$ (33%)
**NBI 3**: R = $(C_2H_4O)_4CH_3$ (32%)

**NBI 4**: R = $(C_2H_4O)_4CH_3$ (53%)

**NBI 5**: R = $(C_2H_4O)_4CH_3$ (45%)

**Scheme 3.5**: Synthesis of bolaamphiphilic NBI derivatives, **NBI 1-5**.

# Chapter 4

# Entropically Driven Self-assembly of π-Amphiphiles in Water

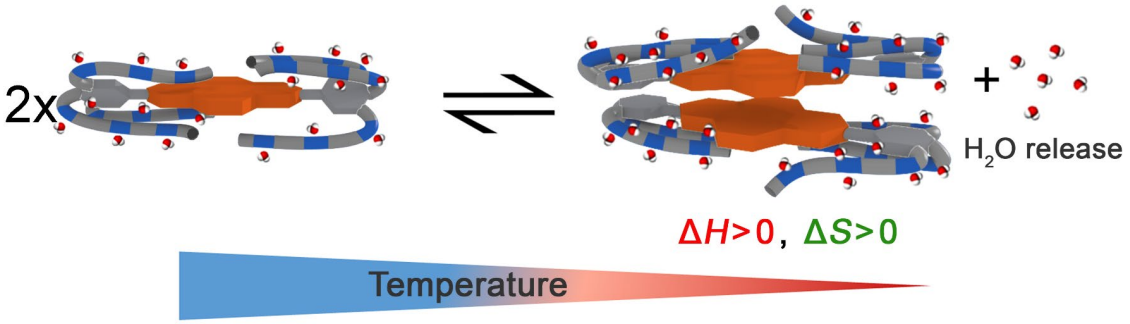


**ABSTRACT**: Self-assembly of amphiphilic dyes and π-systems are more difficult to understand and to control in water compared to organic solvents due to the hydrophobic effect. Herein, we elucidate in detail the self-assembly of a series of archetype bolaamphiphiles bearing a naphthalene bisimide (NBI) π-core with appended oligo ethylene glycol (OEG) dendrons of different size. By utilizing temperature-dependent UV-vis spectroscopy and isothermal titration calorimetry (ITC), we have dissected the enthalpic and entropic parameters pertaining to the molecules' self-assembly. All investigated compounds show an enthalpically disfavored aggregation process leading to aggregate growth and eventually, precipitation at elevated temperature, which is attributed to the dehydration of oligo ethylene glycol units and their concomitant conformational changes. Back-folded conformation of the side chains plays a major role, as revealed by molecular dynamics (MD) and two dimensional NMR (2D NMR) studies, in directing the association. The sterical effect imparted by the jacketing of monomers and dimers also changes the aggregation mechanism from isodesmic to weakly anti-cooperative.

This chapter was published in: P. P. N. Syamala, B. Soberats, D. Görl, S. Gekle and F. Würthner, *Chem. Sci.*, 2019, **10**, 9358-9366. Reproduced from reference[279] with permission from The Royal Society of Chemistry. MD simulations were performed by Prof. Stephan Gekle and AFM measurements were conducted by Dr. Vladimir Stepanenko.

## 4.1 Introduction

Self-assembled nano- and mesoscale structures play a major role in nature and particularly in living organisms.[236-239] The sophisticated functionalities of these structures are imputable to the interplay of hydrogen bonds (H-bonds)[240] as well as solvophobic effects,[54] derived to the unique role of water as a solvent.[16, 239] The desire to mimic and understand such naturally occurring self-assembled systems has prompted the investigation of various amphiphilic/bolaamphiphilic molecules consisting of non-polar hydrophobic cores attached with water solubilizing side chains.[241] Through these investigations, a wide variety of nanometric supramolecular aggregates of different morphologies (tubular, fibrillar, micellar, vesicular) has been prepared *via* exploring solvophobic effects,[176, 242, 243] H-bonding,[22, 146, 163, 174] electrostatic screening,[17, 148] metal-ion coordination,[186, 244, 245] variation of hydrophilic/hydrophobic balance,[21, 65] and co-solvent modulation.[25, 168, 246]

However, different from the very intensively conducted studies on the enthalpic and entropic contributions that govern supramolecular host-guest complex formation in water,[103, 107, 189] studies devoted to an in-depth understanding of the thermodynamic profile of self-assembly processes of π-amphiphiles in water remains scarce.[55] Nevertheless, such an understanding is warranted not only from a supramolecular design perspective, but also in therapeutic, and materials sciences.

In this direction, we have identified that π-conjugated cores of perylene bisimide dyes appended with six oligo ethylene glycol (OEG) chains as very useful amphiphilic molecules, whose self-assembly processes can be easily followed by various spectroscopic and microscopic techniques.[24, 64, 67, 173] But only very recently we unveiled our serendipitous discovery that the self-assembly of OEG substituted perylene bisimide (PBI) derivatives in water is not driven by enthalpic dispersion and electrostatic forces as in organic solvents,[64] but by entropic factors, albeit the process can be shifted to an enthalpic route by the addition of only small amounts of an organic co-solvent.[68] We attributed this intriguing behavior to the exclusion of water molecules from the OEG side chains which leads to a dominant entropic contribution to the self-assembly in pure aqueous environment, which was also later demonstrated for other dye assemblies by Ghosh *et al.*[165] Whilst these interesting results warrant further studies, our PBI systems aggregated too strongly in water, evading an in-depth thermodynamic characterization including isothermal titration calorimetry (ITC). Due to the smaller π-core, naphthalene bisimides (NBIs) appeared to be more

promising because their self-assembly requires higher concentrations, which is beneficial for methods like NMR and ITC.

Herein, we report our detailed studies on the self-assembly of a series of naphthalene bisimides functionalized with OEG chains of different glycol units (**NBI 1**: *n*=2, **NBI 2**: *n*=3, and **NBI 3**: *n*=4) in water (Figure 4.1a). By means of UV-vis spectroscopy and ITC studies, we have achieved the dissection of entropic and enthalpic contributions to their self-assembly. Remarkably, we found that enthalpy, entropy, and free energy changes of **NBIs 1**-**3** aggregation in water strongly depend on the interaction of water molecules with the ether oxygen and accordingly on the OEG chain length (Figure 4.1b). Additional structural investigations by molecular dynamics (MD) and 2D-NMR techniques revealed back-folding of glycol chains with sequestration of the NBI π-cores from water, to be of importance as well.

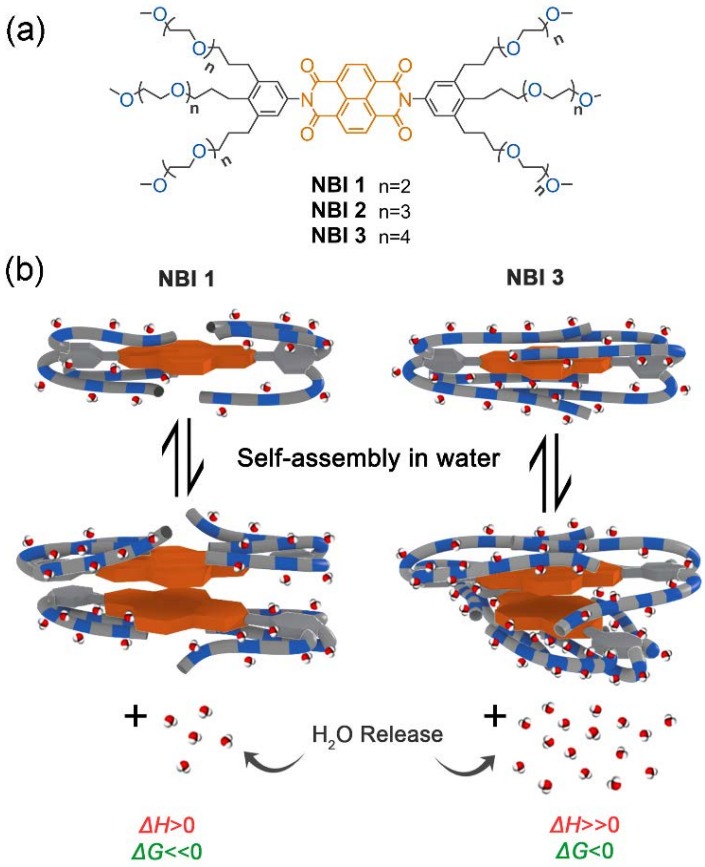


**Figure 4.1**: (a) Chemical structures of **NBI 1-3**. (b) Schematic illustration of self-assembly of **NBI 1** and **NBI 3** and corresponding changes in the thermodynamic parameters.

## 4.2 Results and discussion

### 4.2.1 Temperature-dependent self-assembly and morphology of the aggregates

To investigate the aqueous self-assembly behavior of **NBI**s **1-3**, initially we performed temperature-dependent UV-vis experiments below the cloud point (*vide infra*). For comparison, first we measured the absorption spectra of the NBIs in $CHCl_3$ (Figure A1). In an organic solvent of intermediate polarity like $CHCl_3$, **NBI 1** exist in monomeric form and shows an absorption maximum at 384 nm. In water, even at a dilute concentration of $9.7 \times 10^{-5}$ M, this absorption maximum is shifted to 364 nm, suggesting an H-type aggregated state (Figure 4.2a). While monitoring the temperature-dependent UV-vis spectra of **NBI 1** in a range of 10 °C to 50 °C in water, we observed a decrease in the ratio of these two vibronic bands, with a concomitant hypochromic shift. This clearly indicates an increase in the degree of aggregation with increasing temperature.[163] Similarly, both **NBI 2** and **NBI 3** exhibit an inverse temperature response where the aggregation is favored at elevated temperatures (Figure A2). Unlike the majority of supramolecular systems that disassemble upon heating, we have previously observed that bolaamphiphilic PBIs attached with OEG brushes show an inverse temperature response, where the aggregation is favored at higher temperatures.[68] This unique thermodynamic signature is now also manifested in the current NBI series as corroborated by temperature-dependent UV-vis experiments. It is noteworthy that the spectral changes upon aggregation are by far less pronounced for NBIs compared to PBIs due to the much smaller transition dipole moment of their $S_0 \rightarrow S_1$ transition.

At higher temperatures, we observed the phase separation of the NBIs from the aqueous phase. This is attributed to the lower critical solution temperature (LCST) phenomenon, which is typical for OEG appended systems.[230] The specific temperature denoting the onset of this precipitation, called cloud point ($T_{cp}$), can be determined by monitoring the transmittance at a wavelength where the molecule does not absorb (here 800 nm). The phase separation from the binary solution is characterized by an abrupt drop in transmittance. The knowledge of $T_{cp}$ is quintessential for our self-assembly studies since it sets the upper limit for the temperature window where aggregation can be monitored. Furthermore, it gives clue towards the amount of water molecules forming H-bonds to OEG chains, as the $T_{cp}$ increases with the extent of hydration. **NBI 1**, containing the shortest glycol chain, shows a $T_{cp}$ of 59 °C at a concentration of $1 \times 10^{-3}$ M in water, while **NBI 2** and **NBI 3** show phase separation at 78 and 88 °C, respectively, at the same concentration

(Figure 4.2b). Since the clouding is mainly associated with the dehydration of glycol units, an increase in the $T_{cp}$ suggests an increase in the extent of hydration with elongation of glycol chains.

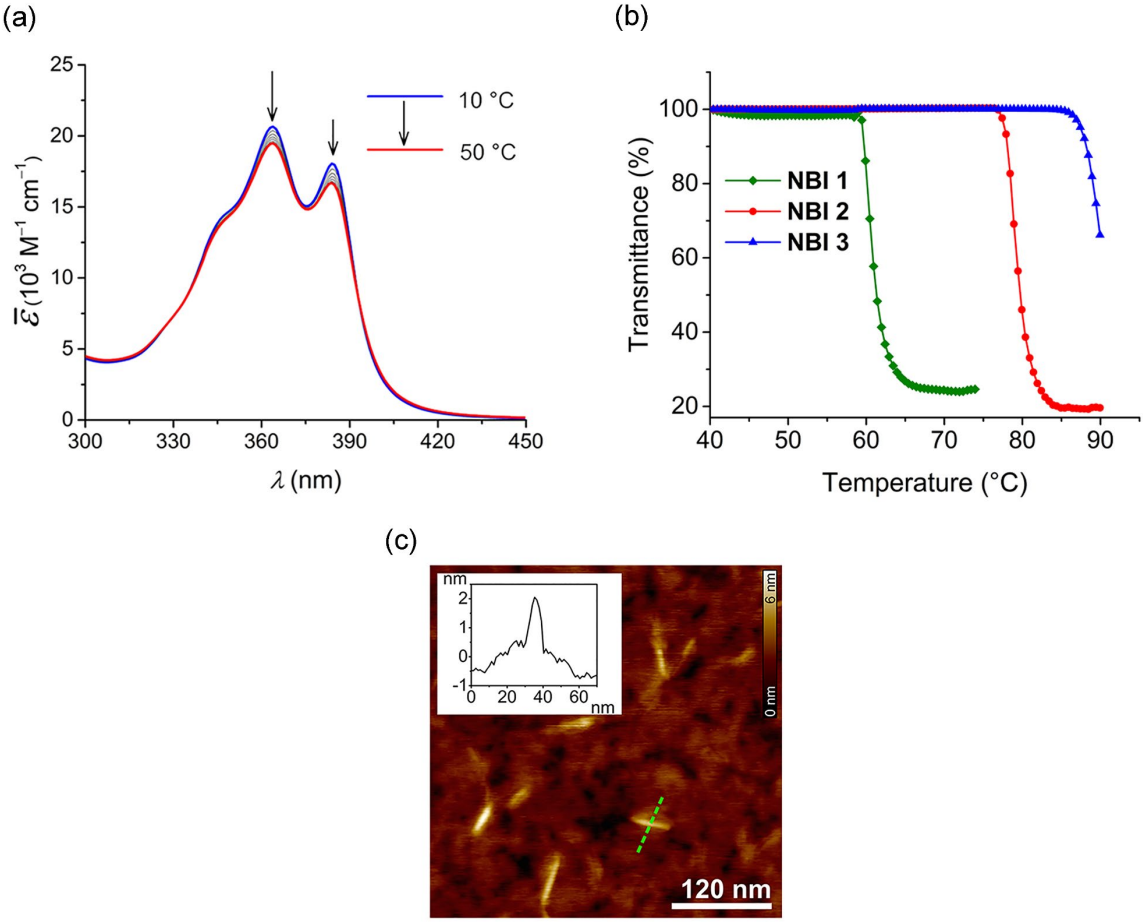


**Figure 4.2**: (a) Temperature-dependent UV-vis spectra (density corrected) of **NBI 1** in water ($c$ = 9.7 × $10^{-5}$ M). Arrows indicate spectral changes upon heating. (b) Cloud points ($T_{cp}$) determined by measuring transmittance at 800 nm as a function of temperature for **NBI 1** ($c$ = 1.0 × $10^{-3}$ M), **NBI 2** ($c$ = 0.99 × $10^{-3}$ M) and **NBI 3** ($c$ = 1.0 × $10^{-3}$ M) in water (Heating rate: 0.1 °C/ min). (c) AFM height image of **NBI 1** prepared by spin-coating from water ($c$ = 5.2 × $10^{-3}$ M) on silicon wafer (2000 rpm) and corresponding cross-section analysis for the dashed green line in image (Inset).

In order to characterize the morphology of the aggregates formed below $T_{cp}$, stock solutions of NBIs in water at 22 °C were spin coated onto silicon wafer treated with argon plasma and visualized using atomic force microscopy (AFM). The microscopy images for **NBI 1** obtained by tapping mode reveal short nanorods with a diameter of ~2 nm and average size distribution of 20–45 nm, suggesting a one dimensional (1-D) self-assembly (Figure 4.2c). The presence of anisotropic aggregates was further confirmed *via* DLS measurements, which showed size dependence upon variation of the scattering angle (Figure A4a).[247]

Similarly morphological investigations performed on **NBI 2** as well as **NBI 3** suggested nanorod like self-assembled species with a diameter of ~2 nm (Figure A3).

### 4.2.2 Thermodynamic profiling of NBI self-assembly

In an attempt to obtain a comprehensive thermodynamic profile for the self-assembly of **NBI**s **1**-**3** in water, we explored concentration-dependent UV-vis studies below $T_{cp}$ to monitor their transformation from monomers to 1D - aggregates. Figure 4.3a displays the spectral changes observed in our concentration-dependent experiment performed on **NBI 1** at 25 °C.

It was observed that with an increase in concentration, the absorption maximum shifts to 364 nm compared to the monomeric absorption maximum (381 nm), correlating to the spectral changes observed in temperature-dependent measurements. This suggests the formation of an H-type excitonically coupled stack.[248] Moreover, the transition from the monomeric to aggregated state is characterized by the presence of two isosbestic points (324 nm and 394 nm), implying an equilibrium between monomeric and aggregated species.

Figure 4.3a inset shows the corresponding plot of the degree of association ($\alpha_{agg}$) versus the logarithm of concentration. It was observed that the best fit for the data points was obtained with an isodesmic model, i.e., an equal association constant for each monomer addition.[48]

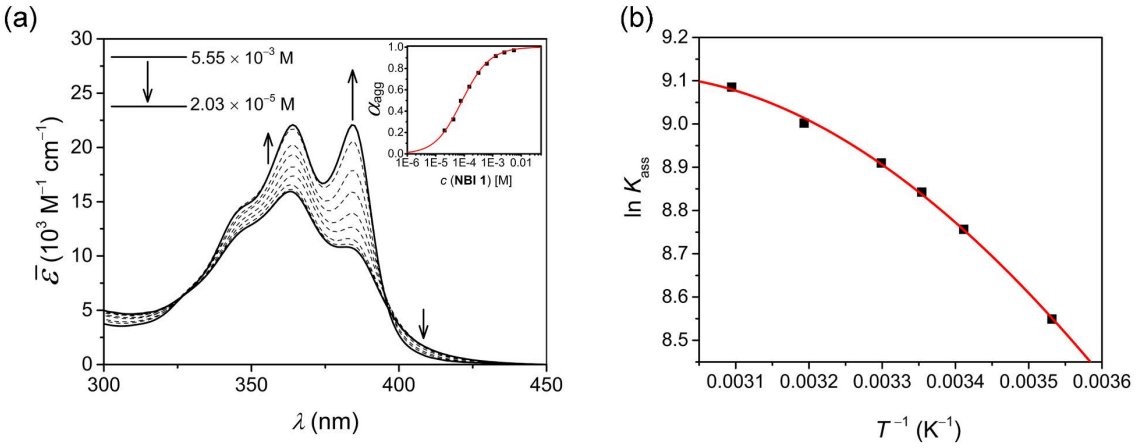


**Figure 4.3**: (a) Apparent absorption co-efficient for concentration-dependent UV-vis spectra of **NBI 1** in water at 25 °C. The arrows indicate the spectral changes upon decreasing the concentration. Plot of the degree of aggregation, $\alpha_{agg}$ against concentration and analysis of the data based on the isodesmic model is shown in inset. (b) Plot of the natural logarithm of association constant (ln $K_{ass}$) against reciprocal of temperature and corresponding fit according to Clarke-Glew equation.

From this, the logarithm of the association constant, log $K_{ass}$ = 3.8, and the standard Gibbs free energy of association ($\Delta G°_{ass}$) of −21.9 kJ mol$^{-1}$ was estimated for **NBI 1** (at 25 °C). From the concentration-dependent UV/vis studies, the critical aggregation concentration (CAC) of 0.33 mM was also determined for **NBI 1** at 25 °C (Figure A9a).[22] To delve deeper into the understanding of thermodynamic parameters associated with the self-assembly, we performed the same experiment at different temperatures, from 10 to 50 °C (Figure A5).

Previously, the van't Hoff equation has been successfully utilized to derive standard enthalpy ($\Delta H°_{ass}$) and standard entropy ($\Delta S°_{ass}$) changes of self-assembly by assuming a linear relationship of the natural logarithm of aggregation constants with respect to temperature.[249, 250] However, this method is only valid when the enthalpy and entropy changes remain constant with changes in temperature.[251] Processes in water, however, are usually associated with wide fluctuations in these parameters, thus impeding an accurate description of the self-assembly process.[55, 200, 252] This limitation can be surpassed by taking the heat capacity changes into account. One such modification is Clarke-Glew method, where the isobaric temperature dependence of rate constants is described around a reference temperature, $\theta$.[203, 204] This approach allows the calculation of the change in heat capacity at constant pressure, $\Delta C_p$, which is inaccessible by the van't Hoff equation due to its inherent assumptions. According to the simplified form of Clarke-Glew method (also referred as extended/integrated van't Hoff equation), the change in association constant with respect to temperature can be expressed by eqn. (4.1).

$$ln\ [K(T)] = ln\ [K(\theta)] + \frac{\Delta H(\theta)}{R}\left[\frac{1}{\theta} - \frac{1}{T}\right] + \frac{\Delta C_p(\theta)}{R}\left[\frac{\theta}{T} - 1 + ln\left(\frac{T}{\theta}\right)\right] \qquad (4.1)$$

where ln $[K(T)]$ is the natural logarithm of the equilibrium constant at temperature $T$, ln $[K(\theta)]$ is the natural logarithm of the equilibrium constant at the reference temperature $\theta$, $\Delta H(\theta)$ is the enthalpy change at the reference temperature, and $\Delta C_p$ is the change in heat capacity at constant pressure.

While plotting the natural logarithm of the association constant *versus* the inverse of temperature, indeed a much better fit is obtained with the non-linear Clarke-Glew equation as compared to the van't Hoff equation (Figure 4.3b). Accordingly, a standard enthalpy of 11.2 kJ mol$^{-1}$ and a heat capacity change of −289 J mol$^{-1}$ K$^{-1}$ can be calculated for the self-assembly of **NBI 1**. With an elevation in temperature, an increase in aggregation strength is observed, quantitatively supporting our temperature-dependent UV-vis measurements.

Furthermore, the negative slope of the curve suggests the endothermic nature of self-association over a broad temperature range, which is hence enthalpically disfavored.

Similarly, concentration-dependent UV-vis experiments were conducted for **NBI 2** and **NBI 3** at different temperatures (Figure A6, A7). In both cases, we observed that the mechanism of self-assembly differs from the isodesmic model and is better described by a weak anti-cooperative process with a cooperativity factor of $\sigma = 2$ and $\sigma = 3$ for **NBI 2** and **NBI 3**, respectively. By fitting the data according to the Goldstein-Stryer model[52] utilized for (anti)cooperative aggregation processes, a logarithm of the association constant, log $K_{ass} = 3.3$, and a standard Gibbs free energy, $\Delta G°_{ass} = -18.8$ kJ mol$^{-1}$ was determined for **NBI 2** at 25 °C, suggesting a weaker aggregation tendency as compared to **NBI 1**. Using the Clarke-Glew plot, a standard enthalpy change of 18.1 kJ mol$^{-1}$ is calculated, which shows that the self-assembly of **NBI 2** is enthalpically more disfavored than **NBI 1** (Figure A8a). **NBI 3** exhibited the weakest aggregation tendency of all three derivatives, with log $K_{ass} = 2.8$ and a standard Gibbs free energy, $\Delta G°_{ass} = -16.4$ kJ mol$^{-1}$ at 25 °C. The self-assembly, in this case, is disfavored by a standard enthalpy ($\Delta H°_{ass}$) of 23.2 kJ mol$^{-1}$ (Figure A8b). Furthermore, the CAC estimated for **NBI 2** (1.6 mM) and **NBI 3** (3.5 mM) at 25 °C confirms the decreasing tendency of aggregation while increasing the glycol chain length from **NBI 1** to **NBI 3** (Figure A9b,c).

The thermodynamic signature at 25 °C obtained for the three derivatives is represented in Figure 4.4, which depicts that the self-assembly for all the NBI derivatives in water is enthalpically disfavored and entropically driven. Furthermore, this penalty in the standard enthalpy of association ($\Delta H°_{ass}$) and the gain in standard entropy of association ($\Delta S°_{ass}$) is augmented as the OEG chain length is increased from **NBI 1** to **NBI 3**. Since our cloud point measurements suggest an increase in hydration with chain elongation, this trend can be attributed to the increased number of water molecules that are removed for well-hydrated monomer units upon aggregation. On the other hand, the aggregation tendency decreases with an increase of glycol units, as reflected by increased $\Delta G°_{ass}$ values.

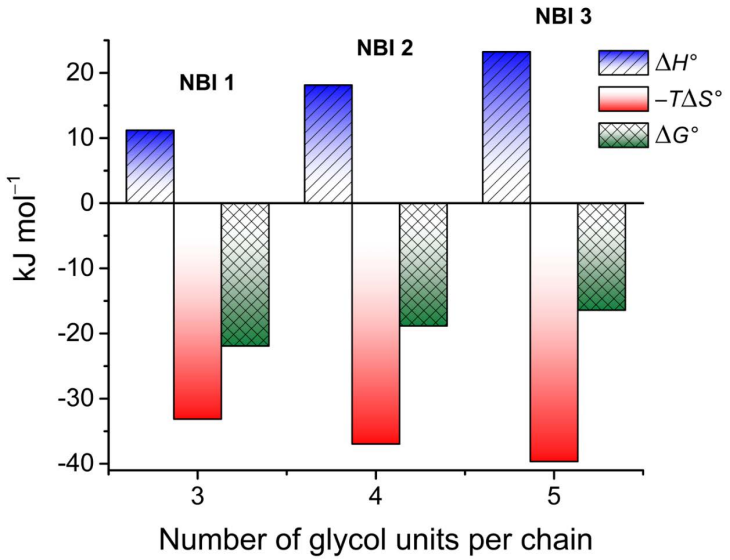


**Figure 4.4**: Thermodynamic profile for the self-assembly of **NBI 1-3** in water obtained by concentration-dependent UV-vis experiments.

In order to validate the thermodynamic parameters obtained by our UV-vis experiments, we resorted to an independent technique to derive the enthalpy, entropy, and free energy of association. This technique is given with an ITC dilution experiment that allows direct determination of enthalpy and gathers insight into its temperature dependency, which is inaccessible *via* other methods. Even though ITC is well established for natural[205, 253] and synthetic host-guest interactions,[103, 254-256] the advent of this technique to probe self-assembly is quite recent. [68, 212, 214, 257]

In a typical ITC dilution experiment, aliquots of a concentrated solution of the aggregated species is titrated into the pure solvent taken in the cell. The dissociation of the aggregate is then accompanied by non-constant heat signals along with constant heat of dilution.[212] From this, enthalpy and other thermodynamic parameters can be determined. Figure 4.5a shows the evolution of heat per injection of a concentrated aqueous **NBI 1** solution ($c$ = 5.2 × $10^{-3}$ M) into pure water at 25 °C leading to its disassembly, which depicts an exothermic heat flow, i.e., the dis-assembly process is enthalpically disfavored. The corresponding enthalpogram could be well fitted to an isodesmic model (Figure 4.5b).[213, 258] A standard enthalpy change of −13.8 kJ $mol^{-1}$ for dis-assembly (or +13.8 kJ $mol^{-1}$ for the corresponding self-assembly) and the logarithm of the association constant, log $K_{ass}$= 3.8 at 25 °C was determined for **NBI 1**, which is indeed in good concordance with the previously obtained values from UV-vis experiments (*vide supra*). Also, a CAC value of 0.21 mM was deduced for **NBI 1** from the aforementioned ITC dilution experiment (Figure A10).[165]

The accompanying heat of dilution estimated from the overall heat evolved during injection of **NBI 1** is provided in Table A1. Accordingly, different from our previous study of a strongly aggregating PBI,[68] here we could for the first time quantify the entropically driven self-assembly thermodynamics in water and derive values for $\Delta H°_{ass}$ and $K_{ass}$ of high accuracy. The thermodynamic parameters obtained by both these methods are tabulated in Table 4.1.

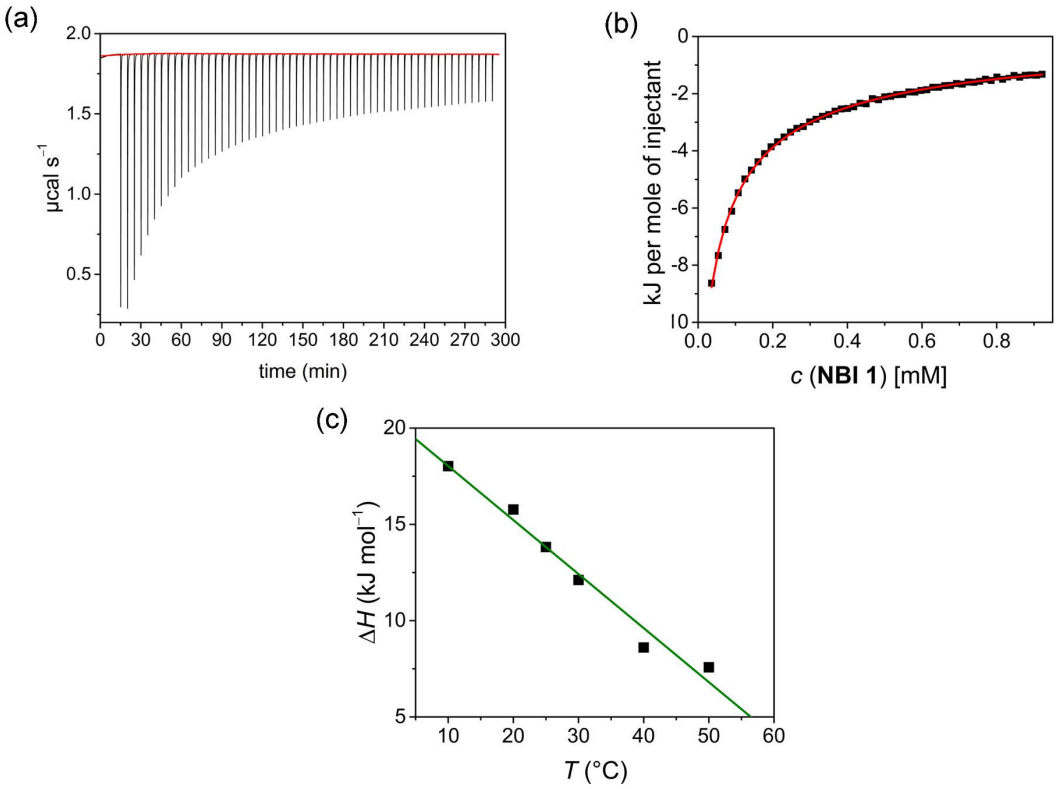


**Figure 4.5**: (a) Heat release per injection of an aqueous solution of **NBI 1** ($c$ = 5.2 × $10^{-3}$ M) into pure water at 25 °C. (b) Corresponding enthalpogram and fit according to the isodesmic model (red line). (c) Enthalpy of self-assembly for **NBI 1** at different temperatures (10 –50 °C) determined by ITC dilution experiment and corresponding linear fit.

Successively, to understand the influence of temperature on the enthalpy of self-assembly, we repeated the ITC dilution experiment at different temperatures, from 10 to 50 °C (Figure A11). It was observed that with increasing temperature, the enthalpy of association for **NBI 1** is concomitantly decreased (Figure 4.5c). It is expected that an elevation in temperature decreases the H-bond strength between the water molecules and OEG chains,[259] thus reducing the enthalpic penalty associated with the dehydration of water molecules during self-assembly. The increased aggregation tendency of these systems at higher temperatures could be traced to this easiness in the release of H-bonded water molecules.

**Table 4.1**: Thermodynamic parameters deduced for **NBI 1-3** using UV-vis and ITC dilution experiments.

| | **log $K_{ass}$** | | **CAC (mM)** | | **$\Delta H°_{ass}$ (kJ mol$^{-1}$)** | | **$T\Delta S°_{ass}$ (kJ mol$^{-1}$)** | | **$\Delta G°_{ass}$ (kJ mol$^{-1}$)** | | **$\Delta C_p$ (J mol$^{-1}$K$^{-1}$)** | |
|---|---|---|---|---|---|---|---|---|---|---|---|---|
| | UV-vis[1] | ITC[2] | UV-vis[3] | ITC[4] | UV-vis[5] | ITC[2] | UV-vis[6] | ITC[6] | UV-vis[7] | ITC[7] | UV-vis[5] | ITC[8] |
| **NBI 1** | 3.8 | 3.8 | 0.33 | 0.21 | 11.2 | 13.8 | 33.1 | 35.8 | −21.9 | −22.0 | −289 | −280 |
| **NBI 2** | 3.3 | - | 1.6 | - | 18.1 | - | 36.9 | - | −18.8 | - | −324 | - |
| **NBI 3** | 2.8 | - | 3.5 | - | 23.2 | - | 39.6 | - | −16.4 | - | −411 | - |

[1]Measured by concentration-dependent UV-vis experiment at 25 °C and calculated using the isodesmic model (**NBI 1**) or Goldstein-Stryer model (**NBI 2** and **NBI 3**). [2]Measured by ITC dilution experiment at 25 °C and calculated using the isodesmic model. [3]Measured by concentration-dependent UV-vis experiment at 25 °C. [4]Measured by ITC dilution experiment at 25 °C. [5]Measured by concentration-dependent UV-vis experiment at different temperatures and calculated using Clarke-Glew eqn. (4.1). [6]Calculated according to the relation $T\Delta S°_{ass} = \Delta H°_{ass} - \Delta G°_{ass}$. [7]Calculated according to the relation $\Delta G°_{ass} = -RT \ln K_{ass}$. [8]Measured by ITC dilution experiment at different temperatures and calculated using a linear fit.

The resulting heat capacity change for **NBI 1** aggregation was quantified as −280 J mol$^{-1}$K$^{-1}$ using eqn. (4.2),

$$\Delta C_p = \left(\frac{\delta(\Delta H)}{\delta T}\right)_p \tag{4.2}$$

Similar dilution experiments in pure water were also performed for **NBI 2** and **NBI 3** at 25 °C (Figure A12, A13). Here also the dilution experiments revealed exothermic signals for disassembly, accordingly the self-assembly is endothermic. Intriguingly, in both cases, we observed heat signals associated with two distinct processes (Figure A12b, A13b). Such two-step processes with similar heat signature have been previously reported for host-guest studies of ions with macrocycles which follow negative cooperative mechanism.[260] We assume that since the aforementioned derivatives aggregate *via* a weak anti-cooperative mechanism, the first injections might represent the dissociation of fully aggregated aliquots

into monomers, whereas the latter injections show the dissociation into the dimeric species. Unfortunately, the currently available model was not able to describe these processes and hence hampers the accurate determination of aggregation parameters for **NBI 2** and **NBI 3**. Furthermore, the lack of saturation at the end-point of dilution experiment due to lower aggregation tendency impedes the estimation of CAC for **NBI 2** and **NBI 3** *via* ITC.

Thus, we could independently confirm by both UV-vis studies and ITC dilution experiments that the self-assembly of **NBI**s **1**-**3** in water is entropically driven and primarily attributable to the release of water molecules from the glycol units. Here the length of the OEG side chains plays a prominent role for both the enthalpic and entropic contributions to the aqueous self-assembly of our NBI series. In order to obtain deeper insights into the role of molecular structure in orchestrating this specific aggregation trend in water, structural attributes, especially the conformational nature of glycol units has to be investigated in detail.

### 4.2.3 Structural characterization *via* molecular dynamics (MD) and 2D NMR studies

After procuring quantitative information about the thermodynamic signature associated with the self-assembly, we pondered upon the role of molecular structure in directing the association process. For this, we employed all atoms molecular dynamics (MD) simulations in pure water on **NBI 1** and **NBI 3**, which have the shortest and the longest OEG chains, respectively, in the series. Interestingly, both NBIs show a back-folded conformation of glycol chains around the naphthalene core in the monomeric form (Figure 4.6a, d). A similar observation was previously discussed by Meijer and Pavan *et al.* and has been attributed to the shielding of the hydrophobic surface from the surrounding bulk water.[146, 147] Figure 4.6b and e show the density profiles of C-atoms of OEG chain over the aromatic cores for **NBI 1** and **NBI 3**. As seen clearly, the preferred orientation of side chains during the MD regime resides over the core instead of extending into the bulk water.

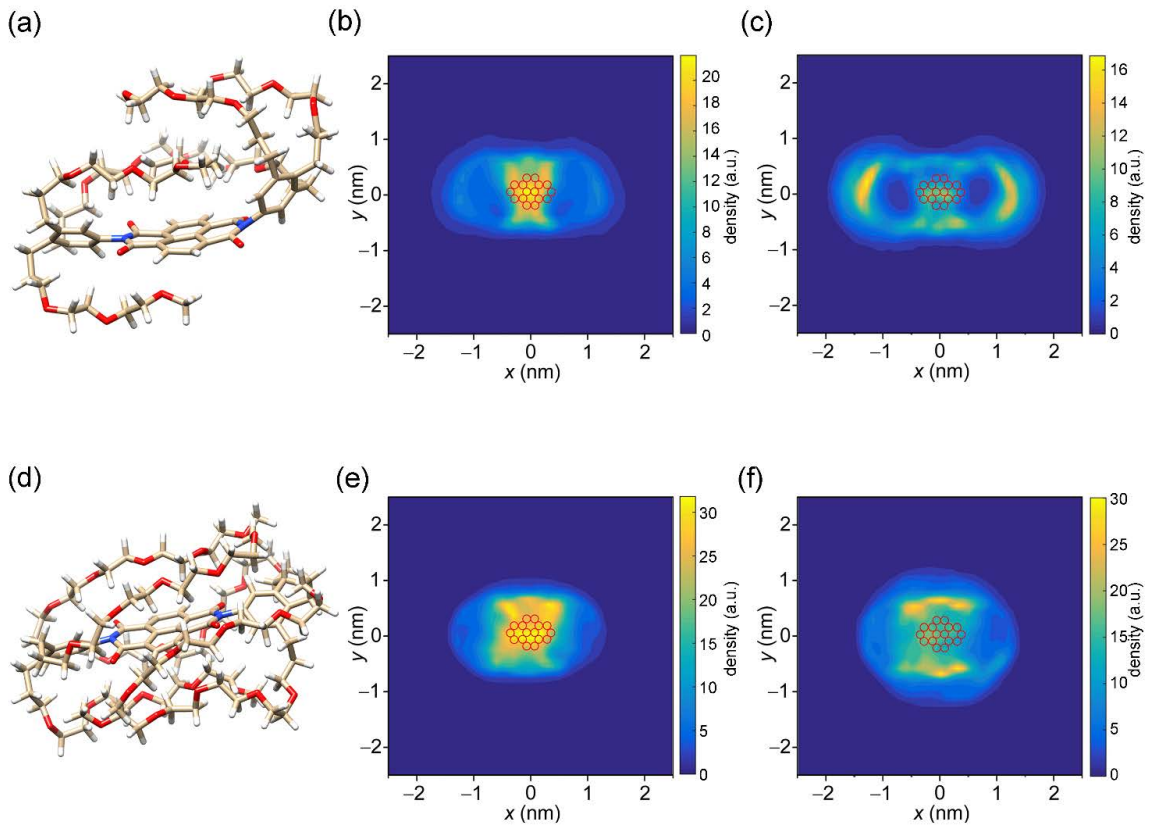


**Figure 4.6**: Snapshot showing back-folding of glycol chains for (a) **NBI 1** and (d) **NBI 3** in monomeric state from MD simulations (water molecules are omitted for clarity). Density of side-chain carbon atoms over naphthalene core (red circles) for (b) **NBI 1** monomer, (c) **NBI 1** stack, (e) **NBI 3** monomer, and (f) **NBI 3** stack.

Next, two such pre-equilibrated monomers were immersed into a periodic simulation box filled with explicit water molecules and allowed to equilibrate over the MD regime. The distance between the two monomers (0.4 nm) suggests an explicit π- π stacking, with a rotational offset of 10° (Figure A15a, A16a). A snapshot from the trajectory of **NBI 1** stacking depicts that the glycol chains still prefer a back-folded orientation in the aggregated state (Figure A14a). However, the tail density is now more distributed around the π -core, suggesting that some of the back-folding was replaced in order to accommodate the incoming monomer (Figure 4.6c). This release of ordered chains might contribute to the conformational entropy of side chains, aiding overall entropy of the association, along with the removal of hydrated water molecules.

Similarly, for **NBI 3**, stacking interactions were studied *via* MD simulations (Figure A14b). Here we see again that the glycol chains are folded over the naphthalene core in both monomeric and dimeric form. However, due to the increased length of OEG units, the

density of back-folded conformation is concomitantly higher as compared to **NBI 1** (Figure 4.6f). The rotational offset for the **NBI 3** stack (~60°) is significantly larger compared to **NBI 1**, which could be rationalized by the steric hindrance of back-folded glycol chains (Figure A16b).

To experimentally verify the presence of back-folding as suggested by MD simulations and to unravel the aggregate structure, we conducted detailed one-dimensional (1D) and two dimensional (2D) NMR studies. The $^{1}$H NMR spectrum of **NBI 1** in $CDCl_3$ shows well-resolved sharp signals corresponding to the monomeric state (Figure 4.7a). In contrast, the naphthalene core protons are significantly broadened as well as up-field shifted in $D_2O$, indicating an aggregated state aided by π-π stacking. Insights into the aggregate structure were probed subsequently *via* $^{1}$H-$^{1}$H rotating-frame Overhauser effect spectroscopy (ROESY).

Figure 4.7c, d show selected regions of superimposed ROESY and COSY spectra of **NBI 1** in $D_2O$. Nuclear Overhauser effect (NOE) correlations could be observed between the naphthalene core protons ($H^a$) and the glycol protons ($H^e$/$H^{e'}$), which is in compliance with the back-folded conformation of side chains. The coupling between the naphthalene core protons and phenyl protons suggests a slightly rotated offset between **NBI 1** monomers in the stacked conformation as predicted by MD simulations. A tentative assignment of NOE correlations with a snapshot from the MD regime of **NBI 1** is given in Figure 4.7e. Similarly, for both **NBI 2** and **NBI 3**, through-space interactions could be traced between glycol chain protons ($H^e$/$H^{e'}$) and core protons ($H^a$), thus corroborating the presence of back-folded conformations in these systems (Figure A17, A18) and validating the structural predictions from MD simulations. It should be noted that no NOE correlations were observed in the 2D-NMR studies of **NBI 3** in an organic solvent (ACN), suggesting that the back-folded conformation is exclusive to water (Figure A19). Since the primary goal of such a conformation is to screen the hydrophobic unit from bulk water, this entropically disfavored ordering of chains is not essential in organic solvents, and they probably exist in an extended manner.

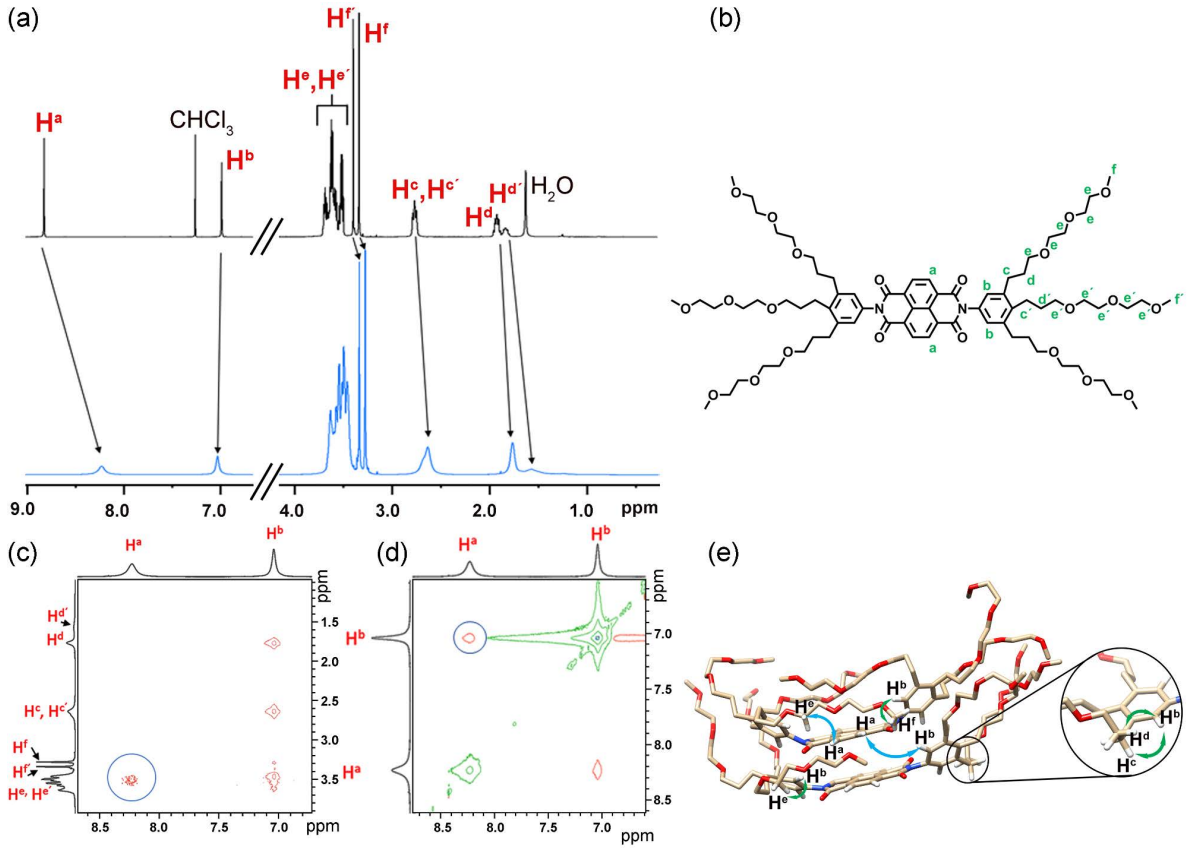


**Figure 4.7**: (a) Relevant sections of $^1$H NMR spectrum of **NBI 1** monomer in $CDCl_3$ ($c$ = 7.1 x $10^{-3}$ M) (black) and in the aggregated state in $D_2O$ ($c$ = 4.9 x $10^{-3}$ M) (blue) at 295 K. (b) Chemical structure of **NBI 1** with the significant protons assigned. Selected region of superposed ROESY-NMR and COSY-NMR spectra of **NBI 1** showing NOEs between glycol chains and naphthalene core (c) and phenyl protons and naphthalene core (d) in $D_2O$ ($c$ = 4.9 x $10^{-3}$ M) (circles). (e) Snapshot of **NBI 1** stack from MD simulations with tentative assignment of NOE interactions: Major interactions (glycol-naphthalene core and phenyl-naphthalene core) are depicted by blue arrows and the rest by green arrows. (Only hydrogen atoms involved in the interactions are shown for clarity).

In the thermodynamic analysis of the current system, we have observed that the elongation of glycol units from **NBI 1** to **NBI 3** is associated with a nearly ten-fold decrease in association constant and a concomitant drop in the magnitude of free energy. Combined results from MD simulations and NMR studies suggest that the back-folding of glycol chains is orchestrating this effect. Furthermore, the change of aggregation mechanism from isodesmic to weak anti-cooperativity can also be attributed to the more pronounced jacketing of monomer and dimer species by the longer OEG chains.

In addition, our results also relate to the studies on biomolecules. Here, previously it was observed that the substitution of proteins with polyethylene glycol (PEG) results in a decrease in binding affinity due to the interactions between PEG chains and the active site of the protein.[261, 262] Meijer *et al.* predicted that this could be ascribed to the back-folding

of the glycol chains operative in water.[263] Our current studies prove that the back-folding indeed interferes with the association process by shielding the hydrophobic surface from the surrounding bulk water. Accordingly, we can conclude that OEG and PEG chains play a pivotal role in directing the thermodynamics of aggregation in water.

## 4.3 Conclusions

In this contribution, three archetype bolaamphiphilic naphthalene bisimides were studied to derive an understanding of the different factors that contribute to the entropically driven self-assembly of bolaamphiphilic moieties substituted with OEG units in water. By utilizing UV-vis and ITC dilution experiments, we have successfully dissected the thermodynamic parameters of the aggregation process. The entropically favored nature of the self-assembly is attributed to the release of water molecules from the glycol units, which is enthalpically penalized. Further, we were able to show that a thermodynamic tuning of π-core aggregation in water can be achieved by modulating the length of solubilizing OEG chains. With the elongation of the side chains, the enthalpic, as well as entropic parameters also increase, attributed to an increment in dehydrated water molecules upon aggregation. However, this augmentation in their length hinders the self-assembly *via* a back-folding process as revealed by MD simulations and 2D-NMR studies, resulting in a decrease of the magnitude of Gibbs free energy and deviation from the isodesmic mechanism. Our current study sheds light on the fundamental aspects of bolaamphiphilic aggregation in water and opens up a strategy for more predictable aqueous self-assembly processes of oligo- and polyethylene glycol functionalized amphiphilic molecules.

# Chapter 5

# Modulation of the Self-assembly of π-Amphiphiles in Water from Enthalpy- to Entropy-Driven by Enwrapping Substituents

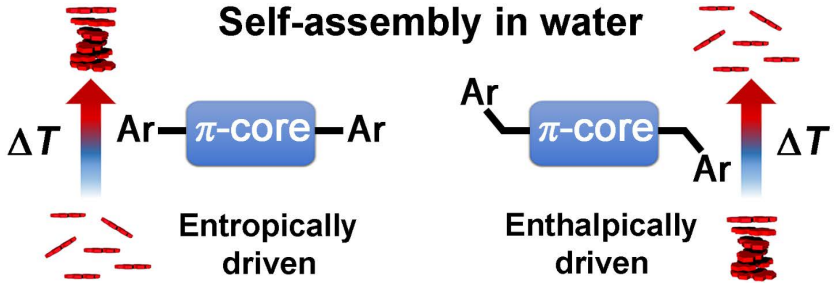


**ABSTRACT**: Depending on the connectivity of solubilizing oligo ethylene glycol (OEG) side chains to the π-cores of amphiphilic naphthalene and perylene bisimide dyes, self-assembly in water occurs either upon heating or cooling. Here we show that this effect originates from differences in the enwrapping capability of the π-cores by the OEG chains. Rylene bisimides bearing phenyl substituents with three OEG chains attached directly to the hydrophobic π-cores are strongly sequestered by the OEG chains. These molecules self-assemble at elevated temperatures in an entropy-driven process according to temperature- and concentration-dependent UV-vis spectroscopy and calorimetric dilution studies. In contrast, for rylene bisimides where phenyl substituents with three OEG chains are attached *via* a methylene spacer, leading to much weaker sequestration, self-assembly originates upon cooling in an enthalpy-driven process. Our explanation for this controversial behavior is that the aggregation in the latter case is dictated by the release of 'high energy water' from the hydrophobic π-surfaces as well as dispersion interactions between the π-scaffolds

This chapter was published in: P. P. N. Syamala and F. Würthner, *Chem. Eur. J.*, 2020, **26**, 8426-8434. Reproduced from reference.[347] AFM measurements were performed by Dr. Vladimir Stepanenko.

which drive the self-assembly in an enthalpically driven process. In contrast, for the former case, we suggest that in addition to the conventional explanation of dehydration of hydrogen-bonded water molecules from OEG units, it is in particular the increase in conformational entropy of back-folded OEG side chains upon aggregation that provides the pronounced gain in entropy that drives the aggregation process. Thus, our studies revealed that a subtle change in the attachment of solubilizing substituents could switch the thermodynamic signature for the self-assembly of amphiphilic dyes in water from enthalpy- to entropy-driven.

## 5.1 Introduction

Self-assembly has emerged as an efficient method for the development of functional materials possessing enticing properties, including self-healing and stimuli-responsiveness among many others.[54, 264, 265] Such emergent functions of larger entities are encoded in the monomer design, which forecasts the dominant non-covalent forces that take part in the formation of targeted architectures.[266] In nature, these interactions are often not primarily governed by the specific non-covalent bonds between the self-assembling molecules but by the solvation properties of water, which plays a prominent role in the generation of these dynamic structures.[16, 239, 241]

Emulating nature's strategy for artificial supramolecular aggregates has proved to be challenging since our understanding of the role of water in these systems is still at its infancy.[249] Nevertheless, a wide variety of nano-scale structures in aqueous media has been generated, e.g., for peptide amphiphiles[266-268] and π-amphiphiles consisting of diverse hydrophobic cores including hexabenzocoronenes,[37, 269, 270] naphthalene[21, 62, 164], and perylene bisimides,[16, 24, 168, 173, 242, 243] benzene tri-carboxamides,[17, 18, 146] oligo-phenylenes,[26, 271] phenylene ethynylenes,[272, 273] and phenylene vinylenes,[30, 274] etc.

While the distinct mechanisms mediating the self-assembly of aforementioned structures at room temperature in water have been explored in detail, providing insights into isodesmic, cooperative, and anti-cooperative models, understanding of thermodynamic factors which drive the self-assembly, *viz.* enthalpy or entropy, is yet to transpire.[55] This gap in the knowledge is probably related to the fact that the majority of the supramolecular aggregations are performed in organic media under the control of enthalpic factors (termed 'ordinary temperature response') assisted by non-covalent bond formation and reduction in degrees of freedom associated with self-assembly (Figure 5.1c).[275] However, in aqueous

environments, as given in nature, there are many examples for entropically driven self-assembly processes (Figure 5.1a), where the aggregation is favored at elevated temperatures (termed 'inverse temperature response') including tobacco mosaic virus,[276] *β*-amyloids,[277] collagen fibrils,[278] etc. In contrast, among synthetic supramolecular systems, such cases are still rare.[68, 149, 165, 230, 275, 279] Nevertheless, the design principles which underpin this bifurcated thermal response can have wider implications ranging from the development of thermoresponsive materials to drug screening. For example, enthalpically driven drug-protein interactions are known to evade undesirable physicochemical properties[280] and ligands that bind with an entropic advantage can adopt multiple binding modes and thus circumvent the development of resistance.[58] This, in turn, calls for a detailed understanding of the enthalpic and entropic factors that govern self-assembly and rational design strategies which can encode this information into monomeric building blocks.

We have previously reported that self-assembly of perylene bisimide dyes, appended with oligo ethylene glycol chains, is driven by entropic factors in water.[68] While mechanistic studies on the self-assembly process were hampered for this derivative due to its strong aggregation tendency, recently we succeeded in obtaining an understanding of the entropically driven self-assembly for amphiphilic dyes in water utilizing smaller naphthalene bisimide homologs.[279] During these investigations, we came across a surprising observation that the glycol chains in these molecules are back-folded to the aromatic core to sequester the hydrophobic surfaces from the surrounding bulk water. We reasoned that this specific orientation might be crucial in directing the self-assembly toward an entropically driven process. If this hypothesis is correct, molecules without this specific orientation of glycol chains should accordingly self-assemble in water driven by enthalpic factors as in the organic solvent. To gain deeper understanding of these processes and to realize control over the enthalpically and entropically driven self-assembly in water, we designed an array of bolaamphiphilic rylene bisimide dyes where the orientation of glycol chains was modified by a subtle change in the monomer design. **PBI 6** and **NBI 4**, designed analogous to our previous molecules and an example of Ghosh *et al.*,[163] consists of a perylene and naphthalene bisimide core, respectively, and are appended on both sides with a phenyl substituent bearing three oligo ethylene glycol (OEG) chains (henceforth referred to as wedge) (Figure 5.1b). In contrast, for **PBI 7** and **NBI 5**, this amphiphilic wedge is attached *via* a methylene spacer to disfavor the back folding. In organic solvents, all the

newly designed dyes self-assemble at lower temperatures and disassemble at elevated temperatures, characteristic of an enthalpically driven self-assembly process. Interestingly, in water, **PBI 6** and **NBI 4** follow an entropically driven self-assembly, which is favored at higher temperatures, whilst **PBI 7** and **NBI 5** show common enthalpically driven self-assembly, favored at lower temperatures. Combined utilization of UV-vis spectroscopy and isothermal titration calorimetry (ITC) allowed us to gain deeper insights into the thermodynamic properties pertaining to their self-assembly. Structural insights obtained by 2D NMR and PM7 optimizations point towards the crucial role of the orientation of glycol chains in orchestrating such bias of self-assembly in water.

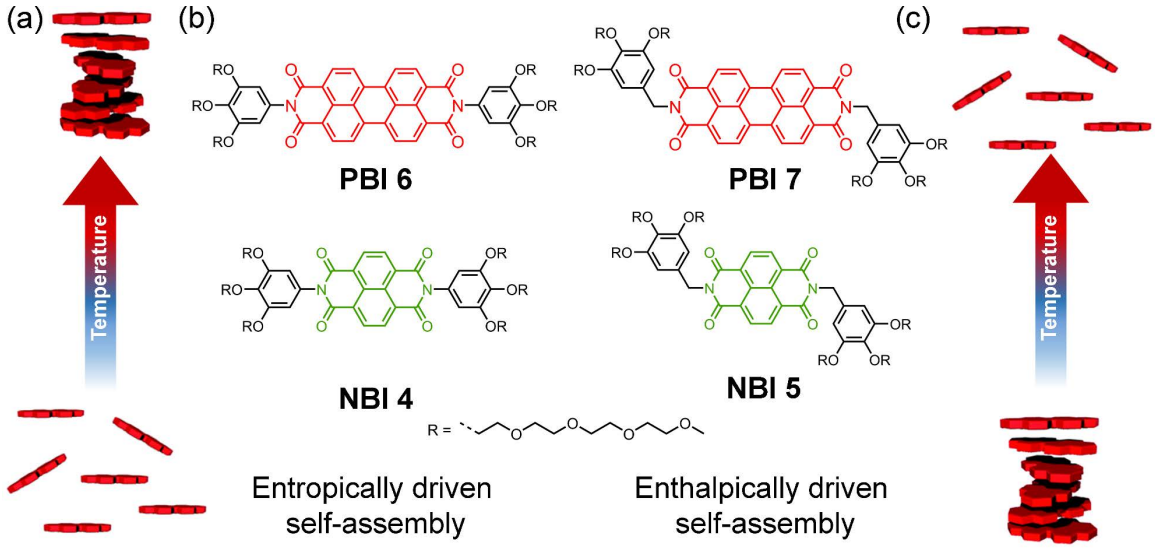


**Figure 5.1**: Schematic representation of entropically driven (a) and enthalpically driven (c) self-assembly. (b) Chemical structures of **PBI 6-7** and **NBI 4-5**.

## 5.2 Results and discussion

### 5.2.1 Temperature-dependent self-assembly and morphology of the aggregates

The thermodynamic fingerprint of bolaamphiphilic PBIs and NBIs was first probed by temperature-dependent UV-vis measurements. Generally, moieties that self-assemble in an entropically driven fashion show an increased aggregation tendency at higher temperatures and undergo disaggregation at lower temperatures. The reverse is true for enthalpically driven self-assembly, where the aggregation is favored at lower temperatures. First, we investigated the temperature-dependent changes of all the molecules in an organic solvent. In a solvent of intermediate polarity like $CHCl_3$, both **PBI 6** and **PBI 7** exist like many other perylene bisimides with solubilizing groups at imide positions in their monomeric

form[64] in a wide concentration range and exhibit typical vibronic progressions of the $S_0 \rightarrow S_1$ electronic transition (Figure A20a, b). However, in a polar solvent like MeOH, both PBIs self-assemble into supramolecular aggregates, owing to the stabilization by dispersion interactions originating from π-π stacking.[64] At lower temperatures, the transition corresponding to the 0-1 vibronic progression at 491 nm is prominent for **PBI 6** compared to that at 527 nm (0-0 transition), suggesting the formation of an H-type aggregate (Figure A21a).[64] However, with an increase in temperature, the ratio of the 0-0/0-1 transition intensity increases along with a concomitant hyperchromism, suggesting disaggregation. Similarly, temperature-dependent measurements of **PBI 7** in MeOH also revealed the formation of H-type aggregate at lower temperatures, which disassembles and regains the vibronic progression of the monomer at higher temperatures (Figure A21b).

Akin to the PBIs mentioned above, naphthalene bisimide derivatives **NBI 4** and **NBI 5** also exist in monomeric form in $CHCl_3$ (Figure A20c, d) and undergo self-assembly in MeOH at lower temperatures (Figure A21c,d). However, the propensity of aggregation is much lower compared to their PBI homologs attributed to a less extended π-core.[48] Here also, the H-type aggregates formed upon cooling disassemble at elevated temperatures, indicated by the hyperchromism along with the reinstating of monomer vibronic structure. In a gist, all the derivatives presented in the current work undergo an 'ordinary temperature response' in MeOH, where the aggregation is favored at lower temperatures, driven by enthalpic factors.

Subsequently, we have investigated the temperature-dependent self-assembly of all the derivatives in water. **PBI 6**, even at very low concentrations, exists in an aggregated state in water with a prominent 0-1 transition (at 498 nm) suggesting a co-facial packing of the molecules with an H-type excitonic coupling (Figure 5.2a). Surprisingly, upon increasing the temperature, we observed a pronounced hypochromic shift for the bands at 498 nm and 545 nm along with a decrease in the ratio of 0-0/0-1 transitions, opposite to its behavior in MeOH. These spectral changes point towards an increased degree of association, *i.e.*, aggregate growth into larger structures as reported before for an analogous PBI derivative in water.[68] Similarly, **NBI 4**, which exhibits a vibronic progression of its monomeric state at lower temperatures, undergoes aggregate growth at elevated temperatures as indicated by hypochromism along with a concomitant decrease in the ratio of the vibronic transition at 384 nm with respect to that at 363 nm (Figure 5.2c). In both cases, spectral changes upon temperature variation in water are contrary to the behavior in MeOH and point towards an

increasing tendency of association with temperature, indicating the contribution of entropic factors in driving the self-assembly.

**PBI 7**, where the amphiphilic wedge is attached *via* a $CH_2$ spacer, also exhibits H-type aggregation due to co-facial stacking in water (Figure 5.2b). However, unlike **PBI 6**, here we observed the emergence of the 0-0 vibronic transition of the monomer band at 537 nm upon increasing temperature, suggesting a partial disassembly of the aggregate. In an even more pronounced fashion, **NBI 5** also disassembles at higher temperatures as indicated by hyperchromism and monomer-like vibronic progression, identical to its behavior in MeOH (Figure 5.2d). Both these observations indicate the 'ordinary temperature response' exhibited by **PBI 7** and **NBI 5** in water, where the aggregate formation is disfavored at higher temperatures.

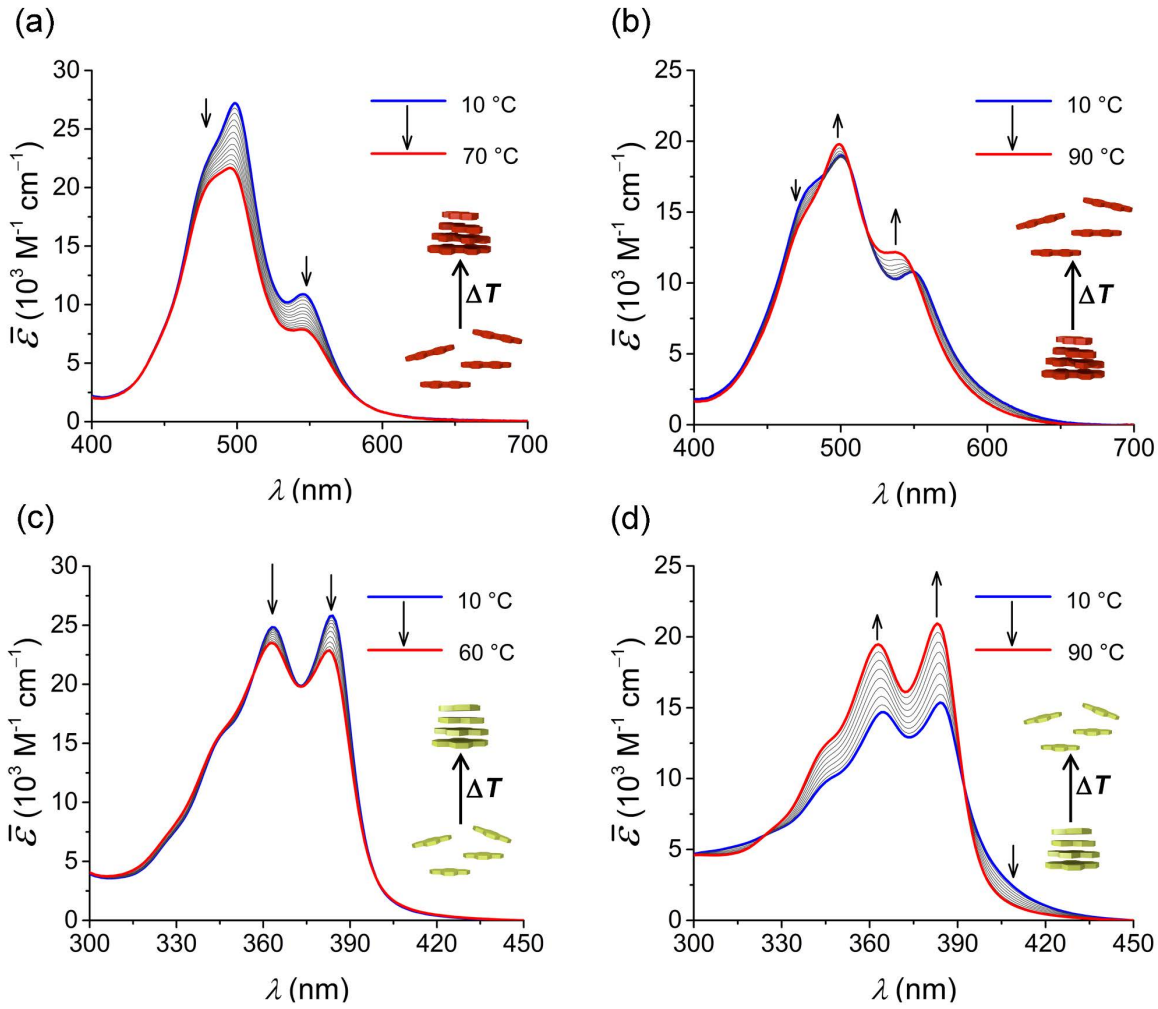


**Figure 5.2**: Temperature-dependent UV-vis spectra (density corrected) of (a) **PBI 6** ($c$ = 9.9 × $10^{-6}$M), (b) **PBI 7** ($c$ = 9.8 × $10^{-6}$ M), (c) **NBI 4** ($c$ = 3.9 × $10^{-5}$ M) and (d) **NBI 5** ($c$ = 1.0 × $10^{-4}$ M) in water. Arrows indicate spectral changes upon heating.

Unfortunately, quantitative insights into the thermodynamic parameters of the self-assembly are difficult to derive from these temperature-dependent UV-vis measurements since the fraction of aggregated species covered in the accessible temperature window remained narrow. Nevertheless, these experiments reveal a surprising bias of self-assembly in water, where bolaamphiphilic molecules with amphiphilic wedge directly connected to the core undergo an entropically driven self-assembly, favored at higher temperatures, whereas those having the wedge connected through a methylene spacer undergo enthalpically driven self-assembly, like in organic solvents.

To obtain insights into the morphology of aggregates in water, atomic force microscopy (AFM) measurements were performed on all the derivatives by spin coating aqueous stock solutions at 22 °C (Figure A22). Predominantly, island-like clusters were observed for **PBI 6**, **PBI 7**, and **NBI 4** with height profiles ranging from 1.0-1.8 nm. Closer inspection revealed that these lamellar structures are formed by the bundling of one-dimensional nanofibers, which might be due to the interdigitation of long side chains at higher concentrations. For **NBI 5**, we observed shorter nanoparticles with a height of 1.5-1.8 nm.

### 5.2.2 Thermodynamic profiling of self-assembly

Intrigued by the unique bias of the self-assembly in water by subtle substituent variation, we decided to obtain deeper insights into the parameters which pertain to the association as well as their self-assembly mechanism in this solvent. For this, we applied concentration-dependent UV-vis studies as an effective tool since a broader range of aggregated species can be covered, surpassing the limitations of our previous experiments. Initially, we measured the UV-vis spectra of **PBI 6** and **PBI 7** at different concentrations in water at 25 °C (Figure A23). However, very little changes in their vibronic structure were observed with varying concentrations owing to the high aggregation tendency of these extended π-scaffolds in water. The naphthalene derivatives **NBI 4** and **NBI 5** appeared to be suitable candidates in this respect since their smaller π-core assert moderate aggregation constants in aqueous media.

At lower concentrations, **NBI 4** in water shows distinct vibronic progression akin to monomeric spectra with an absorption maximum, $\lambda_{max}$, at 384 nm, corresponding to the 0-0 transition (Figure 5.3c). With an increase in concentration, we could observe a hypochromic shift along with the absorption maximum shifting to the 0-1 transition at 363 nm, correlating to the spectral changes observed in temperature-dependent measurements.

Such a pattern is characteristic of an H-type excitonic coupling, where the π-surfaces are arranged co-facially in an aggregate. While plotting the corresponding degree of aggregation against the dimensionless product $c$ (**NBI 4**)$K_e$, we noticed a deviation from the sigmoidal transition characteristic for the isodesmic self-assembly. An analysis by Goldstein-Stryer model[52, 244] revealed that **NBI 4** aggregates in a weakly anti-cooperative fashion with a cooperativity factor $\sigma = 5$ and a nucleus size of 2.

In such processes, the nucleation is more favored than the elongation toward extended aggregates. It is likely that this anti-cooperativity arises from the sterical congestion imparted by the oligo ethylene glycol wedges upon self-assembly in a discotic stack. Noticeably, the association constant of elongation regime in water is quite weak ($K_e$= 350 $M^{-1}$ at 25 °C), considering the strong hydrophobic interactions operative in this medium.

Similarly, for **NBI 5** concentration-dependent studies were performed in water at 25 °C (Figure 5.3d). With increasing concentration, $\lambda_{max}$ at 384 nm is shifted to 365 nm, implying the formation of an H-type aggregate as in the previous case. However, unlike **NBI 4**, the transition from monomers to aggregate trace a sigmoidal shape within this concentration regime explained well by the isodesmic model.[48]

Even though the two derivatives differ only by a $CH_2$ group in imide substituents, the aggregation constant of **NBI 5** ($K$= 9.1×10$^3$ $M^{-1}$ at 25 °C) is 25-fold higher than that of **NBI 4**. Such an increase in binding strength is unlikely to be caused by the hydrophobic nature of the $CH_2$ group alone and might reside in the specific geometry of the amphiphilic wedges.

In an attempt to quantify the thermodynamic parameters encoded in the self-assembly of **NBI 4** and **NBI 5**, we performed these concentration-dependent experiments at different temperatures from 10 °C to 50 °C (Figure A24, A25). The corresponding natural logarithms of the association constants were then plotted against the inverse of temperature, as shown in Figure 5.3e, f. The association constants of **NBI 4** indeed increases with rising temperatures (Figure 5.3e), which corroborates with our temperature-dependent UV-vis measurements. Furthermore, **NBI 4** reveals a non-linear relationship between the association constants with respect to temperature. The traditional van't Hoff plot is inadequate to describe such systems which deviate from linearity due to the assumption of constant enthalpy and entropy at different temperatures.[251] Hence, we utilized a simplified Clarke-Glew equation (also referred to as integrated/extended van't Hoff equation) by

incorporating the change in heat capacity at constant pressure, $\Delta C_p$.[203, 204, 279] According to this, the natural logarithm of association constant at temperature $T$ is expressed as:

$$\ln\ [K(T)] = \ln\ [K(\theta)] + \frac{\Delta H(\theta)}{R}\left[\frac{1}{\theta} - \frac{1}{T}\right] + \frac{\Delta C_p(\theta)}{R}\left[\frac{\theta}{T} - 1 + \ln\left(\frac{T}{\theta}\right)\right] \qquad (5.1)$$

where, $\ln\,[K(\theta)]$ is the natural logarithm of the equilibrium constant at the reference temperature $\theta$, $\Delta H(\theta)$ is the enthalpy change at the reference temperature and $\Delta C_p$ is the change in heat capacity at constant pressure.

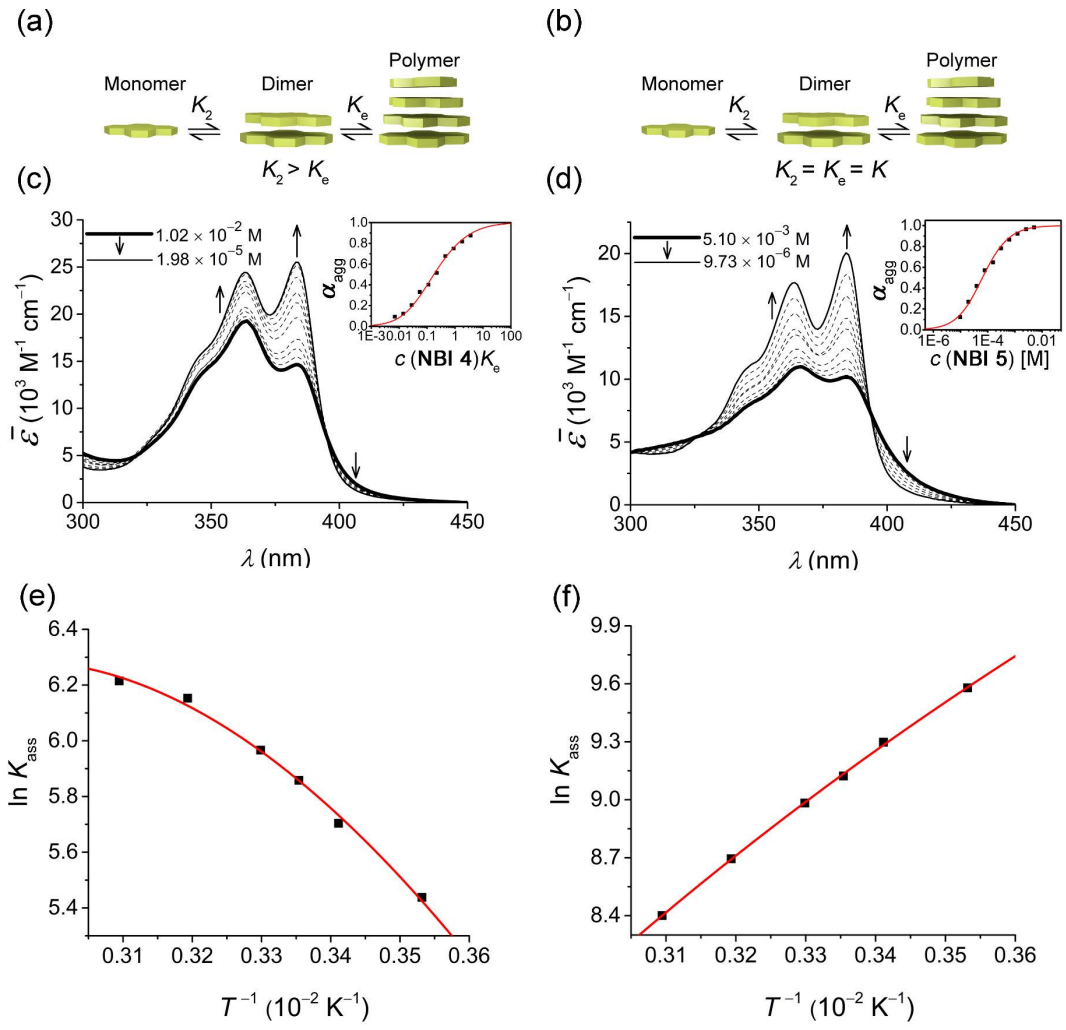


**Figure 5.3**: Schematic diagram showing self-assembly *via* (a) anti-cooperative and (b) isodesmic mechanism. (c) Concentration-dependent UV-vis spectra of **NBI 4** in water at 25 °C. Inset: Corresponding plot of the fraction of aggregated species, $\alpha_{agg}$, against dimensionless product $c$ (**NBI 4**)$K_e$ and analysis of the data based on the Goldstein-Stryer model. (d) Concentration-dependent UV-vis spectra of **NBI 5** in water at 25 °C. Inset: Corresponding plot of the fraction of aggregated species, $\alpha_{agg}$, against concentration and analysis of the data based on the isodesmic model. Plot of the natural logarithm of the association constant ($\ln K_{ass}$) against reciprocal of temperature and corresponding fit according to Clarke-Glew equation for (e) **NBI 4** and (f) **NBI 5**.

Indeed, the present method provides a better fit for the variation of association constants with temperature. Such a curve exhibits a negative slope, suggesting that the self-assembly process is endothermic (enthalpically disfavored). The standard enthalpy change of association, $\Delta H°_{ass}$, of 17.0 kJ mol$^{-1}$ derived from the Clarke-Glew equation, indeed supports this observation. However, the entropic component, $-T\Delta S°_{ass}$ occupies a value of −31.5 kJ mol$^{-1}$, making the overall process spontaneous with a $\Delta G°_{ass}$ of −14.5 kJ mol$^{-1}$. Furthermore, the Clarke-Glew equation also allows us to calculate a heat capacity change at a constant pressure of −419 J mol$^{-1}$ K$^{-1}$ for **NBI 4**. The endothermic nature of **NBI 4** self-assembly in water is further confirmed by an independent method, *i.e.*, isothermal titration calorimetry (ITC). In order to trace the heat signals associated with the self-assembly of current derivatives, we performed an ITC dilution experiment where a concentrated aqueous solution of the corresponding molecule was injected into pure water taken in the cell.[212, 214, 257] While performing this, we observed that **NBI 4** gives exothermic signals upon dilution (or dissociation), confirming that the association process is endothermic (enthalpically disfavored) (Figure A26a, b).

**NBI 5** exhibits a linear relationship between the logarithm of its association constant and the reciprocal of temperature, and in contrast to **NBI 4**, a decrease in association constants was observed with elevated temperatures (Figure 5.3f). The positive slope of the curve suggests an exothermic self-assembly process, which is enthalpically favored. A standard enthalpy change, $\Delta H°_{ass}$, of −21.9 kJ mol$^{-1}$ and a standard entropy change, $-T\Delta S°_{ass}$, of −0.6 kJ mol$^{-1}$ is deduced for the self-assembly of **NBI 5** from Clarke-Glew equation. Agreeing with our previous observations of a higher aggregation tendency for **NBI 5**, the change in standard free energy, $\Delta G°_{ass}$, possesses a value of −22.6 kJ mol$^{-1}$, which is considerably lower than that of **NBI 4**. Finally, a heat capacity change at constant pressure, $\Delta C_p$, of −128 J mol$^{-1}$K$^{-1}$ is estimated for the self-assembly of **NBI 5**. ITC dilution experiment was also conducted here to verify the exothermic nature of **NBI 5** self-assembly (Figure A26c, d). The dilution of **NBI 5** aggregate initially gave endothermic signals (corresponding to disassembly), which subsided after a few injections while reaching saturation, and showed constant exothermic signals corresponding to the heat of injection. This supports our observation from UV-vis experiments that the self-assembly of **NBI 5** is enthalpy driven. The combined thermodynamic signature for **NBI 4** and **NBI 5** aggregation at 25 °C is depicted in Figure 5.4.

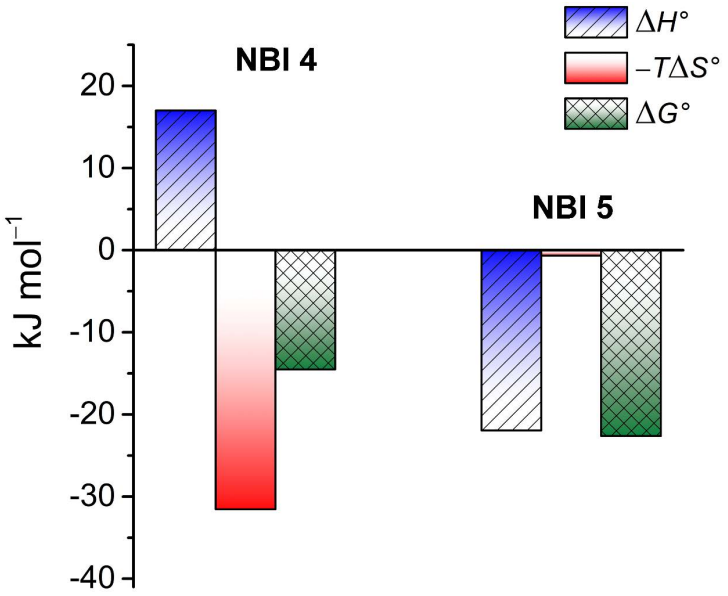


**Figure 5.4**: Thermodynamic profiles for the self-assembly of **NBI 4** and **NBI 5** in water obtained by concentration-dependent UV-vis experiments.

### 5.2.3 Structural insights by 2D NMR and PM7 calculations

In order to obtain structural insights to explain the striking difference in the self-assembly characteristics of the two molecules with and without a methylene spacer, we resorted to 1D and 2D NMR studies. The $^{1}$H NMR of **NBI 4** in $CDCl_3$ shows sharp and well-resolved signals, suggesting a monomeric state (Figure A27). However, in $D_2O$, the naphthalene core protons are upfield shifted and broadened, suggesting a self-assembled state aided by π-π stacking. In **NBI 5**, the naphthalene protons are more upfield shifted and broadened in comparison to **NBI 4** at the same concentration (Figure A28). This corroborates with the higher aggregation tendency observed for **NBI 5** in our UV-vis studies.

Subsequently, the discrepancies between the aggregate structure of both compounds were probed *via* $^{1}$H-$^{1}$H rotating-frame Overhauser effect spectroscopy (ROESY). In Figure 5.5, a selected region of the ROESY spectrum of **NBI 4** in $D_2O$ is shown. Interestingly, nuclear Overhauser effect (NOE) correlations could be observed between the glycol chain protons ($H^{e}/H^{e'}$, $H^{f}$) and naphthalene core protons ($H^{a}$) of the **NBI 4**, indicating that the OEG chains are proximal to the hydrophobic core. Such a correlation can only be explained if the chains are back-folded over the aromatic core and not extended into the bulk solvent. Recently, we have observed such a folding process on analogous naphthalene bisimide derivatives in molecular dynamics (MD) and 2D NMR studies.[279] Previously, other groups have attributed this conformation of side chains to the shielding of the π-surface due to

hydrophobic effect.[146, 147] It should be noted that this process is exclusive to aqueous media and was not observed for the ROESY studies of **NBI 4** in an organic solvent (Figure A29). Cross peaks corresponding to such a folding process could not be observed in the ROESY spectrum of **NBI 5** in $D_2O$ (Figure A30).

In an effort to understand what leads to the proximity of these chains to the core in the case of **NBI 4** and not in **NBI 5,** we resorted to semi-empirical PM7 calculations in water (Figure A31). The optimized geometry of **NBI 4** in water shows that the phenyl ring of the amphiphilic wedge is oriented nearly coplanar to the naphthalene core. This facilitates the OEG chains to fold backward to sequester the hydrophobic component from the bulk water. In contrast, the amphiphilic wedge is oriented almost orthogonal to the naphthalene core in **NBI 5** imparted by the $sp^3$ hybridization of the $CH_2$ spacer group. As a result, the glycol chains in **NBI 5** are extended away from the π-core, and thus their propensity to fold backward is limited compared to that of **NBI 4**.

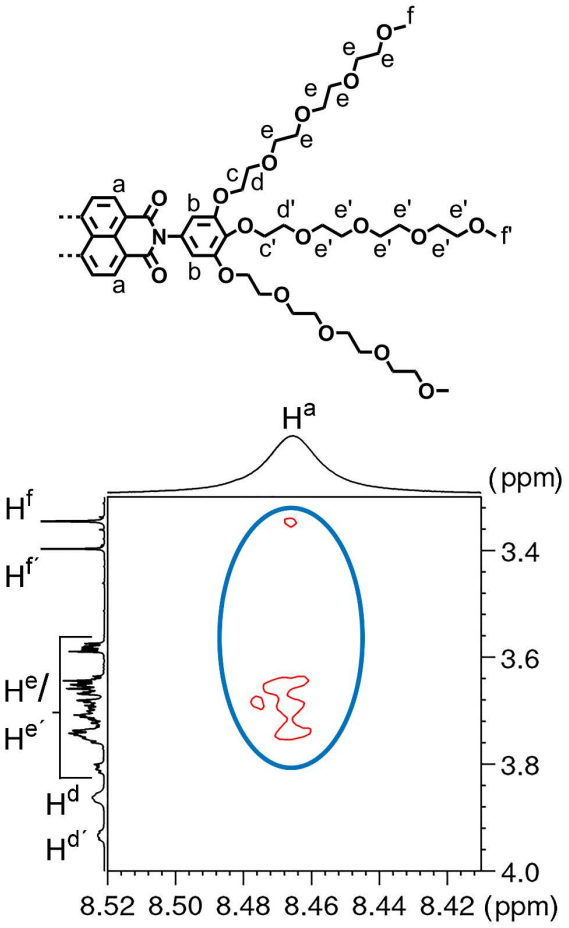


**Figure 5.5**: Partial chemical structure of **NBI 4** with significant protons assigned (above). Selected region of $^1$H-$^1$H ROESY spectrum of **NBI 4** in $D_2O$ ($c$ = 5.0 × $10^{-3}$ M) showing NOEs between glycol chains and naphthalene core (circle).

### 5.2.4 Interpretation of the enthalpy vs. entropy-driven aggregation

The common explanation for entropy-driven aggregation processes, as observed for **NBI 4** and **PBI 6** is a release of hydrated $H_2O$ molecules forming H-bonds with the glycol units (Figure 5.6).[275, 281] This explanation is reasonable and has been adopted in our previous work[68, 230, 279], because sterically demanding wedges as given with OEG side chains cannot accommodate larger amounts of coordinated water molecules without sterical encumbrance upon close cofacial stacking of the dyes. Accordingly, a significant amount of these glycol-bound water molecules have to be released to aid the association. The energy-intensive process of breaking these H-bonds surpasses the enthalpic gain arising from π-π stacking, making the overall enthalpy of aggregation positive. However, the removal of hydrated water molecules into the bulk solvent leads to a surge in the entropy, which drives the self-assembly.

However, taking into account the structural characterizations and the differences in the thermodynamic signature for the aggregation processes of the here investigated dyes, we propose that another effect plays a major role and that the aggregation processes of **NBI 4** and **PBI 6** are primarily governed by the gain in entropy originating from the release of the back-folded OEG chains. Indeed, to sequester the hydrophobic π -surfaces of these rylene dyes, a large number of otherwise freely rotating bonds have to be frozen in a specific conformation. The concomitant entropic loss by freezing such a multitude of conformationally mobile sections has to be huge, and accordingly, the release of OEG chains upon π-π stacking of the dyes will provide a considerable gain in entropy.[282] This view is also supported by the quite low aggregation constant determined by UV-vis experiments for **NBI 4** considering the solvophobic effects operative in water. Back-folding of glycol chains restricts the π-π stacking due to steric hindrance, which in turn decreases the aggregation constant. Furthermore, we observed that the mechanism of aggregation of **NBI 4** deviates from the isodesmic model and is better described by a weakly anti-cooperative model. The anti-cooperativity observed for **NBI 4** can also be attributed to such sterical constraint, which is aided by the back-folding process, as observed in our ROESY experiments.

Our results might also be of relevance for biological systems, for which the entropically driven host-guest binding and self-assembly is in general attributed to an increase in entropy of water molecules upon release into the bulk.[59, 283-285] Here also, back-folded side

chains might often be redistributed more flexibly upon aggregation, which could contribute to the overall entropy *via* an increase in the conformational entropy of the chains.

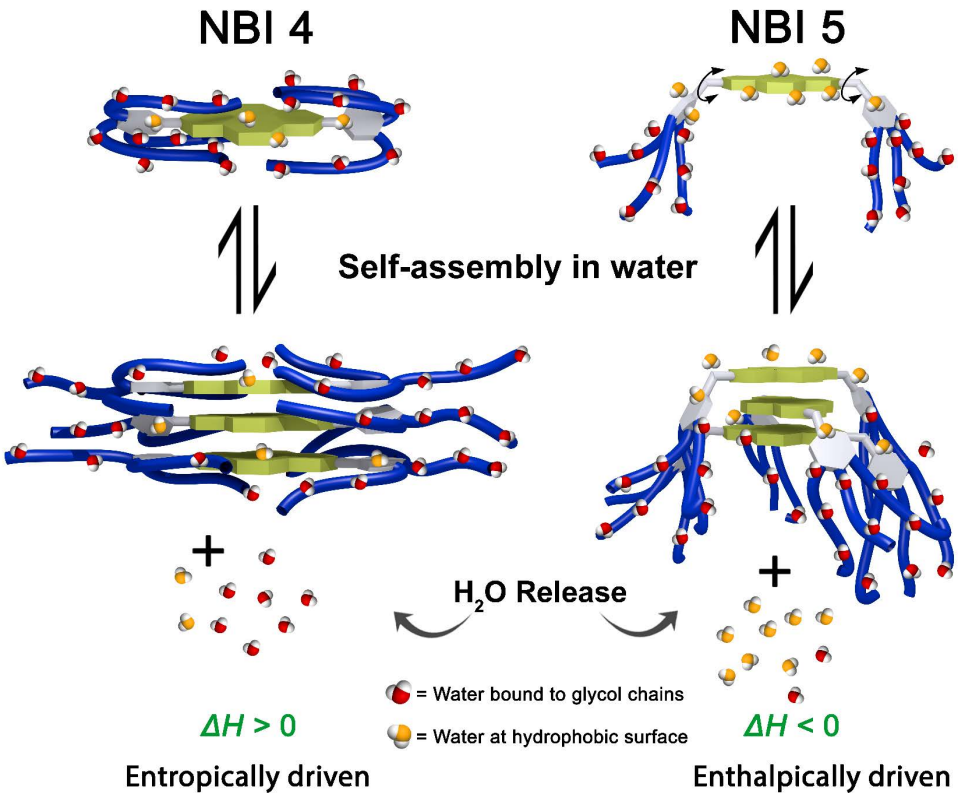


**Figure 5.6**: Schematic representation of self-assembly processes of **NBI 4** (left) and **NBI 5** (right) in water. At glycol chains, H-bonded water molecules are indicated in red, while the 'high-energy' water molecules at hydrophobic surfaces are shown in orange. The double-headed arrows in **NBI 5** structure represents the possible rotation of the wedges.

In contrast to these dyes, the thermodynamic signatures of **NBI 5** and **PBI 7** reveal that the association of these molecules is primarily driven by enthalpic factors. The lack of spatial correlations of the side chains and the π-core in 2D NMR studies of **NBI 5** indicates that the hydration shells of glycol chains are mostly arranged in an extended fashion away from the rylene core (Figure 5.6). Thus, during the self-assembly of monomers by π-π stacking, there is no significant increase in the degrees of freedom of side chains upon aggregation due to the lack of back-folding. This, in turn, means that the thermodynamic signature is primarily arising from the contributions of the hydrophobic NBI core, which probably stacks co-facially in a cogwheel type arrangement as reported for a similar derivative by Percec *et al.*[286] The water molecules at such non-polar surfaces are known to be energetically frustrated due to the less-favored H-bonding capacity with respect to bulk water and are termed as 'high energy water.'[103, 107] Upon association, these water molecules are released into the bulk, leading to a large energetic gain that drives the self-assembly *via*

favorable enthalpy, leading to a non-classical hydrophobic interaction. Furthermore, dispersion forces from the π-π interactions might also contribute to the favorable stacking.[15] Unlike **NBI 4**, the π-stacking of **NBI 5** is not counteracted by the folded chains since they are extended away from the core. This leads to a higher association constant, as revealed by concentration-dependent studies. Furthermore, the lack of sterical constraints for the more flexibly attached OEG wedges (due to a rotatable methylene group) allows **NBI 5** to aggregate in an isodesmic manner.

## 5.3 Conclusions

The understanding of the relevant thermodynamic parameters is quintessential to control self-assembly processes. In this regard, we demonstrated here the importance of conformational effects with a subtle modification, *i.e.*, the addition of a simple $CH_2$ spacer unit, to modulate an aggregation process from enthalpically to entropically driven for archetypal rylene bisimide dyes in water. In an organic solvent like methanol, all the studied molecules aggregate upon cooling and dissociate upon heating. In water, however, molecules where the amphiphilic wedge is directly attached to the π-core (**PBI 6** and **NBI 4**) exhibit entropically driven self-assembly where the aggregation is favored at higher temperatures. In contrast, compounds where the wedge is attached *via* a methylene spacer (**PBI 7** and **NBI 5**) aggregate upon cooling driven by enthalpic factors. In-depth concentration- and temperature-dependent UV-vis studies allowed us to extract the thermodynamic parameters of their self-assembly, which was further confirmed by ITC measurements. Structural insights obtained by 2D NMR and PM7 studies point towards the role of the orientation of side chains in orchestrating this bifurcated thermal response. We hypothesize that many, if not all, amphiphilic systems characterized by such back folded conformations in water will aggregate in an entropy-driven fashion due to the substantial gain in entropy upon the liberation of conformationally frozen rotatable hydrophilic side chains. Therefore, the elucidation of the temperature-dependent self-assembly of other π-amphiphiles in water will be of high interest. Further, we suggest considering this phenomenon also for supramolecular interactions involving biomacromolecules.

# Chapter 6

# Tunable Thermoresponsiveness of Perylene Bisimide Dyes in Water by Variation of Imide Substituents

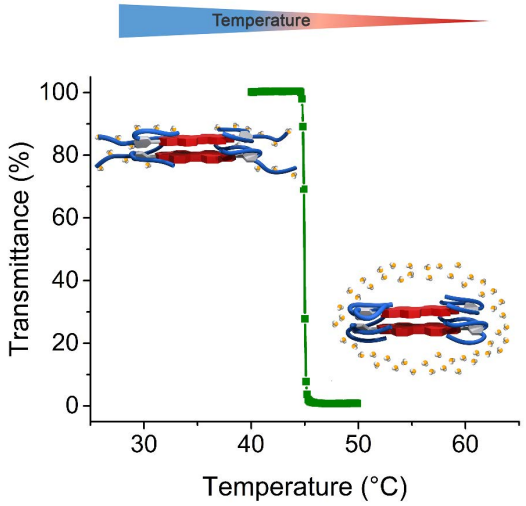


**ABSTRACT**: Lower Critical Solution Temperature (LCST) associated phase transition is widely used to generate smart materials that alter their properties in response to temperature stimulus. Here, we have investigated the self-assembly and phase separation behavior for perylene bisimide (PBI) dyes (**PBI 1-6)** bearing water-soluble oligo ethylene glycol units (OEG) at their imide positions. UV-vis and calorimetric studies have revealed their unusual aggregate formation at higher temperatures driven by entropic factors and subsequent precipitation associated with the LCST phenomenon. The onset temperature of this phase separation is highly sensitive to the structure of the OEG units. Contrary to covalent polymers, this behavior could not be correlated with the hydrophobicity of the molecules. NMR studies revealed that the organization of individual monomers within the self-assembled structure leads to differential hydration of side chains, which in turn determines the cloud points. The insights obtained from this study can be used to tune the LCST behavior of self-assembled π-amphiphiles in water.

Studies on **PBI 1** and **PBI 3** in water were conducted by Dr. Daniel Görl as part of his doctoral thesis.[60]

## 6.1 Introduction

The dynamic and reversible nature of non-covalent bonds has been exploited to generate supramolecular materials which possess superior self-healing and acclimatizing properties, compared to conventional polymers.[54, 264, 287] Some of these functional architectures are 'smart,' in the sense that they can respond to external stimuli like light,[288-292] heat,[293-297] chemical additives,[298-300] redox characteristics,[301-303] etc. and undergo significant changes in their conformation and/or properties.[265, 304, 305] Among these, temperature is one of the most attractive extrinsic triggers to modulate supramolecular structures and properties as it is non-invasive, easily accessible, and completely reversible.[306] Its versatility is evident with numerous reports which detail temperature-triggered applications in drug delivery,[307-310] catalysis,[311-313] and sensing.[230, 314-316]

Most of the artificial thermoresponsive materials utilize the Lower Critical Solution Temperature (LCST) phenomenon in water, where a miscibility gap is observed above a critical temperature. The onset of this phase separation at a particular concentration is termed as 'cloud point' ($T_{cp}$). Since the earliest report of LCST transition in poly(N-isopropylacrylamide) by Heskins and Guillet,[317] thermoresponsive behavior of many covalent polymers has been identified[318-321] and exploited for a wide variety of applications.[322, 323] In contrast, the reports on such LCST based transitions in self-assembled discrete molecules are comparatively rare.[230, 324-335] Typically, the thermoresponsive behavior for small-molecule assemblies is imparted by conjugating a π-core with oligo or polyethylene glycol (OEG/PEG) chains, which undergo temperature-sensitive hydrophilicity changes.[329] Below the cloud point, the ethylene glycol units are hydrophilic and well-hydrated, which accounts for their solubility in water. Upon increasing the temperature, the entropically driven expulsion of solvent molecules renders the side chains hydrophobic, which leads to their precipitation from the dissolved state.

In our group, we have explored several π-chromophores conjugated with OEG chains in the context of their self-assembly behavior in aqueous media.[39, 173, 279, 336] We have also identified that the LCST based transition of such molecules can be utilized to trigger a temperature-sensitive color change[230] or for the generation of aqua materials that undergo a transition from H- to J-type aggregates.[174] However, a precise understanding of the structural features that can modulate their phase transition at a defined temperature still remains elusive. Such information is not only imperative to tailor the thermoresponsiveness based on the desired property of the materials, but also for performing fundamental self-

assembly studies in water, as a low-lying cloud point can hamper temperature-dependent measurements used to estimate thermodynamic parameters of aggregation. To address these issues, we decided to investigate the structural components that modulate the cloud points for archetypal bolaamphiphilic perylene bisimides (PBIs). Selection of this π-chromophore is motivated by its excellent photophysical and self-assembly characteristics, which makes it a suitable candidate to engender materials that exhibit temperature-triggered responses in their optoelectronic features.[48, 63, 239]

Herein, we report on the self-assembly, and thermoresponsive features for a series of bolaamphiphilic PBIs appended with water-soluble OEG brushes at imide positions (Scheme 6.1). Various structural features of the hydrophilic brush were systematically modified to find their influence on the cloud point, keeping the hydrophobic π-core constant. They undergo an entropically driven self-assembly and macroscopic phase separation at the cloud point, which in turn is determined by the structure of the corresponding imide substituents (Figure 6.1). Turbidity measurements, as well as NMR studies to verify the hydration profile of aggregates, revealed that unlike conventional polymers, the phase separation is not dependent on the hydrophobicity of monomers, but rather the hydration of the self-assembled structure dictated by packing arrangements. Our study provides a general guideline to modulate the thermoresponsiveness of self-assembled discrete molecules by *de novo* design of hydrophilic OEG units.

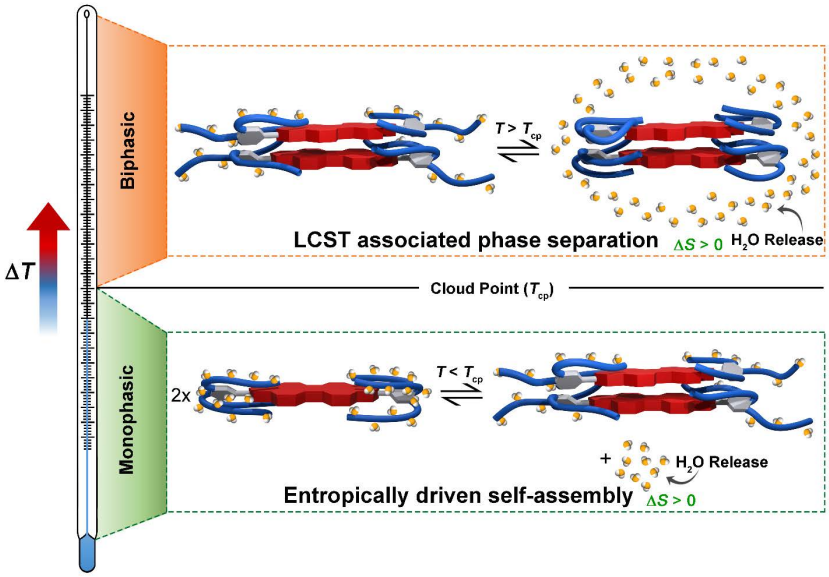


**Figure 6.1**: Schematic illustration showing the temperature-dependent behavior of bolaamphiphilic PBIs presented in this work. Below the cloud point, they undergo self-assembly favored by entropy and above the cloud point, they undergo macroscopic phase separation.

## 6.2 Results

### 6.2.1 Molecular design

For the present work, we have chosen bolaamphiphilic PBIs where the hydrophilic brush is appended on both sides of a PBI core (Scheme 6.1). The polar brushes, conjugated on the imide nitrogen, consists of a phenyl ring bearing three OEG chains at 3,4,5 positions. Since we were interested in obtaining insights into the effect of the amphiphilic unit in modulating the transition temperature, the central π-core was kept constant, and different structural aspects of the OEG brush were altered.

At first, we studied the effect of hydrophilic units in varying the cloud points of our PBI derivatives. For this, we systematically increased the glycol chain length from three glycol units (**PBI 1**) to four (**PBI 2**) and five (**PBI 3**). Since the hydrophobicity of a polymer is known to affect its LCST behavior, we synthesized **PBI 4**, which has an ethyl unit at the chain terminal and compared it to **PBI 3**, which has the same OEG chain length, but a methyl terminal. Finally, we assumed that the propylene unit, which tethers the OEG chain and the phenyl ring, might also impart an effect on the $T_{cp}$ due to its hydrophobic nature. Originally, this alkyl spacer was introduced to our perylene bisimide derivatives to conserve its luminescence characteristics, by preventing fluorescence quenching which occurs *via* a photoinduced electron transfer (PET) process.[337] To study the effect of this spacer, we synthesized **PBI 5** and **PBI 6**, where the side chains were directly attached to the phenyl ring in the absence of a spacer group. They were then compared to their homologs **PBI 1** and **PBI 3** possessing the same OEG length, but with the propylene spacer.

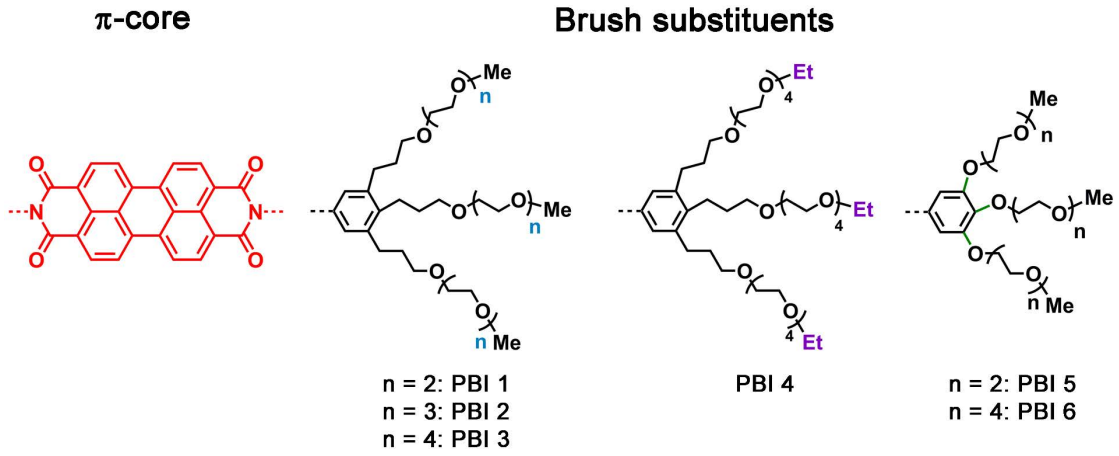


**Scheme 6.1**: Chemical structures of **PBI 1-6**.

### 6.2.2 Self-assembly in organic solvents and water

In order to obtain insights into the self-assembly of the synthesized bolaamphiphilic PBIs, first, we investigated their temperature-dependent behavior *via* UV-vis spectroscopy. All the PBIs exist in their monomeric form in $CHCl_3$ over a wide concentration range, exhibiting the vibronic structure corresponding to $S_0 \rightarrow S_1$ transition reported for core-unsubstituted PBIs.[63] In a more polar solvent like ACN, **PBI**s **1-6** self-assemble into supramolecular polymers which is attributed to the stabilization of π-π contacts by dispersion interactions.[64] At lower temperatures, the transition at 490 nm corresponding to the 0-1 vibronic progression is prominent compared to the 0-0 transition at 520 nm, in contrast to the fine structure in the monomer (Figure 6.2). This indicates the formation of a cofacially stacked aggregate with an H-type excitonic coupling. Upon increasing the temperature, the ratio of the 0-0/0-1 transition intensity increases along with a concomitant hyperchromism, suggesting depolymerization. Such a self-assembly where the aggregation is favoured at lower temperatures and disfavored at higher temperatures, is driven by enthalpic factors and is termed as 'ordinary temperature response'.

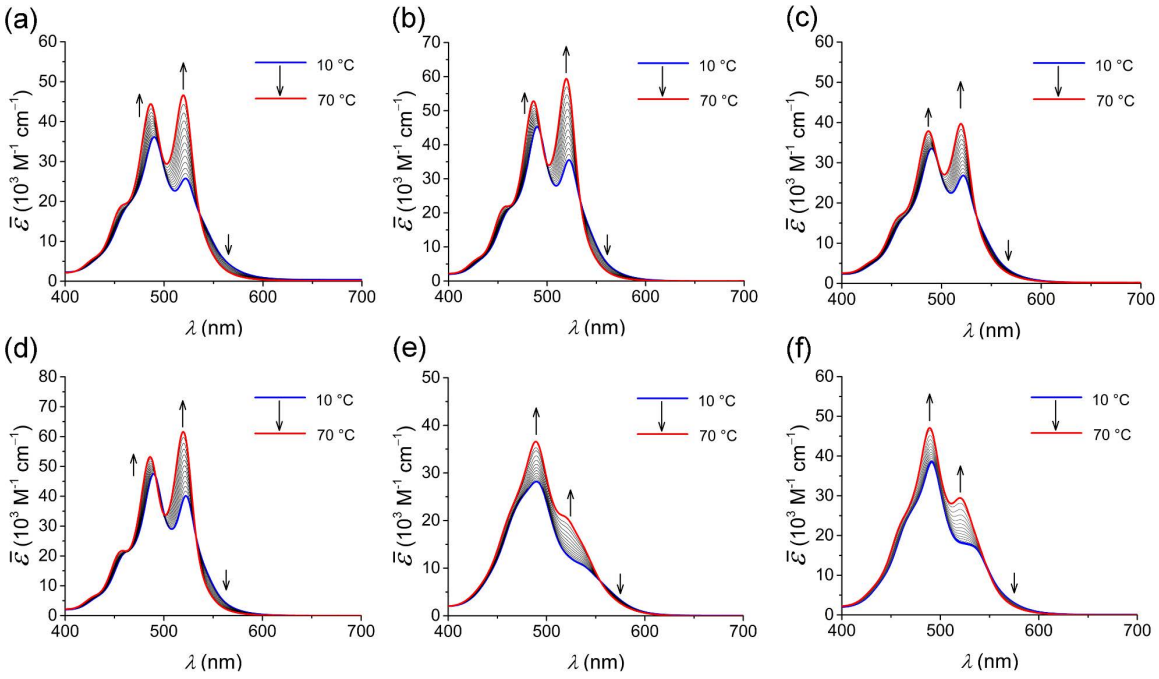


**Figure 6.2**: Temperature-dependent UV-vis spectra (density corrected) of (a) **PBI 1** ($c = 5.3 \times 10^{-4}$ M), (b) **PBI 2** ($c = 4.9 \times 10^{-4}$ M), (c) **PBI 3** ($c = 5.1 \times 10^{-4}$ M), (d) **PBI 4** ($c = 5.2 \times 10^{-4}$ M), (e) **PBI 5** ($c = 5.2 \times 10^{-4}$ M), and (f) **PBI 6** ($c = 5.2 \times 10^{-4}$ M) in acetonitrile. Arrows indicate spectral changes upon heating.

Subsequently, we examined the temperature-dependent self-assembly of **PBI 1-6** in water (Figure 6.3). Here also, we observed spectral characteristics of an H-type aggregate at lower temperatures for all the derivatives akin to their behavior in ACN. Interestingly, an increase in temperature was accompanied by a decrease in the ratio of the 0-0/0-1 transitions along with a hypochromism and eventual precipitation, contrary to its behavior in ACN. The temperature window accessible for these experiments were regulated by their phase transition temperature, which varies widely for PBI derivatives with different hydrophilic brushes (*vide infra*). This spectral signature points toward a more favored aggregation propensity at higher temperatures, characteristic of an entropically driven self-assembly or 'inverse temperature response.'

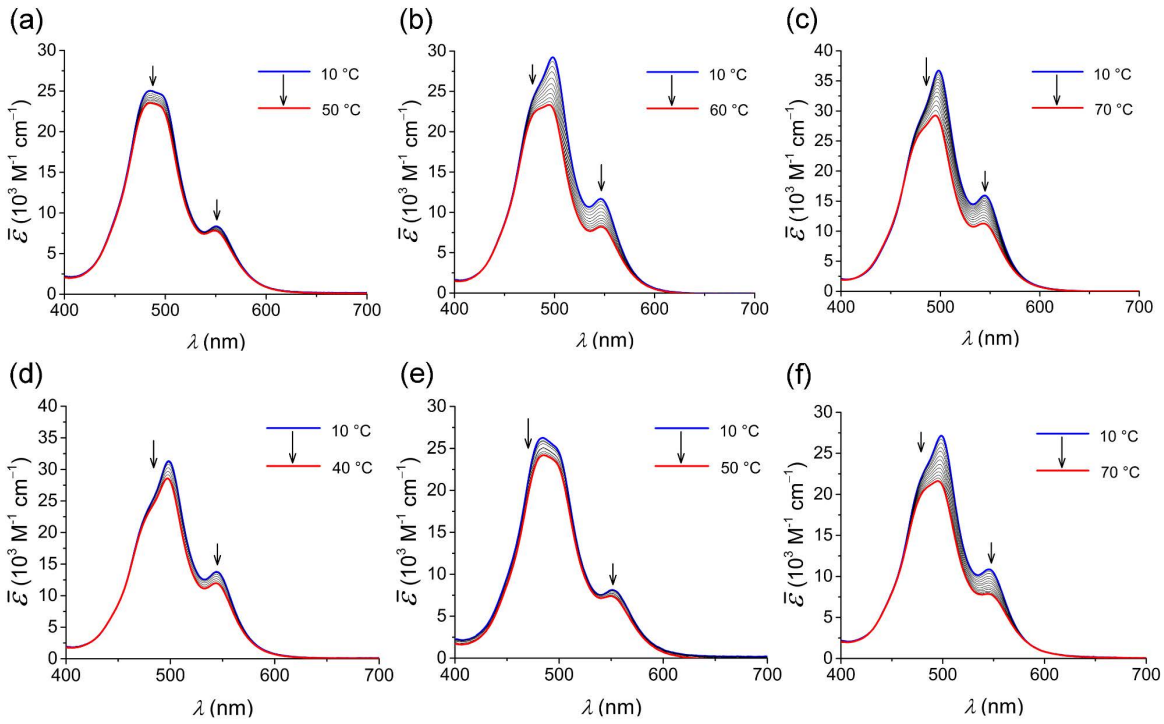


**Figure 6.3**: Temperature-dependent UV-vis spectra (density corrected) of (a) **PBI 1** ($c$ = 3.2 × $10^{-5}$ M), (b) **PBI 2** ($c$ = 1.0 × $10^{-5}$ M), (c) **PBI 3** ($c$ = 3.3 × $10^{-5}$ M), (d) **PBI 4** ($c$ = 1.0 × $10^{-5}$ M), (e) **PBI 5** ($c$ = 1.0 × $10^{-5}$ M), and (f) **PBI 6** ($c$ = 0.99 × $10^{-5}$ M) in water. Arrows indicate spectral changes upon heating. Fig. 6.4c is reproduced with permission from reference[68]. Copyright 2016 Wiley-VCH Verlag GmbH & Co. KGaA, Weinheim.

In an effort to corroborate the observation of an entropically driven self-assembly in water, we performed ITC dilution experiments where the thermodynamic fingerprint of self-assembly can be tracked by the heat signals generated upon disassembly (Figure 6.4). Here, an aqueous stock solution of PBI bolaamphiphile ($c \approx 5\times10^{-3}$ M) was injected into pure water. The dissociation of the self-assembled PBIs traced exothermic signals, suggesting that the reverse phenomenon, *i.e.*, association, proceeds in an endothermic manner (Figure

6.4a-d). *i.e.*, the self-assembly of these PBI derivatives is not only entropically favorable as observed in temperature-dependent UV-vis experiments, but also enthalpically disfavored despite of favorable π-π interactions. For **PBI 1** and **PBI 5** with the shortest glycol chains, we were not able to observe heat signals associated with disassembly, due to their high aggregation propensity in water.

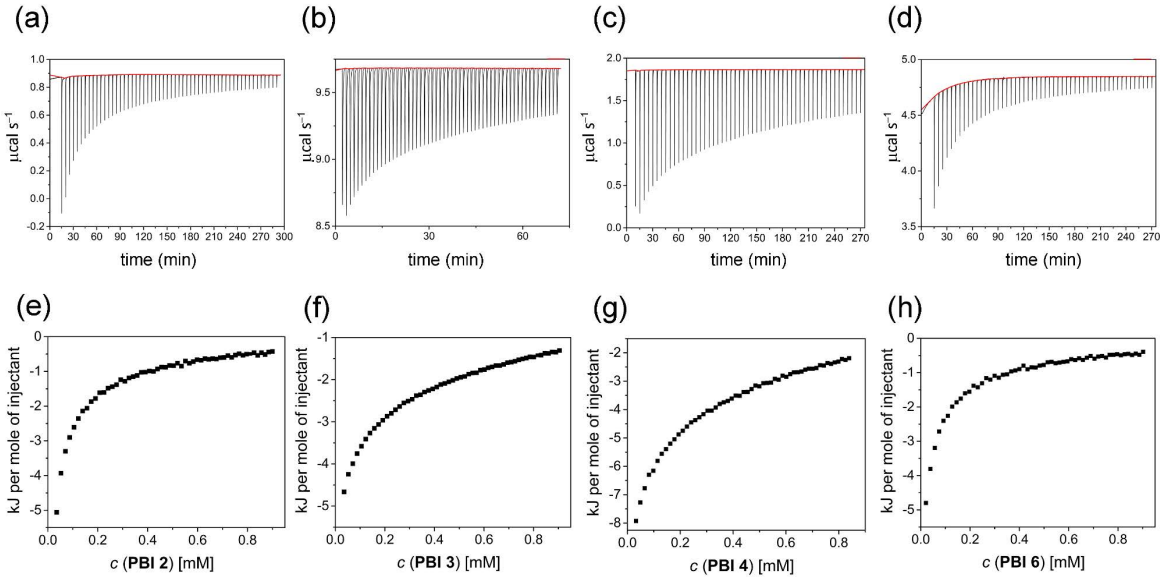


**Figure 6.4**: Evolution of heat per injection of (a) **PBI 2** ($c$ = 5.0 × $10^{-3}$ M), (b) **PBI 3** ($c$ = 5.1 × $10^{-3}$ M), (c) **PBI 4** ($c$ =4.7× $10^{-3}$ M) and (d) **PBI 6** ($c$ = 5.1 × $10^{-3}$ M) in water at 22°C and corresponding enthalpograms (e, f, g, and h respectively). Fig. 6.4c and g are reproduced with permission from reference[68]. Copyright 2016 Wiley-VCH Verlag GmbH & Co. KGaA, Weinheim.

### 6.2.1 Thermoresponsiveness of PBIs in water

Intrigued by the phase separation of bolaamphiphilic PBIs at higher temperatures during our UV-vis studies, we were further interested in obtaining insights into this thermoresponsive behavior. Generally, the oligo ethylene glycol units as in our PBI derivatives are efficiently accommodated in the water network due to ideal O-O distances, which accounts for their higher solubility compared to other polyethers.[338] Typically, each ethylene oxide is surrounded by a primary and a secondary hydration shell consisting of a total of four water molecules (below 30°C),[281] which possess a lower diffusion rate than the bulk water due to the formation of H-bonds.[339] However, upon increasing the temperature, these H-bonds are disrupted, leading to an entropically driven dehydration, which renders the side chains hydrophobic and triggers their phase separation from water. If sufficiently larger aggregates are formed at the thermal transition, $T_{cp}$ can be easily

measured using thermooptical methods, where the transmittance at a particular wavelength (where the solute does not absorb, here 800 nm) is tracked at varying temperature.[340]

We performed turbidity measurements on all PBI derivatives in water at the same concentration ($c = 5 \times 10^{-4}$ M) to compare their thermoresponsive behavior. A drastic drop in the transmittance was observed for all the investigated dyes over the threshold temperature with the appearance of a precipitate in the cuvette at a well-defined cloud point (Table 6.1).

**Table 6.1**: Cloud-points of **PBI 1-6** along with the structural features of their brush substituents.

| | **No. of oxygen atoms per chain** | **Spacer alkyl group** | **Terminal alkyl group** | **log *P*** [1] | **Cloud point, $T_{cp}$** [2] **(°C)** |
|---|---|---|---|---|---|
| **PBI 1** | 3 | Pr | Me | 9.57 | 51 |
| **PBI 2** | 4 | Pr | Me | 9.29 | 62 |
| **PBI 3** | 5 | Pr | Me | 9.00 | 69 |
| **PBI 4** | 5 | Pr | Et | 11.14 | 45 |
| **PBI 5** | 3 | - | Me | 4.97 | 51 |
| **PBI 6** | 5 | - | Me | 4.40 | 66 |

[1]Calculated using ChemAxon software. [2]Determined by transmittance measurements at 800 nm in water.

The turbidity measurements of the first three PBIs (**PBI 1**, **PBI 2** & **PBI 3**) where the glycol chain length was systematically increased, is shown in Figure 6.5. While **PBI 1** with the shortest glycol chain length (3O atoms per chain) showed $T_{cp}$ at 51 °C, **PBI 2** with an additional glycol unit precipitated nearly 11 °C higher ($T_{cp}$ = 62 °C). Further increasing the chain length exhibited a similar trend where **PBI 3** showed a cloud point at 69 °C.

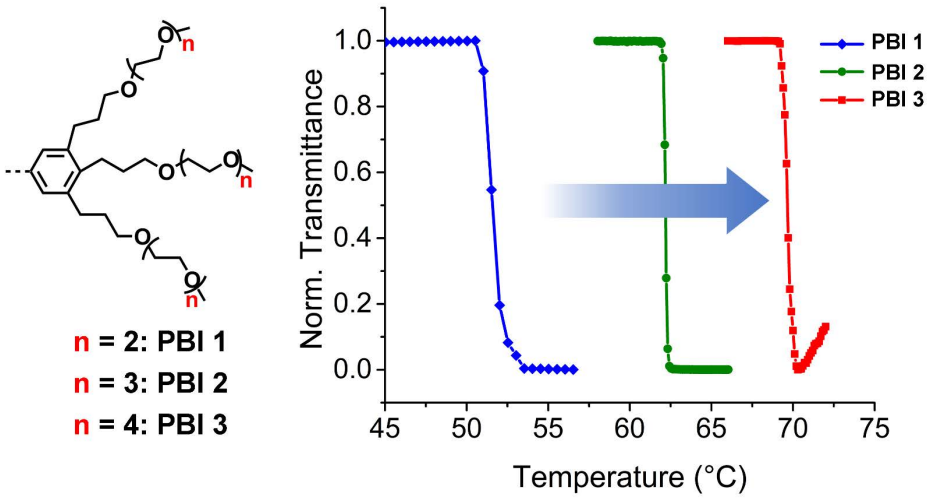


**Figure 6.5**: Normalized transmittance at 800 nm as a function of temperature for **PBI 1**, **PBI 2**, and **PBI 3** ($c$ = 5 × $10^{-4}$ M) in water (Heating rate: 0.1°C/min). The arrow shows the increase in cloud points with an increase in the glycol chain length.

Next, we were interested in the role of the hydrophobic component of these brush substituents, specifically the alkyl unit which decorates the chain termini, in determining the cloud point. For this purpose, **PBI 4** with an ethyl terminal unit was compared to **PBI 3** with the same glycol chain length, but a methyl terminus (Figure 6.6). In contrast to the high phase separation temperature of **PBI 3** ($T_{cp}$ = 69 °C), **PBI 4** showed a cloud point at only 45 °C, an abrupt drop of onset temperature by 24 °C. This shows that minor structural changes in the amphiphilic segment can have a remarkable influence on the thermoresponsiveness of bolaamphiphilic dyes.

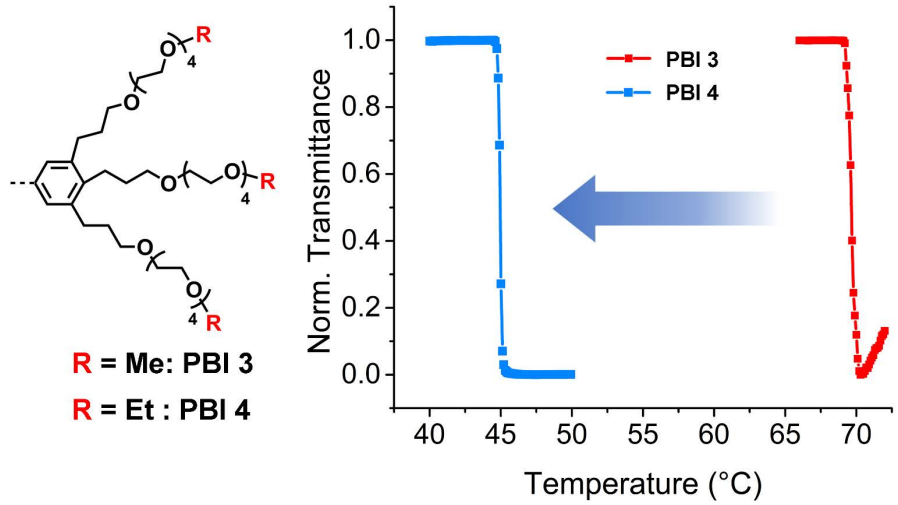


**Figure 6.6**: Normalized transmittance at 800 nm as a function of temperature for **PBI 3**, and **PBI 4** ($c$ = 5 × $10^{-4}$ M) in water (Heating rate: 0.1°C/min). The arrow shows the decrease in cloud points with an increase in terminal alkyl length.

Inspired by the above result, it might be that the hydrophobic propylene spacer, which tethers the phenyl ring and the oxygen atom of glycol chains, might also have a drastic influence on the $T_{cp}$. However, no discernable change in the cloud points is observed between **PBI 5** and its parent compound **PBI 1**, where both showed clouding at 51 °C (Figure 6.7). Likewise, **PBI 6** shows almost the same cloud point as **PBI 3**, where both have five oxygen atoms per chain.

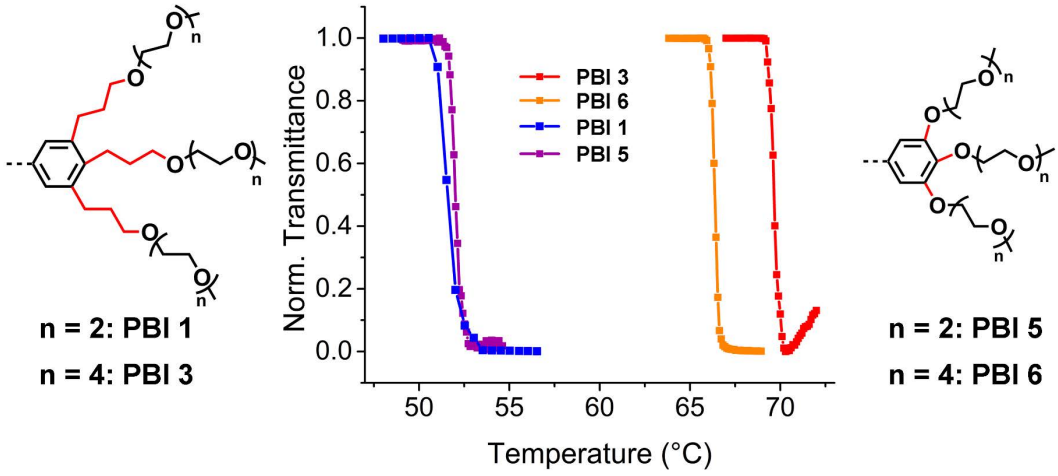


**Figure 6.7**: Normalized transmittance at 800 nm as a function of temperature for **PBI 3**, **PBI 6**, **PBI 1**, and **PBI 5** ($c = 5 \times 10^{-4}$ M) in water (Heating rate: 0.1°C/min).

For all the PBI derivatives, turbidity measurements were conducted for two consecutive cycles to demonstrate that cooling the solution after phase separation to a temperature less than the cloud point restores its initial transmittance (Figure A32). For **PBI 4**, we performed this exemplarily for ten cycles, and no loss in transmittance was observed even after such prolonged heating and cooling routine (Figure 6.8). This indicates the highly reversible nature of hydration/dehydration transition for the bolaamphiphilic dyes used in the present work. Such fatigue-less phase transition is crucial while exploring the application of these dyes as thermoresponsive materials. All the cloud points measured for the derivatives discussed in this work are tabulated in Table 6.1, along with the structural features of their amphiphilic segments.

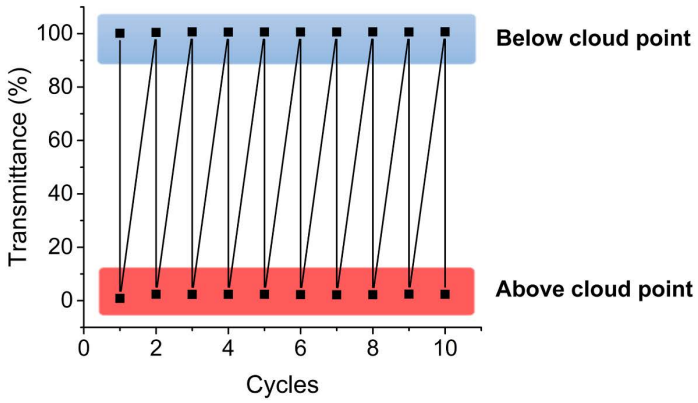


**Figure 6.8**: Transmittance below (40 °C) and above (50 °C) the cloud point for **PBI 4** ($c = 5 \times 10^{-4}$ M) in water for ten cycles (Heating rate: 0.1 °C/min).

Intrigued by the decisive influence of the position of alkyl units within a brush in modulating the thermoresponsive behavior, we were interested in obtaining further insights into their role in the hydration profile of self-assembled structures. For this, we performed $^{1}$H NMR measurements on **PBI 4** in $D_2O$ at different temperatures. NMR spectroscopy has been previously used to probe the local hydration of polymers on a molecular level.[341-345] Well-hydrated polymer parts lead to high chain mobility and, as a result, yields sharper signals, whereas non-optimally hydrated parts decrease the chain mobility and lead to broadening of NMR signals.[306, 346] By tracking the signals over a temperature window, information can be obtained on which polymer components undergo changes in their hydration.

In $CDCl_3$, **PBI 4** shows well-resolved sharp signals, suggesting a monomeric distribution. However, in $D_2O$, the aromatic signals are up-field shifted, pointing towards an aggregate formation arising from the π-π stacking (Figure A33). An excerpt from the variation of NMR spectra in $D_2O$ at different temperatures is shown in Figure 6.9. In $CDCl_3$, the terminal ethyl group manifests as overlapped triplets at 1.22-1.17 ppm (h/h') and as a quartet (g/g') around 3.5 ppm. The propylene spacer protons are well separated from terminal alkyl protons, and they appear as a triplet (d/d') at 2.7 ppm and two quintets (e/e') at 1.9 and 1.8 ppm. While most of these signals are significantly broadened in $D_2O$, some fine structure is maintained by the terminal alkyl chains, suggesting that they are well hydrated, even after the formation of aggregates. However, upon increasing the temperature, this fine structure is lost, and the signals are broadened, indicating the dehydration of these ethyl units. The spacer protons, on the other hand, are broadened even at lower temperatures, presumably due to non-optimal solvation and from the shielding

arising from the aggregate formation. Moreover, elevated temperatures hardly changed their structure apart from minor upfield shifts due to the favorable aggregation at higher temperatures. These observations point to the fact that while terminal alkyl units are well hydrated and exposed to the bulk water, the spacer units are screened away from the aqueous medium and, as a result, undergo no temperature-dependent hydration changes. This might shed light on the diverse behavior of hydrophobic units at different parts of the OEG brushes.

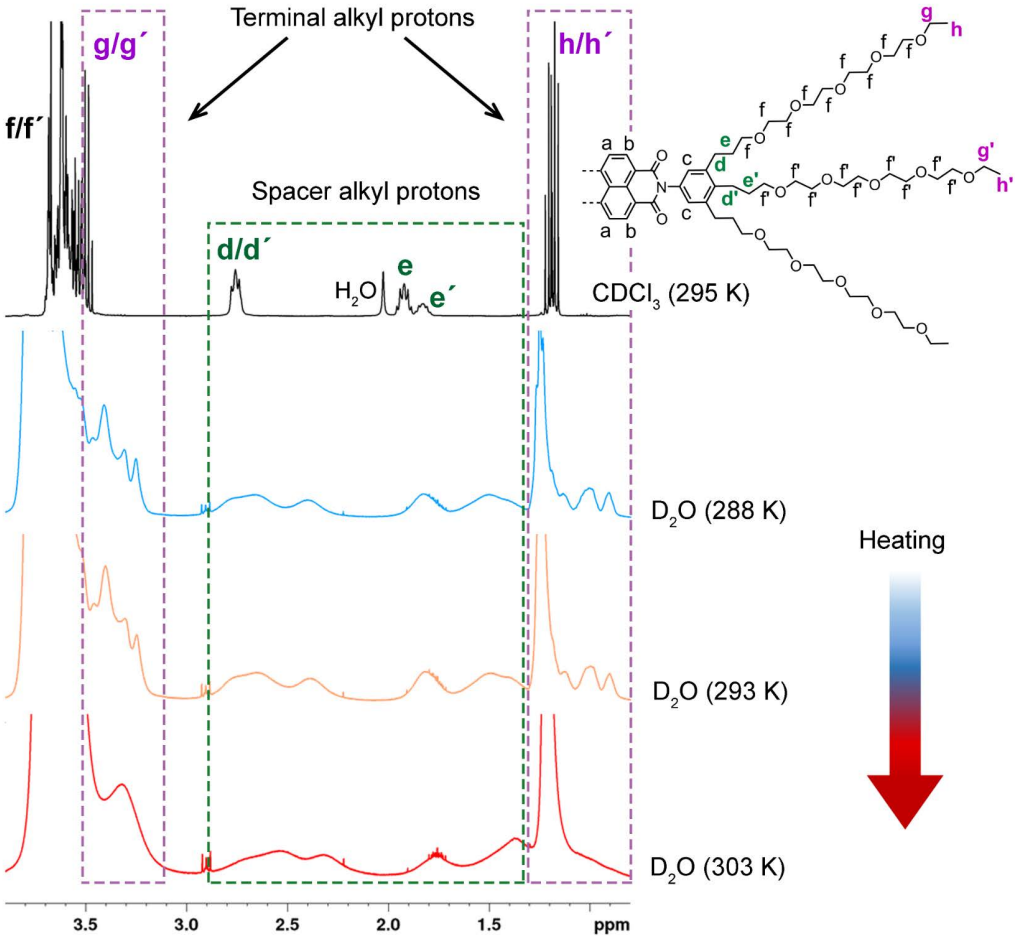


**Figure 6.9**: Excerpt of $^{1}$H NMR of **PBI 4** in $CDCl_3$ at 295 K (top) and in $D_2O$ ($c$ = 5 × $10^{-3}$ M) at different temperatures. The partial chemical structure of **PBI 4** is also provided with significant protons assigned. (Internal standard for $D_2O$: 3-(Trimethylsilyl)propionic-2,2,3,3-$d_4$ acid sodium salt).

## 6.3 Discussion

At first, we observed that all the investigated dyes in the present work undergo an enthalpically driven self-assembly in an organic solvent (ACN) and entropically driven self-assembly in water. Previously, for similar rylene bisimide dyes, we have identified that

the glycol chains are partly back-folded in water to cover the hydrophobic π-scaffold from the solvent medium.[68, 279, 347] Upon aggregation, some of these conformationally restricted chains are released along with the expulsion of hydrated water molecules, which accounts for the entropic favorability of the self-assembly here. In an organic solvent, on the other hand, the lack of this back-folding leads to an aggregation dictated by π-π stacking, which is enthalpic in nature.

Subsequently, we investigated the phase separation of PBI derivatives in water associated with the LCST phenomenon using turbidity measurements. In general, the cloud point of polymers and small molecule-OEG conjugates are explained on the basis of their hydrophobicity/hydrophilicity where a decrease in $T_{cp}$ is observed with increasing hydrophobicity.[348-351] The logarithm of partition coefficient (log *P*), defined as the ratio of concentrations of a compound in two immiscible solvents (water and octanol), can be used to define the hydrophobicity of a molecule, where an increase in hydrophobicity is signified by an increase in log *P* value.[352] Computational determination of log *P* using atom-based approaches[353, 354] is widely used in the pharmaceutical sciences to predict the distribution of drugs in various body parts.[355] Here, we computed the log *P* values of **PBI 1**-**6** using ChemAxon software[356] (for details, see Chapter 9) and compared it to the cloud points, in an effort to understand the modulation of transition temperatures (Table 6.1). Surprisingly, no clear correlation was observed between the hydrophobicity of the PBI derivatives and their phase transition behavior. In a supramolecular polymer, packing of individual monomers can dictate the distribution of hydrophobic patches that are exposed to water, and this might attribute to the anomalies obtained between log *P* values and the LCST behavior of the aggregates formed. Hence, we propose that the hydration of supramolecular assemblies *in lieu* of the hydrophobicity of monomers might provide a better understanding of the thermoresponsive behavior of such supramolecular systems.

In the first series (**PBI 1**, **PBI 2,** and **PBI 3**), we systematically increased the hydrophilic glycol chain length and observed a concomitant increase in the $T_{cp}$. With an increase in OEG dendron length that decorate the periphery of the assemblies, the amount of water molecules that hydrate them also increases. As a result, an increased energetic cost is involved in dehydrating these solvent molecules, which pushes their phase separation to higher temperatures.

In the second series (**PBI 3** and **PBI 4**), we extended the terminal alkyl group from methyl to ethyl and found a drastic drop in the $T_{cp}$ by 24 °C. While it is tempting to correlate this

observation to the larger log *P* value of the latter, we see in the following section that an even more substantial difference in partition co-efficient induces no change in the $T_{cp}$. In our NMR studies, we observed that these terminal alkyl units are optimally hydrated since they are exposed to the bulk water and undergo temperature-dependent hydration changes. We assume that along with poor miscibility arising from the direct interaction of these alkyl units with water, they might interact laterally with themselves as a result of hydrophobic effect and cluster the chains close to each other. This might hinder the effective hydration of the succeeding glycol units and result in an abrupt drop of phase transition temperature.[357, 358]

Finally, we investigated the influence of the spacer alkyl group (**PBI 5**, **PBI 6**) and found no appreciable change in the cloud points. Temperature-dependent NMR studies on **PBI 4** has revealed that unlike periphery alkyl chains, these spacer groups are non-optimally hydrated and undergo little changes in their hydration with temperature. In an H-type aggregate of **PBI 4**, these propylene units are arranged near the central hydrophobic column composed of π-cores and are screened from the bulk water. As a result, they impose no discernible consequences on the hydration of the glycol chains, unlike the terminal alkyl units. This might point towards their lack of influence in modulating cloud point temperatures.

While here we have exemplarily demonstrated the tuning of $T_{cp}$ within a range of 45 °C to 69 °C, it is indeed possible to widen this temperature window both below and above these extremes. For example, increasing the terminal alkyl chain for a shorter derivative (e.g., **PBI 1**) will afford thermoresponsiveness in the lower window and especially in physiologically relevant temperatures. Increasing the chain length further than five oxygen atoms (per chain) can afford transition in the higher temperature range. Since the current method relies on the modulation of the hydrophilic brush substituent rather than the hydrophobic core, thermoresponsiveness of other π-amphiphiles can also be tuned using the same strategy.

## 6.4 Conclusions

Precise control of phase transition temperature is quintessential to develop LCST based thermoresponsive materials. In this regard, we developed a rational design strategy where this information can be encoded on the imide substituents for a series of bolaamphiphilic perylene bisimide dyes. All the molecules investigated in the present work self-assemble

in an entropically driven fashion in water and undergo macroscopic phase separation at a temperature determined by the structure of the brush substituents. With the increasing chain length of the OEG units, the cloud point increases as a result of improved hydration. Terminal alkyl units impart a drastic reduction in the $T_{cp,}$ whereas, spacer alkyl groups do not influence the phase separation temperature. This differential behavior of diverse components of imide substituents can be attributed to the packing behavior of monomers within an aggregate and resultant changes in the hydration of the supramolecular assembly. We presume that our guidelines for tuning the cloud point can be adopted for other π-conjugated systems and result in the development of novel optoelectronic materials that respond to external stimuli.

# Chapter 7

# Summary

The mastery of nature in creating complex architectures by self-assembly, that drive vital biological functions, is unparalleled. While it is hard to replicate these intricate structures by artificial molecules, the association of amphiphilic π-systems has proven to be suitable for understanding the basic principles of self-organization in water. In the last decades, considerable progress has been made in the thermodynamic understanding of aggregation of π-conjugated molecules in organic media. However, transferring this knowledge to aqueous supramolecular chemistry proved to be challenging due to the decisive role water plays in the construction of non-covalent arrays. Hence, the general aim of this thesis encompassed an understanding of the structural parameters that regulate the thermodynamics of self-assembly as well as stimuli-responsive properties of π-amphiphiles in water.

**Chapter 2** provides an overview of the association phenomenon in aqueous media and the tools required to extract the thermodynamic parameters of self-assembly. At first, the driving forces which dictate aggregation and host-guest binding are described with major focus devoted to the hydrophobic effect, the release of high-energy water, and dispersion interactions. Subsequently, the self-assembly of π-amphiphiles constituting diverse aromatic hydrophobic cores are detailed where different consequences on thermodynamic and morphological features of aggregation are realized through molecular design strategies. In the last section, analytical techniques utilized to quantify the thermodynamic parameters of self-assembly are outlined along with some representative examples. While spectroscopic techniques remain popular attributing to its versatility, isothermal titration calorimetry (ITC) and differential scanning calorimetry (DSC), which directly determine heat flow upon self-assembly, are advantageous and can be used complementarily along with conventional methods.

As water-soluble π-conjugated molecules, we synthesized bolaamphiphilic perylene bisimides and naphthalene bisimides (Scheme 7.1) using multi-step procedures, as model systems to explore aqueous self-assembly (**Chapter 3**). Three types of OEG side chains were used to render them water soluble, which differ in their connectivity to the π-scaffold,

length of hydrophilic units, and the attachment of side chains to the phenyl ring of the wedge. The final synthetic step to obtain symmetrical rylene bisimides is carried out *via* an imidization reaction with the amino derivative of brush substituent and the corresponding tetracarboxylic acid bisanhydride precursor.

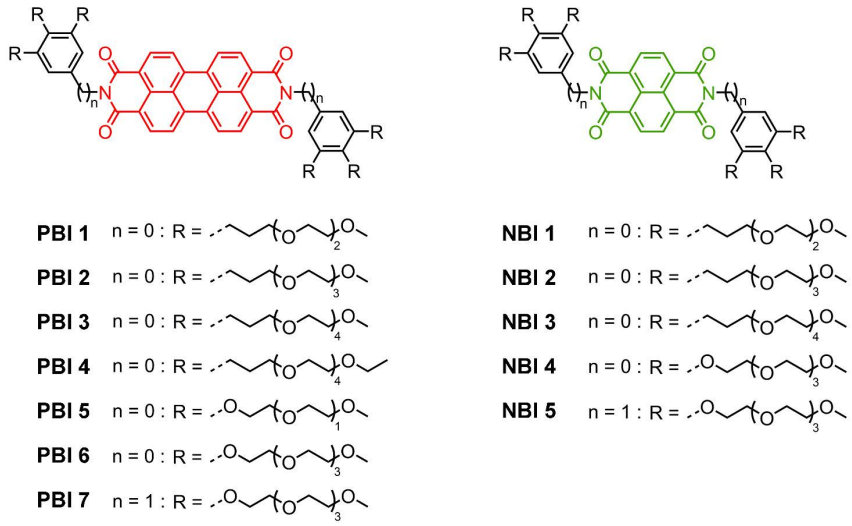


**Scheme 7.1**: Chemical structures of bolaamphiphilic PBIs and NBIs described in this thesis.

At first, we were interested in obtaining quantitative insights into the entropically-driven self-assembly, which was recognized initially for a bolaamphiphilic PBI derivative (**Chapter 4**).[68] Since the larger PBI π-core of this molecule hampered self-assembly studies in water due to its pronounced aggregation tendency, here we employed smaller naphthalene bisimide chromophore, to attenuate the propensity of association and enable thermodynamic analysis by spectroscopic and calorimetric methods. We hypothesized that the entropic favorability in these amphiphilic systems was imparted by the oligo ethylene glycol chains introduced for water solubility. Hence, to study its effect, we investigated in detail the aggregation parameters in water for **NBI 1**, **NBI 2**, and **NBI 3**, where the length of the side chains was systematically varied (Figure 7.1a).

Unlike the majority of supramolecular systems, **NBI 1-3** showed an enhanced aggregation tendency with an increase in temperature, suggesting the entropic parameters which drive their self-assembly. Temperature-dependent UV-vis studies and ITC dilution measurements were able to independently dissect the thermodynamic parameters pertaining to their aggregation and found that the enthalpic penalty, as well as entropic favorability, increases with chain length (Figure 7.1b). Furthermore, with an increase in the number of glycol units, the mechanism which dictates the aggregate formation for

**NBI 1-3** varies from isodesmic to weakly anti-cooperative. ITC studies at different temperatures also revealed that the enthalpic penalty of association decreases with an increase in temperature due to the weakening of H-bond strength (between water molecules and the OEG chains), which accounts for their enhanced association at higher temperatures. Molecular Dynamics (MD) simulations of monomeric and stacked **NBI 1** and **NBI 3** have shown an intriguing orientation of glycol chains, which are back-folded to screen the hydrophobic core from the bulk water. This specific conformation of side chains, which was experimentally confirmed by $^{1}$H-$^{1}$H ROESY measurements, accounts for the decrease in binding constants as well as deviation from the isodesmic mechanism, due to steric impediment arising with elongation of side chains. Furthermore, the removal of ordered OEG units also increases the conformational entropy of side chains and contributes to the overall entropic favorability of association. In a gist, we were able to successfully obtain a quantitative picture of the entropically driven self-assembly for naphthalene bisimides using spectroscopic and calorimetric methods and demonstrated that their thermodynamic profile of aggregation is heavily influenced by the OEG side chains.

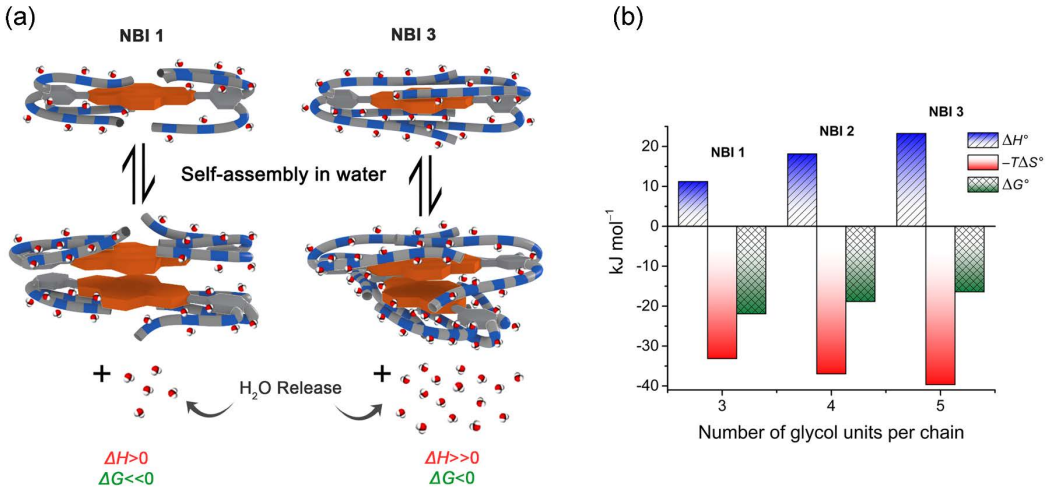


**Figure 7.1**: (a) Schematic illustration showing the self-assembly of **NBI 1** and **NBI 3** in water and corresponding changes in the thermodynamic parameters. (b) Thermodynamic profile for the self-assembly of **NBI 1-3** in water.

Subsequently, we pondered upon whether a control over the bifurcated thermal response of entropically driven and commonly observed enthalpically driven self-assembly can be achieved by rational design strategies (**Chapter 5**). We hypothesized that the back-folded conformation of side chains observed in **Chapter 4** might be crucial in directing favorable aggregation with heating, as their release will lead to a surge in the entropy of the system, as explained before. To study this effect, we synthesized **PBI 6**, **PBI 7**, **NBI 4**, and **NBI 5**

containing the same hydrophilic brush at imide positions, but only differ in their connectivity to the central π-core. For **PBI 6** and **NBI 4**, this brush is connected directly to the perylene and naphthalene bisimide cores, whereas for **PBI 7** and **NBI 5**, this was appended *via* a methylene linker, to disrupt the back-folding.

Temperature-dependent UV-vis studies have revealed that all the molecules aggregate at lower temperatures in an organic solvent (MeOH) driven by enthalpic factors. In water, **PBI 6** and **NBI 4** self-assemble in an entropic fashion, whereas **PBI 7** and **NBI 5** in an enthalpic fashion. In-depth concentration-dependent studies were able to deduce the thermodynamic profile for **NBI 4** and **NBI 5**, which was further confirmed by calorimetric studies (Figure 7.2b). The association tendency, as well as the self-assembly mechanism, strongly deviates between **NBI 4** and **NBI 5** despite the minor difference of a methylene group. **NBI 4** aggregates in a weak anti-cooperative fashion with less binding strength, whereas **NBI 5** associate according to an isodesmic mechanism with high aggregation tendency. 2D NMR and PM7 studies have demonstrated a marked difference in the conformation of side chains in both derivatives. **NBI 4**, where the amphiphilic wedge is directly attached, favors back-folding of side chains whereas **NBI 5**, where this connectivity is employed *via* a methylene group disfavors this specific orientation, presumably due to the $sp^3$ hybridization of the $CH_2$ unit. This accounts for the thermodynamic bias observed for PBI and NBI derivatives with and without the spacer employed in this study. The self-assembly in the former case is accompanied by the release of these restricted side-chains, which leads to an increase in the entropy of self-assembly along with the expulsion of hydrated water molecules from side chains (Figure 7.2a). On the other hand, the aggregation in the latter case is directed mainly by π-π interactions, which is enthalpic in nature. The sterical encumbrance imparted by back-folded glycol chains also restricts the π-π stacking in the case of **NBI 4**, resulting in a weaker binding strength and anti-cooperative mechanism. This study demonstrates that aggregate formation can be induced either upon heating or cooling by changing the conformation of side chains, which can be achieved by modulating the connectivity of amphiphilic brush to the central π-core.

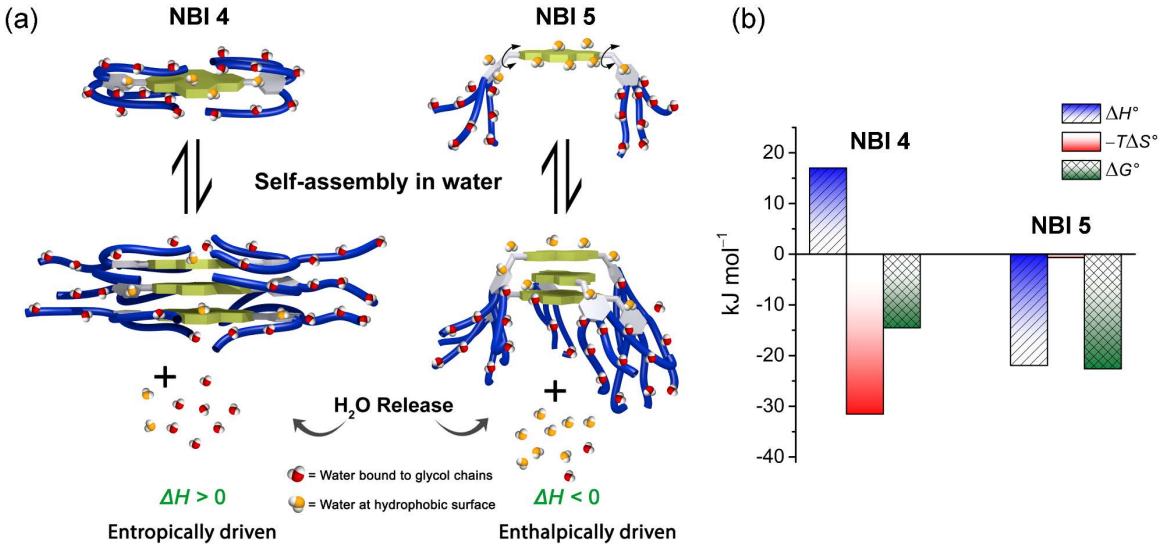


**Figure 7.2**: (a) Schematic illustration showing the self-assembly of **NBI 4** and **NBI 5** in water and corresponding changes in the thermodynamic parameters. (b) Thermodynamic profile for the self-assembly of **NBI 4** and **NBI 5** in water.

Lower Critical Solution Temperature (LCST) is widely employed to generate thermoresponsive materials that change their properties in a small temperature interval. The oligo ethylene glycol chains used to render rylene bisimides water-soluble, imparts this LCST phenomenon to many derivatives employed here, due to its hydrophilicity changes upon temperature increase. In the last part of the thesis (**Chapter 6**), we explored the structural parameters that regulate the phase transition temperature for perylene bisimide derivatives (**PBI 1-6**), as precise control of this behavior is quintessential for self-assembly studies as well as to generate 'smart' materials. All the molecules studied in this work underwent an entropically driven self-assembly yielding H-aggregates in water and subsequently phase separated at higher temperatures (Figure 7.3a). Different structural components of the side chains were systematically varied to study their influence on the onset temperature of this precipitation which was monitored by turbidity measurements. We found that the with an increase in the length of hydrophilic units, the cloud point increases, whereas hydrophobic units at the chain termini decrease the phase transition temperature (Figure 7.3b). In contrast, spacer hydrophobic groups have no appreciable influence in modulating cloud points as they are screened away from the bulk water, due to the arrangement of monomers within a supramolecular assembly. The insights obtained from this study demonstrate that the thermoresponsive behavior of bolaamphiphilic PBIs can be programmed into their imide substituents within a temperature range of 45 °C and 69 °C.

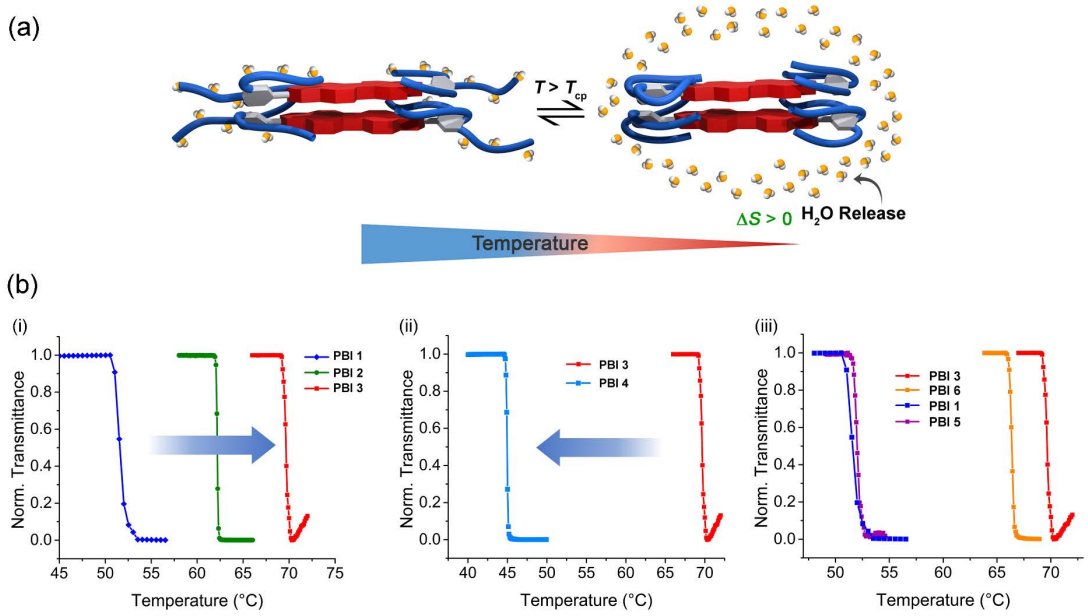


**Figure 7.3**: (a) Schematic illustration showing the LCST associated phase separation of a PBI derivative. (b) Turbidity measurements showing the influence of glycol chain length (i), terminal alkyl length (ii), and spacer alkyl length (iii) on the cloud points of **PBI 1-6**.

In conclusion, the present work demonstrates how different thermodynamic aspects of self-assembly and stimuli-responsive properties in water can be encoded on the structure of π-amphiphiles consisting of perylene or naphthalene bisimide cores. Since these features are primarily dictated by the water-soluble oligo ethylene glycol units rather than the hydrophobic core itself, the same design principles can be presumably extrapolated for other π-conjugated systems.

# Chapter 8

# Zusammenfassung

Die Natur ist dazu in der Lage, komplexe Strukturen durch Selbstorganisation auszubilden, die zur Steuerung wichtiger biologischer Funktionen benötigt werden. Aufgrund der hohen Komplexität dieser Strukturen ist es allerdings schwierig, diese durch künstliche Moleküle nachzuahmen. Die Aggregation amphiphiler π-Systeme erwies sich dennoch als geeignet, einige der grundlegenden Prinzipien von selbstorganisationsphänomenen in Wasser zu verstehen. So wurden in den letzten Jahrzehnten zunächst erhebliche Fortschritte beim thermodynamischen Verständnis der Aggregation π-konjugierter Moleküle in organischen Medien erzielt. Die Übertragung dieses Wissens auf die supramolekulare Chemie in Wasser erwies sich jedoch aufgrund des einzigartigen Wasserstoffbrückennetzwerks dieses Lösungsmittels als sehr schwierig. Das Ziel dieser Arbeit bestand deshalb darin, die Strukturparameter zu verstehen, welche die thermodynamischen Eigenschaften der Selbstorganisation sowie die stimuli-responsiven Merkmale von π-Amphiphilen in Wasser regulieren.

Das **2. Kapitel** gibt einen Überblick über die Selbstassemblierung in wässrigem Medium und wie die thermodynamischen Parameter dieser Selbstorganisation bestimmt werden. Zunächst wurden die treibenden Kräfte beschrieben, welche die Selbstorganisation sowie die Bindung zwischen Wirt und Gast bestimmen. Hierbei lag der Schwerpunkt der Ausführungen auf dem hydrophoben Effekt, der Freisetzung von energiereichem Wasser und den Dispersionswechselwirkungen. Anschließend folgt eine detaillierte Beschreibung der Selbstorganisation von π-Amphiphilen mit verschiedenen hydrophoben aromatischen Kernen. Es werden Konsequenzen eines unterschiedlichen Moleküldesigns für die thermodynamischen und morphologischen Merkmale der entstandenen Aggregate gezeigt. Im letzten Abschnitt dieses Kapitels werden die Analysetechniken zur Quantifizierung der thermodynamischen Kenngrößen der Selbstorganisation, sowie einige repräsentative Beispiele beschrieben. Aufgrund ihrer vielseitigen Anwendungsmöglichkeiten kommen spektroskopische Techniken häufig bei der Untersuchung thermodynamischer Parameter zum Einsatz. Allerdings kann auch auf andere Techniken bei der Untersuchung

zurückgegriffen werden. Hierbei sind besonders die isotherme Titrationskalorimetrie (ITC) und die Dynamische Differentialkalorimetrie (DSC) hervorzuheben, da mit diesen Methoden die Wärmeströme während der Selbstorganisation direkt bestimmt werden können.

Als wasserlösliche π-konjugierte Moleküle synthetisierten wir unterschiedliche bolaamphiphile Perylenbisimide und Naphthalenbisimide als Modellverbindungen, um deren Aggregationsverhalten in wässriger Lösung zu untersuchen (Abbildung 8.1) (**Kapitel 3**). Es wurden unterschiedliche hydrophile OEG-Seitenketten benutzt, welche alle einen pinselartigen Aufbau besitzen. Die Seitenketten unterscheiden sich in ihrer Konnektivität zum π-Gerüst, der Länge der hydrophilen Einheiten und der Art der Verbindung zwischen den OEG-Ketten und dem Phenylring. Bei der Synthese wird der letzte Schritt zur Gewinnung symmetrischer Rylenbisimide über eine Imidisierungsreaktion mit dem Aminoderivat des Pinselsubstituenten und dem entsprechenden Tetracarbonsäurebisanhydridderivat durchgeführt.

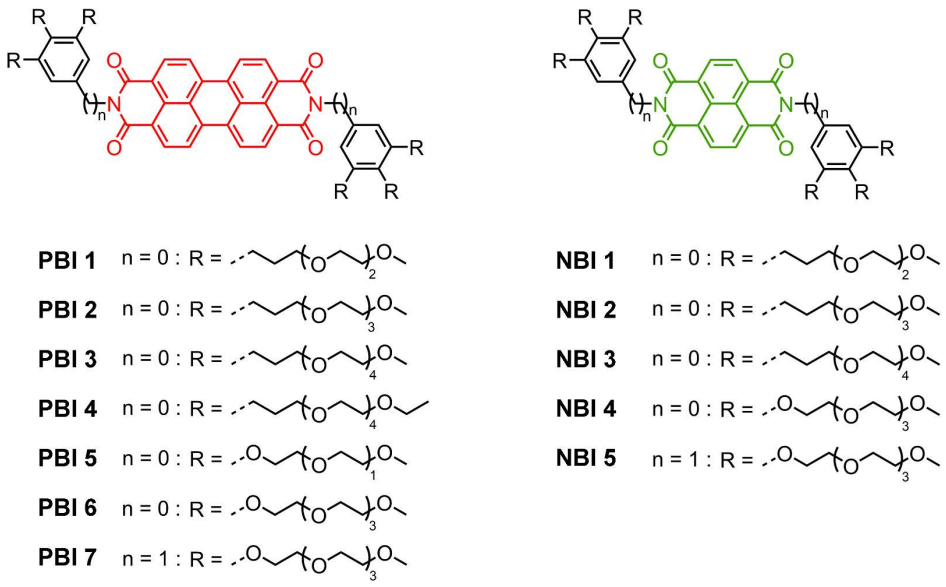


**Abbildung 8.1**: Chemische Struktur der beschriebenen bolaamphiphilen PBIs und NBIs.

Zunächst waren wir daran interessiert, quantitative Einblicke in die entropische Triebkraft der Selbstorganisation zu erhalten, die erstmals für ein bolaamphiphiles PBI Derivat erkannt wurde (**Kapitel 4**).[68] Da das verhältnismäßig große PBI π-System dieses Moleküls aufgrund seiner ausgeprägten Aggregationstendenz Selbstorganisationsstudien in Wasser nur schwer durchführbar machte, wurde das kleinere Naphthalinbisimid verwendet, um so die Assoziationsneigung in Wasser zu verringern. Dies ermöglichte uns eine

thermodynamische Analyse mit spektroskopischen und kalorimetrischen Methoden. Wir stellten die Hypothese auf, dass die entropisch begünstigte Aggregation in diesen amphiphilen Systemen durch die wasserlöslichkeitsvermitteltenden Oligoethylenglykolketten verursacht wird. Um diese Hypothese zu bestätigen, untersuchten wir detailliert die Aggregationsparameter von **NBI 1**, **NBI 2**, und **NBI 3**, in Wasser, wobei die Länge der OEG-Ketten systematisch variiert wurde (Abbildung 8.2a).

Im Gegensatz zu den meisten supramolekularen Systemen zeigten **NBI 1-3** eine erhöhte Aggregationstendenz mit steigender Temperatur, was auf eine entropisch getriebene Selbstorganisation hinweist. Temperaturabhängige UV/Vis-Studien und ITC-Verdünnungsreihen konnten die thermodynamischen Kenngrößen ihrer Aggregation unabhängig voneinander analysieren. Es zeigte sich, dass mit Zunahme der Kettenlänge die Aggregation zwar enthalpisch benachteiligt wird, dafür aber entropisch begünstigt wird. (Abbildung 8.2b). Darüber hinaus beobachtet man für **NBI 1-3** mit zunehmender Anzahl von Glykoleinheiten einen übergang von isodesmischer zu schwach antikooperativer Aggregation. Außerdem zeigten die ITC-Studien, dass die ungünstige Enthalpie der Aggregation mit steigender Temperatur geringer wird. Der Grund dafür ist die Schwächung der Wasserstoffbrückenbindungen zwischen Wassermolekülen und den OEG-Ketten. Diese Schwächung ist ebenfalls für die verstärkte Assemblierungstendenz bei höheren Temperaturen verantwortlich. Die Molekulardynamik-Simulationen (MD) von **NBI 1** und **NBI 3** in monomerer wie auch in assemblierter Form haben eine interessante Orientierung der Glykolketten gezeigt. Sie sind über den hydrophoben Kern zurückgefaltet, um diesen von umliegenden Wassermolekülen abzuschirmen. Diese spezifische Konformation der Ketten, die experimentell durch $^{1}$H-$^{1}$H-ROESY-Messungen bestätigt wurde, erklärt die Abnahme der Bindungskonstanten sowie die Abweichung vom isodesmischen Mechanismus. Dies geschieht aufgrund einer sterischen Hinderung, die durch die Verlängerung der Glykolketten entsteht. Darüber hinaus erhöht die Entfernung geordneter OEG-Einheiten auch die Konformationsentropie dieser Ketten und trägt zur allgemeinen entropischen Begünstigung der Selbstassemblierung bei. Zusammenfassend konnten wir mit spektroskopischen und kalorimetrischen Methoden ein quantitatives Bild der entropisch getriebenen Selbstorganisation für Naphthalinbisimide erhalten und zeigen, dass ihr thermodynamisches Aggregationsprofil stark von der Länge der OEG-Ketten beeinflusst wird.

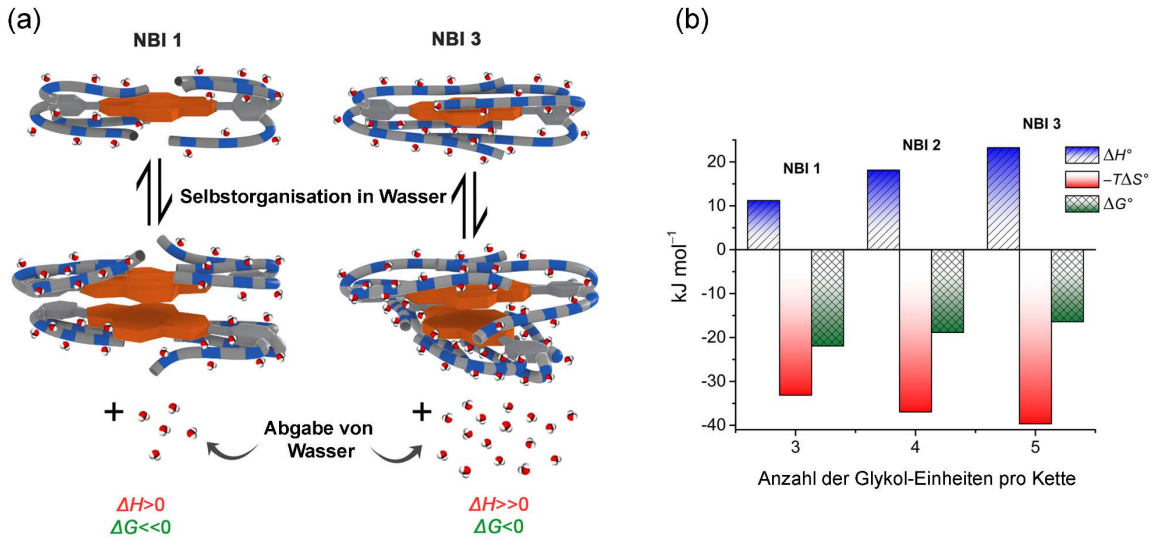


**Abbildung 8.2**: (a) Schematische Darstellung der Selbstorganisation von **NBI 1** und **NBI 3** in Wasser sowie die einhergende Veränderungen der thermodynamischen Parameter. (b) Thermodynamisches Profil für die Selbstassemblierung von **NBI 1**-**3** in Wasser.

Darauf aufbauend wollten wir untersuchen, ob die Thermodynamik der Selbstassemblierung zwischen der häufiger beobachtbaren enthalpisch getriebenen und der entropisch getriebenen Selbstorganisation mittels eines gezielten Moleküldesigns reguliert werden kann. (**Kapitel 5**). Wir stellten die Hypothese auf, dass die in **Kapitel 4** beobachtete rückgefaltete Konformation der OEG-Ketten entscheidend für die Steuerung einer begünstigen Aggregation bei erhöhten Temperaturen sein könnte. Dies wäre auf einen Anstieg der Entropie des Systems bei der Freisetzung der OEG-Ketten vom hydrophoben Kern zurückzuführen. Um diesen Effekt zu untersuchen, synthetisierten wir **PBI 6**, **PBI 7**, **NBI 4** und **NBI 5**, die an den Imidpositionen identische amphiphile Reste mit pinselartigem Aufbau enthielten. Sie unterschieden sich allerdings in ihrer Konnektivität zum zentralen π-System. Bei **PBI 6** und **NBI 4** ist der Phenylring der Kopfgruppe direkt mit den Perylen- beziehungsweise Naphthalinbisimidkernen verbunden, während bei **PBI 7** und **NBI 5** diese über einen Methylenlinker angehängt wurde, um somit die Rückfaltung zu verhindern.

Temperaturabhängige UV/Vis-Studien haben gezeigt, dass in einem organischen Lösungsmittel (MeOH) bei niedrigeren Temperaturen alle Moleküle aufgrund von enthalpisch getriebenen Faktoren aggregieren. Hingegen, aggregierten **PBI 6** und **NBI 4** in Wasser entropisch, während sich **PBI 7** und **NBI 5** auch in Wasser enthalpisch organisierten. In eingehenden konzentrationsabhängigen Studien konnte anschließend das thermodynamische Profil für **NBI 4** und **NBI 5** abgeleitet werden, welches durch kalorimetrische Studien unterstützt werden konnte (Abbildung 8.3b). Die

Aggregationstendenz sowie der Selbstorganisationsmechanismus unterscheiden sich trotz der großen Ähnlichkeit im Moleküldesign und des geringen Unterschieds von einer Methylengruppe stark zwischen **NBI 4** und **NBI 5**. **NBI 4** aggregiert schwach antikooperativ mit geringerer Bindungsstärke, während **NBI 5** nach einem isodesmischen Mechanismus mit hoher Aggregationskonstante assoziiert. 2D-NMR- und PM7-Untersuchungen haben einen deutlichen Unterschied in der Konformation der Glykolketten in beiden Derivaten gezeigt. Im Falle von **NBI 4**, bei dem der Phenylring der hydrophilen Kopfgruppe direkt mit dem Kern verbunden ist, ist die Rückfaltung der Seitenketten über den hydrophoben Kern möglich. Im Gegensatz dazu verhindert bei **NBI 5** die Methylengruppe zwischen dem Phenylring der hydrophilen Kopfgruppe und dem Kern, die Rückfaltung. Diese spezielle Orientierung entsteht vermutlich aufgrund der $sp^3$-Hybridisierung der $CH_2$-Einheit. Hierdurch können die unterschiedlichen thermodynamischen Parameter, die zu der Selbstassemblierung von sowohl PBI- wie auch NBI-Derivaten beitragen, erklärt werden. Ist der löslichkeitsvermittelnde Rest direkt mit dem Kern verbunden, führt eine Selbstorganisation gezwungenermaßen zu einer Entfaltung der rückgefalteten OEG-Ketten, was mit dem Ausstoß hydratisierter Wassermoleküle aus den Ketten und somit einer Erhöhung der Entropie des Systems einhergeht (Abbildung 8.3a). Anderseits wird die Aggregation im Fall von **NBI 5** hauptsächlich durch π-π Wechselwirkungen gesteuert, welche enthalpischer Natur sind. Die durch rückgefaltete Glykolketten verursachte sterische Belastung schränkt auch die π-π-Stapelung im Fall von **NBI 4** ein, was zu der schwächeren Bindungsstärke und einem antikooperativen Mechanismus führt. Diese Studie zeigt, dass die Aggregatbildung entweder beim Erhitzen oder Abkühlen durch Ändern der Konformation der Oligoethylenglykolketten induziert werden kann, was durch Modikfikation der Konnektivität der amphiphilen Pinsel mit dem zentralen π-Kern erreicht wird.

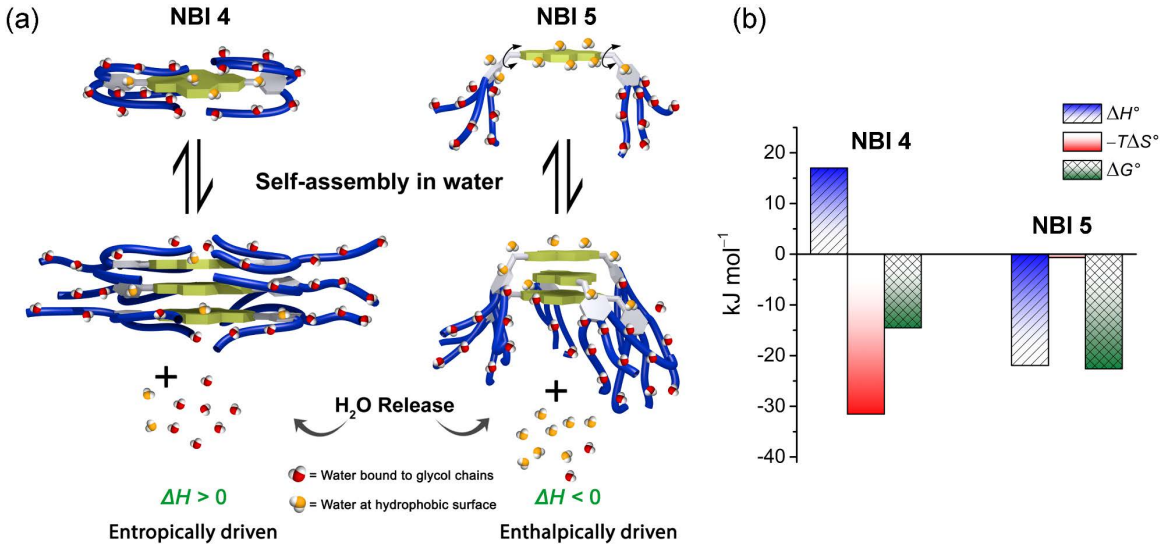


**Abbildung 8.3**: (a) Schematische Darstellung der Selbstorganisation von **NBI 4** und **NBI 5** in Wasser sowie die entsprechenden Veränderungen der thermodynamischen Parameter. (b) Thermodynamisches Profil für die Selbstorganisation von **NBI 4** und **NBI 5** in Wasser.

Die untere kritische Lösungstemperatur (LCST) wird häufig verwendet, um thermoresponsive Materialien zu erzeugen, die ihre Eigenschaften innerhalb eines kleinen Temperaturintervalls ändern. Die verwendeten OEG-Ketten verleihen vielen der hier verwendeten Derivaten aufgrund der Hydrophilieänderungen bei einem Temperaturanstieg ebensolche Eigenschaften. Im letzten Teil der Arbeit (**Kapitel 6**) haben wir die Strukturparameter untersucht, welche die Phasenübergangstemperatur für Perylenbisimidderivate (**PBI 1-6**) regulieren, da eine genaue Kontrolle dieses Verhaltens sowohl für Selbstorganisationsstudien wie auch für die Erzeugung von "intelligenten" Materialien von entscheidender Bedeutung ist. Alle in diesem Teil der Arbeit untersuchten Moleküle zeigten eine entropisch getriebenen Selbstassemblierung, wobei H-Aggregate in Wasser erhalten wurden und anschließend eine Phasentrennung bei weiterer Erhöhung der Temperatur beobachtet wurde. (Abbildung 8.4a). Die verschiedenen Strukturkomponenten der Seitenketten wurden systematisch variiert, um durch Trübungsmessungen ihren Einfluss auf die Temperatur der Präzipitation zu untersuchen. Wir fanden heraus, dass die zunehmende Länge der hydrophilen Einheiten die Trübungspunkte erhöht, während hydrophobe Einheiten an den Kettenenden die Phasenübergangstemperatur senken (Abbildung 8.4b). Die Alkyleinheit zwischen den OEG-Ketten und dem Phenylring hat dagegen keinen nennenswerten Einfluss auf die Trübungspunkte, da sie aufgrund der Molekülstruktur vom umgebenden Wasser abgeschirmt werden. Die aus dieser Studie gewonnenen Erkenntnisse zeigen, dass das thermoresponsive Verhalten von

bolaamphiphilen PBIs mittels ihrer Imidsubstituenten im Temperaturbereich zwishen 45 °C und 69 °C programmiert werden kann.

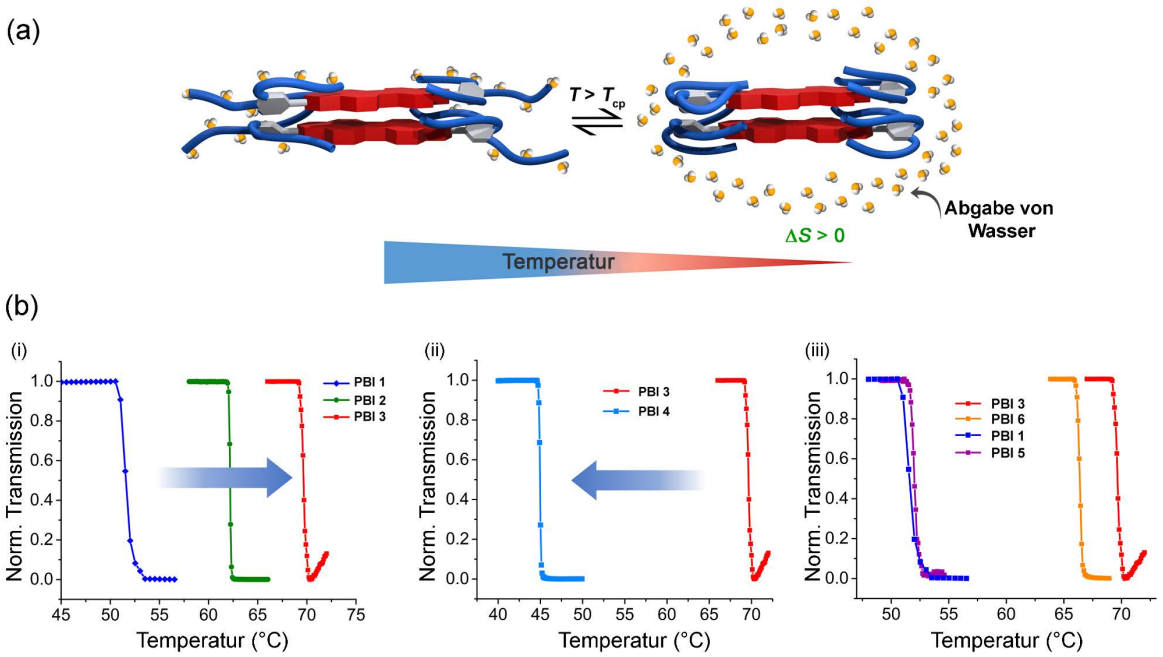


**Abbildung 8.4**: (a) Die schematische Darstellung zeigt die LCST bedingte Phasentrennung eines PBI-Derivats (b) Trübungsmessungen zeigen den Einfluss der Glykolkettenlänge (i), der terminalen Alkyllänge (ii) und der Art der Verbindung zwischen den OEG-Ketten und dem Phenylring (iii) auf die Trübungspunkte der **PBI 1-6**.

Zusammenfassend zeigt die vorliegende Arbeit, wie verschiedene thermodynamische Aspekte der Selbstorganisation sowie die stimuli-responsiven Merkmale in Wasser mittels der Struktur von π-Amphiphilen mit Perylen- oder Naphthalinbisimidkernen programmiert werden können. Da diese Merkmale in erster Linie von den wasserlöslichen Oligoethylenglykoleinheiten und nicht vom hydrophoben Kern selbst bestimmt werden, können dieselben Konstruktionsprinzipien vermutlich auf andere π-konjugierte Systeme angewendet werden.

# Chapter 9

# Experimental Section

## 9.1 Materials and methods

**General:** Reagents were purchased from commercial suppliers and used as received without further purification. Solvents were distilled and dried according to standard procedures. Gravity column chromatography was performed with commercial glass columns using silica gel 60M (particle size 0.04-0.063 mm) as stationary phase, whereas flash column chromatography was carried out with PuriFlash 420 system from *Interchim* using commercially available silica gel columns from *Interchim* (PF-30SIHP-F0025). NMR spectra were recorded on an Avance III HD (400 MHz or 600 MHz) from Bruker at 295 K. Gel permeation chromatography was performed with a recycling semi-preparative gel permeation chromatography (Shimadzu Prominence CBM or JAI LaborACE L-C5060) using chloroform stabilized with ethanol as eluent. The NMR spectra were calibrated to the residual protic solvent peak unless otherwise stated, and the chemical shifts ($\delta$) are recorded in parts per million (ppm). Multiplicities for proton signals are abbreviated as s, d, t, q, quint, m and dd for singlet, doublet, triplet, quartet, quintet, multiplet, and doublet of doublets, respectively. High-resolution mass spectra (HRMS) were recorded with microTOF focus (Bruker Daltonics, Germany).

**UV-vis spectroscopy:** UV-vis absorption spectra were recorded using Perkin-Elmer Lambda 40P or JASCO V-770 spectrophotometers. The measurements were carried out in quartz cuvettes using either spectroscopic grade chloroform, methanol, acetonitrile, or deionized water prepared by water purification system PURELAB classic (ELGA, France). Temperature control was accomplished by Perkin Elmer PTP-1+1 and JASCO PAC-743R Peltier systems. Extinction coefficients were calculated from Lambert-Beer's law and are density corrected in the case of temperature-dependent measurements.

Cloud points were determined by temperature-dependent transmittance measurements at 800 nm using Perkin-Elmer Lambda 40P or JASCO V-770 spectrophotometers and is referred to as the temperature at which the transmittance is 90% of the initial transmittance. The heating rate was 0.1 °C/min.

**Steady-state fluorescence spectroscopy:** Emission spectra were recorded on Edinburgh Instruments FLS980 Fluorescence Spectrometer, equipped with a double monochromator for emission and excitation, under magic-angle setup. The fluorescent quantum yields were determined by the optical dilution method ($OD_{max} < 0.05$) using *N*,*N*'-Bis(2,6-diisopropylphenyl)-3,4:9,10-tetracarboxylic acid bisimide ($\Phi_{fl} = 1$ in $CHCl_3$) as reference.

**Isothermal titration calorimetry (ITC):** ITC measurements were performed using MicroCal VP-ITC (GE Healthcare, USA) or PEAQ-ITC (Malvern). The stock solutions, as well as solvent (water), was degassed by applying a vacuum before the measurements. The temperature of the sample solutions and water was adjusted to the respective temperature prior to the measurement using a MicroCal ThermoVac (GE Healthcare, USA). The enthalpograms were derived by integrating the raw heat signals and were fitted with I2-ITC package for **NBI 1**-**3**.[213, 258]

**Atomic force microscopy (AFM):** AFM measurements were performed under ambient conditions using a Bruker Multimode 8 SPM system operating in tapping mode in air. Silica cantilevers (OMCL-AC200TS, Olympus) with a resonance frequency of ~150 kHz and a spring constant of ~10 N $m^{-1}$ were used. The samples were prepared by spin-coating solutions onto either silicon wafer (treated by Argon plasma) or mica.

**Dynamic light scattering (DLS)**: DLS measurements were performed at room temperature on a Beckman Coulter N5 submicron particle analyzer equipped with a 25mW Helium-Neon Laser (632.8 nm) using 10 mm Hellma quartz cuvettes.

**Molecular Dynamics (MD) calculations**:

**Force field creation**

Force fields were derived based on the GROMOS 54A7 parameter set.[359] Topology files for naphthalene bisimide derivatives (**NBI 1** and **NBI 3**) were created using the Automated Topology Builder[360] and are publicly available under the molecule IDs #246516 and #246528, respectively. Two additional dihedrals between the core and the attached phenyl rings were added manually so as to match the molecular potential energy during rotation of the dihedral with the DFT-derived values for a biphenyl system.[361]

**Simulation procedure**

Simulations were carried out using GROMACS[362] in the NPT ensemble using a Nosé-Hoover thermostat and a Parrinello-Rahman barostat. The temperature was set to 300K,

and the pressure was maintained at 1 atmosphere. The time step was 1fs, and electrostatic interactions were calculated using Particle-Mesh-Ewald summation. The box contained 4008 water molecules for the **NBI 1** monomer; 13998 water molecules for the **NBI 1** dimer; 3950 water molecules for the **NBI 3** monomer and 23705 water molecules for the **NBI 3** dimer. The SPC/E water model was used.

Density plots were averaged over 500 ns for **NBI 1** monomer; 210 ns for **NBI 1** dimer; 500 ns for **NBI 3** monomer and 150 ns for **NBI 3** dimer.

**Data analysis**

To illustrate the back-folding of the side chains, the time-averaged density of all carbon atoms in the side chains was determined in a body-fitted coordinate system centered around the naphthalene core (illustrated by the red circles in the density plots). To compute the stacking distance, first, the distance vector between the geometric centers of the two naphthalene cores was determined. In a stacked configuration, the two naphthalene cores are typically arranged parallel to each other such that this vector is almost, but not exactly, parallel to the normal vector with respect to either of the naphthalene planes. The trajectory of stacking distance shows the projection of the distance vector onto the normal vector to the first naphthalene plane. To compute the tilt angle in between naphthalene cores, first, the connection vector between the two nitrogen atoms of each naphthalene core was determined. Taking the scalar product between the two connecting vectors leads to the tilt angle.

**PM7 calculations:**

Structural optimization of **NBI 4** and **NBI 5** was carried out using semi-empirical PM7 Hamiltonian[363] in MOPAC2016.[364] Solvent effects have been included implicitly using the COSMO model for water.[365]

**Partition co-efficient (log *P*) calculations:**

Partition co-efficient was calculated using ChemAxon[356] software based on the method by Vishwanadhan *et al*.[354] The electrolyte concentration was chosen 0 mol/dm$^3$.

## 9.2 Synthesis

The following compounds were synthesized according to literature reported procedures: **55a**,[231] **55b**,[231] **55c**,[231] **57**,[232] **58a**,[230] **58c**,[68] **59a**,[230] **59c**,[68] **61**,[233] **65**,[234] **66**,[234] **67**,[234] **68**,[233] **PBI 1**,[230] **PBI 3**,[68] and **PBI 5**.[234] Compounds **54**,[366] **63**,[367] and **70**[368] are reported before, but were synthesized using different synthetic routes.

**1-phenyl-2,5,8,11,14-pentaoxahexadecane (53)**

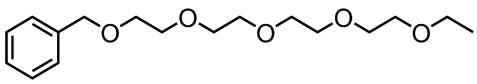

Diethyleneglycol mono benzyl ether (15.1 g, 76.94 mmol) was dissolved in anhydrous THF (100 mL) in a round bottom flask and cooled to 0°C. Sodium hydride (6.0 g, 55-65% in mineral oil) was added slowly into the above solution in an ice bath and stirred until no hydrogen gas was evolved. To the above solution at 0°C, diethylene glycol monoethyl ether *p*-toluene-sulfonate (28.84 g, 100.03mmol) dissolved in anhydrous THF (75 mL) was added dropwise using a dropping funnel. The reaction mixture was stirred at 0 °C for one hour and subsequently at room temperature overnight. The excess sodium hydride was quenched by the addition of MeOH at 0 °C. The solvent was evaporated under vacuum, and the residue was dissolved in DCM, filtered off the insoluble solid, and the filtrate was concentrated under reduced pressure. The resulting residue was purified by silica gel column chromatography (ethyl acetate (50%)/*n*-hexane) to obtain the product (**53**) as a colorless oil (16.8 g, 53.7 mmol, 70%).

$^1$H NMR (400 MHz, $CDCl_3$): $\delta$ = 7.35-7.24 (m, 5H), 4.56 (s, 2H), 3.68-3.61 (m, 14H), 3.58-3.55 (m, 2H), 3.50 (q, $^3J$ = 7.0 Hz, 2H), 1.19 (t, $^3J$ = 7.0 Hz, 3H) ppm. $^{13}$C NMR (100 MHz, $CDCl_3$): $\delta$ = 138.4, 128.4, 127.8, 127.6, 73.3, 70.72, 70.67, 69.8, 69.4, 66.6, 15.2 ppm. HRMS (ESI, positive, ACN/$CHCl_3$): *m*/*z* calcd for $C_{17}H_{28}O_5Na$: 335.1834; found: 335.1828 $[M+Na]^+$.

**3,6,9,12-tetraoxatetradecan-1-ol (54)**

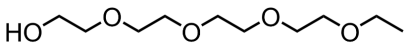

1-phenyl-2,5,8,11,14-pentaoxahexadecane (**53**) (15.1 g, 48.3 mmol) was dissolved in ethyl acetate (100 mL) and charged into a round bottom flask. Argon was purged through the solution for five minutes, and then 1 g 10% Pd/C was added. The reaction mixture was again purged with argon and was allowed to stir at room temperature overnight under $H_2$

atmosphere (1 atm). It was then filtered over celite and washed with ethyl acetate. The solution was concentrated by rotatory evaporation under reduced pressure, and the colorless oil obtained was used without further purification. (10.7 g, 48.3 mmol, quant.).

$^{1}$H NMR (400 MHz, $CDCl_3$): $\delta$ = 3.64-3.48 (m, 16H), 3.43 (q, $^{3}J$ = 7.0 Hz, 2H), 3.06 (t, $^{3}J$ = 5.9 Hz, 1H), 1.11 (t, $^{3}J$ = 7.0 Hz, 3H) ppm. $^{13}$C NMR (100 MHz, $CDCl_3$): $\delta$ = 72.5, 70.53, 70.50, 70.4, 70.2, 69.7, 66.5, 61.5, 15.0 ppm. HRMS (ESI, positive, ACN/$CHCl_3$): *m*/*z* calcd for $C_{10}H_{22}O_5Na$: 245.1364; found: 245.1362 $[M+Na]^+$.

**3,6,9,12,15-pentaoxaoctadec-17-yne (55d)**

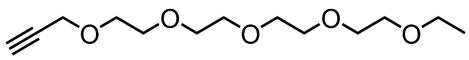

3,6,9,12-tetraoxatetradecan-1-ol (**54**) (11.1 g, 50.03 mmol) was dissolved in anhydrous THF (100 mL) in a round bottom flask and cooled to 0°C. Sodium hydride (3.0 g, 55-65% in mineral oil) was added slowly into the above solution in an ice bath and stirred until no hydrogen gas was evolved. To the above solution at 0°C, propargyl bromide (8.4 mL, 75.04 mmol, 80% in toluene) was added dropwise using a dropping funnel. The reaction mixture was stirred at 0 ºC for one hour and then at room temperature overnight. The excess sodium hydride was quenched by the addition of MeOH at 0 °C. The solvent was evaporated under vacuum, and the residue was dissolved in DCM, filtered off the insoluble solids, and the filtrate was concentrated under reduced pressure. The resulting residue was purified by silica gel column chromatography (ethyl acetate (70%)/*n*-hexane) to obtain the product (**55d**) as a pale yellow oil (12.4 g, 47.6 mmol, 95%).

$^{1}$H NMR (400 MHz, $CDCl_3$): $\delta$ = 4.16 (d, $^{4}J$ = 2.4 Hz, 2H), 3.68-3.59 (m, 14H), 3.56-3.53 (m, 2H), 3.48 (q, $^{3}J$ = 7.0 Hz, 2H), 2.40 (t, $^{4}J$ = 2.4 Hz, 1H), 1.16 (t, $^{3}J$ = 7.0 Hz, 3H) ppm. $^{13}$C NMR (100 MHz, $CDCl_3$): $\delta$ = 79.6, 74.5, 70.68, 70.64, 70.61, 70.5, 70.4, 69.8, 69.1, 66.6, 58.4, 15.2 ppm. HRMS (ESI, positive, ACN/$CHCl_3$): *m*/*z* calcd for $C_{13}H_{24}O_5Na$: 283.1521; found: 283.1515 $[M+Na]^+$.

**14,14',14''-(5-Nitrobenzene-1,2,3-triyl) tris(2,5,8,11-tetraoxatetradec-13-yne) (58b)**

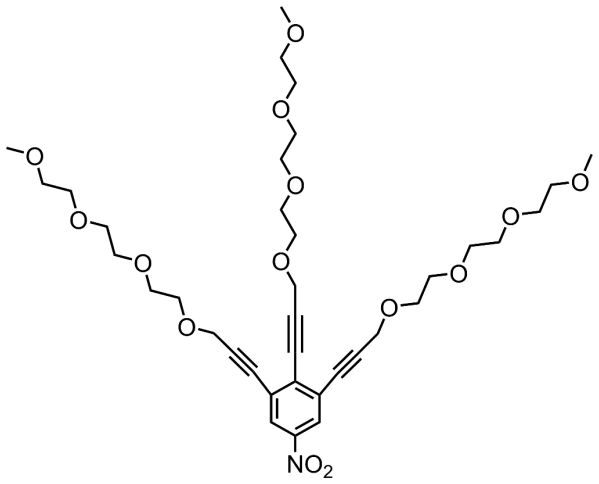

2-Bromo-1,3-diiodo-5-nitrobenzene (**57**, 7.0 g, 15.4 mmol) was dissolved in triethylamine (100 mL) and flushed with nitrogen for 10 minutes. Bis(triphenylphosphine)-palladium(II)-dichloride (1.05 g, 1.5 mmol) and copper(I) iodide (285 mg, 1.5 mmol) were added into the solution and flushed with nitrogen for another half hour. Compound **55b** (8.0 g, 39.5 mmol) was then slowly added into the reaction mixture and stirred for 8 hours at room temperature. After the completion of the reaction (monitored by TLC), another aliquot of bis(triphenylphosphine)-palladium(II)-dichloride (1.05 g, 1.5 mmol) and copper(I) iodide (285 mg, 1.5 mmol) were added into the reaction mixture and flushed with nitrogen for half-hour, followed by the slow addition of **55b** (4.5 g, 22.2 mmol). The reaction mixture was heated to 75 °C for one hour, and cooled down to room temperature and concentrated by rotary evaporation under reduced pressure. Subsequently, it was filtered through a silica plug by washing with ethyl acetate and methanol. The solvent was removed by rotary evaporation, and the crude product was purified by column chromatography, first with methanol (3%)/ethyl acetate and then with methanol (1.5%)/ dichloromethane to yield **58b** as a dark viscous oil (3.7 g, 5.11 mmol, 33%).

$^{1}$H NMR (400 MHz, $CDCl_3$): $\delta$ = 8.18 (s, 2H), 4.51 (s, 2H), 4.45 (s, 4H), 3.80-3.73 (m, 6H), 3.69-3.60 (m, 28H), 3.53-3.50 (m, 6H), 3.348 (s, 6H), 3.346 (s, 3H) ppm. $^{13}$C NMR (100 MHz, $CDCl_3$): $\delta$ = 146.3, 133.1, 127.1, 126.2, 98.8, 92.3, 82.8, 82.7, 71.9, 70.7, 70.65, 70.63, 70.60, 70.49, 70.46, 69.4, 69.3, 59.13, 59.11, 59.0 ppm. HRMS (ESI, positive, ACN/$CHCl_3$): *m*/*z* calcd for $C_{36}H_{53}NO_{14}Na$: 746.3363; found: 746.3382 $[M+Na]^+$.

**18,18',18''-(5-nitrobenzene-1,2,3-triyl)tris(3,6,9,12,15-pentaoxaoctadec-17-yne) (58d)**

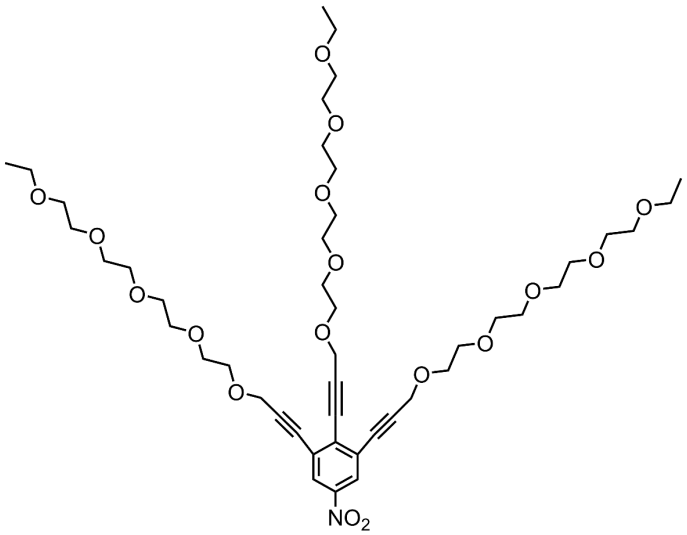

2-Bromo-1,3-diiodo-5-nitrobenzene (**57**, 4.0 g, 8.81 mmol) was dissolved in triethylamine (150 mL) and flushed with nitrogen for 10 minutes. Bis(triphenylphosphine)-palladium(II)-dichloride (618 mg, 0.88 mmol) and copper(I) iodide (167 mg, 0.88 mmol) were added into the solution and flushed with nitrogen for another half hour. Compound **55d** (5.7 g, 22.0 mmol) was then slowly added into the reaction mixture and stirred for 8 hours at room temperature. After the completion of the reaction (monitored by TLC), another aliquot of bis(triphenylphosphine)-palladium(II)-dichloride (618 mg, 0.88 mmol) and copper(I) iodide (167 mg, 0.88 mmol) were added into the reaction mixture and flushed with nitrogen for half-hour, followed by the slow addition of **55d** (3.4 g, 13.2 mmol). The reaction mixture was heated to 75 °C for one hour, and cooled down to room temperature and concentrated by rotary evaporation under reduced pressure. Subsequently, it was filtered through a silica plug by washing with ethyl acetate and methanol. The solvent was removed by rotary evaporation, and the crude product was purified by silica gel column chromatography, first with methanol (6%)/ethyl acetate and then with methanol (1.75%)/ dichloromethane to yield **58d** as a dark viscous oil (2.7 g, 3.0 mmol, 34%).

$^{1}$H NMR (400 MHz, $CDCl_3$): $\delta$ = 8.17 (s, 2H), 4.49 (s, 2H), 4.44 (s, 4H), 3.78-3.72 (m, 6H), 3.69-3.58 (m, 36H), 3.55-3.52 (m, 6H), 3.47 (q, $^{3}J$ = 7.0 Hz, 6H), 1.15 (t, $^{3}J$ = 7.0 Hz, 9H) ppm. $^{13}$C NMR (100 MHz, $CDCl_3$): $\delta$ = 146.2, 133.1, 127.1, 126.1, 98.8, 92.2, 82.74, 82.72, 70.67, 70.60, 70.58, 70.57, 70.54, 70.43, 70.41, 69.8, 69.4, 69.2, 66.6, 59.0, 58.9, 15.1 ppm. HRMS (ESI, positive, ACN/$CHCl_3$): *m*/*z* calcd for $C_{45}H_{71}NO_{17}Na$: 920.4619; found: 920.4621 $[M+Na]^+$.

**3,4,5-tri(2,5,8,11-tetraoxatetradecan-14-yl)aniline** (**59b**)

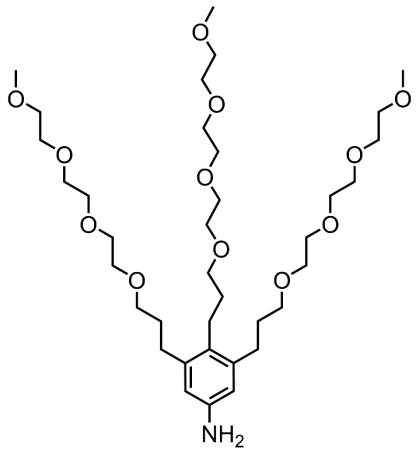

Compound **58b** (1.10 g, 1.52 mmol) was dissolved in ethyl acetate (10 mL) and was transferred into an autoclave. Argon was purged through the solution for five minutes, and 1 g 10% Pd/C was added to the above solution. The reaction mixture was again purged with argon and then by hydrogen. The mixture was allowed to stir at room temperature for four days under $H_2$ atmosphere (10 bar). The reaction mixture was filtered over celite and washed with ethyl acetate and a few drops of methanol. The solution was concentrated by rotatory evaporation, and the residue was purified by flash column chromatography (methanol (1%)/ ethyl acetate) to afford **59b** as a yellow oil (459 mg, 0.65 mmol, 42%).

$^1$H NMR (400 MHz, $CDCl_3$): $\delta$ = 6.40 (s, 2H), 6.68-3.46 (m, 42H), 3.37 (s, 9H), 2.59-2.51 (m, 6H), 1.86-1.79 (m, 4H), 1.73-1.66 (m, 2H) ppm. $^{13}$C NMR (100 MHz, $CDCl_3$): $\delta$ =144.0, 141.1, 128.0, 114.3, 71.9, 71.1, 70.7, 70.6, 70.5, 70.4, 70.1, 70.0, 59.0, 31.3, 31.0, 29.2, 24.2 ppm. HRMS (ESI, positive, MeOH/$CHCl_3$): *m*/*z* calcd for $C_{36}H_{68}NO_{12}$: 706.4742; found: 706.4755 $[M+H]^+$.

**3,4,5-tri(3,6,9,12,15-pentaoxaoctadecan-18-yl)aniline (59d)**

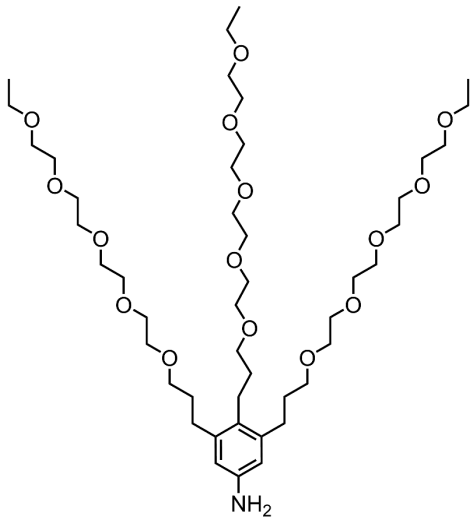

Compound **58d** (1.74 g, 1.93 mmol) was dissolved in ethyl acetate (10 mL) and was transferred into an autoclave. Argon was purged through the solution for five minutes, and 1 g 10% Pd/C was added to the above solution. The reaction mixture was again purged with argon and then by hydrogen. The mixture was allowed to stir at room temperature for four days under $H_2$ atmosphere (10 bar). The reaction mixture was filtered over celite and washed with ethyl acetate and methanol. The solution was concentrated by rotatory evaporation, and the residue was purified by flash column chromatography (methanol (2.5%)/ $NEt_3$ (0.1%)/ DCM) to afford **59d** as a yellow oil (954 mg, 1.08 mmol, 56%).

$^1$H NMR (400 MHz, $CDCl_3$): $\delta$ = 6.42 (s, 2H), 3.65-3.60 (m, 36H), 3.58-3.54 (m, 12H), 3.52-3.43 (m, 12H), 2.58-2.50 (m, 6H), 1.84-1.77 (m, 4H), 1.71-1.64 (m, 2H), 1.17,1.18 (overlapped triplets, $^3J$ = 7.0 Hz, $^3J$ = 7.0 Hz, 9H) ppm. $^{13}$C NMR (100 MHz, $CDCl_3$): $\delta$ =143.2, 141.1, 128.6, 114.8, 71.2, 70.68, 70.65, 70.64, 70.62, 70.21, 70.14, 69.8, 66.6, 31.3, 31.0, 29.3, 24.3, 15.2 ppm. HRMS (ESI, positive, ACN/$CHCl_3$): *m*/*z* calcd for $C_{45}H_{85}NO_{15}Na$: 902.5816; found: 902.5820 $[M+Na]^+$.

**3,4,5-Tris((2,5,8,11-tetraoxatridecan-13-yl)oxy)benzamide (62)**

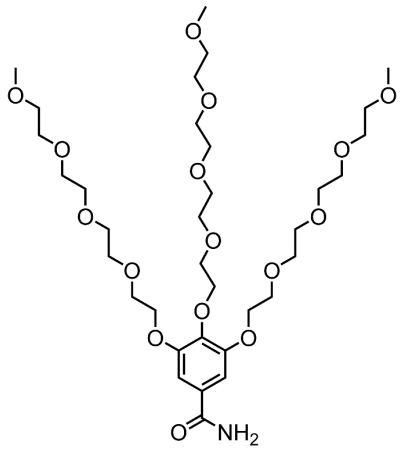

Compound **61** (2g, 2.65 mmol), aqueous $NH_3$ solution (25%,150 mL), and methanol (160 mL) were charged into a round bottom flask fitted with a gas bubbler. The reaction mixture was stirred at 45°C for five days. After the completion of the reaction, methanol was evaporated under reduced pressure, and the product was extracted with DCM and washed with water and brine solution. The organic phase was dried with anhydrous sodium sulfate. The residue obtained after evaporation of the solvent was purified by silica gel column chromatography (methanol (4%)/chloroform) to obtain compound **62** as a pale yellow viscous oil (1.01g, 1.37 mmol, 51%).

$^1$H NMR (400 MHz, $CDCl_3$): $\delta$ = 7.25 (s, 2H), 4.25-4.20 (m, 6H), 3.81-3.77 (m, 6H), 3.70-3.62 (m, 30H), 3.56-3.53 (m,6H), 3.38 (s, 6H), 3.37 (s, 3H) ppm. $^{13}$C NMR (100 MHz, $CDCl_3$): $\delta$ = 168.8, 152.2, 142.0, 128.6, 108.6, 72.4, 71.98, 71.91, 70.7, 70.68, 70.64, 70.62, 70.57, 70.56, 70.54, 70.52, 69.8, 69.1, 59.09, 59.05 ppm. HRMS (ESI, positive, ACN/$CHCl_3$): *m*/*z* calcd for $C_{34}H_{61}NO_{16}Na$: 762.3888; found: 762.3888 $[M+Na]^+$.

**3,4,5-Tris((2,5,8,11-tetraoxatridecan-13-yl)oxy)aniline (63)**

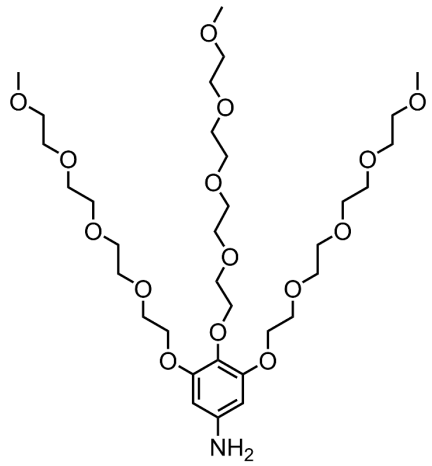

Compound **62** (250 mg, 0.338 mmol) was stirred with aqueous KOH solution (2M, 12mL) in a round bottom flask at 0°C. Bromine in water solution (35µL in 5 mL $H_2O$, 0.676 mmol) was added slowly to the suspension using a dropping funnel. After the addition was completed, the reaction mixture was stirred for 12 h at 90°C. The reaction was cooled to room temperature, and the product was extracted using DCM and washed with water and brine. The organic phase was dried with anhydrous sodium sulfate, and the solvent was evaporated under vacuum. The residue was finally purified by silica gel column chromatography (methanol (4%)/chloroform) to obtain the compound **63** as a yellow viscous oil (57 mg, 0.080 mmol, 24%).

$^1$H NMR (400 MHz, $CDCl_3$): $\delta$ = 5.95 (s, 2H), 4.07 (t, $^3J$ = 5.1 Hz, 4H), 4.00 (t, $^3J$ = 5.2 Hz, 2H), 3.78 (t, $^3J$ = 5.1 Hz, 4H), 3.72 (t, $^3J$ = 5.2 Hz, 2H), 3.70-3.67 (m, 6H), 3.65-3.60 (m, 24H), 3.53-3.50 (m, 6H), 3.35 (s, 9H) ppm. $^{13}$C NMR (100 MHz, $CDCl_3$): $\delta$ = 153.2, 142.4, 131.2, 95.7, 72.4, 71.9, 70.8, 70.7, 70.64, 70.63, 70.61, 70.55, 70.52, 70.48, 69.7, 68.7, 59.0 ppm. HRMS (ESI, positive, MeOH): *m*/*z* calcd for $C_{33}H_{61}NO_{15}Na$: 734.3938; found: 734.3946 $[M+Na]^+$.

**2-(3,4,5-Tris((2,5,8,11-tetraoxatridecan-13-yl)oxy)benzyl)isoindoline-1,3-dione (69)**

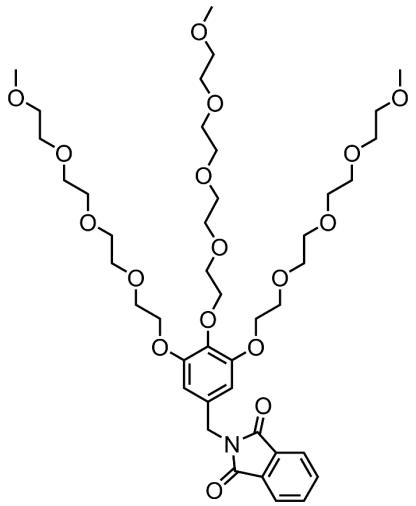

Phthalimide (456 mg, 3.1 mmol), triphenylphosphine (820 mg, 3.1 mmol), and **68** (1.47 g, 2.0 mmol) were suspended in 50 ml dry THF under nitrogen and cooled to 0 °C. To it, a solution of DEAD (40% in toluene, 1.4 mL, 3.0 mmol) in 5 mL dry THF was added dropwise and was stirred overnight. The solvent was removed under vacuum, and the resulting residue was purified by silica gel column chromatography (methanol (3%)/$CHCl_3$) to obtain the product as a colorless oil (1.21g, 1.41 mmol, 70%).

$^1$H NMR (400 MHz, $CDCl_3$): 7.81 (dd, $^3J$ = 5.5 Hz, $^4J$ = 2.9 Hz, 2H), 7.68 (dd, $^3J$ = 5.5 Hz, $^4J$ = 3.0 Hz, 2H), 6.65 (s, 2H), 4.69 (s, 2H), 4.10 (t, $^3J$ = 5.0 Hz, 4H), 4.05 (t, $^3J$ = 5.1 Hz, 2H), 3.79 (t, $^3J$ = 5.0 Hz, 4H) 3.72 (t, $^3J$ = 5.2 Hz, 2H) 3.69-3.59 (m, 30H), 3.52-3.49 (m, 6H), 3.34 (s, 6H), 3.33 (s, 3H) ppm.$^{13}$C NMR (100 MHz, $CDCl_3$): 168.0, 152.6, 138.0, 134.0, 132.1, 131.8, 123.4, 108.3, 72.2, 71.9, 70.8, 70.69, 70.64, 70.60, 70.56, 70.51, 69.7, 68.8, 59.0, 41.7 ppm. HRMS (MALDI, positive, $CHCl_3$): *m*/*z* calcd for $C_{42}H_{65}NO_{17}Na$: 878.4150; found: 878.4142 $[M+Na]^+$.

**3,4,5-Tris((2,5,8,11-tetraoxatridecan-13-yl)oxy)benzyl amine (70)**

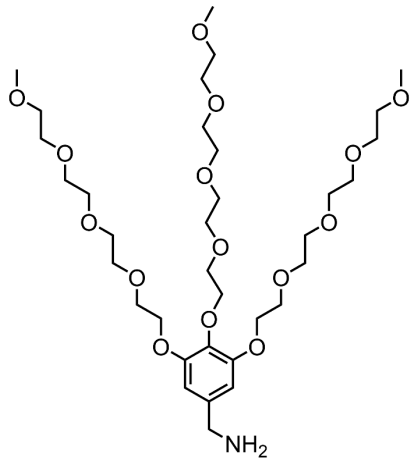

To a solution of **69** (1.06 g, 1.24 mmol) in ethanol, 80 % hydrazine monohydrate (0.96 mL, 15.8 mmol) was added and refluxed for 1.5 hrs. The reaction mixture was filtered and evaporated under vacuum. The resultant residue was dissolved in DCM, filtered off from the insoluble solids, and washed with water followed by brine and was dried with anhydrous sodium sulfate. This was evaporated into dryness and used for the next reaction without further purification (690 mg, 0.95 mmol, 77%).

$^{1}$H NMR (400 MHz, $CDCl_3$): $\delta$ = 6.59 (s, 2H), 4.05 (t, $^{3}J$ = 4.8 Hz, 4H), 4.00 (t, $^{3}J$ = 4.9 Hz, 2H), 3.81 (s, 2H), 3.76 (t, $^{3}J$ = 4.8 Hz, 4H), 3.68 (t, $^{3}J$ = 4.9 Hz, 2H), 3.65-3.63 (m, 6H), 3.60-3.54 (m, 24H), 3.47-3.44 (m, 6H), 3.28 (s, 6H), 3.28 (s, 3H) ppm. $^{13}$C NMR (100 MHz, $CDCl_3$): $\delta$ = 152.2, 136.7, 133.7, 107.2, 72.1, 71.82, 71.80, 71.79, 70.61, 70.54, 70.53, 70.47, 70.45, 70.42, 70.37, 70.34, 70.25, 69.6, 68.5, 58.9, 45.1 ppm. HRMS (ESI, positive, ACN/$CHCl_3$): *m*/*z* calcd for $C_{34}H_{63}NO_{15}Na$: 748.4089; found: 748.4081 $[M+Na]^+$.

**_N,N_'-[3,4,5-tri(2,5,8,11-tetraoxatetradecan-14-yl)phenyl] perylene-3,4:9,10-tetracarboxylic acid bisimide (PBI 2)**

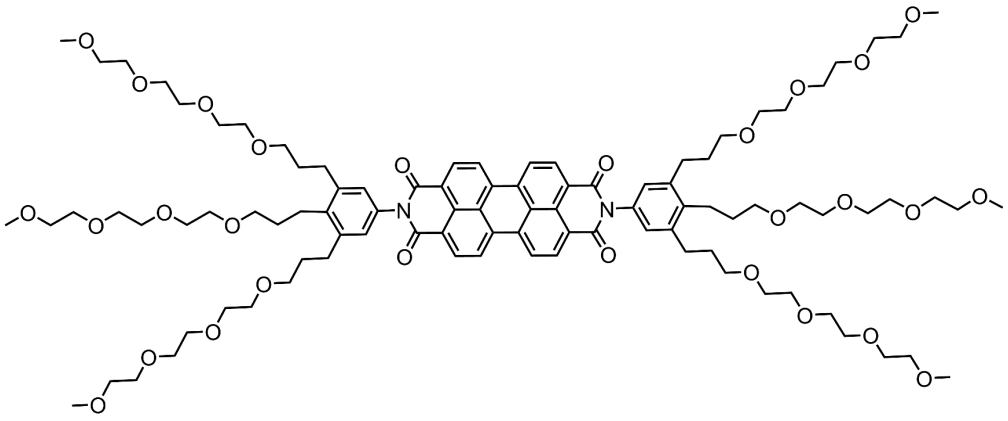

Perylene-3, 4: 9, 10-tetracarboxylic acid bisanhydride (93 mg, 0.23 mmol), **59b** (420 mg, 0. 59 mmol) and zinc acetate (173 mg, 0.94 mmol) were mixed with imidazole (2 g) and heated at 110 °C for 12 h under nitrogen. After cooling to room temperature, the reaction mixture was dissolved in dichloromethane and was extracted with 1M HCl and washed with brine. The organic fraction was purified by silica gel column chromatography (methanol (1%): chloroform) and by GPC (chloroform) to obtain **PBI 2** as a red waxy solid. (308 mg, 0.17 mmol, 73%).

$^{1}$H NMR (400 MHz, $CDCl_3$): 8.74 (d, $^{3}J$ = 7.9 Hz, 4H), 8.69 (d, $^{3}J$ = 8.1 Hz, 4H,), 7.00 (s, 4H), 3.72–3.50 (m, 84 H), 3.39 (s, 6H), 3.34 (s, 12H), 2.76 (t, $^{3}J$ = 7.6 Hz, 12H), 1.92 (quint, $^{3}J$ = 7.0 Hz, 8H), 1.87-1.80 (m, 4H) ppm. $^{13}$C NMR (100 MHz, $CDCl_3$): 163.7, 141.5, 138.9, 135.0, 132.6, 131.9, 129.9, 126.9, 126.8, 123.7, 123.4, 72.07, 72.02, 71.3, 70.79, 70.78, 70.72, 70.70, 70.67, 70.61, 70.3, 70.1, 59.19, 59.15, 30.9, 30.7, 29.3, 25.2 ppm. HRMS (ESI, positive, ACN/$CHCl_3$): *m*/*z* calcd for $C_{96}H_{138}N_2O_{28}Na_2^{2+}$: 906.4615; found: 906.4613 $[M+2Na]^{2+}$. UV-vis ($CHCl_3$): $\lambda_{max}$ = 528 nm ($\varepsilon$ = 93000 $M^{-1}$ $cm^{-1}$), 491 nm ($\varepsilon$ = 56000 $M^{-1}$ $cm^{-1}$). Fluorescence ($CHCl_3$): $\lambda_{max}$ = 536 nm, $\lambda_{ex}$ = 470 nm, $\Phi_{fl}$ = 89%.

***N,N'*-[3,4,5-tri(3,6,9,12,15-pentaoxaoctadecan-18-yl)phenyl] perylene-3,4:9,10-tetracarboxylic acid bisimide (PBI 4)**

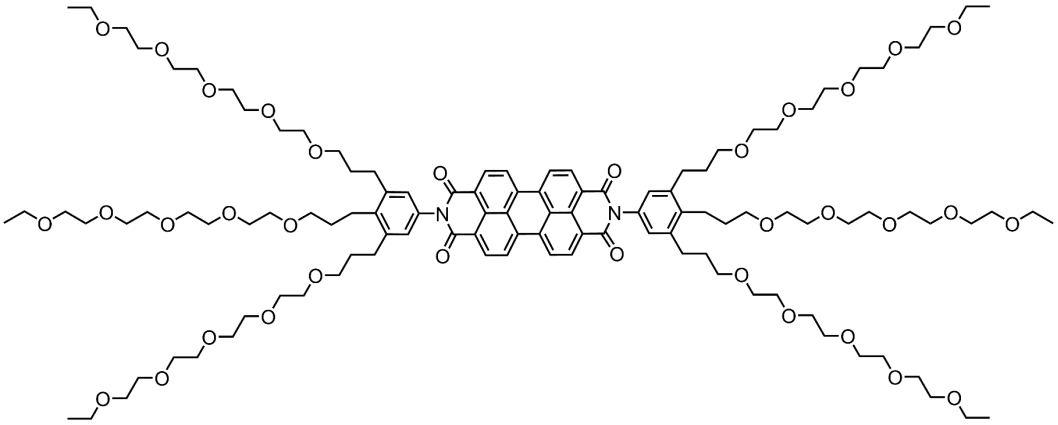

Perylene-3, 4: 9, 10-tetracarboxylic acid bisanhydride (75 mg, 0.19 mmol), **59d** (420 mg, 0. 47 mmol) and zinc acetate (140 mg, 0.76 mmol) were mixed with imidazole (2 g) and heated at 110 °C for 12 h under nitrogen. After cooling to room temperature, the reaction mixture was dissolved in dichloromethane and was extracted with 1M HCl and washed with brine. The organic fraction was purified by silica gel column chromatography (methanol (2.5%): chloroform) and by GPC (chloroform) to obtain **PBI 4** as a red waxy solid. (246 mg, 0.11 mmol, 60%).

$^{1}$H NMR (400 MHz, $CDCl_3$): 8.74 (d, $^{3}J$ = 8.0 Hz, 4H), 8.70 (d, $^{3}J$ = 8.2 Hz, 4H,), 7.00 (s, 4H), 3.70–3.47 (m, 120 H), 2.76 (t, $^{3}J$ = 7.5 Hz, 12H), 1.92 (quint, $^{3}J$ = 7.0 Hz, 8H), 1.83 (quint, $^{3}J$ = 7.1 Hz, 4H), 1.2,1.17 (overlapped triplets, $^{3}J$ = 7.0 Hz, $^{3}J$ = 7.0 Hz, 18H) ppm. $^{13}$C NMR (100 MHz, $CDCl_3$): 163.7, 141.5, 138.9, 135.0, 132.6, 131.9, 129.9, 126.9, 126.8, 123.7, 123.4, 71.3, 70.79, 70.75, 70.72, 70.70, 70.69, 70.67, 70.36, 70.18, 69.95, 69.92, 66.77, 66.74, 30.9, 30.7, 29.3, 25.2, 15.3, 15.2 ppm. HRMS (ESI, positive, ACN/$CHCl_3$): *m*/*z* calcd for $C_{114}H_{174}N_2O_{34}Na_2^{2+}$: 1080.5871; found: 1080.5883 $[M+2Na]^{2+}$. UV-vis ($CHCl_3$): $\lambda_{max}$ = 528 nm ($\varepsilon$ = 97000 $M^{-1}$ $cm^{-1}$), 492 nm ($\varepsilon$ = 58000 $M^{-1}$ $cm^{-1}$). Fluorescence ($CHCl_3$): $\lambda_{max}$ = 537 nm, $\lambda_{ex}$ = 470 nm, $\Phi_{fl}$ = 88%.

**_N,N'_-[3,4,5-tris((2,5,8,11-tetraoxatridecan-13-yl)oxy)phenyl] perylene-3,4:9,10-tetracarboxylic acid bisimide (PBI 6)**

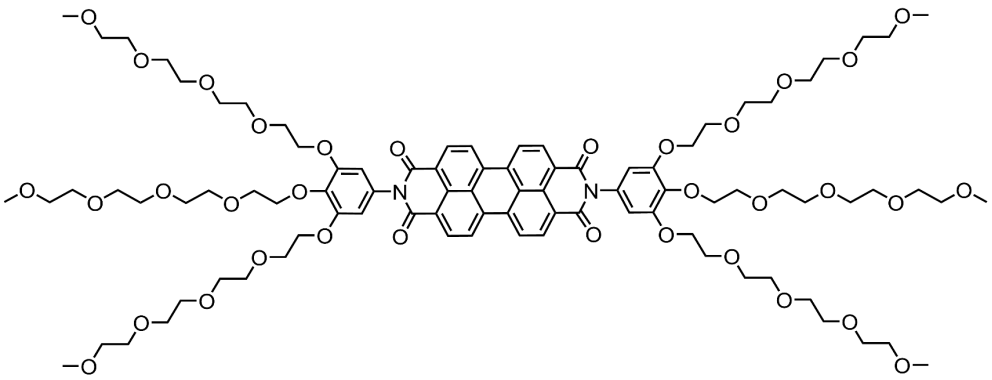

Perylene-3, 4: 9, 10-tetracarboxylic acid bisanhydride (13.3 mg, 0.03 mmol), **63** (57 mg, 0. 08 mmol) and zinc acetate (25 mg, 0.13 mmol) were mixed with imidazole (1 g) and heated at 110 °C for 12 h under nitrogen. After cooling to room temperature, the reaction mixture was dissolved in dichloromethane and was extracted with 1M HCl and washed with brine. The organic fraction was dried with anhydrous sodium sulfate and purified by column chromatography (methanol (4%): chloroform), followed by preparative TLC (methanol (5%): chloroform) and finally by GPC (chloroform) to obtain **PBI 6** as a red waxy solid. (26 mg, 0.01 mmol, 43%).

$^{1}$H NMR (400 MHz, $CDCl_3$): $\delta$ = 8.71 (d, 4H, $^{3}J$ = 7.9 Hz), 8.61 (d, 4H, $^{3}J$ = 8.1 Hz), 6.61 (s, 4H), 4.24 (t, $^{3}J$ = 5.1 Hz, 4H), 4.15 (t, $^{3}J$ = 4.9 Hz, 8H), 3.86-3.83 (m, 12H), 3.77–3.74 (m, 4 H), 3.72–3.61 (m, 56 H), 3.58–3.55 (m, 4 H), 3.54–3.51 (m, 8 H) 3.39 (s, 6H), 3.35 (s, 12H) ppm. $^{13}$C NMR (100 MHz, $CDCl_3$): 163.0, 153.1, 138.3, 134.0, 131.2, 130.1, 128.8, 125.8, 123.2, 123.1, 108.0, 72.5, 72.05, 72.0, 70.8, 70.79, 70.73, 70.72, 70.70, 70.65, 70.63, 70.57, 69.6, 68.9, 59.17, 59.12 ppm. HRMS (ESI, positive, ACN/$CHCl_3$): *m*/*z* calcd for $C_{90}H_{128}N_2O_{34}^{2+}$: 890.4174; found: 890.4177 $[M+2H]^{2+}$. UV-vis ($CHCl_3$): $\lambda_{max}$ = 528 nm ($\varepsilon$ = 92000 $M^{-1}$ $cm^{-1}$), 492 nm ($\varepsilon$ = 55000 $M^{-1}$ $cm^{-1}$). Fluorescence ($CHCl_3$): $\lambda_{max}$ = 537 nm, $\lambda_{ex}$ = 470 nm, $\Phi_{fl}$ = 3%.

***N,N'*-[3,4,5-tris((2,5,8,11-tetraoxatridecan-13-yl)oxy)benzyl] perylene-3,4:9,10-tetracarboxylic acid bisimide (PBI 7)**

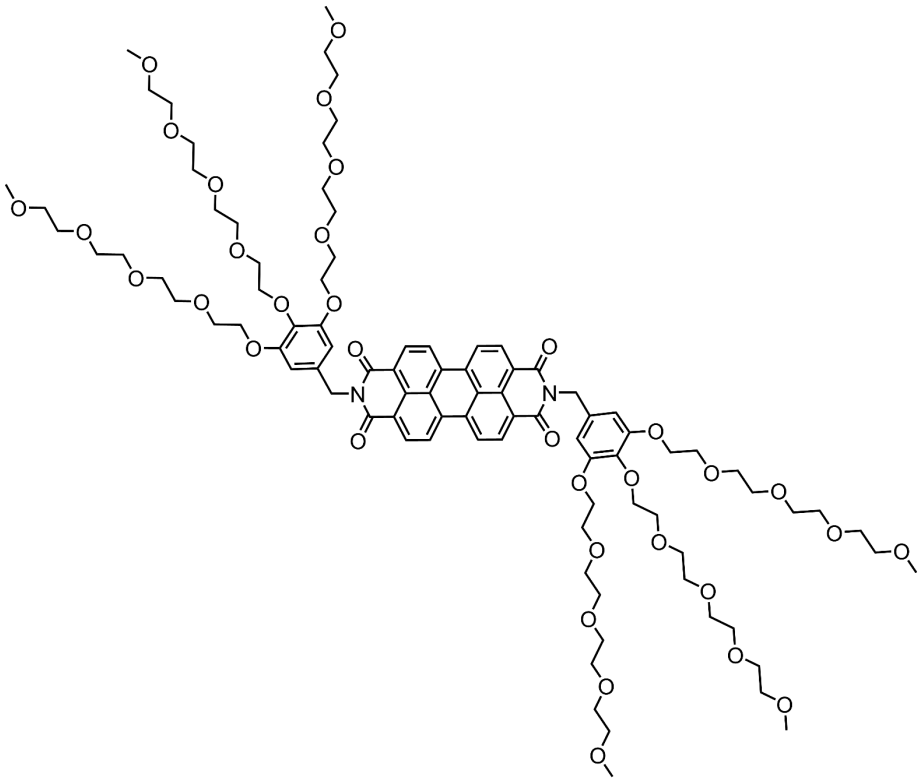

Perylene-3, 4: 9, 10-tetracarboxylic acid bisanhydride (64 mg, 0.16 mmol), **70** (300 mg, 0. 41 mmol) and zinc acetate (119 mg, 0.65 mmol) were mixed with imidazole (2 g) and heated at 110 °C for 12 h under nitrogen. After cooling to room temperature, the reaction mixture was dissolved in dichloromethane and was extracted with 1M HCl and washed with brine. The organic fraction was purified by column chromatography (methanol (6%): chloroform) and by GPC (chloroform) to obtain **PBI 7** as a red waxy solid. (120 mg, 0.06 mmol, 40%).

$^{1}$H NMR (400 MHz, $CDCl_3$): 8.66 (d, 4H, $^{3}J$ = 8.0 Hz), 8.59 (d, 4H, $^{3}J$ = 8.1 Hz), 6.84 (s, 4H), 5.28 (s, 4H), 4.15 (t, $^{3}J$ = 5.1 Hz, 8H), 4.08 (t, $^{3}J$ = 5.2 Hz, 4H), 3.82 (t, $^{3}J$ = 5.0 Hz, 8H), 3.75–3.60 (m, 64 H), 3.54–3.50 (m, 12 H), 3.35 (s, 12H), 3.35 (s, 6H) ppm. $^{13}$C NMR (100 MHz, $CDCl_3$): 163.4, 152.6, 138.0, 134.8, 132.5, 131.8, 129.5, 126.5, 123.3, 109.1, 72.3, 72.0, 70.9, 70.77, 70.70, 70.67, 70.63, 70.58, 69.8, 68.9, 59.1, 43.8 ppm. HRMS (ESI, positive, MeOH): *m*/*z* calcd for $C_{92}H_{130}N_2O_{34}Na_2^{2+}$: 926.4150; found: 926.4164 $[M+2Na]^{2+}$. UV-vis ($CHCl_3$): $\lambda_{max}$ = 529 nm ($\varepsilon$ = 88000 $M^{-1}$ $cm^{-1}$), 492 nm ($\varepsilon$ = 52000 $M^{-1}$ $cm^{-1}$). Fluorescence ($CHCl_3$): $\lambda_{max}$ = 537 nm, $\lambda_{ex}$ = 470 nm, $\Phi_{fl}$ = 9%.

**_N,N'_-[3,4,5-tris(3-(2-(2-methoxyethoxy)ethoxy)propyl)phenyl] naphthalene-1,4,5,8-tetracarboxylic acid bisimide (NBI 1)**

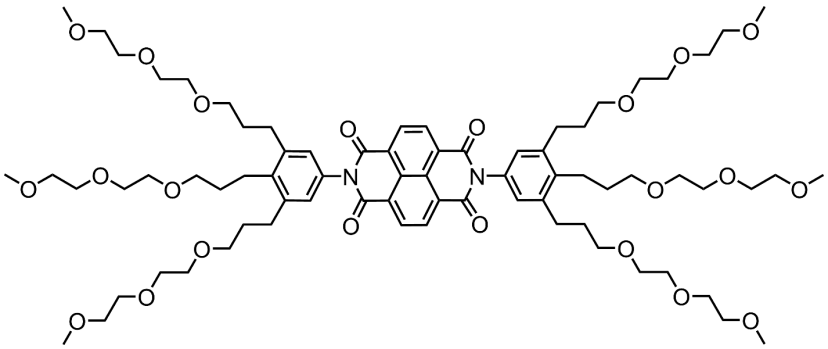

1,4,5,8-Naphthalenetetracarboxylic dianhydride (31 mg, 0.11 mmol), 3,4,5-tris(3-(2-(2-methoxyethoxy)ethoxy)propyl)aniline (**59a**, 169 mg, 0.29 mmol) and acetic acid (5 mL) were charged into a pressure tube and heated at 110 °C for 12 h under nitrogen. After cooling to room temperature, the residue was extracted with water and DCM. The organic phase was washed with saturated sodium bicarbonate solution and brine and dried with anhydrous sodium sulfate. The solvent was evaporated under vacuum, and the residue was purified first by flash column chromatography (methanol (0.5%)/chloroform) and then by GPC (chloroform) to obtain **NBI 1** as a greenish-yellow waxy solid (55 mg, 0.04 mmol, 35%).

$^{1}$H NMR (400 MHz, $CDCl_3$): $\delta$ = 8.82 (s, 4H), 7.00 (s, 4H), 3.71-3.50 (m, 60 H), 3.40 (s, 6H), 3.34 (s, 12H), 2.77 (t, $^{3}J$ = 7.6 Hz, 12H), 1.92 (quint, 8H, $^{3}J$ = 7.0 Hz), 1.87-1.80 (m, 4H) ppm. $^{13}$C NMR (100 MHz, $CDCl_3$): $\delta$ = 163.2, 141.7, 139.3, 132.1, 131.4, 127.28, 127.22, 126.7, 72.1, 72.0, 71.3, 70.87, 70.79, 70.78, 70.68, 70.65, 70.4, 70.2, 59.2, 59.1, 30.8, 30.7, 29.3, 25.2 ppm. HRMS (ESI, positive, ACN/$CHCl_3$): *m*/*z* calcd for $C_{74}H_{110}N_2O_{22}Na$: 1401.7447; found: 1401.7437 $[M+Na]^+$. UV-vis ($CHCl_3$): $\lambda_{max}$ = 381 nm ($\varepsilon$ = 25800 $M^{-1}$ $cm^{-1}$), 361 nm ($\varepsilon$ = 24500 $M^{-1}$ $cm^{-1}$).

***N,N'*-[3,4,5-tri(2,5,8,11-tetraoxatetradecan-14-yl)phenyl] naphthalene-1,4,5,8-tetracarboxylic acid bisimide (NBI 2)**

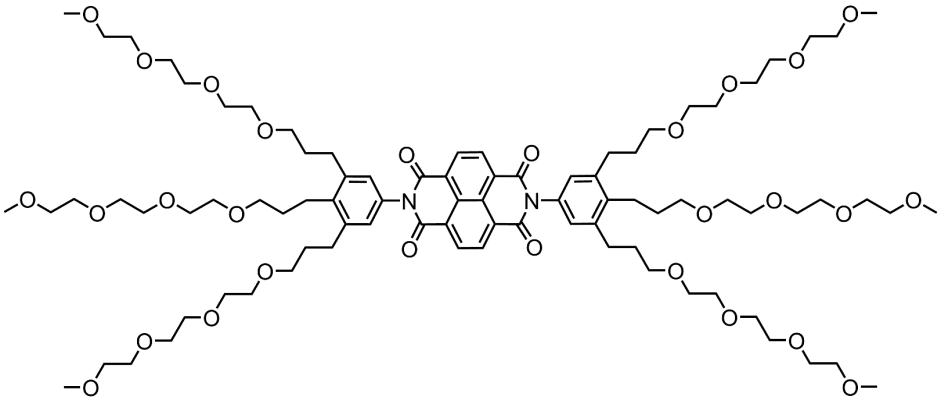

**NBI 2** was synthesized according to the procedure used for **NBI 1** by employing 29 mg (0.108 mmol) of 1,4,5,8-Naphthalenetetracarboxylic dianhydride and 211 mg of aniline derivative **59b** (0.29 mmol). The crude product was purified first by flash column chromatography (methanol (1%)/chloroform) and then by GPC (chloroform) to obtain **NBI 2** as a yellow viscous oil (59 mg, 0.03 mmol, 33%).

$^{1}$H NMR (400 MHz, $CDCl_3$): $\delta$ = 8.80 (s, 4H), 6.97 (s, 4H), 3.70–3.48 (m, 84 H), 3.36 (s, 6H), 3.33 (s, 12H), 2.74 (t, $^{3}J$ = 7.6 Hz, 12H), 1.90 (quint, 8H, $^{3}J$ = 7.0 Hz), 1.85-1.77 (m, 4H) ppm. $^{13}$C NMR (100 MHz, $CDCl_3$): $\delta$ = 163.0, 141.6, 139.2, 132.0, 131.3, 127.17, 127.11, 126.6, 71.98, 71.93, 71.1, 70.7, 70.69, 70.63, 70.61, 70.58, 70.53, 70.2, 70.1, 59.0, 30.7, 30.6, 29.2, 25.1 ppm. HRMS (ESI, positive, ACN/$CHCl_3$): *m*/*z* calcd for $C_{86}H_{134}N_2O_{28}Na$: 1665.9020; found: 1665.9020 $[M+Na]^+$. UV-vis ($CHCl_3$): $\lambda_{max}$ = 381 nm ($\varepsilon$ = 26400 $M^{-1}$ $cm^{-1}$), 361 nm ($\varepsilon$ = 25100 $M^{-1}$ $cm^{-1}$).

***N,N'*-[3,4,5-tri(2,5,8,11,14-pentaoxaheptadecan-17-yl)phenyl] naphthalene-1,4,5,8-tetracarboxylic acid bisimide (NBI 3)**

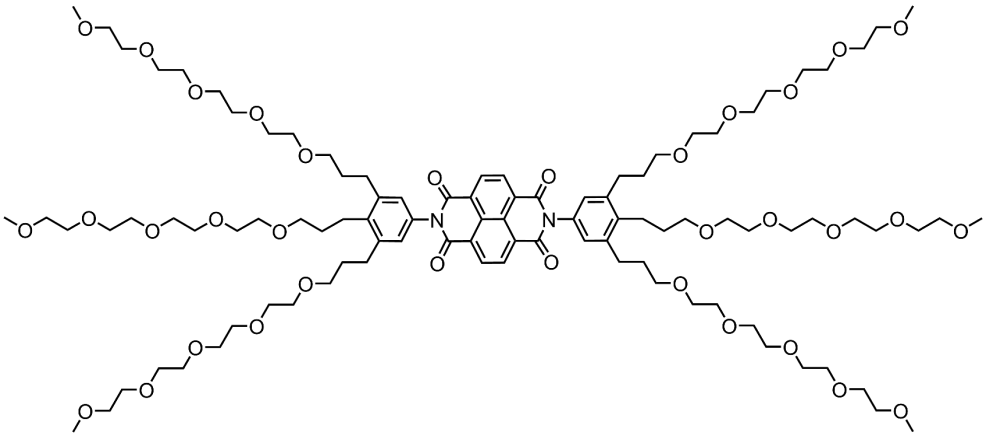

**NBI 3** was synthesized according to the procedure used for **NBI 1** by employing 27 mg (0.100 mmol) of 1,4,5,8-Naphthalenetetracarboxylic dianhydride and 211 mg of aniline derivative **59c** (0.25 mmol). The crude product was purified first by flash column chromatography (methanol (1.5%)/chloroform) and then by GPC (chloroform) to obtain **NBI 3** as a yellow viscous oil (61 mg, 0.03 mmol, 32%).

$^{1}$H NMR (400 MHz, $CDCl_3$): $\delta$ = 8.81 (s, 4H), 6.99 (s, 4H), 3.69–3.51 (m, 108 H), 3.38 (s, 6H), 3.36 (s, 12H), 2.76 (t, $^{3}J$ = 7.6 Hz, 12H), 1.92 (quint, 8H, $^{3}J$ = 7.0 Hz), 1.85-1.80 (m, 4H) ppm. $^{13}$C NMR (100 MHz, $CDCl_3$): $\delta$ = 163.1, 141.7, 139.2, 132.1, 131.4, 127.2, 127.1, 126.7, 72.02, 72.00, 71.2, 70.75, 70.70, 70.66, 70.63, 70.5, 70.3, 70. 1, 59.15, 59.13, 30.8, 30.6, 29.2, 25.2 ppm. HRMS (ESI, positive, ACN/$CHCl_3$): *m*/*z* calcd for $C_{98}H_{158}N_2O_{34}Na$: 1930.0593; found: 1930.0593 $[M+Na]^+$. UV-vis ($CHCl_3$): $\lambda_{max}$ = 381 nm ($\varepsilon$ = 25900 $M^{-1}$ $cm^{-1}$), 361 nm ($\varepsilon$ = 24500 $M^{-1}$ $cm^{-1}$).

***N,N'*-[3,4,5-tris((2,5,8,11-tetraoxatridecan-13-yl)oxy)phenyl] naphthalene-1,4,5,8-tetracarboxylic acid bisimide (NBI 4)**

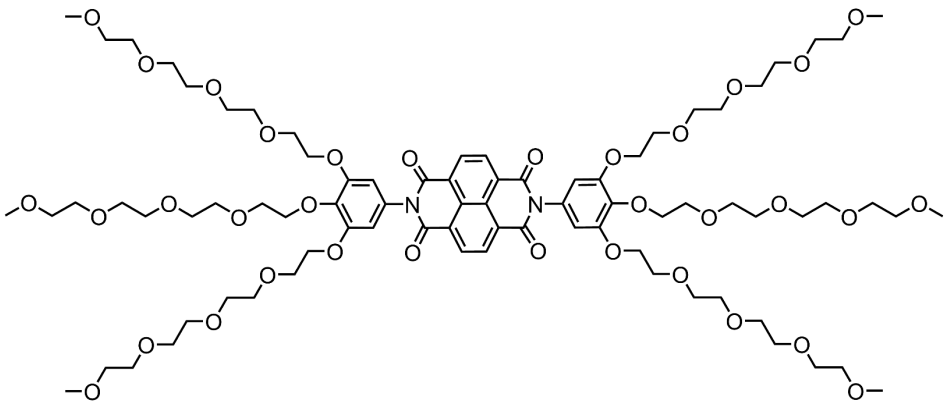

1,4,5,8-Naphthalenetetracarboxylic acid bisanhydride (45 mg, 0.16 mmol), 3,4,5-tris((2,5,8,11-tetraoxatridecan-13-yl)oxy) aniline (**63**) 300 mg, 0.42 mmol) and dry DMF (5 mL) were charged into a pressure tube and heated at 110 °C for 12 h under nitrogen. After cooling to room temperature, the solvent was evaporated under vacuum, and the residue was extracted with DCM and washed with water and brine. The organic phase was dried with anhydrous sodium sulfate, and then the solvent was evaporated under vacuum. The resultant residue was purified first by silica gel flash column chromatography (methanol (1.75%)/chloroform) and then by GPC (chloroform) to obtain **NBI 4** as an orange waxy solid (149 mg, 0.09 mmol, 53%).

$^{1}$H NMR (400 MHz, $CDCl_3$): $\delta$ = 8.82 (s, 4H), 6.56 (s, 4H), 4.23 (t, $^{3}J$ = 5.1 Hz, 4H), 4.15 (t, $^{3}J$ = 5.0 Hz, 8H), 3.85-3.82 (m, 12H), 3.75-3.60 (m, 60H), 3.56-3.50 (m, 12H), 3.37 (s, 6H), 3.35 (s, 12H) ppm. $^{13}$C NMR (100 MHz, $CDCl_3$): $\delta$ = 162.9, 153.3, 138.9, 131.5, 129.7, 127.2, 127.1, 108.2, 72.5, 72.05, 72.01, 70.9, 70.78, 70.75, 70.73, 70.70, 70.68, 70.66, 70.64, 70.60, 69.6, 69.0, 59.16, 59.14 ppm. HRMS (ESI, positive, ACN/$CHCl_3$): *m*/*z* calcd for $C_{80}H_{122}N_2O_{34}Na$: 1677.7776; found: 1677.7726 $[M+Na]^+$. UV-vis ($CHCl_3$): $\lambda_{max}$ = 379 nm ($\varepsilon$ = 26200 $M^{-1}$ $cm^{-1}$), 359 nm ($\varepsilon$ = 24000 $M^{-1}$ $cm^{-1}$).

**_N,N_'-[3,4,5-tris((2,5,8,11-tetraoxatridecan-13-yl)oxy)benzyl] naphthalene-1,4,5,8-tetracarboxylic acid bisimide (NBI 5)**

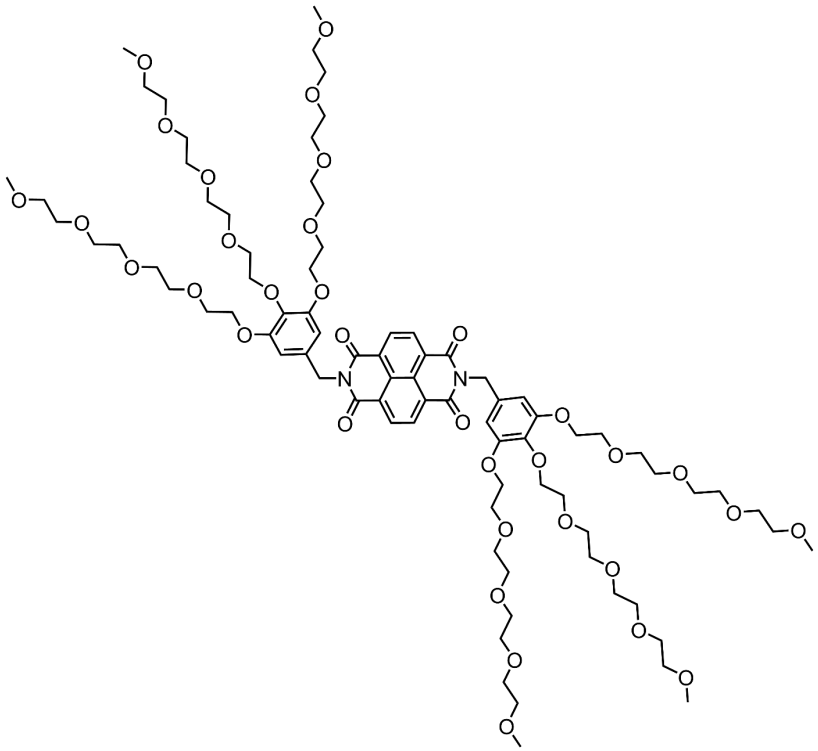

1,4,5,8-Naphthalenetetracarboxylic acid bisanhydride (48 mg, 0.17 mmol), 3,4,5-tris((2,5,8,11-tetraoxatridecan-13-yl)oxy)benzyl amine (**70**) (356 mg, 0.49 mmol) and dry DMF (5 mL) were charged into a pressure tube and heated at 110 °C for 12 h under nitrogen. After cooling to room temperature, the solvent was evaporated under vacuum, and the residue was extracted with DCM and washed with water and brine. The organic phase was dried with anhydrous sodium sulfate, and then the solvent was evaporated under vacuum. The resultant residue was purified first by silica gel column chromatography (methanol (6%)/chloroform) and then by GPC (chloroform) to obtain **NBI 5** as an orange waxy solid (136 mg, 0.08 mmol, 45%).

$^{1}$H NMR (400 MHz, $CDCl_3$): $\delta$ = 8.76 (s, 4H), 6.82 (s, 4H), 5.25 (s, 4H), 4.13 (t, $^{3}J$ = 5.1 Hz, 8H), 4.06 (t, $^{3}J$ = 5.1 Hz, 4H), 3.81 (t, $^{3}J$ = 5.0 Hz, 8H), 3.74-3.60 (m, 64H), 3.54-3.51 (m, 12H), 3.36 (s, 12H), 3.35 (s, 6H) ppm. $^{13}$C NMR (100 MHz, $CDCl_3$): $\delta$ = 162.9, 152.6, 138.2, 132.0, 131.3, 126.8, 126.7, 109.3, 72.3, 72.0, 70.9, 70.76, 70.75, 70.71, 70.67, 70.64, 70.62, 70.57, 69.8, 68.9, 59.1, 44.1 ppm. HRMS (ESI, positive, ACN/$CHCl_3$): *m*/*z* calcd for $C_{82}H_{126}N_2O_{34}Na$: 1705.8089; found: 1705.8014 $[M+Na]^+$. UV-vis ($CHCl_3$): $\lambda_{max}$ = 381 nm ($\varepsilon$ = 26600 $M^{-1}$ $cm^{-1}$), 361 nm ($\varepsilon$ = 22500 $M^{-1}$ $cm^{-1}$).

# Chapter 10

# Appendix

## 10.1 Appendix for Chapter 4

**Monomer UV-vis spectra**

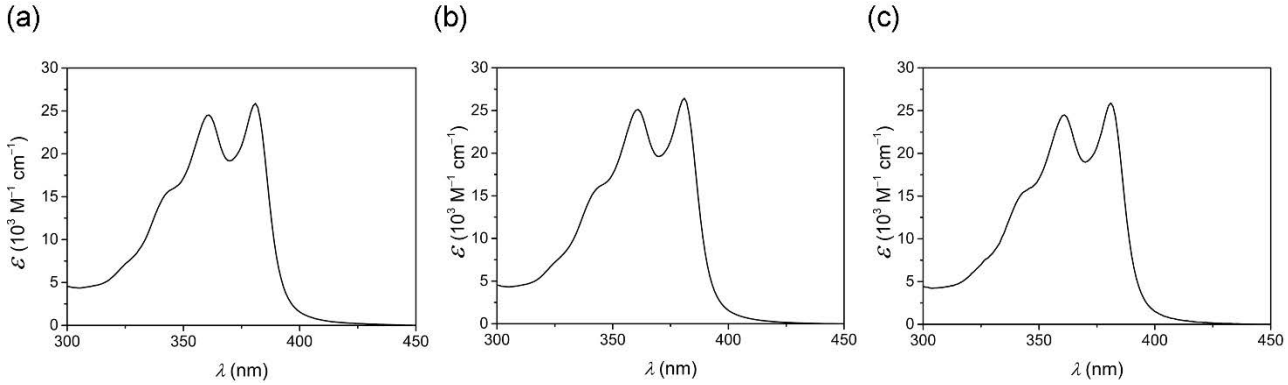


**Figure A1**: UV-vis absorption spectra of monomeric NBIs in $CHCl_3$ at 25 °C: (a) **NBI 1** ($c$ = 3.1 × $10^{-5}$ M), (b) **NBI 2** ($c$ = 6.6 × $10^{-5}$ M) and (c) **NBI 3** ($c$ = 2.4 × $10^{-5}$ M).

**Temperature-dependent UV-vis experiments**

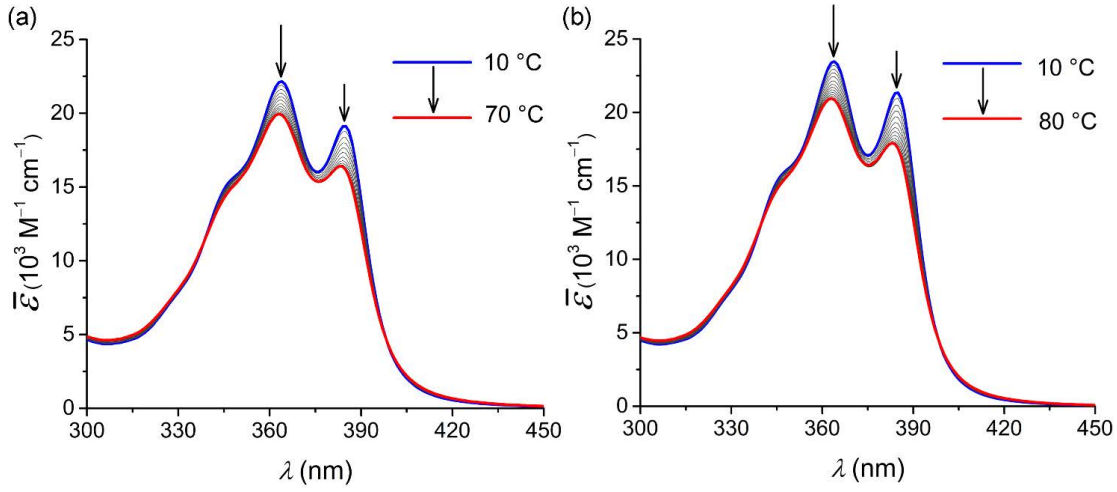


**Figure A2**: Temperature-dependent UV-vis spectra (density corrected) of (a) **NBI 2** ($c$ = 2.5 × $10^{-4}$ M) and (b) **NBI 3** ($c$ = 2.5 × $10^{-4}$ M) in water. Arrows indicate spectral changes upon heating.

**Atomic force microscopy (AFM)**

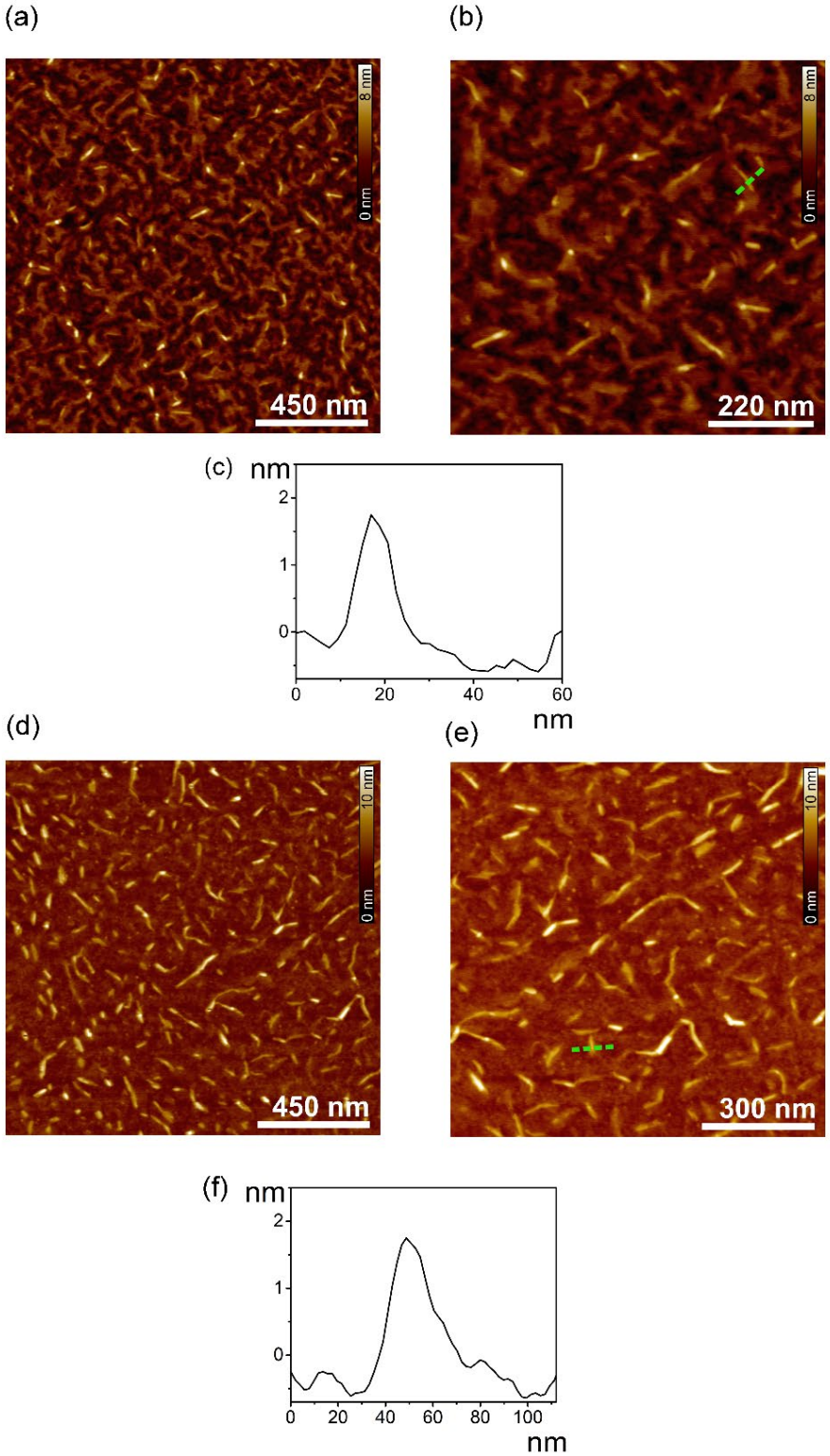


**Figure A3**: AFM height image of **NBI 2** (a, b) in water ($c$ = 1.6 × $10^{-3}$ M) and corresponding cross-section analysis from the dashed green line in image (c). AFM height image of **NBI 3** (d, e) in water ($c$ = 1.6 × $10^{-3}$ M) and corresponding cross-section analysis from the dashed green line in image (f).

## Dynamic light scattering (DLS)

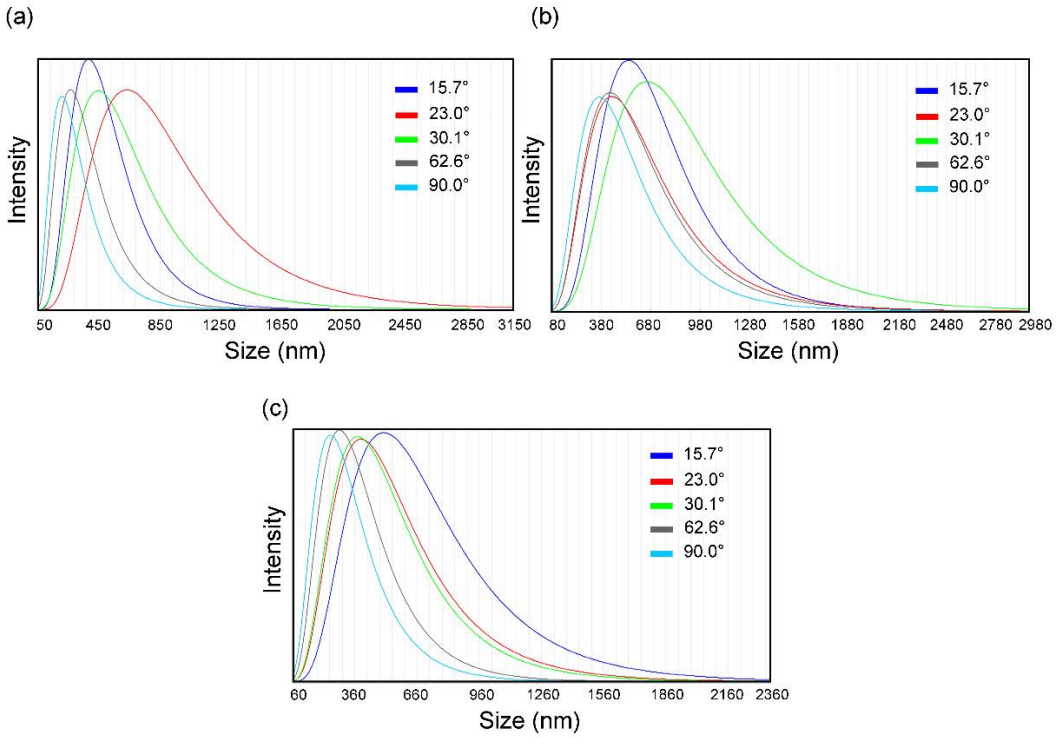


**Figure A4**: Unimodal size distribution from CONTIN analysis of the autocorrelation function of (a) **NBI 1** ($c$ = 1.0 × $10^{-3}$ M), (b) **NBI 2** ($c$ = 1.0 × $10^{-3}$ M) and (c) **NBI 3** ($c$ = 1.0 × $10^{-3}$ M) in water at 25 °C from DLS experiments.

## Variable temperature concentration-dependent UV-vis experiments

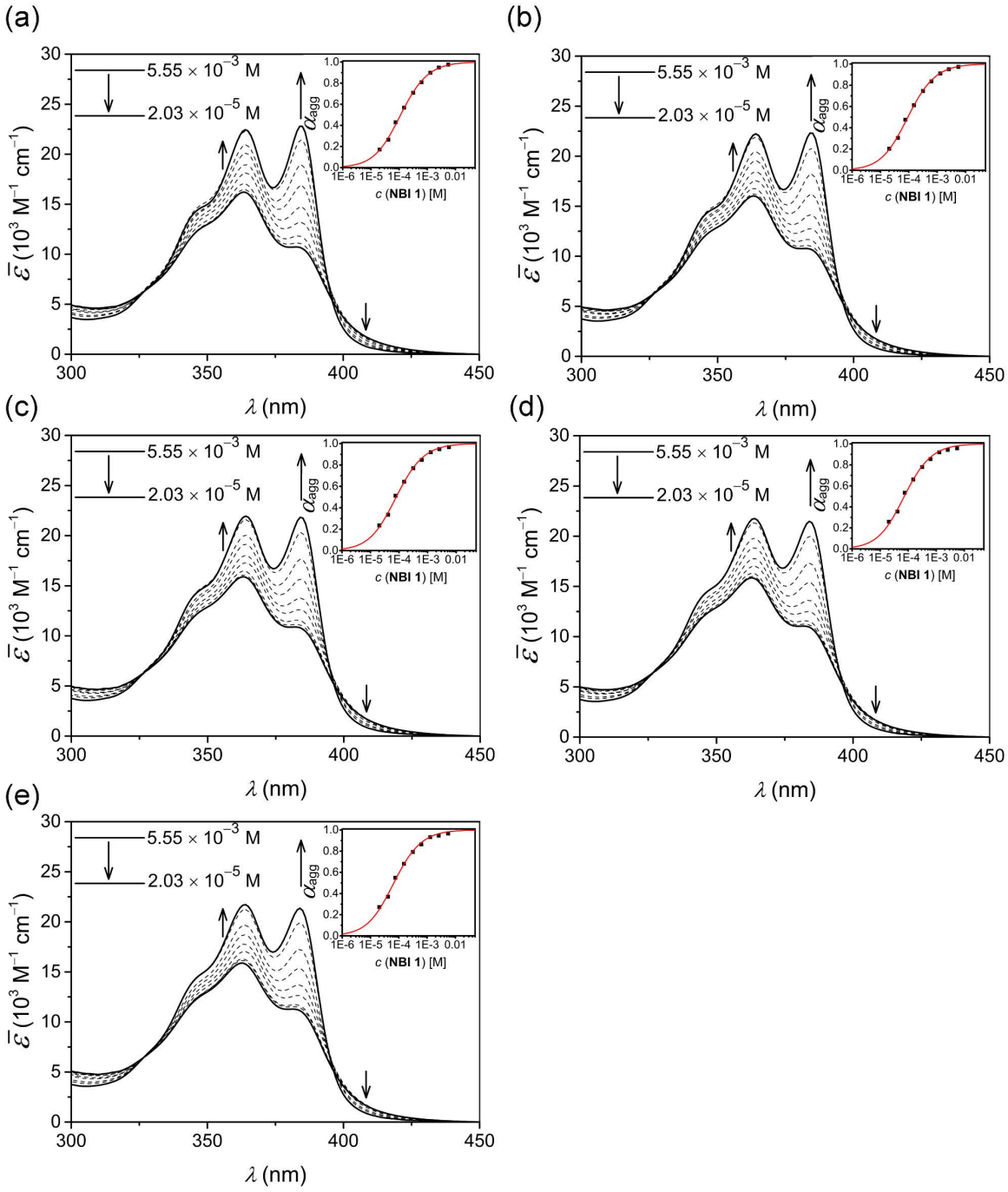


**Figure A5**: Concentration-dependent UV-vis spectra of **NBI 1** in water (density corrected) at (a) 10 °C, (b) 20 °C, (c) 30 °C, (d) 40 °C, and (e) 50 °C. Inset: Corresponding plot of the fraction of aggregated species, $\alpha_{agg}$, against concentration and analysis of the data based on the isodesmic model.

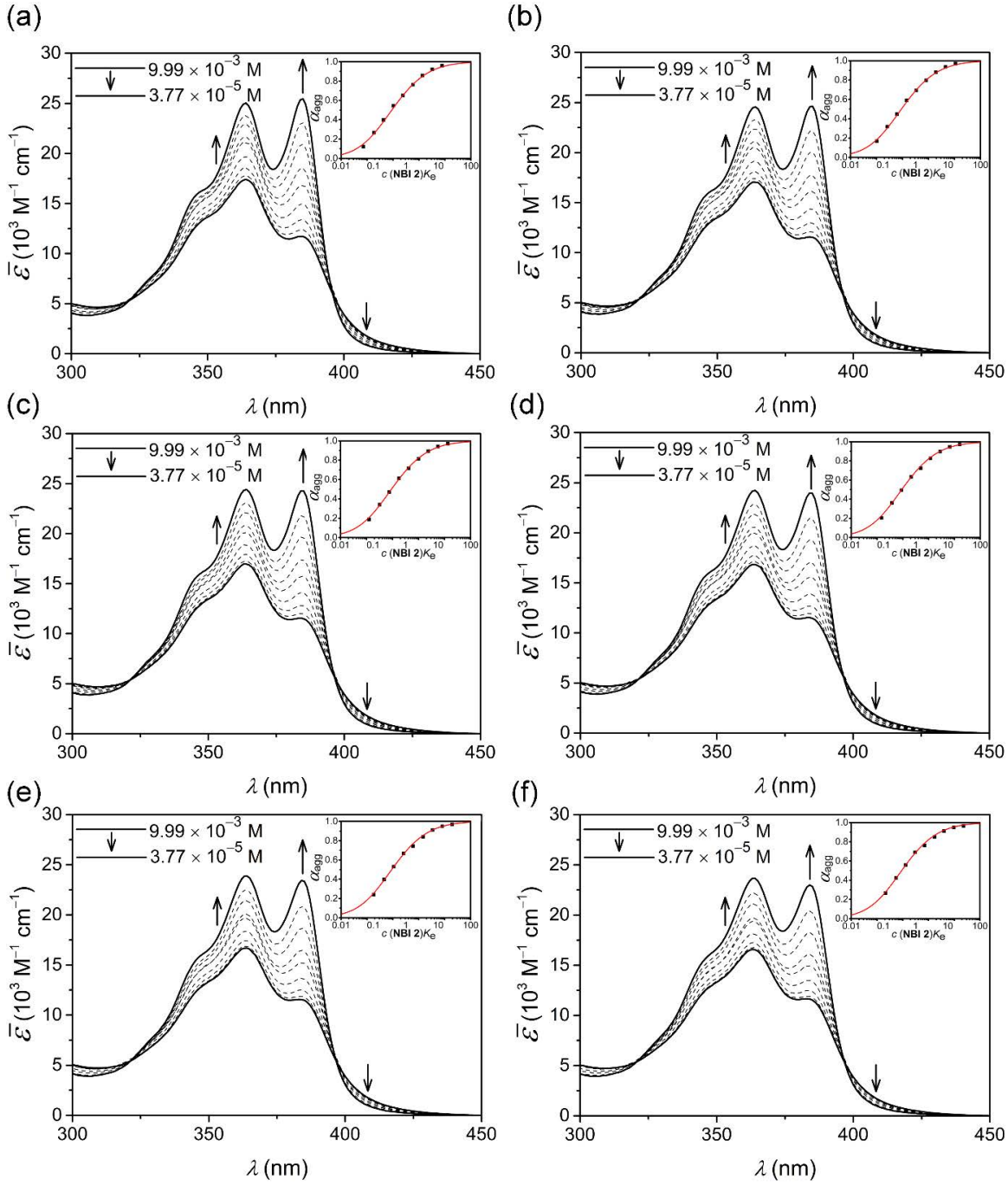


**Figure A6**: Concentration-dependent UV-vis spectra of **NBI 2** in water (density corrected) at (a) 10 °C, (b) 20 °C, (c) 25 °C, (d) 30 °C, (e) 40 °C, and (f) 50 °C. Inset: Corresponding plot of the fraction of aggregated species, $\alpha_{agg}$, against dimensionless product $c$ (**NBI 2**)$K_e$ and analysis of the data based on the Goldstein-Stryer model ($\sigma$ = 2).

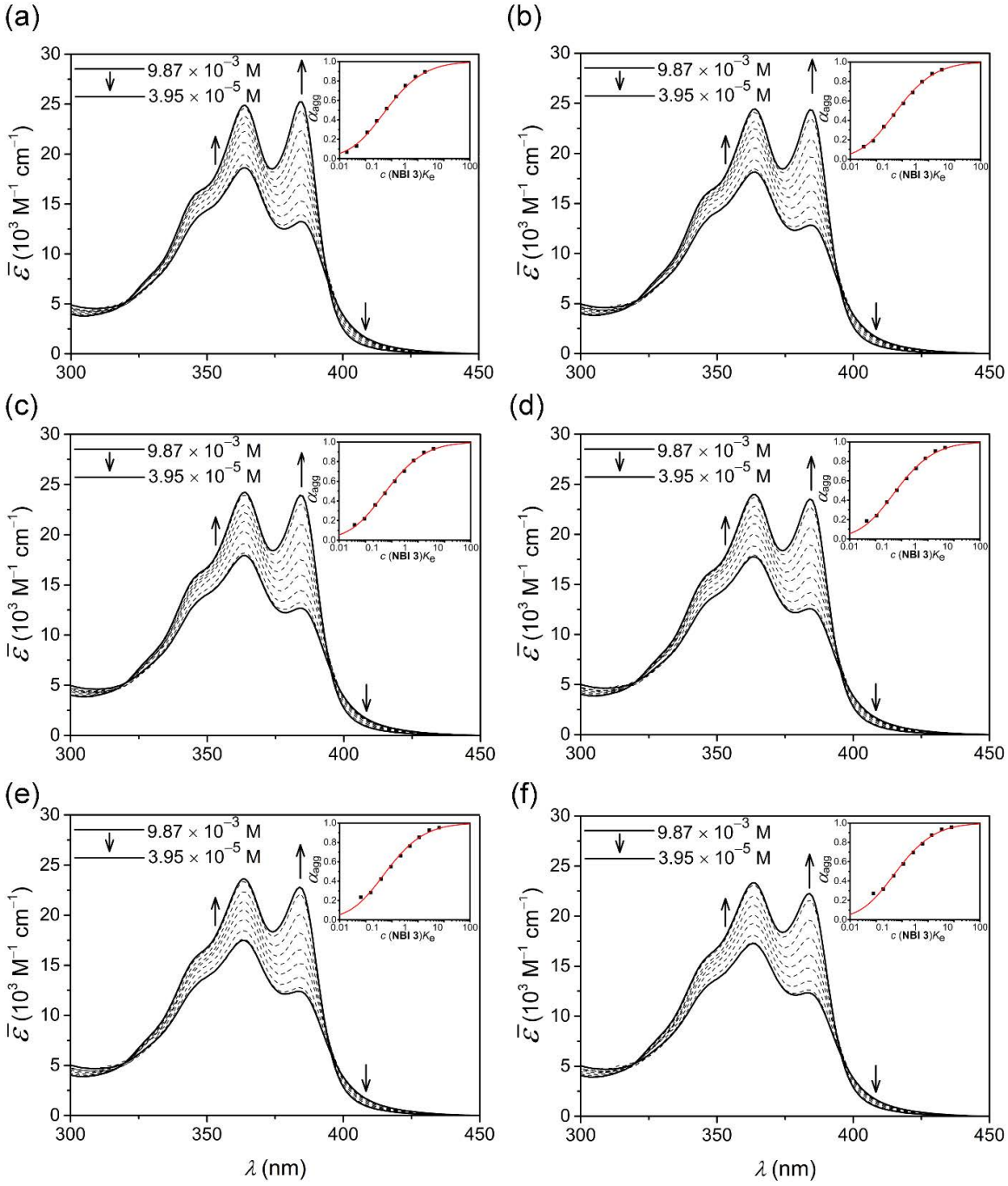


**Figure A7**: Concentration-dependent UV-vis spectra of **NBI 3** in water (density corrected) at (a) 10 °C, (b) 20 °C, (c) 25 °C, (d) 30 °C, (e) 40 °C, and (f) 50 °C. Inset: Corresponding plot of the fraction of aggregated species, $\alpha_{agg}$, against dimensionless product $c$ (**NBI 3**)$K_e$ and analysis of the data based on the Goldstein-Stryer model ($\sigma$ = 3).

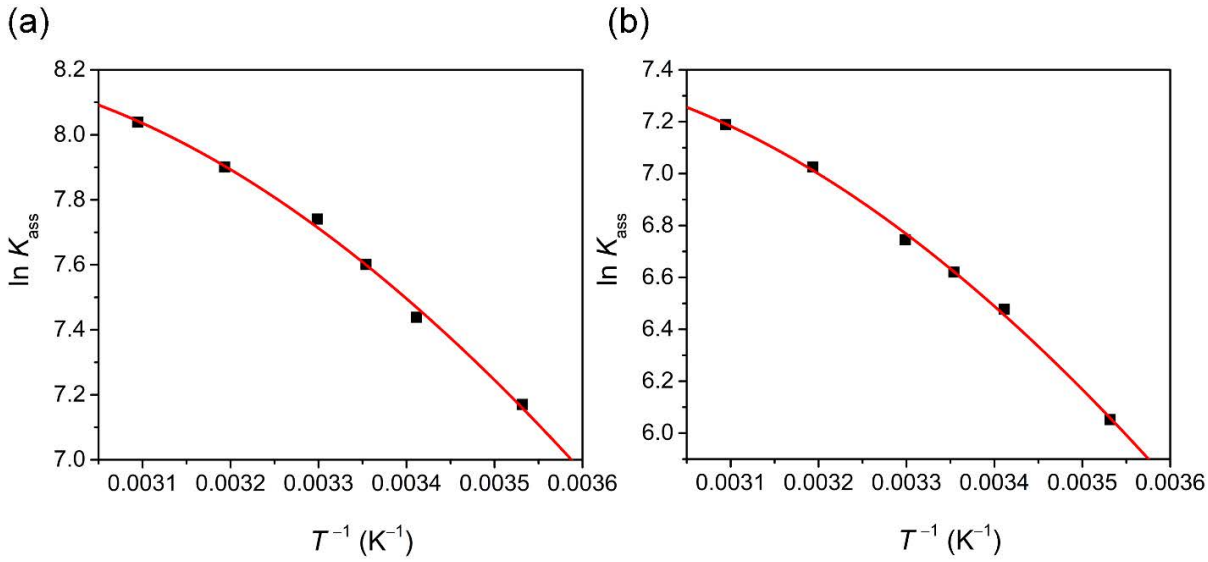


**Figure A8**: Plot of the natural logarithm of association constant (ln $K_{ass}$) for (a) **NBI 2** and (b) **NBI 3** against reciprocal of temperature and corresponding fit according to Clarke-Glew equation.

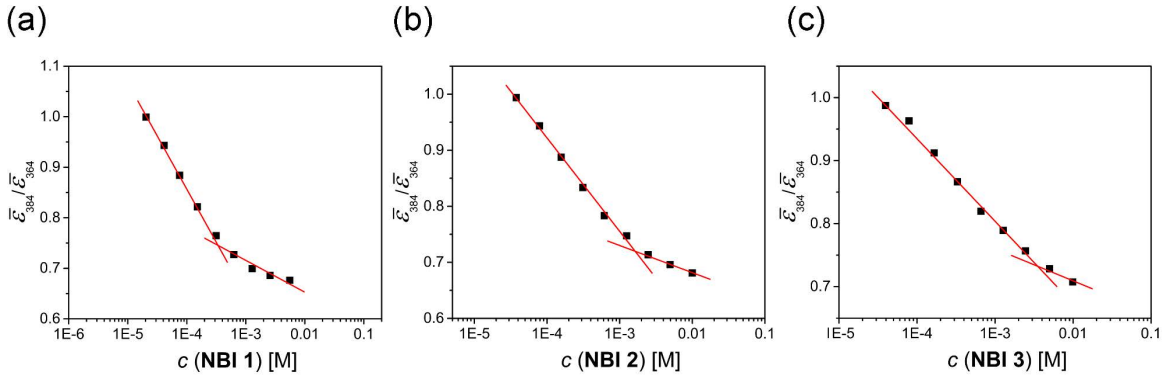


**Figure A9**: Determination of critical aggregation concentration (CAC) for (a) **NBI 1**, (b) **NBI 2**, and (c) **NBI 3** from concentration-dependent UV/vis studies of the corresponding derivative at 25°C in water. The inflection point corresponds to the CAC.

**Isothermal titration calorimetry (ITC)**

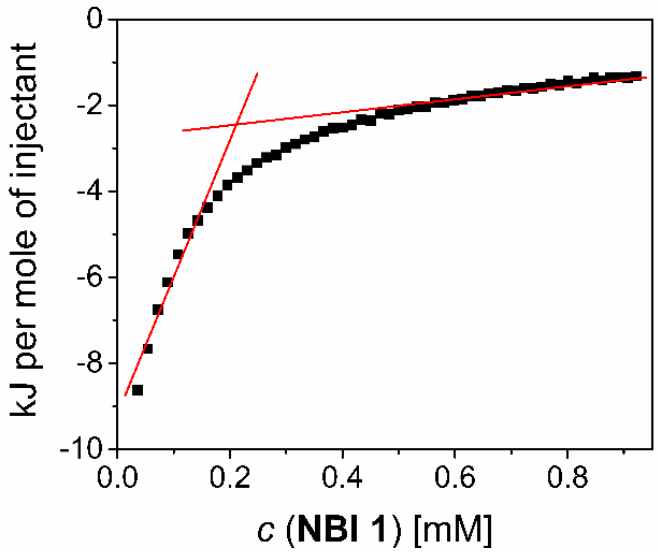


**Figure A10**: Determination of critical aggregation concentration (CAC) for **NBI 1** from ITC dilution experiment at 25 °C in water. The inflection point corresponds to the CAC.

**Table A1**: Heat of dilution for ITC experiments of **NBI 1** at different temperatures.

| **Temperature (°C)** | 10 | 20 | 25 | 30 | 40 | 50 |
|---|---|---|---|---|---|---|
| **$\Delta H°_{dil}$ (kJ mol$^{-1}$)** | 0.18 | -0.14 | -0.45 | -0.70 | -1.27 | -1.57 |

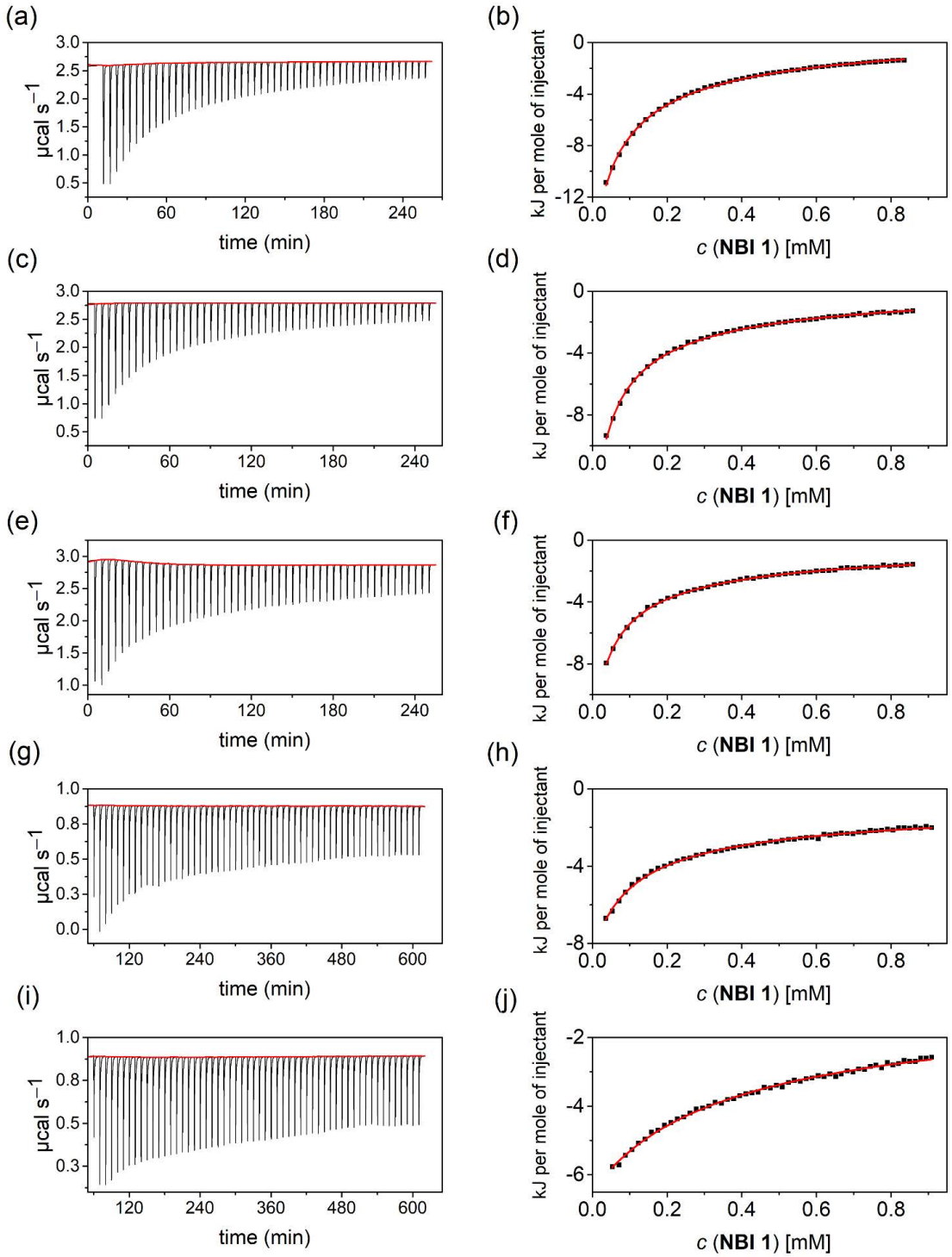


**Figure A11**: Evolution of heat per injection of **NBI 1** in water at (a) 10 °C, (c) 20 °C, (e) 30 °C, (g) 40 °C, and (i) 50 °C. Corresponding enthalpograms at (b) 10 °C, (d) 20 °C, (f) 30 °C, (h) 40 °C, (j) 50 °C and fit according to isodesmic model (red line).

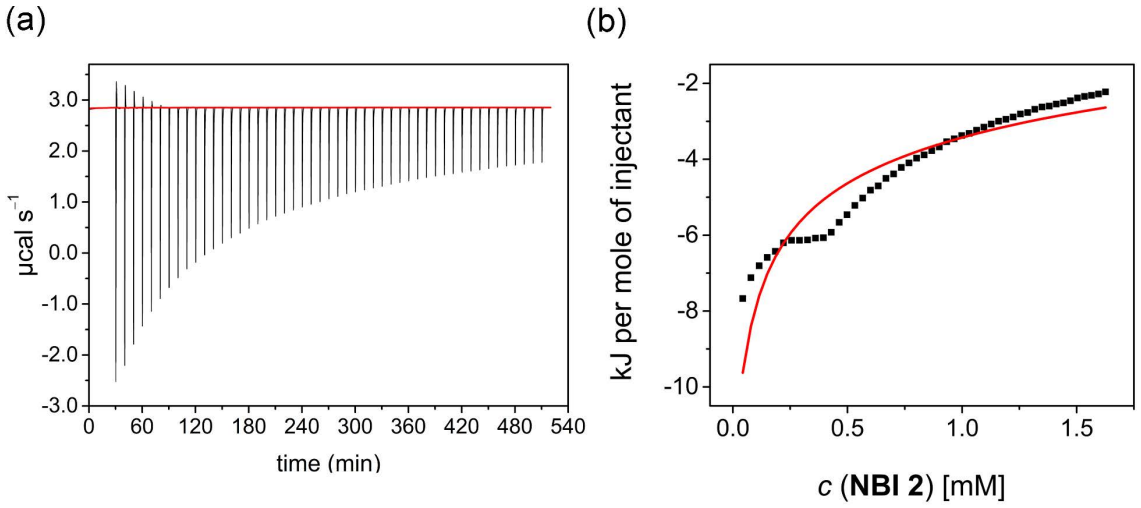


**Figure A12**: (a) Evolution of heat per injection of **NBI 2** in water at 25 °C. (b) Corresponding enthalpogram and fit according to the isodesmic model (red line).

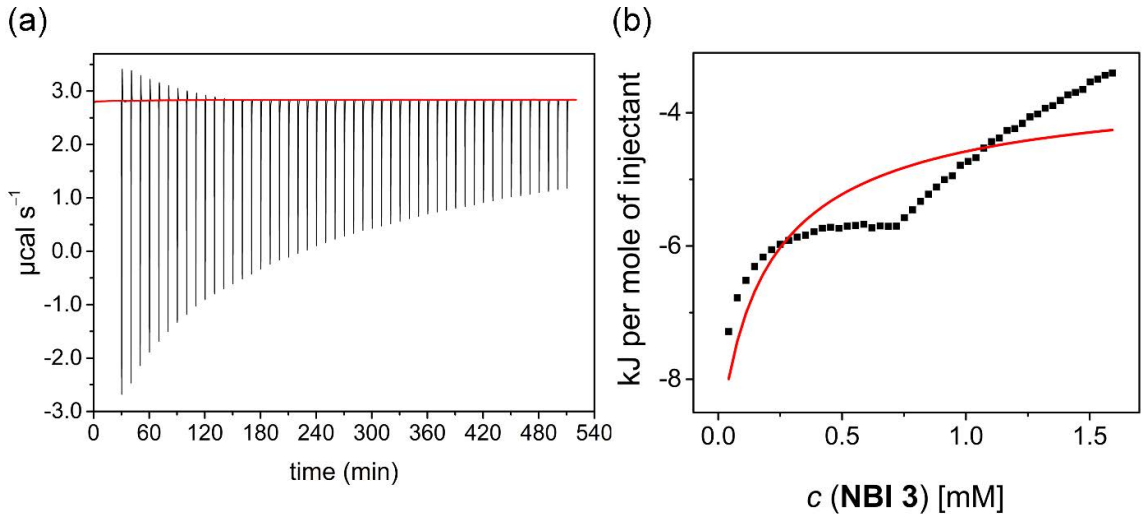


**Figure A13**: (a) Evolution of heat per injection of **NBI 3** in water at 25 °C. (b) Corresponding enthalpogram and fit according to isodesmic model (red line).

**Molecular Dynamics (MD) studies**

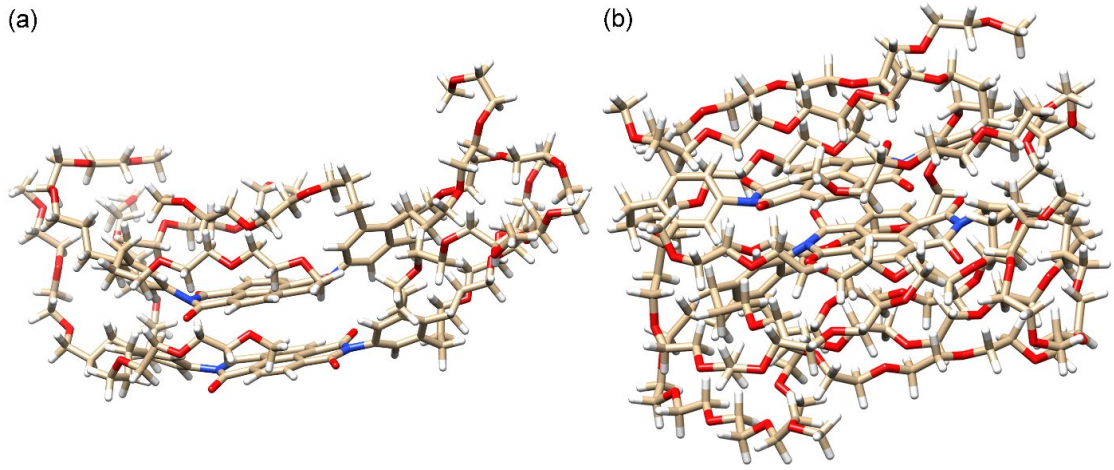


**Figure A14**: Snapshot showing back-folding of glycol chains for (a) **NBI 1** and (b) **NBI 3** in stacked state from MD simulations (water molecules are omitted for clarity).

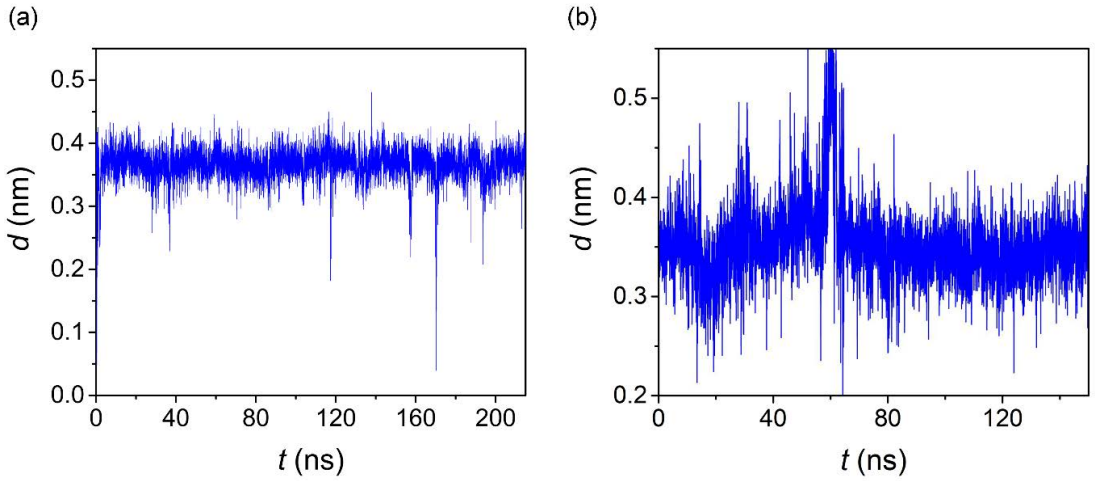


**Figure A15**: Trajectory of stacking distance for **NBI 1** (a) and **NBI 3** (b).

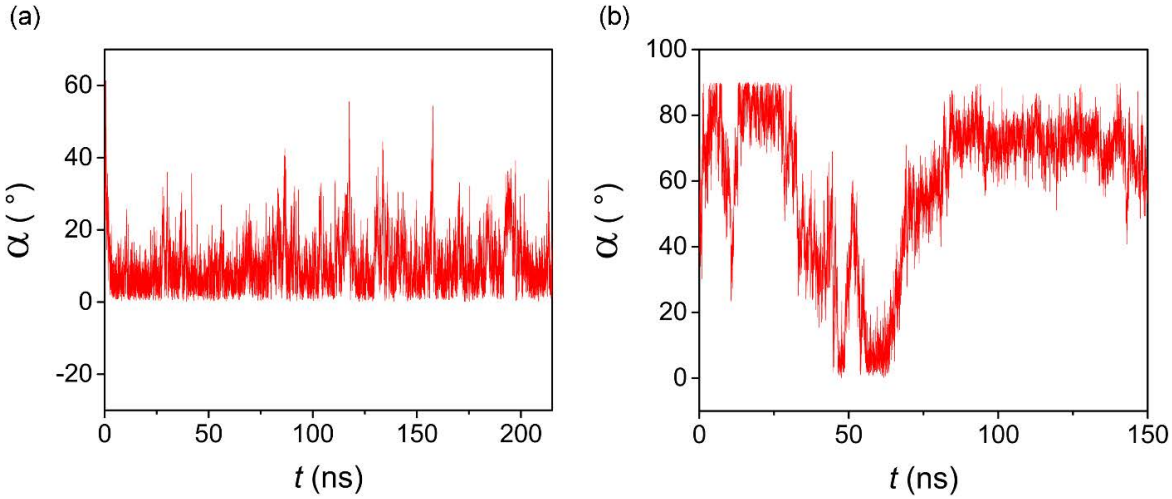


**Figure A16**: Tilt angle between naphthalene cores in the stacked state for **NBI 1** (a) and **NBI 3** (b) in water.

## NMR studies

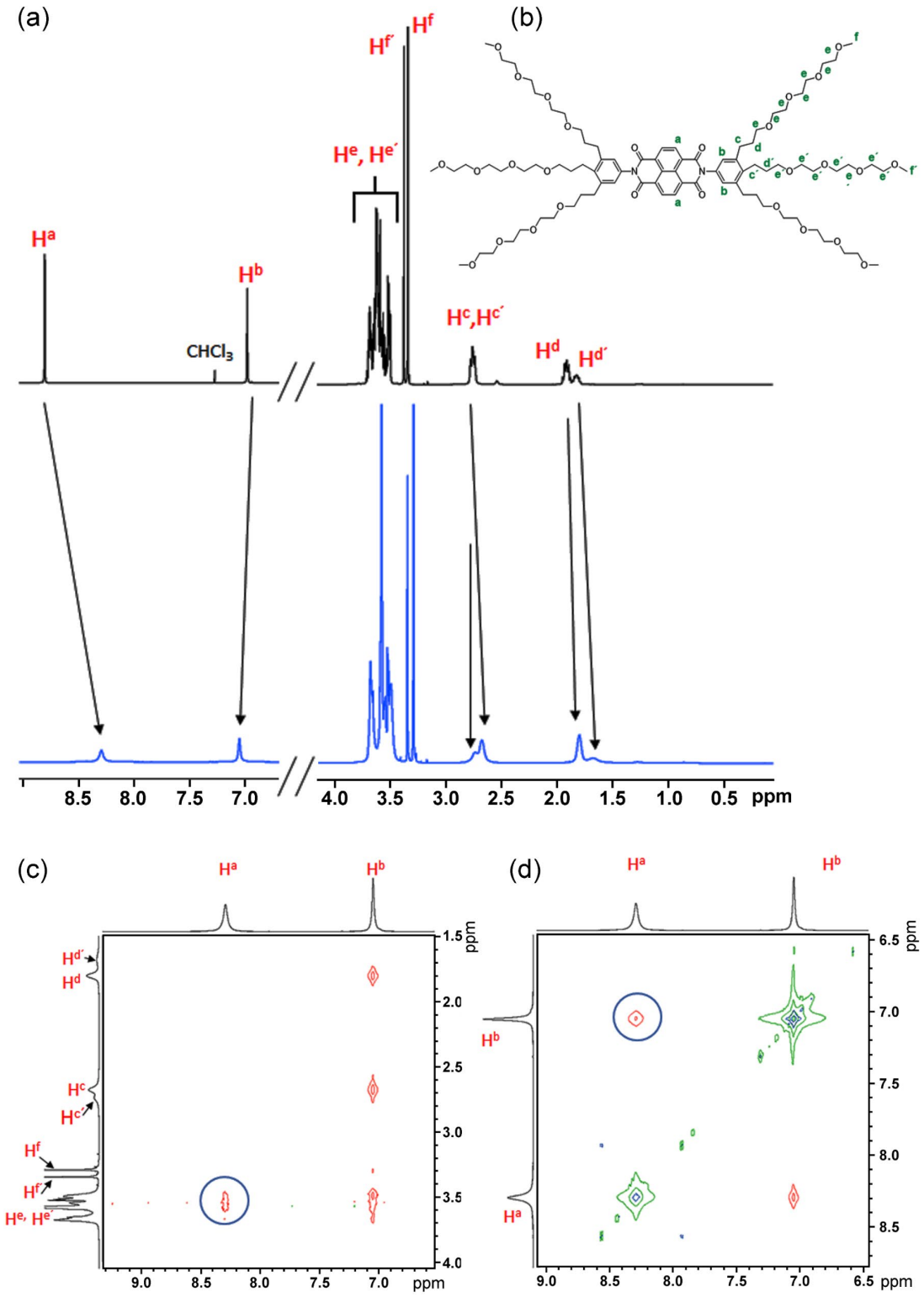


**Figure A17**: (a) Relevant sections of $^1$H NMR spectrum of **NBI 2** monomer in $CDCl_3$ ($c$ = 12.0 × $10^{-3}$ M) (black) and in aggregated state in $D_2O$ ($c$ = 4.9 × $10^{-3}$ M) (blue) at 295 K. (b) Chemical structure of **NBI 2** with the significant protons assigned. Selected region of superposed ROESY-NMR and COSY-NMR spectra of **NBI 2** showing NOEs between glycol chains and naphthalene core (c) and phenyl protons and naphthalene core (d) in $D_2O$ ($c$ = 4.9 × $10^{-3}$ M) (circles).

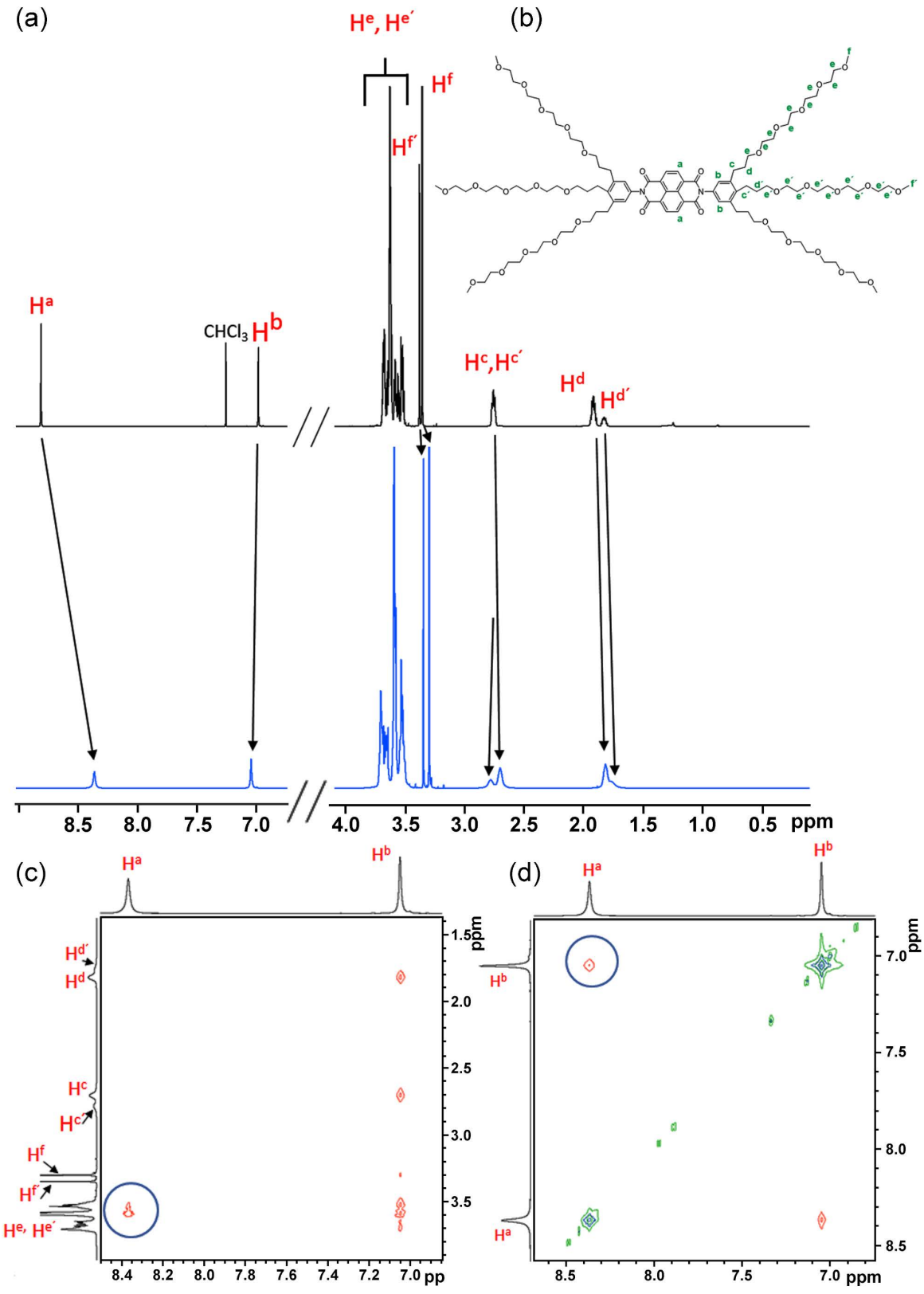


**Figure A18**: (a) Relevant sections of $^1$H NMR spectrum of **NBI 3** monomer in $CDCl_3$ ($c$ = 10.0 × $10^{-3}$ M) (black) and in aggregated state in $D_2O$ ($c$ = 4.9 × $10^{-3}$ M) (blue) at 295 K. (b) Chemical structure of **NBI 3** with the significant protons assigned. Selected region of superposed ROESY-NMR and COSY-NMR spectra of **NBI 3** showing NOEs between glycol chains and naphthalene core (c) and phenyl protons and naphthalene core (d) in $D_2O$ ($c$ = 4.9 × $10^{-3}$ M) (circles).

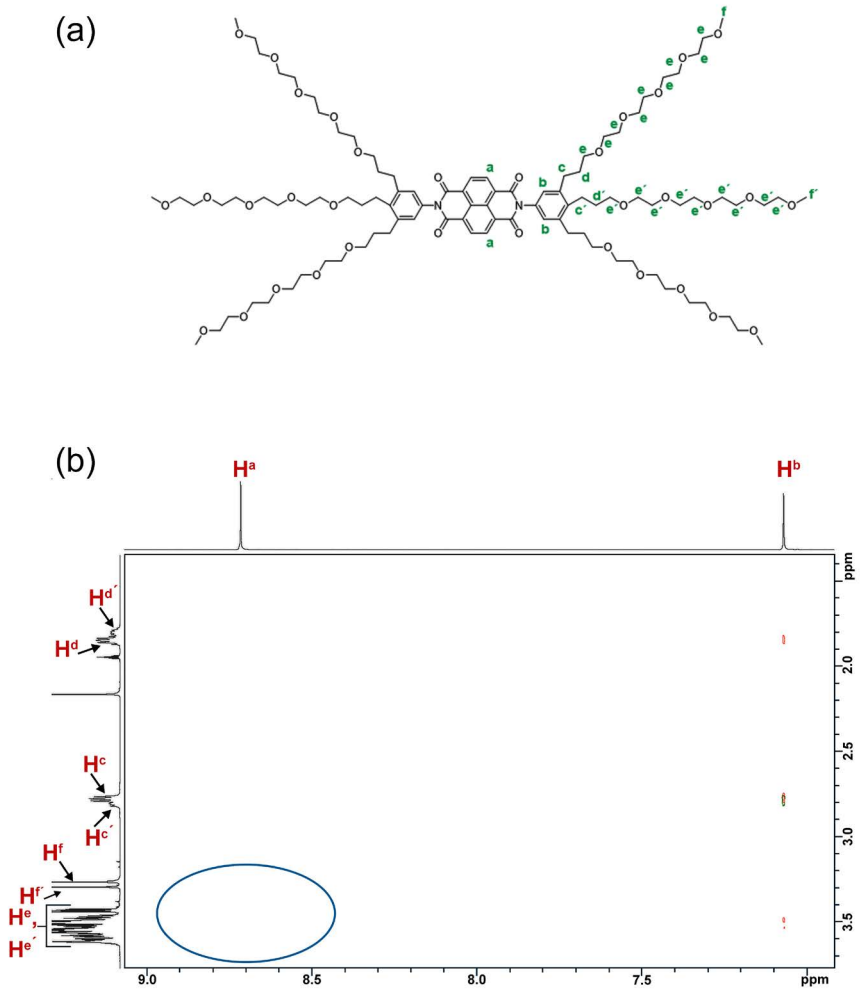


**Figure A19**: (a) Chemical structure of **NBI 3** with the significant protons assigned. (b) Selected region of superposed ROESY-NMR and COSY-NMR spectra of **NBI 3** in ACN ($c$ = 1.0 × $10^{-2}$ M). Blue circle shows the region where NOEs corresponding to back-folding is to expect, but not observed.

## 10.2 Appendix for Chapter 5

**Monomer UV-vis spectra**

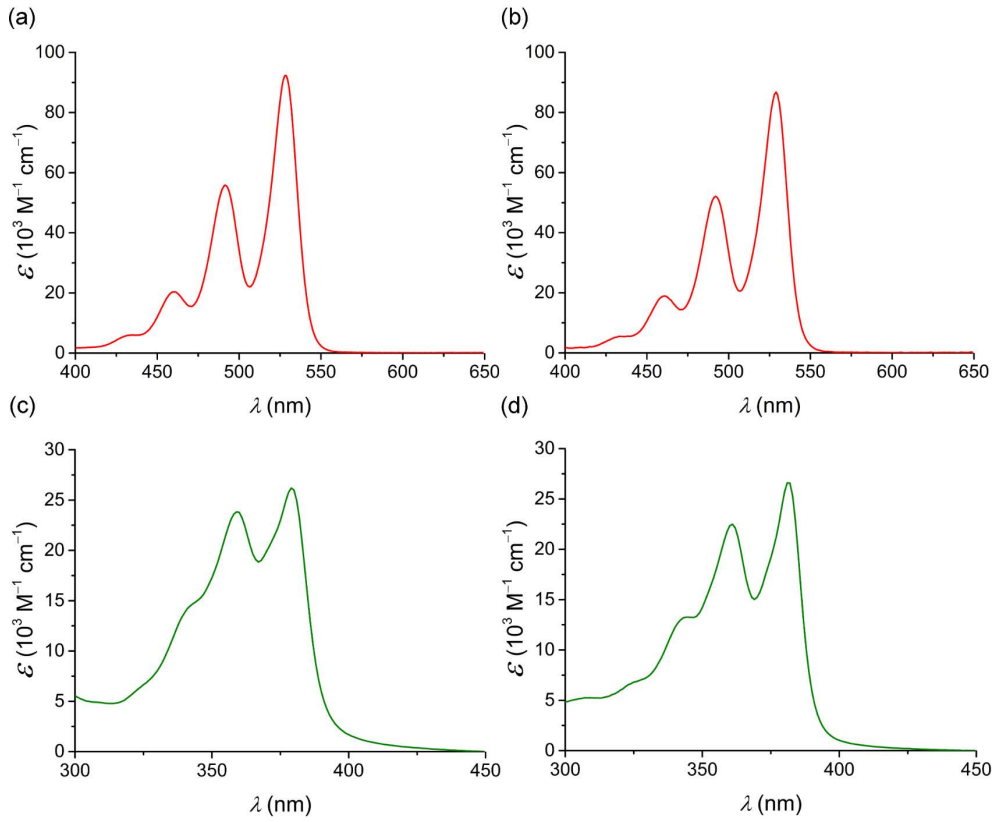


**Figure A20**: Monomer spectra of (a) **PBI 6** ($c$ = 4.6 × $10^{-6}$ M), (b) **PBI 7** ($c$ = 5.0 × $10^{-6}$ M), (c) **NBI 4** ($c$ = 5.9 × $10^{-5}$ M) and (d) **NBI 5** ($c$ = 5.7 × $10^{-5}$ M) in $CHCl_3$ at 25 °C.

## Temperature-dependent UV-vis experiments

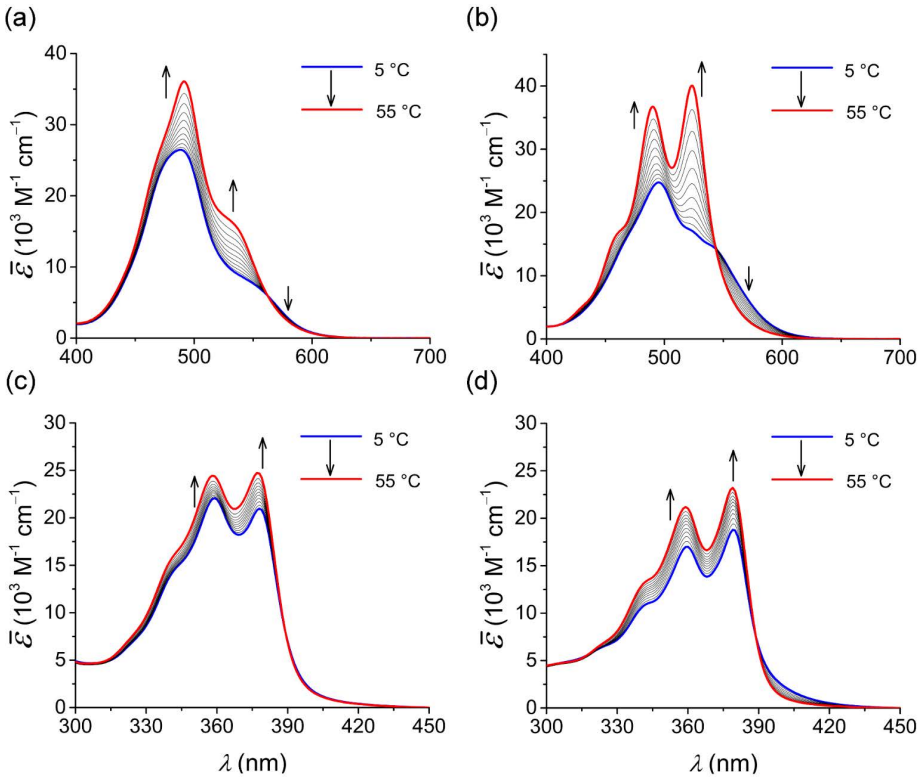


**Figure A21**: Temperature-dependent UV-vis spectra (density corrected) of (a) **PBI 6** ($c$ = 1.1 × $10^{-4}$ M), (b) **PBI 7** ($c$ = 1.0 × $10^{-4}$ M), (c) **NBI 4** ($c$ = 6.4 × $10^{-4}$ M) and (d) **NBI 5** ($c$ = 6.3 × $10^{-4}$ M) in methanol. Arrows indicate spectral changes upon heating.

## Atomic force microscopy (AFM)

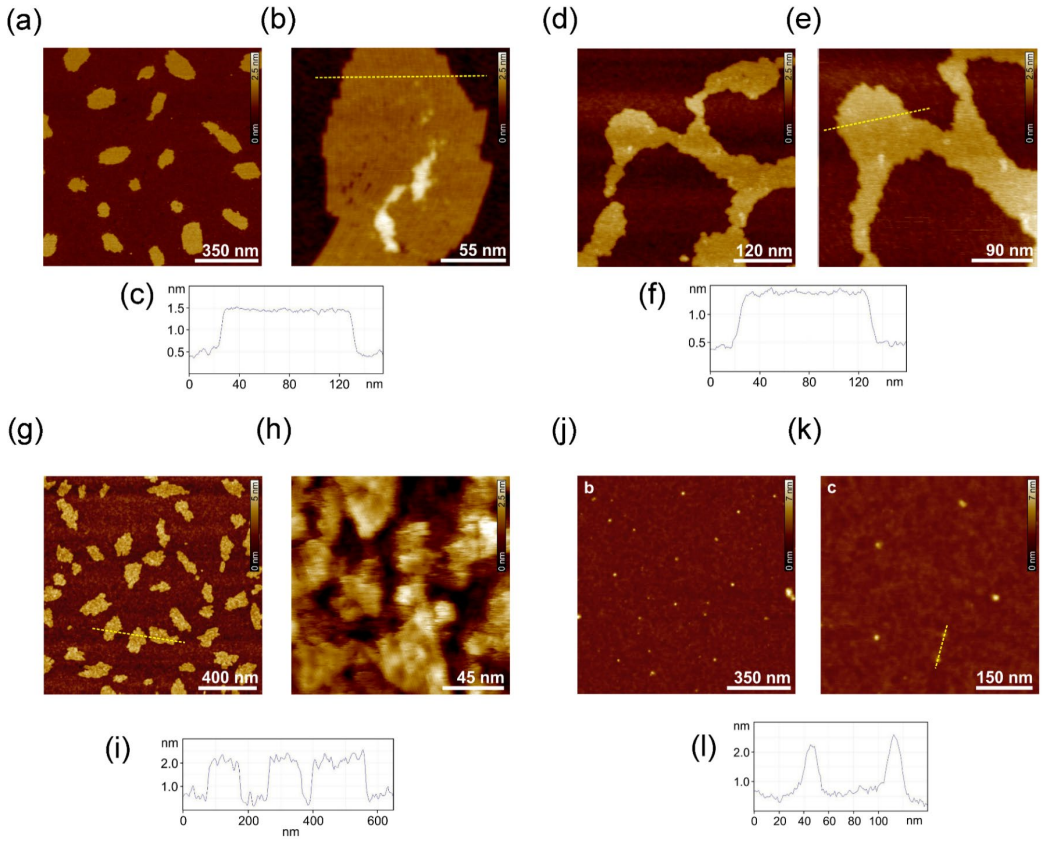


**Figure A22**: AFM height images of **PBI 6** ($c$ = 1.2 × $10^{-4}$ M) (a, b), **PBI 7** ($c$ = 1.2 × $10^{-4}$ M) (d, e) on mica and **NBI 4** ($c$ = 5.0 × $10^{-3}$ M) (g, h), **NBI 5** ($c$ = 5.0 × $10^{-3}$ M) (j, k) on silicon-wafer by spin-coating of aqueous solution at 22 °C. Corresponding cross-section analysis from the dashed yellow line in height images is also shown for **PBI 6** (c), **PBI 7** (f), **NBI 4** (i), and **NBI 5** (l).

## Concentration-dependent UV-vis experiments

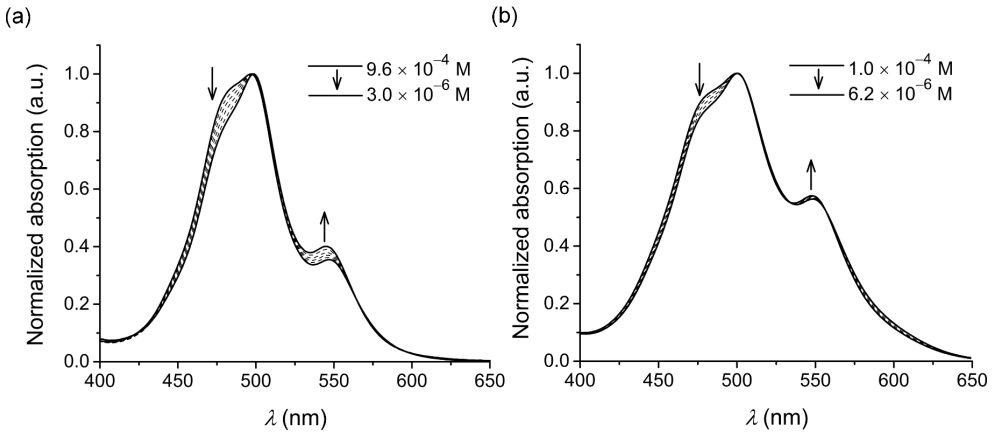


**Figure A23**: Concentration-dependent UV-vis spectra of (a) **PBI 6** and (b) **PBI 7** in water at 25 °C. Arrows indicate spectral changes upon dilution.

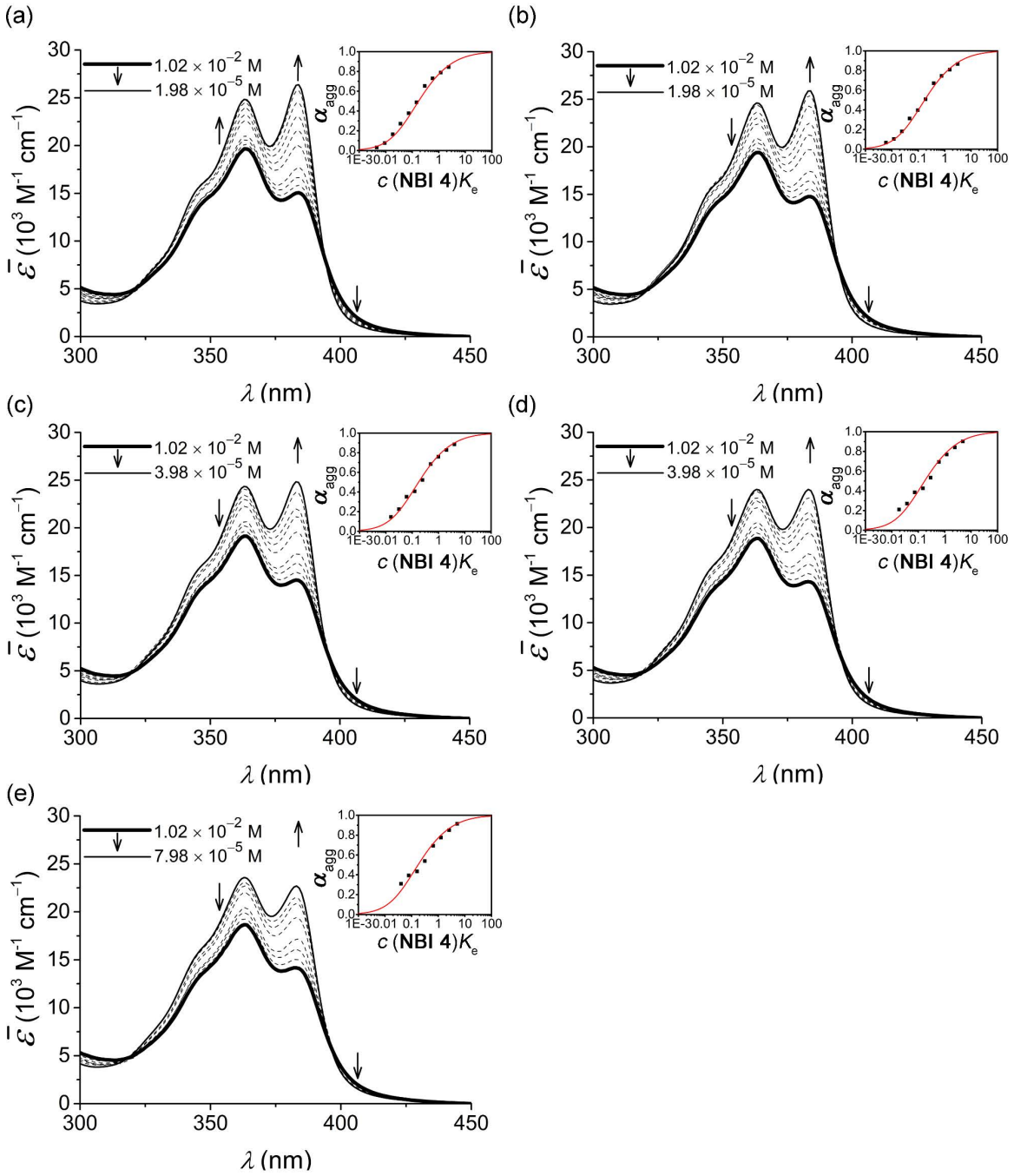


**Figure A24**: Concentration-dependent UV-vis spectra of **NBI 4** in water (density corrected) at (a) 10 °C, (b) 20 °C, (c) 30 °C, (d) 40 °C, and (e) 50 °C. Arrows indicate spectral changes upon dilution. Inset: Corresponding plot of the fraction of aggregated species, $\alpha_{agg}$, against dimensionless product $c$ (**NBI 4**)$K_e$ and analysis of the data based on the Goldstein-Stryer model ($\sigma$ = 5).

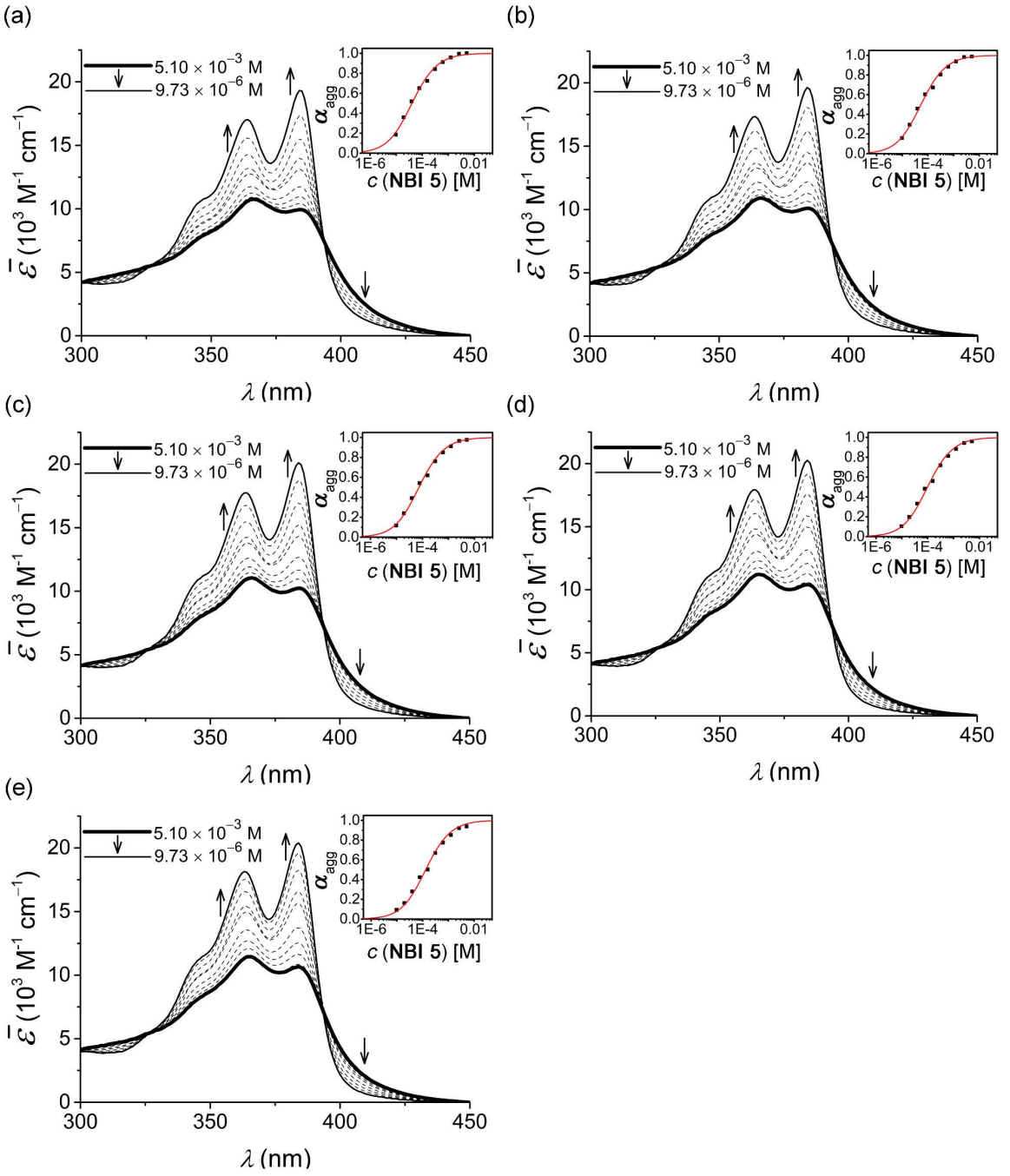


**Figure A25**: Concentration-dependent UV-vis spectra of **NBI 5** in water (density corrected) at (a) 10 °C, (b) 20 °C, (c) 30 °C, (d) 40 °C, and (e) 50 °C. Arrows indicate spectral changes upon dilution. Inset: Corresponding plot of the fraction of aggregated species, $\alpha_{agg}$, against concentration and analysis of the data based on the isodesmic model.

**Isothermal titration calorimetry (ITC)**

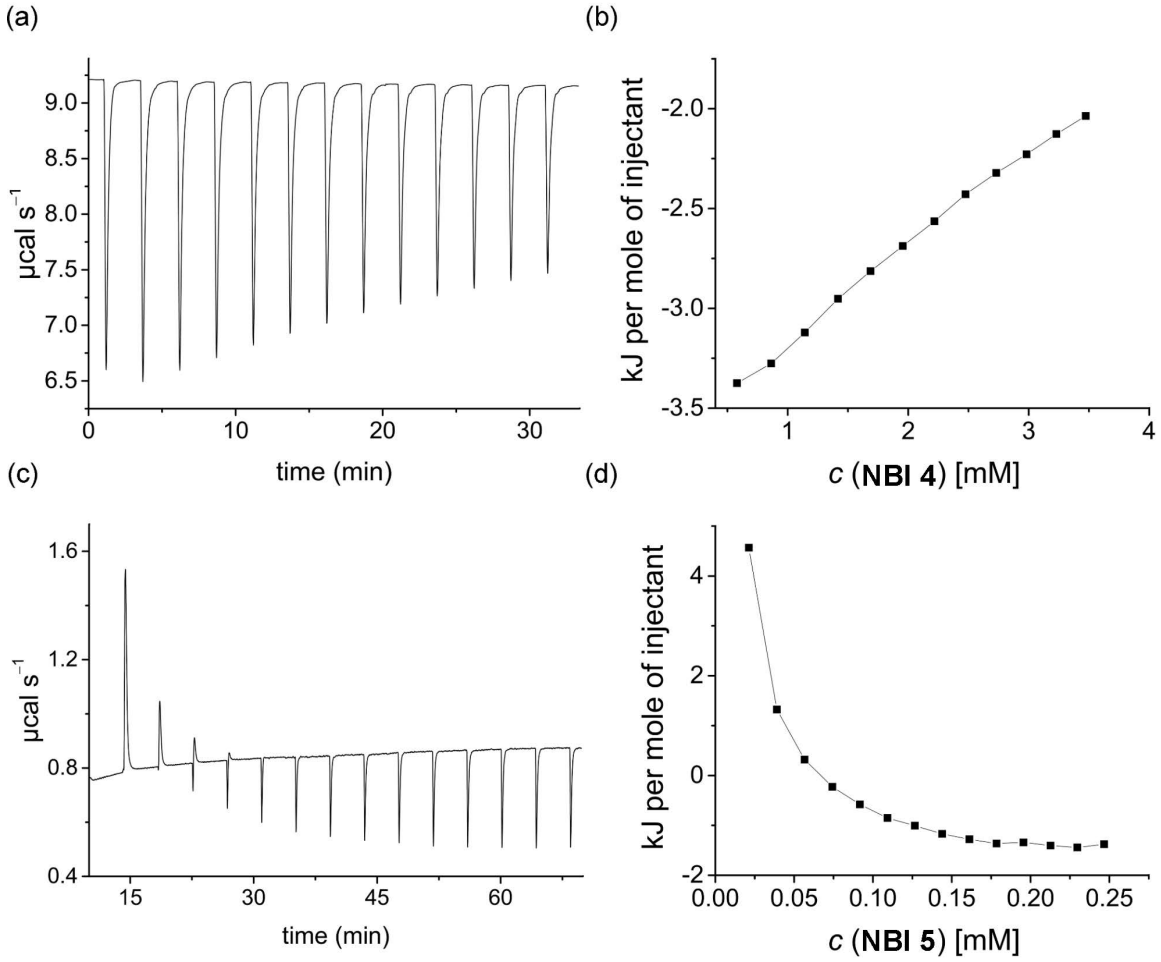


**Figure A26**: Evolution of heat per injection of (a) **NBI 4** ($c$ = 1.9 × 10$^{-2}$ M), (c) **NBI 5** ($c$ = 5.1 × 10$^{-3}$ M) in water at 25 °C and corresponding enthalpograms (b and d respectively). Lines connecting the data points are guide to the eye.

**NMR studies**

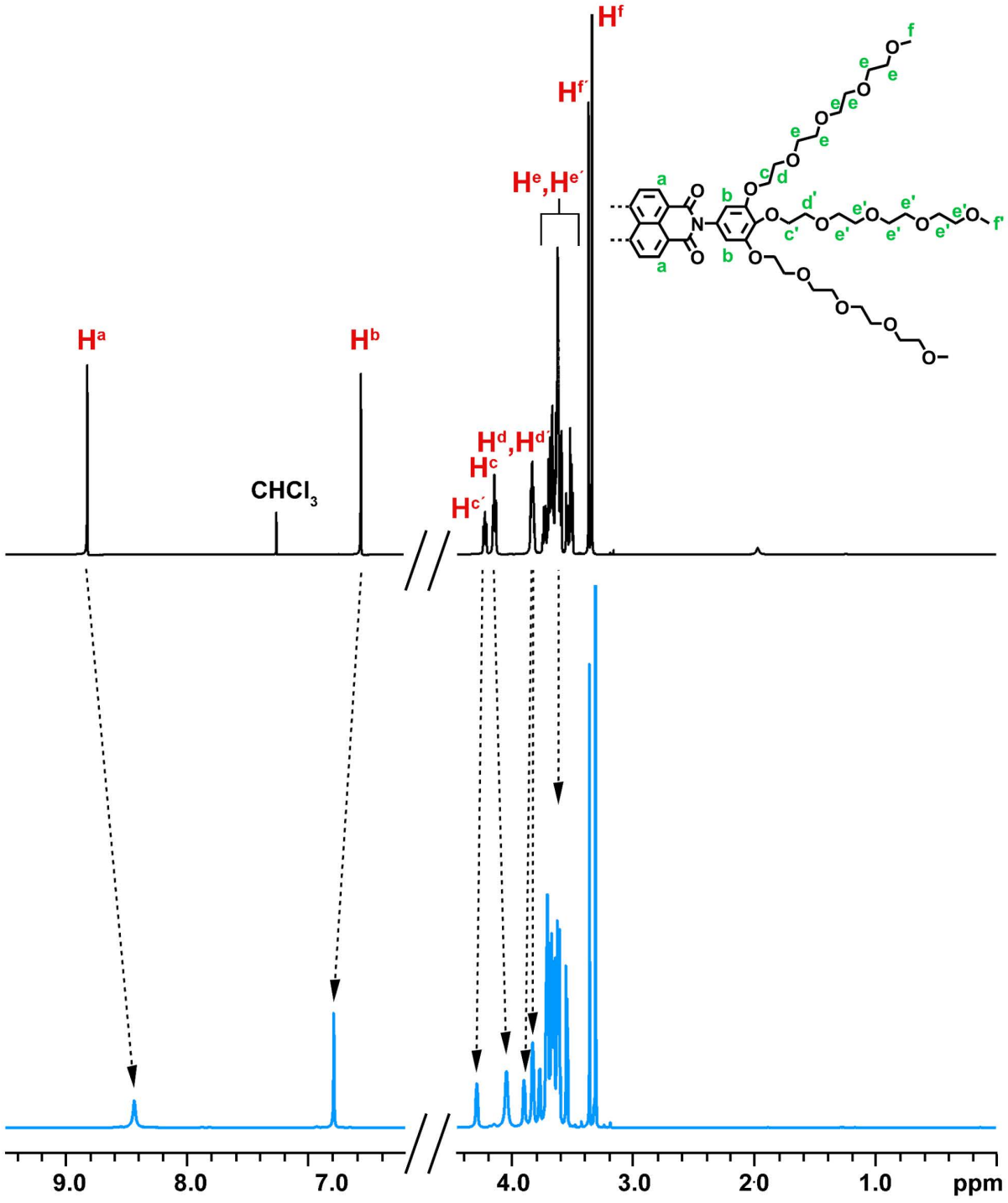


**Figure A27**: Relevant sections of $^1$H NMR spectrum of **NBI 4** in $CDCl_3$ ($c$ = 11.0 × $10^{-3}$ M) (top) and in $D_2O$ ($c$ = 5.0 × $10^{-3}$ M) (bottom) at 295 K. Partial chemical structure of **NBI 4** with the significant protons assigned is also shown.

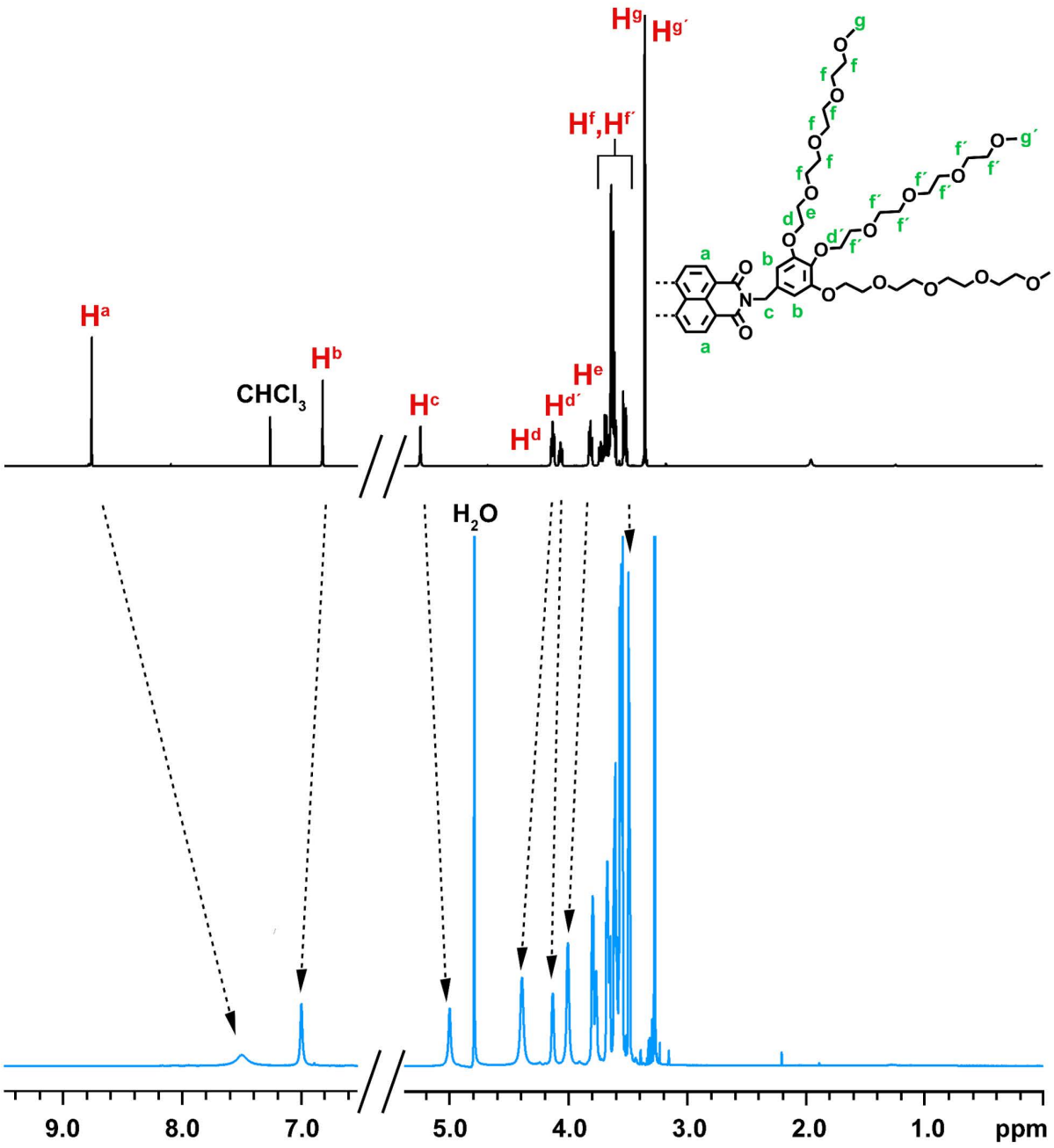


**Figure A28**: Relevant sections of $^{1}$H NMR spectrum of **NBI 5** in $CDCl_3$ ($c$ = 10.0 × $10^{-3}$ M) (top) and in $D_2O$ ($c$ = 4.9 × $10^{-3}$ M) (bottom) at 295 K. Partial chemical structure of **NBI 5** with the significant protons assigned is also shown.

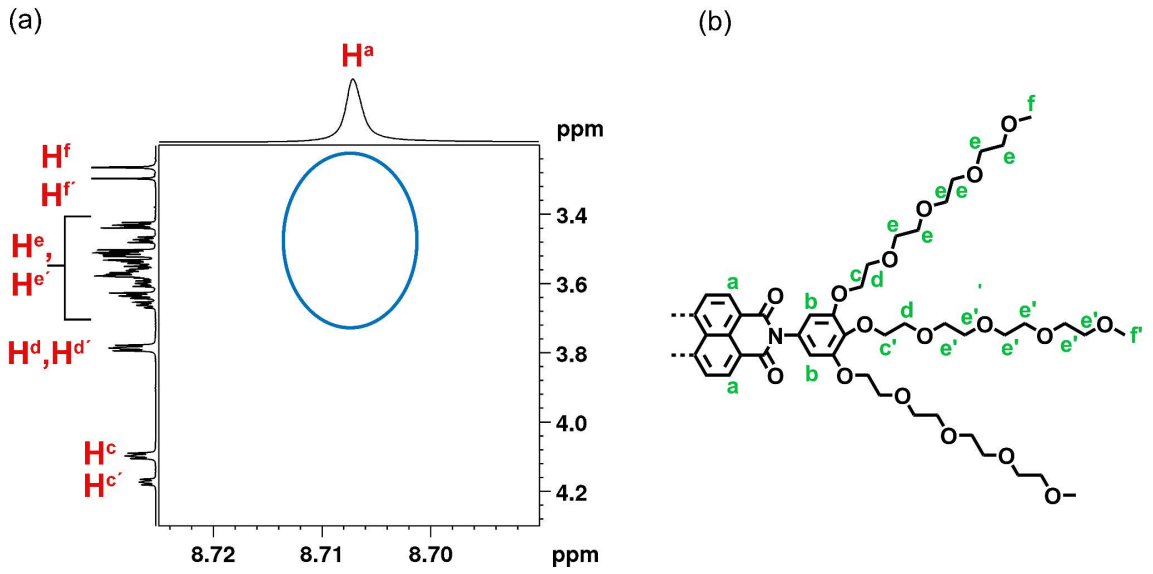


**Figure A29**: (a) Selected region of $^{1}$H-$^{1}$H ROESY spectrum of **NBI 4** in $CD_3CN$ ($c$ = 6.9 × $10^{-3}$ M). The blue circle shows the region where NOEs corresponding to back-folding is to expect, but not observed. (b) Partial chemical structure of **NBI 4** with the significant protons assigned.

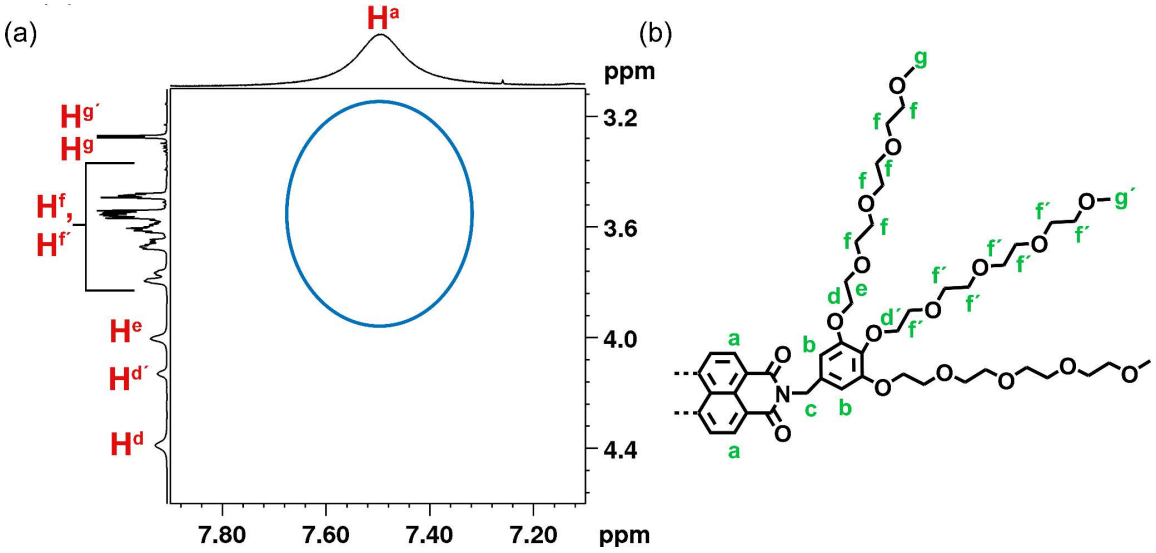


**Figure A30**: (a) Selected region of $^{1}$H-$^{1}$H ROESY spectrum of **NBI 5** in $D_2O$ ($c$ = 4.9 × $10^{-3}$ M). The blue circle shows the region where NOEs corresponding to back-folding is to expect, but not observed. (b) Partial chemical structure of **NBI 5** with the significant protons assigned.

**PM7 calculations**

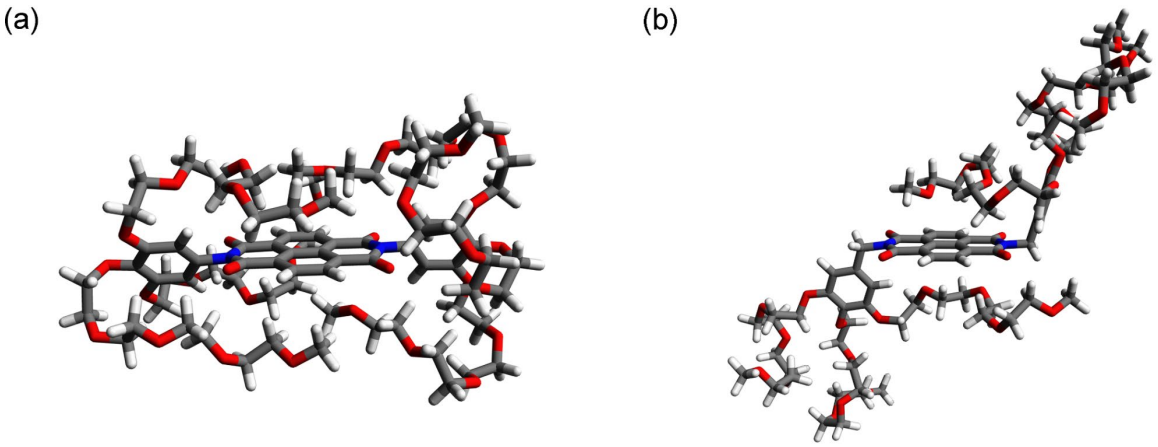


**Figure A31**: Geometry-optimized structures of (a) **NBI 4** and (b) **NBI 5** in water obtained by the PM7 method in MOPAC.

## 10.3 Appendix for Chapter 6

**Cloud point measurements**

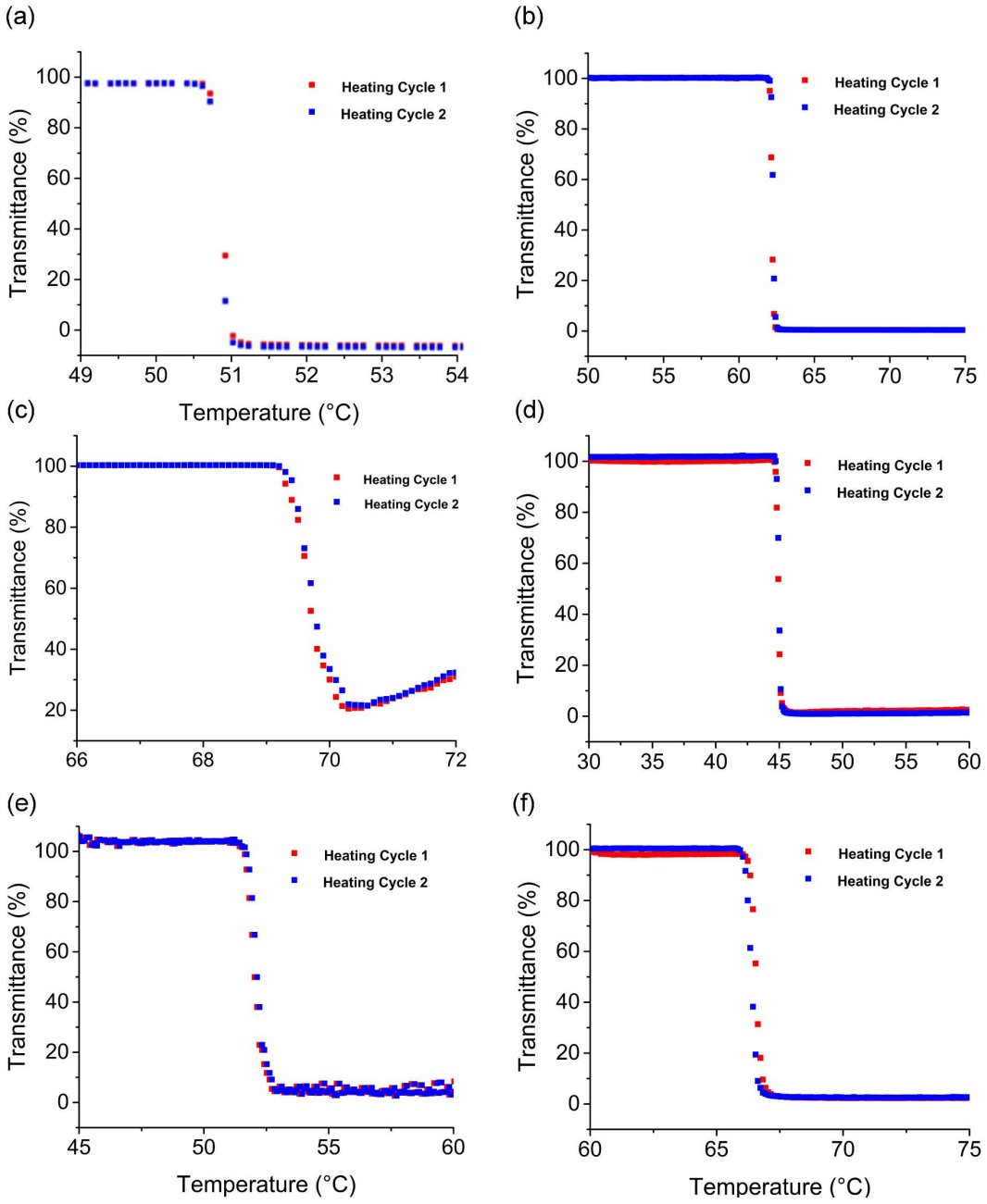


**Figure A32**: Cloud points determined by measuring transmittance at 800 nm as a function of temperature for (a) **PBI 1**, (b) **PBI 2**, (c) **PBI 3**, (d) **PBI 4**, (e) **PBI 5**, and (f) **PBI 6** ($c = 5 \times 10^{-4}$ M) in water (Heating rate: 0.1 °C/min). Fig. A32c is reproduced with permission from reference[68]. Copyright 2016 Wiley-VCH Verlag GmbH & Co. KGaA, Weinheim.

**NMR studies**

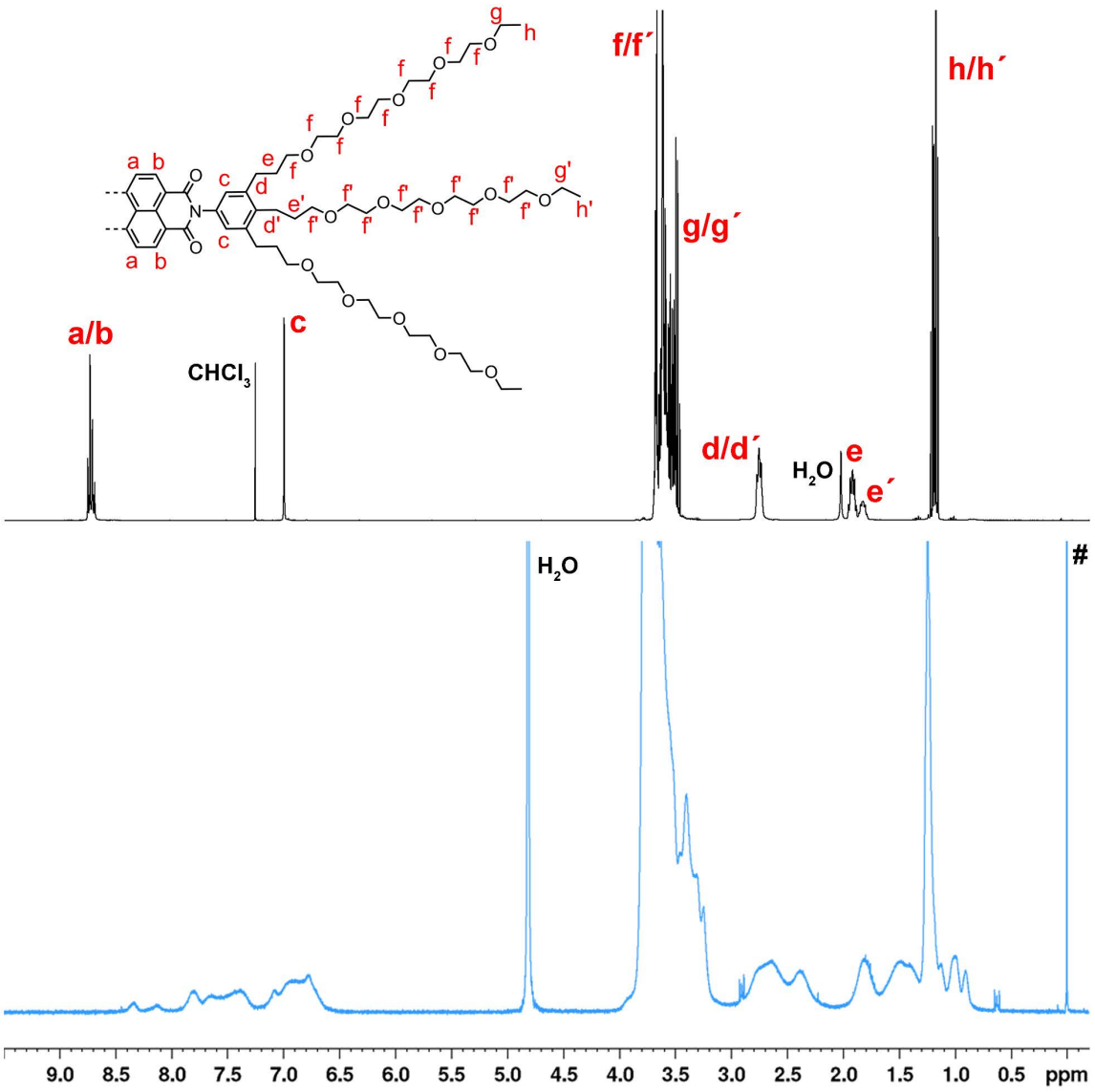


**Figure A33**: $^{1}$H NMR spectrum of **PBI 4** in $CDCl_3$ (black) and $D_2O$ (blue) at 295 K. Partial chemical structure of **PBI 4** with the significant protons assigned is also shown. (#: Internal standard for $D_2O$: 3-(Trimethylsilyl)propionic-2,2,3,3-$d_4$ acid sodium salt)

# References


1 R. Ludwig, *Angew. Chem. Int. Ed.*, 2001, **40**, 1808-1827.

2 G. V. Oshovsky, D. N. Reinhoudt and W. Verboom, *Angew. Chem. Int. Ed.*, 2007, **46**, 2366-2393.

3 J. Israelachvili, *Intermolecular and Surface Forces*, Academic Press, San Diego, third edn., 2010.

4 D. Chandler, *Nature*, 2005, **437**, 640-647.

5 C. Tanford, *Ben Franklin Stilled the Waves: An Informal History of Pouring Oil on Water: With Reflections on the Ups and Downs of Scientific Life in General*, Duke University Press, Durham, 1989.

6 L. Rayleigh, *Proc. R. Soc. Lond.*, 1889, **47**, 364–367.

7 J. Traube, *Justus Liebigs Ann. Chem.*, 1891, **265**, 27-55.

8 A. Pockels, *Nature*, 1891, **43**, 437-439.

9 I. Langmuir, *J. Am. Chem. Soc.*, 1917, **39**, 1848-1906.

10 M. E. Schott, in *The Posthumous Nobel Prize in Chemistry. Volume 2. Ladies in Waiting for the Nobel Prize*, American Chemical Society, 2018, pp. 151-182.

11 E. Gorter and F. Grendel, *J. Exp. Med.*, 1925, **41**, 439-443.

12 W. Kauzmann, *Adv. Prot. Chem.*, 1959, 1-64.

13 P. W. Snyder, M. R. Lockett, D. T. Moustakas and G. M. Whitesides, *Eur. Phys. J. Spec. Top.*, 2014, **223**, 853-891.

14 A. Biela, N. N. Nasief, M. Betz, A. Heine, D. Hangauer and G. Klebe, *Angew. Chem. Int. Ed.*, 2013, **52**, 1822-1828.

15 F. Biedermann, in *Comprehensive Supramolecular Chemistry II*, ed. J. L. Atwood, Elsevier, Oxford, 2017.

16 D. Görl, X. Zhang and F. Würthner, *Angew. Chem. Int. Ed.*, 2012, **51**, 6328-6348.

17 P. Besenius, G. Portale, P. H. H. Bomans, H. M. Janssen, A. R. A. Palmans and E. W. Meijer, *Proc. Natl. Acad. Sci. U. S. A.*, 2010, **107**, 17888-17893.

18 N. M. Matsumoto, R. P. M. Lafleur, X. Lou, K.-C. Shih, S. P. W. Wijnands, C. Guibert, J. W. A. M. van Rosendaal, I. K. Voets, A. R. A. Palmans, Y. Lin and E. W. Meijer, *J. Am. Chem. Soc.*, 2018, **140**, 13308-13316.

19 S. Cantekin, T. F. A. de Greef and A. R. A. Palmans, *Chem. Soc. Rev.*, 2012, **41**, 6125-6137.

20 S. M. C. Schoenmakers, C. M. A. Leenders, R. P. M. Lafleur, X. Lou, E. W. Meijer, G. M. Pavan and A. R. A. Palmans, *Chem. Commun.*, 2018, **54**, 11128-11131.

21 M. R. Molla and S. Ghosh, *Phys. Chem. Chem. Phys.*, 2014, **16**, 26672-26683.

22 P. Rajdev, S. Chakraborty, M. Schmutz, P. Mesini and S. Ghosh, *Langmuir*, 2017, **33**, 4789-4795.

23 P. Pramanik, D. Ray, V. K. Aswal and S. Ghosh, *Angew. Chem. Int. Ed.*, 2017, **56**, 3516-3520.

24 M. Sun, K. Müllen and M. Yin, *Chem. Soc. Rev.*, 2016, **45**, 1513-1528.

25 X. Lin, H. Kurata, D. D. Prabhu, M. Yamauchi, T. Ohba and S. Yagai, *Chem. Commun.*, 2017, **53**, 168-171.

26 Z. Huang, S.-K. Kang, M. Banno, T. Yamaguchi, D. Lee, C. Seok, E. Yashima and M. Lee, *Science*, 2012, **337**, 1521-1526.

27 Z. Huang, H. Lee, E. Lee, S.-K. Kang, J.-M. Nam and M. Lee, *Nat. Commun.*, 2011, **2**, 459.

28 Y. Kim, W. Li, S. Shin and M. Lee, *Acc. Chem. Res.*, 2013, **46**, 2888-2897.

29 F. J. M. Hoeben, I. O. Shklyarevskiy, M. J. Pouderoijen, H. Engelkamp, A. P. H. J. Schenning, P. C. M. Christianen, J. C. Maan and E. W. Meijer, *Angew. Chem. Int. Ed.*, 2006, **45**, 1232-1236.

30 J. F. Hulvat, M. Sofos, K. Tajima and S. I. Stupp, *J. Am. Chem. Soc.*, 2005, **127**, 366-372.

31 A. P. H. J. Schenning, E. Peeters and E. W. Meijer, *J. Am. Chem. Soc.*, 2000, **122**, 4489-4495.

32 F. García and L. Sánchez, *Chem. Eur. J.*, 2010, **16**, 3138-3146.

33 F. García, G. Fernández and L. Sánchez, *Chem. Eur. J.*, 2009, **15**, 6740-6747.

34 R. E. Hughes, S. P. Hart, D. A. Smith, B. Movaghar, R. J. Bushby and N. Boden, *J. Phys. Chem. B*, 2002, **106**, 6638-6645.

35 T. Bast and R. Hentschke, *J. Phys. Chem.*, 1996, **100**, 12162-12171.

36 B. El Hamaoui, L. Zhi, W. Pisula, U. Kolb, J. Wu and K. Müllen, *Chem. Commun.*, 2007, 2384-2386.

37 J. P. Hill, W. Jin, A. Kosaka, T. Fukushima, H. Ichihara, T. Shimomura, K. Ito, T. Hashizume, N. Ishii and T. Aida, *Science*, 2004, **304**, 1481-1483.

38 G. Zhang, W. Jin, T. Fukushima, A. Kosaka, N. Ishii and T. Aida, *J. Am. Chem. Soc.*, 2007, **129**, 719-722.

39 V. Grande, C.-A. Shen, M. Deiana, M. Dudek, J. Olesiak-Banska, K. Matczyszyn and F. Würthner, *Chem. Sci.*, 2018, **9**, 8375-8381.

40 Y. Q. Xu, Z. Y. Li, A. Malkovskiy, S. G. Sun and Y. Pang, *J. Phys. Chem. B*, 2010, **114**, 8574-8580.

41 V. Grande, F. Doria, M. Freccero and F. Würthner, *Angew. Chem. Int. Ed.*, 2017, **56**, 7520-7524.

42 S. Sreejith, P. Carol, P. Chithra and A. Ajayaghosh, *J. Mater. Chem.*, 2008, **18**, 264-274.

43 S. Bujosa, E. Castellanos, A. Frontera, C. Rotger, A. Costa and B. Soberats, *Org. Biomol. Chem.*, 2020, **18**, 888-894.

44 C. López, M. Ximenis, F. Orvay, C. Rotger and A. Costa, *Chem. Eur. J.*, 2017, **23**, 7590-7594.

45 M. Wehner and F. Würthner, *Nat. Rev. Chem.*, 2020, **4**, 38-53.

46 M. Hartlieb, E. D. H. Mansfield and S. Perrier, *Polym. Chem.*, 2020, **11**, 1083-1110.

47 J. Matern, Y. Dorca, L. Sánchez and G. Fernández, *Angew. Chem. Int. Ed.*, 2019, **58**, 16730-16740.

48 Z. Chen, A. Lohr, C. R. Saha-Möller and F. Würthner, *Chem. Soc. Rev.*, 2009, **38**, 564-584.

49 R. B. Martin, *Chem. Rev.*, 1996, **96**, 3043-3064.

50 M. M. Smulders, M. M. Nieuwenhuizen, T. F. de Greef, P. van der Schoot, A. P. Schenning and E. W. Meijer, *Chem. Eur. J.*, 2010, **16**, 362-367.

51 D. H. Zhao and J. S. Moore, *Org. Biomol. Chem.*, 2003, **1**, 3471-3491.

52 R. F. Goldstein and L. Stryer, *Biophys. J.*, 1986, **50**, 583-599.

53 J. Gershberg, F. Fennel, T. H. Rehm, S. Lochbrunner and F. Würthner, *Chem. Sci.*, 2016, **7**, 1729-1737.

54 T. F. A. De Greef, M. M. J. Smulders, M. Wolffs, A. P. H. J. Schenning, R. P. Sijbesma and E. W. Meijer, *Chem. Rev.*, 2009, **109**, 5687-5754.

55 P. S. Cremer, A. H. Flood, B. C. Gibb and D. L. Mobley, *Nat. Chem.*, 2018, **10**, 8-16.

56 J. M. Fox, M. Zhao, M. J. Fink, K. Kang and G. M. Whitesides, *Annu. Rev. Biophys.*, 2018, **47**, 223-250.

57 B. Breiten, M. R. Lockett, W. Sherman, S. Fujita, M. Al-Sayah, H. Lange, C. M. Bowers, A. Heroux, G. Krilov and G. M. Whitesides, *J. Am. Chem. Soc.*, 2013, **135**, 15579-15584.

58 G. Klebe, *Nat. Rev. Drug Discovery*, 2015, **14**, 95-110.

59 R. Alberstein, Y. Suzuki, F. Paesani and F. A. Tezcan, *Nat. Chem.*, 2018, **10**, 732-739.

60 D. Görl, Ph.D. Thesis, Julius-Maximilians-Universität Würzburg, 2015.

61 F. J. Hoeben, P. Jonkheijm, E. W. Meijer and A. P. H. J. Schenning, *Chem. Rev.*, 2005, **105**, 1491-1546.

62 M. Al Kobaisi, S. V. Bhosale, K. Latham, A. M. Raynor and S. V. Bhosale, *Chem. Rev.*, 2016, **116**, 11685-11796.

63 F. Würthner, C. R. Saha-Möller, B. Fimmel, S. Ogi, P. Leowanawat and D. Schmidt, *Chem. Rev.*, 2016, **116**, 962-1052.

64 Z. Chen, B. Fimmel and F. Würthner, *Org. Biomol. Chem.*, 2012, **10**, 5845-5855.

65 X. Zhang, Z. Chen and F. Würthner, *J. Am. Chem. Soc.*, 2007, **129**, 4886-4887.

66 X. Zhang, S. Rehm, M. M. Safont-Sempere and F. Würthner, *Nat. Chem.*, 2009, **1**, 623-629.

67 X. Zhang, D. Görl, V. Stepanenko and F. Würthner, *Angew. Chem. Int. Ed.*, 2014, **53**, 1270-1274.

68 D. Görl and F. Würthner, *Angew. Chem. Int. Ed.*, 2016, **55**, 12094-12098.

69 H. S. Frank and M. W. Evans, *J. Chem. Phys.*, 1945, **13**, 507-532.

70 M. B. Hillyer and B. C. Gibb, *Annu. Rev. Phys. Chem.*, 2016, **67**, 307-329.

71 B. Guillot, *J. Mol. Liq.*, 2002, **101**, 219-260.

72 M. W. Mahoney and W. L. Jorgensen, *J. Chem. Phys.*, 2000, **112**, 8910-8922.

73 R. Kumar, J. R. Schmidt and J. L. Skinner, *J. Chem. Phys.*, 2007, **126**, 204107.

74 H. S. Frank and W.-Y. Wen, *Discuss. Faraday Soc.*, 1957, **24**, 133-140.

75 P. Wernet, D. Nordlund, U. Bergmann, M. Cavalleri, M. Odelius, H. Ogasawara, L. Å. Näslund, T. K. Hirsch, L. Ojamäe, P. Glatzel, L. G. M. Pettersson and A. Nilsson, *Science*, 2004, **304**, 995-999.

76 W. Blokzijl and J. B. F. N. Engberts, *Angew. Chem. Int. Ed.*, 1993, **32**, 1545-1579.

77 R. L. Baldwin, *Proc. Natl. Acad. Sci. U. S. A.*, 2012, **109**, 7310-7313.

78 A. Ben-Naim, *J. Phys. Chem.*, 1978, **82**, 792-803.

79 A. Ben-Naim and Y. Marcus, *J. Chem. Phys.*, 1984, **81**, 2016-2027.

80 G. A. Jeffrey, *Acc. Chem. Res.*, 1969, **2**, 344-352.

81 J. Turner, A. K. Soper and J. L. Finney, *Mol. Phys.*, 1990, **70**, 679-700.

82 P. Buchanan, N. Aldiwan, A. K. Soper, J. L. Creek and C. A. Koh, *Chem. Phys. Lett.*, 2005, **415**, 89-93.

83 A. Ben-Naim, *Water and Aqueous Solutions: Introduction to a Molecular Theory.*, Plenum, New York, 1974.

84 C. Tanford, *Science*, 1978, **200**, 1012-1018.

85 D. Ben-Amotz, *Annu. Rev. Phys. Chem.*, 2016, **67**, 617-638.

86 W. P. Jencks, *Catalysis in Chemistry and Enzymology*, McGraw-Hill, New York, 1969.

87 F. H. Stillinger, *J. Solution Chem.*, 1973, **2**, 141-158.

88 K. Lum, D. Chandler and J. D. Weeks, *J. Phys. Chem. B*, 1999, **103**, 4570-4577.

89 J. G. Davis, K. P. Gierszal, P. Wang and D. Ben-Amotz, *Nature*, 2012, **491**, 582-585.

90 I. T. S. Li and G. C. Walker, *Proc. Natl. Acad. Sci. U. S. A.*, 2011, **108**, 16527-16532.

91 H. Lee, F. Dehez, C. Chipot, H. K. Lim and H. Kim, *J. Chem. Theory Comput.*, 2019, **15**, 1538-1545.

92 B. J. Berne, J. D. Weeks and R. Zhou, *Annu. Rev. Phys. Chem.*, 2009, **60**, 85-103.

93 J. Baz and N. Hansen, *J. Phys. Chem. C*, 2019, **123**, 8027-8036.

94 K. P. Murphy, *Biophys. Chem.*, 1994, **51**, 311-326.

95 N. T. Southall, K. A. Dill and A. D. J. Haymet, *J. Phys. Chem. B*, 2002, **106**, 521-533.

96 V. M. Krishnamurthy, B. R. Bohall, V. Semetey and G. M. Whitesides, *J. Am. Chem. Soc.*, 2006, **128**, 5802-5812.

97 J. Mecinović, P. W. Snyder, K. A. Mirica, S. Bai, E. T. Mack, R. L. Kwant, D. T. Moustakas, A. Héroux and G. M. Whitesides, *J. Am. Chem. Soc.*, 2011, **133**, 14017-14026.

98 V. M. Krishnamurthy, G. K. Kaufman, A. R. Urbach, I. Gitlin, K. L. Gudiksen, D. B. Weibel and G. M. Whitesides, *Chem. Rev.*, 2008, **108**, 946-1051.

99 L. Wang, B. J. Berne and R. A. Friesner, *Proc. Natl. Acad. Sci. U. S. A.*, 2011, **108**, 1326-1330.

100 D. B. Smithrud, T. B. Wyman and F. Diederich, *J. Am. Chem. Soc.*, 1991, **113**, 5420-5426.

101 P. Setny, R. Baron and J. A. McCammon, *J. Chem. Theory Comput.*, 2010, **6**, 2866-2871.

102 R. Baron, P. Setny and J. A. McCammon, *J. Am. Chem. Soc.*, 2010, **132**, 12091-12097.

103 F. Biedermann, V. D. Uzunova, O. A. Scherman, W. M. Nau and A. De Simone, *J. Am. Chem. Soc.*, 2012, **134**, 15318-15323.

104 D. Shetty, J. K. Khedkar, K. M. Park and K. Kim, *Chem. Soc. Rev.*, 2015, **44**, 8747-8761.

105 A. Waghe, J. C. Rasaiah and G. Hummer, *J. Chem. Phys.*, 2012, **137**, 044709.

106 S. Vaitheeswaran, H. Yin, J. C. Rasaiah and G. Hummer, *Proc. Natl. Acad. Sci. U. S. A.*, 2004, **101**, 17002-17005.

107 F. Biedermann, W. M. Nau and H.-J. Schneider, *Angew. Chem. Int. Ed.*, 2014, **53**, 11158-11171.

108 M. V. Rekharsky, Y. H. Ko, N. Selvapalam, K. Kim and Y. Inoue, *Supramol. Chem.*, 2007, **19**, 39-46.

109 M. V. Rekharsky, F. P. Schwarz, Y. B. Tewari and R. N. Goldberg, *J. Phys. Chem.*, 1994, **98**, 10282-10288.

110 T. Young, R. Abel, B. Kim, B. J. Berne and R. A. Friesner, *Proc. Natl. Acad. Sci. U. S. A.*, 2007, **104**, 808-813.

111 A. S. Bayden, D. T. Moustakas, D. Joseph-McCarthy and M. L. Lamb, *J. Chem. Inf. Model.*, 2015, **55**, 1552-1565.

112 F.-G. Klärner, B. Kahlert, A. Nellesen, J. Zienau, C. Ochsenfeld and T. Schrader, *J. Am. Chem. Soc.*, 2006, **128**, 4831-4841.

113 J. M. Farrell, V. Grande, D. Schmidt and F. Würthner, *Angew. Chem. Int. Ed.*, 2019, **58**, 16504-16507.

114 K. Shoyama and F. Würthner, *J. Am. Chem. Soc.*, 2019, **141**, 13008-13012.

115 R. Renner, M. Stolte and F. Würthner, *ChemistryOpen*, 2020, **9**, 32-39.

116 M. Kinoshita and T. Hayashi, *Phys. Chem. Chem. Phys.*, 2017, **19**, 25891-25904.

117 F. London, *Z. Phys. Chem. Abt.*, 1930, 222-251.

118 J. P. Wagner and P. R. Schreiner, *Angew. Chem. Int. Ed.*, 2015, **54**, 12274-12296.

119 P. Atkins and J. De Paula, *Physical Chemistry*, Oxford University Press, Oxford, eight edn., 2006.

120 S. Grimme, *Chem. Eur. J.*, 2012, **18**, 9955-9964.

121 J. Antony, R. Sure and S. Grimme, *Chem. Commun.*, 2015, **51**, 1764-1774.

122 L. Yang, C. Adam, G. S. Nichol and S. L. Cockroft, *Nat. Chem.*, 2013, **5**, 1006-1010.

123 J. Hwang, B. E. Dial, P. Li, M. E. Kozik, M. D. Smith and K. D. Shimizu, *Chem. Sci.*, 2015, **6**, 4358-4364.

124 M. S. Cubberley and B. L. Iverson, *J. Am. Chem. Soc.*, 2001, **123**, 7560-7563.

125 T. Liu and H.-J. Schneider, *Angew. Chem. Int. Ed.*, 2002, **41**, 1368-1370.

126 H.-J. Schneider, *Acc. Chem. Res.*, 2015, **48**, 1815-1822.

127 H.-J. Schneider and M. Wang, *J. Org. Chem.*, 1994, **59**, 7464-7472.

128 S. He, F. Biedermann, N. Vankova, L. Zhechkov, T. Heine, R. E. Hoffman, A. De Simone, T. T. Duignan and W. M. Nau, *Nat. Chem.*, 2018, **10**, 1252-1257.

129 H. Matter, M. Nazaré, S. Güssregen, D. W. Will, H. Schreuder, A. Bauer, M. Urmann, K. Ritter, M. Wagner and V. Wehner, *Angew. Chem. Int. Ed.*, 2009, **48**, 2911-2916.

130 C. D. Tatko and M. L. Waters, *Org. Lett.*, 2004, **6**, 3969-3972.

131 D. Pal and P. Chakrabarti, *J. Biomol. Struct. Dyn.*, 2001, **19**, 115-128.

132 C. D. Tatko and M. L. Waters, *Protein Sci.*, 2004, **13**, 2515-2522.

133 E. T. Kool, J. C. Morales and K. M. Guckian, *Angew. Chem. Int. Ed.*, 2000, **39**, 990-1009.

134 B. A. Ikkanda, S. A. Samuel and B. L. Iverson, *J. Org. Chem.*, 2014, **79**, 2029-2037.

135 T. Rehm and C. Schmuck, *Chem. Commun.*, 2008, 801-813.

136 L. Brunsveld, J. A. J. M. Vekemans, J. H. K. K. Hirschberg, R. P. Sijbesma and E. W. Meijer, *Proc. Natl. Acad. Sci. U. S. A.*, 2002, **99**, 4977-4982.

137 C. M. A. Leenders, L. Albertazzi, T. Mes, M. M. E. Koenigs, A. R. A. Palmans and E. W. Meijer, *Chem. Commun.*, 2013, **49**, 1963-1965.

138 C. M. A. Leenders, M. B. Baker, I. A. B. Pijpers, R. P. M. Lafleur, L. Albertazzi, A. R. A. Palmans and E. W. Meijer, *Soft Matter*, 2016, **12**, 2887-2893.

139 M. Fujita, M. Tominaga, A. Hori and B. Therrien, *Acc. Chem. Res.*, 2005, **38**, 369-378.

140 P. Mal, B. Breiner, K. Rissanen and J. R. Nitschke, *Science*, 2009, **324**, 1697-1699.

141 B. Honig and A. Nicholls, *Science*, 1995, **268**, 1144-1149.

142 T. H. Rehm and C. Schmuck, *Chem. Soc. Rev.*, 2010, **39**, 3597-3611.

143 F. Corbellini, L. Di Costanzo, M. Crego-Calama, S. Geremia and D. N. Reinhoudt, *J. Am. Chem. Soc.*, 2003, **125**, 9946-9947.

144 C. Kulkarni, E. W. Meijer and A. R. A. Palmans, *Acc. Chem. Res.*, 2017, **50**, 1928-1936.

145 P. J. M. Stals, J. F. Haveman, R. Martin-Rapun, C. F. C. Fitie, A. R. A. Palmans and E. W. Meijer, *J. Mater. Chem.*, 2009, **19**, 124-130.

146 M. B. Baker, L. Albertazzi, I. K. Voets, C. M. Leenders, A. R. A. Palmans, G. M. Pavan and E. W. Meijer, *Nat. Commun.*, 2015, **6**, 6234-6246.

147 M. Garzoni, M. B. Baker, C. M. A. Leenders, I. K. Voets, L. Albertazzi, A. R. A. Palmans, E. W. Meijer and G. M. Pavan, *J. Am. Chem. Soc.*, 2016, **138**, 13985-13995.

148 C. Schaefer, I. K. Voets, A. R. A. Palmans, E. W. Meijer, P. van der Schoot and P. Besenius, *ACS Macro Lett.*, 2012, **1**, 830-833.

149 H. Fenniri, B. L. Deng, A. E. Ribbe, K. Hallenga, J. Jacob and P. Thiyagarajan, *Proc. Natl. Acad. Sci. U. S. A.*, 2002, **99**, 6487-6492.

150 H. Fenniri, B.-L. Deng and A. E. Ribbe, *J. Am. Chem. Soc.*, 2002, **124**, 11064-11072.

151 V. Saez Talens, P. Englebienne, T. T. Trinh, W. E. M. Noteborn, I. K. Voets and R. E. Kieltyka, *Angew. Chem. Int. Ed.*, 2015, **54**, 10502-10506.

152 R. Scott Lokey and B. L. Iverson, *Nature*, 1995, **375**, 303-305.

153 B. A. Ikkanda and B. L. Iverson, *Chem. Commun.*, 2016, **52**, 7752-7759.

154 M. Kumar and S. J. George, *Nanoscale*, 2011, **3**, 2130-2133.

155 H. Shao, T. Nguyen, N. C. Romano, D. A. Modarelli and J. R. Parquette, *J. Am. Chem. Soc.*, 2009, **131**, 16374-16376.

156 H. Shao, J. Seifert, N. C. Romano, M. Gao, J. J. Helmus, C. P. Jaroniec, D. A. Modarelli and J. R. Parquette, *Angew. Chem. Int. Ed.*, 2010, **49**, 7688-7691.

157 M. Kumar, N. L. Ing, V. Narang, N. K. Wijerathne, A. I. Hochbaum and R. V. Ulijn, *Nat. Chem.*, 2018, **10**, 696-703.

158 M. Kumar, N. Jonnalagadda and S. J. George, *Chem. Commun.*, 2012, **48**, 10948-10950.

159 M. Kumar, P. Brocorens, C. Tonnelé, D. Beljonne, M. Surin and S. J. George, *Nat. Commun.*, 2014, **5**, 5793.

160 S. Dhiman, A. Jain and S. J. George, *Angew. Chem. Int. Ed.*, 2017, **56**, 1329-1333.

161 S. Dhiman, A. Jain, M. Kumar and S. J. George, *J. Am. Chem. Soc.*, 2017, **139**, 16568-16575.

162 M. R. Molla and S. Ghosh, *Chem. Eur. J.*, 2012, **18**, 9860-9869.

163 P. Rajdev, M. R. Molla and S. Ghosh, *Langmuir*, 2014, **30**, 1969-1976.

164 A. Sikder, D. Ray, V. K. Aswal and S. Ghosh, *Angew. Chem. Int. Ed.*, 2019, **58**, 1606-1611.

165 P. Dey, P. Rajdev, P. Pramanik and S. Ghosh, *Macromolecules*, 2018, **51**, 5182-5190.

166 A. Sikder, D. Ray, V. K. Aswal and S. Ghosh, *Chem. Eur. J.*, 2019, **25**, 10464-10471.

167 X. Zhang, D. Görl and F. Würthner, *Chem. Commun.*, 2013, **49**, 8178-8180.

168 M. Ogasawara, X. Lin, H. Kurata, H. Ouchi, M. Yamauchi, T. Ohba, T. Kajitani, T. Fukushima, M. Numata, R. Nogami, B. Adhikari and S. Yagai, *Mater. Chem. Front.*, 2018, **2**, 171-179.

169 T. Heek, C. Fasting, C. Rest, X. Zhang, F. Würthner and R. Haag, *Chem. Commun.*, 2010, **46**, 1884-1886.

170 T. Heek, F. Würthner and R. Haag, *Chem. Eur. J.*, 2013, **19**, 10911-10921.

171 S. Rehm, V. Stepanenko, X. Zhang, T. H. Rehm and F. Würthner, *Chem. Eur. J.*, 2010, **16**, 3372-3382.

172 Z. Chen, U. Baumeister, C. Tschierske and F. Würthner, *Chem. Eur. J.*, 2007, **13**, 450-465.

173 D. Görl, X. Zhang, V. Stepanenko and F. Würthner, *Nat. Commun.*, 2015, **6**, 7009-7017.

174 V. Grande, B. Soberats, S. Herbst, V. Stepanenko and F. Würthner, *Chem. Sci.*, 2018, **9**, 6904-6911.

175 E. Krieg, H. Weissman, E. Shimoni, A. Bar On and B. Rybtchinski, *J. Am. Chem. Soc.*, 2014, **136**, 9443-9452.

176 J. Baram, H. Weissman, Y. Tidhar, I. Pinkas and B. Rybtchinski, *Angew. Chem. Int. Ed.*, 2014, **53**, 4123-4126.

177 E. Krieg, A. Niazov-Elkan, E. Cohen, Y. Tsarfati and B. Rybtchinski, *Acc. Chem. Res.*, 2019, **52**, 2634-2646.

178 J. Baram, H. Weissman and B. Rybtchinski, *J. Phys. Chem. B*, 2014, **118**, 12068-12073.

179 E. Krieg, E. Shirman, H. Weissman, E. Shimoni, S. G. Wolf, I. Pinkas and B. Rybtchinski, *J. Am. Chem. Soc.*, 2009, **131**, 14365-14373.

180 E. Krieg, H. Weissman, E. Shirman, E. Shimoni and B. Rybtchinski, *Nat. Nanotechnol.*, 2011, **6**, 141-146.

181 J. Wu, J. Li, U. Kolb and K. Müllen, *Chem. Commun.*, 2006, 48-50.

182 E. Lee, J. K. Kim and M. Lee, *Angew. Chem. Int. Ed.*, 2009, **48**, 3657-3660.

183 E. Lee, J.-K. Kim and M. Lee, *J. Am. Chem. Soc.*, 2009, **131**, 18242-18243.

184 D.-W. Lee, T. Kim, I.-S. Park, Z. Huang and M. Lee, *J. Am. Chem. Soc.*, 2012, **134**, 14722-14725.

185 T. Kim, H. Lee, Y. Kim, J.-M. Nam and M. Lee, *Chem. Commun.*, 2013, **49**, 3949-3951.

186 H.-J. Kim, S.-K. Kang, Y.-K. Lee, C. Seok, J.-K. Lee, W.-C. Zin and M. Lee, *Angew. Chem. Int. Ed.*, 2010, **49**, 8471-8475.

187 Y. Wang, Z. Huang, Y. Kim, Y. He and M. Lee, *J. Am. Chem. Soc.*, 2014, **136**, 16152-16155.

188 S. Shin, S. Lim, Y. Kim, T. Kim, T.-L. Choi and M. Lee, *J. Am. Chem. Soc.*, 2013, **135**, 2156-2159.

189 F. Biedermann and H.-J. Schneider, *Chem. Rev.*, 2016, **116**, 5216-5300.

190 C. Shao, M. Grüne, M. Stolte and F. Würthner, *Chem. Eur. J.*, 2012, **18**, 13665-13677.

191 F. Würthner, S. Yao, T. Debaerdemaeker and R. Wortmann, *J. Am. Chem. Soc.*, 2002, **124**, 9431-9447.

192 W. West and S. Pearce, *J. Phys. Chem.*, 1965, **69**, 1894-1903.

193 F. Würthner and S. Yao, *Angew. Chem. Int. Ed.*, 2000, **39**, 1978-1981.

194 Y. C. Yang, J. R. Ward and R. P. Seiders, *Inorg. Chem.*, 1985, **24**, 1765-1769.

195 A. Weißenstein and F. Würthner, *Chem. Commun.*, 2015, **51**, 3415-3418.

196 D. Zhao and J. S. Moore, *J. Org. Chem.*, 2002, **67**, 3548-3554.

197 A. Arnaud, J. Belleney, F. Boue, L. Bouteiller, G. Carrot and V. Wintgens, *Angew. Chem. Int. Ed.*, 2004, **43**, 1718-1721.

198 M. M. J. Smulders, A. P. H. J. Schenning and E. W. Meijer, *J. Am. Chem. Soc.*, 2008, **130**, 606-611.

199 P. Jonkheijm, P. van der Schoot, A. P. H. J. Schenning and E. W. Meijer, *Science*, 2006, **313**, 80-83.

200 G. Weber, *J. Phys. Chem.*, 1995, **99**, 1052-1059.

201 H. S. Harned and N. D. Embree, *J. Am. Chem. Soc.*, 1934, **56**, 1050-1053.

202 F. P. Schmidtchen, in *Analytical Methods in Supramolecular Chemistry*, ed. C. A. Schalley, Wiley-VCH, Weinheim, second edn., 2012, pp. 67-103.

203 E. C. W. Clarke and D. N. Glew, *Trans. Faraday Soc.*, 1966, **62**, 539-547.

204 M. J. Blandamer, *Chemical Equilibria in Solution*, Ellis Horwood, Chichester, 1992.

205 M. Kabiri and L. D. Unsworth, *Biomacromolecules*, 2014, **15**, 3463-3473.

206 L. K. S. von Krbek, C. A. Schalley and P. Thordarson, *Chem. Soc. Rev.*, 2017, **46**, 2622-2637.

207 P. Thordarson, *Chem. Soc. Rev.*, 2011, **40**, 1305-1323.

208 I. Herrera and M. A. Winnik, *J. Phys. Chem. B*, 2016, **120**, 2077-2086.

209 I. Wadsö, *Chem. Soc. Rev.*, 1997, **26**, 79-86.

210 D. E. Wilcox, *Inorg. Chim. Acta*, 2008, **361**, 857-867.

211 L. S. Roselin, M.-S. Lin, P.-H. Lin, Y. Chang and W.-Y. Chen, *Biotechnol. J*, 2010, **5**, 85-98.

212 A. Arnaud and L. Bouteiller, *Langmuir*, 2004, **20**, 6858-6863.

213 N. J. Buurma and I. Haq, *J. Mol. Biol.*, 2008, **381**, 607-621.

214 I. Turcu and M. Mic, *J. Phys. Chem. B*, 2013, **117**, 9083-9093.

215 K. Bouchemal, F. Agnely, A. Koffi, M. Djabourov and G. Ponchel, *J. Mol. Recognit.*, 2010, **23**, 335-342.

216 S. Paula, W. Sues, J. Tuchtenhagen and A. Blume, *J. Phys. Chem.*, 1995, **99**, 11742-11751.

217 M. M. Kozlov, E. Opatowski and D. Lichtenberg, *J. Therm. Anal. Calorim.*, 1998, **51**, 173-189.

218 R. Zana, *Langmuir*, 1996, **12**, 1208-1211.

219 M. Bellot and L. Bouteiller, *Langmuir*, 2008, **24**, 14176-14182.

220 I. Turcu and M. Bogdan, *J. Phys. Chem. B*, 2012, **116**, 6488-6498.

221 M. Kaushik and S. Kukreti, *Spectrochim. Acta, Part A*, 2003, **59**, 3123-3129.

222 I. Haq, T. C. Jenkins, B. Z. Chowdhry, J. Ren and J. B. Chaires, in *Methods Enzymol.*, Academic Press, 2000, vol. 323, pp. 373-405.

223 M.-V. Salvia, F. Addison, H. Y. Alniss, N. J. Buurma, A. I. Khalaf, S. P. Mackay, N. G. Anthony, C. J. Suckling, M. P. Evstigneev, A. H. Santiago, R. D. Waigh and J. A. Parkinson, *Biophys. Chem.*, 2013, **179**, 1-11.

224 L. Hahn, N. J. Buurma and L. H. Gade, *Chem. Eur. J.*, 2016, **22**, 6314-6322.

225 B. B. Raju, F. M. Winnik and Y. Morishima, *Langmuir*, 2001, **17**, 4416-4421.

226 W. M. Groenewoud, in *Characterisation of Polymers by Thermal Analysis*, ed. W. M. Groenewoud, Elsevier Science B.V., Amsterdam, 2001, pp. 10-60.

227 I. Jelesarov and H. R. Bosshard, *J. Mol. Recognit.*, 1999, **12**, 3-18.

228 G. Ungar and J. L. Feijoo, *Mol. Cryst. Liq. Cryst. Incorporating Nonlinear Opt.*, 1990, **180**, 281-291.

229 L. Chiappisi, G. Lazzara, M. Gradzielski and S. Milioto, *Langmuir*, 2012, **28**, 17609-17616.

230 D. Görl, B. Soberats, S. Herbst, V. Stepanenko and F. Würthner, *Chem. Sci.*, 2016, **7**, 6786-6790.

231 B. A. Scates, B. L. Lashbrook, B. C. Chastain, K. Tominaga, B. T. Elliott, N. J. Theising, T. A. Baker and R. W. Fitch, *Biorg. Med. Chem.*, 2008, **16**, 10295-10300.

232 W. Tao, S. Nesbitt and R. F. Heck, *J. Org. Chem.*, 1990, **55**, 63-69.

233 M. D. Tzirakis, M. N. Alberti, H. Weissman, B. Rybtchinski and F. Diederich, *Chem. Eur. J.*, 2014, **20**, 16070-16073.

234 P. D. Frischmann, L. C. H. Gerber, S. E. Doris, E. Y. Tsai, F. Y. Fan, X. Qu, A. Jain, K. A. Persson, Y.-M. Chiang and B. A. Helms, *Chem. Mater.*, 2015, **27**, 6765-6770.

235 C. Huang, S. Barlow and S. R. Marder, *J. Org. Chem.*, 2011, **76**, 2386-2407.

236 C. M. Dobson, *Nature*, 2003, **426**, 884-890.

237 K. C. Holmes, D. Popp, W. Gebhard and W. Kabsch, *Nature*, 1990, **347**, 44-49.

238 E. Nogales, *Annu. Rev. Biochem*, 2000, **69**, 277-302.

239 E. Krieg, M. M. C. Bastings, P. Besenius and B. Rybtchinski, *Chem. Rev.*, 2016, **116**, 2414-2477.

240 T. P. Knowles, A. W. Fitzpatrick, S. Meehan, H. R. Mott, M. Vendruscolo, C. M. Dobson and M. E. Welland, *Science*, 2007, **318**, 1900-1903.

241 B. N. S. Thota, L. H. Urner and R. Haag, *Chem. Rev.*, 2016, **116**, 2079-2102.

242 A. Ustinov, H. Weissman, E. Shirman, I. Pinkas, X. Zuo and B. Rybtchinski, *J. Am. Chem. Soc.*, 2011, **133**, 16201-16211.

243 M. Hariharan, Y. Zheng, H. Long, T. A. Zeidan, G. C. Schatz, J. Vura-Weis, M. R. Wasielewski, X. Zuo, D. M. Tiede and F. D. Lewis, *J. Am. Chem. Soc.*, 2009, **131**, 5920-5929.

244 M. J. Mayoral, C. Rest, V. Stepanenko, J. Schellheimer, R. Q. Albuquerque and G. Fernández, *J. Am. Chem. Soc.*, 2013, **135**, 2148-2151.

245 G. Golubkov, H. Weissman, E. Shirman, S. G. Wolf, I. Pinkas and B. Rybtchinski, *Angew. Chem. Int. Ed.*, 2009, **48**, 926-930.

246 M. Kumar and S. J. George, *Chem. Eur. J.*, 2011, **17**, 11102-11106.

247 N. K. Allampally, A. Florian, M. J. Mayoral, C. Rest, V. Stepanenko and G. Fernández, *Chem. Eur. J.*, 2014, **20**, 10669-10678.

248 F. C. Spano, *Acc. Chem. Res.*, 2010, **43**, 429-439.

249 N. J. Van Zee, B. Adelizzi, M. F. J. Mabesoone, X. Meng, A. Aloi, R. H. Zha, M. Lutz, I. A. W. Filot, A. R. A. Palmans and E. W. Meijer, *Nature*, 2018, **558**, 100-103.

250 K. Venkata Rao, D. Miyajima, A. Nihonyanagi and T. Aida, *Nat. Chem.*, 2017, **9**, 1133.

251 H. Naghibi, A. Tamura and J. M. Sturtevant, *Proc. Natl. Acad. Sci. U. S. A.*, 1995, **92**, 5597-5599.

252 J. R. Horn, D. Russell, E. A. Lewis and K. P. Murphy, *Biochemistry*, 2001, **40**, 1774-1778.

253 P. W. Snyder, J. Mecinović, D. T. Moustakas, S. W. Thomas, M. Harder, E. T. Mack, M. R. Lockett, A. Héroux, W. Sherman and G. M. Whitesides, *Proc. Natl. Acad. Sci. U. S. A.*, 2011, **108**, 17889-17894.

254 M. V. Rekharsky, T. Mori, C. Yang, Y. H. Ko, N. Selvapalam, H. Kim, D. Sobransingh, A. E. Kaifer, S. Liu, L. Isaacs, W. Chen, S. Moghaddam, M. K. Gilson, K. Kim and Y. Inoue, *Proc. Natl. Acad. Sci. U. S. A.*, 2007, **104**, 20737-20742.

255 M. Ciardi, A. Galán and P. Ballester, *J. Am. Chem. Soc.*, 2015, **137**, 2047-2055.

256 A. Camara-Campos, C. A. Hunter and S. Tomas, *Proc. Natl. Acad. Sci. U. S. A.*, 2006, **103**, 3034-3038.

257 F. Aparicio, F. García and L. Sánchez, *Chem. Eur. J.*, 2013, **19**, 3239-3248.

258 N. J. Buurma and I. Haq, *Methods*, 2007, **42**, 162-172.

259 S. Sun and P. Wu, *Macromolecules*, 2013, **46**, 236-246.

260 R. Molina-Muriel, G. Aragay, E. C. Escudero-Adán and P. Ballester, *J. Org. Chem.*, 2018, **83**, 13507-13514.

261 S. Kubetzko, C. A. Sarkar and A. Plückthun, *Mol. Pharmacol.*, 2005, **68**, 1439-1454.

262 S. Kubetzko, E. Balic, R. Waibel, U. Zangemeister-Wittke and A. Plückthun, *J. Biol. Chem.*, 2006, **281**, 35186-35201.

263 T. F. A. de Greef, M. M. L. Nieuwenhuizen, R. P. Sijbesma and E. W. Meijer, *J. Org. Chem.*, 2010, **75**, 598-610.

264 T. Aida, E. W. Meijer and S. I. Stupp, *Science*, 2012, **335**, 813-817.

265 X. Yan, F. Wang, B. Zheng and F. Huang, *Chem. Soc. Rev.*, 2012, **41**, 6042-6065.

266 F. Tantakitti, J. Boekhoven, X. Wang, R. V. Kazantsev, T. Yu, J. Li, E. Zhuang, R. Zandi, J. H. Ortony, C. J. Newcomb, L. C. Palmer, G. S. Shekhawat, M. O. de la Cruz, G. C. Schatz and S. I. Stupp, *Nat. Mater.*, 2016, **15**, 469-476.

267 B. Kemper, L. Zengerling, D. Spitzer, R. Otter, T. Bauer and P. Besenius, *J. Am. Chem. Soc.*, 2018, **140**, 534-537.

268 M. P. Hendricks, K. Sato, L. C. Palmer and S. I. Stupp, *Acc. Chem. Res.*, 2017, **50**, 2440-2448.

269 K. V. Rao and S. J. George, *Org. Lett.*, 2010, **12**, 2656-2659.

270 M. Yin, J. Shen, W. Pisula, M. Liang, L. Zhi and K. Müllen, *J. Am. Chem. Soc.*, 2009, **131**, 14618-14619.

271 Y. Kim, T. Kim and M. Lee, *Polym. Chem.*, 2013, **4**, 1300-1308.

272 C. Rest, M. J. Mayoral, K. Fucke, J. Schellheimer, V. Stepanenko and G. Fernández, *Angew. Chem. Int. Ed.*, 2014, **53**, 700-705.

273 T. Rudolph, N. Kumar Allampally, G. Fernández and F. H. Schacher, *Chem. Eur. J.*, 2014, **20**, 13871-13875.

274 R. Thirumalai, R. D. Mukhopadhyay, V. K. Praveen and A. Ajayaghosh, *Sci. Rep.*, 2015, **5**, 9842.

275 N. Saito, H. Kobayashi and M. Yamaguchi, *Chem. Sci.*, 2016, **7**, 3574-3580.

276 R. A. Shalaby and M. A. Lauffer, *Arch. Biochem. Biophys.*, 1985, **236**, 390-398.

277 P. Friedhoff, A. Schneider, E.-M. Mandelkow and E. Mandelkow, *Biochemistry*, 1998, **37**, 10223-10230.

278 K. E. Kadler, Y. Hojima and D. J. Prockop, *J. Biol. Chem.*, 1987, **262**, 15696-15701.

279 P. P. N. Syamala, B. Soberats, D. Görl, S. Gekle and F. Würthner, *Chem. Sci.*, 2019, **10**, 9358-9366.

280 G. G. Ferenczy and G. M. Keserű, *Drug Discov. Today*, 2010, **15**, 919-932.

281 T. Shikata, M. Okuzono and N. Sugimoto, *Macromolecules*, 2013, **46**, 1956-1961.

282 G. M. Whitesides, J. P. Mathias and C. T. Seto, *Science*, 1991, **254**, 1312-1319.

283 H. Oshima, T. Hayashi and M. Kinoshita, *Biophys. J.*, 2016, **110**, 2496-2506.

284 T. Hayashi, H. Oshima, T. Mashima, T. Nagata, M. Katahira and M. Kinoshita, *Nucleic Acids Res.*, 2014, **42**, 6861-6875.

285 T. Hayashi, H. Oshima, S. Yasuda and M. Kinoshita, *J. Phys. Chem. B*, 2015, **119**, 14120-14129.

286 C. Roche, H.-J. Sun, P. Leowanawat, F. Araoka, B. E. Partridge, M. Peterca, D. A. Wilson, M. E. Prendergast, P. A. Heiney, R. Graf, H. W. Spiess, X. Zeng, G. Ungar and V. Percec, *Nat. Chem.*, 2016, **8**, 80-89.

287 T. Aida and E. W. Meijer, *Isr. J. Chem.*, 2020, **60**, 33-47.

288 S. Yagai and A. Kitamura, *Chem. Soc. Rev.*, 2008, **37**, 1520-1529.

289 S. Tamesue, Y. Takashima, H. Yamaguchi, S. Shinkai and A. Harada, *Angew. Chem. Int. Ed.*, 2010, **49**, 7461-7464.

290 R. D. Mukhopadhyay, V. K. Praveen, A. Hazra, T. K. Maji and A. Ajayaghosh, *Chem. Sci.*, 2015, **6**, 6583-6591.

291 M. Burnworth, L. Tang, J. R. Kumpfer, A. J. Duncan, F. L. Beyer, G. L. Fiore, S. J. Rowan and C. Weder, *Nature*, 2011, **472**, 334-337.

292 T. Muraoka, C.-Y. Koh, H. Cui and S. I. Stupp, *Angew. Chem. Int. Ed.*, 2009, **48**, 5946-5949.

293 V. R. de la Rosa, P. Woisel and R. Hoogenboom, *Mater. Today*, 2016, **19**, 44-55.

294 R. D. Mukhopadhyay, G. Das and A. Ajayaghosh, *Nat. Commun.*, 2018, **9**, 1987.

295 P. Cordier, F. Tournilhac, C. Soulié-Ziakovic and L. Leibler, *Nature*, 2008, **451**, 977-980.

296 Y. S. Kim, M. Liu, Y. Ishida, Y. Ebina, M. Osada, T. Sasaki, T. Hikima, M. Takata and T. Aida, *Nat. Mat.*, 2015, **14**, 1002-1007.

297 R. P. Sijbesma, F. H. Beijer, L. Brunsveld, B. J. B. Folmer, J. H. K. K. Hirschberg, R. F. M. Lange, J. K. L. Lowe and E. W. Meijer, *Science*, 1997, **278**, 1601-1604.

298 Z. Ge, J. Hu, F. Huang and S. Liu, *Angew. Chem. Int. Ed.*, 2009, **48**, 1798-1802.

299 J. R. Kumpfer and S. J. Rowan, *J. Am. Chem. Soc.*, 2011, **133**, 12866-12874.

300 A. Harada and A. Hashidzume, in *Chemoresponsive Materials: Stimulation by Chemical and Biological Signals*, ed. H.-J. Schneider, The Royal Society of Chemistry, Cambridge, 2015, pp. 167-207.

301 Y. Li, T. Park, J. K. Quansah and S. C. Zimmerman, *J. Am. Chem. Soc.*, 2011, **133**, 17118-17121.

302 M. Nakahata, Y. Takashima, H. Yamaguchi and A. Harada, *Nat. Commun.*, 2011, **2**, 511.

303 A. Klaikherd, C. Nagamani and S. Thayumanavan, *J. Am. Chem. Soc.*, 2009, **131**, 4830-4838.

304 R. K. Mishra, S. Das, B. Vedhanarayanan, G. Das, V. K. Praveen and A. Ajayaghosh, in *Molecular Gels: Structure and Dynamics*, The Royal Society of Chemistry, Cambridge, 2018, pp. 190-226.

305 J. Zhuang, M. R. Gordon, J. Ventura, L. Li and S. Thayumanavan, *Chem. Soc. Rev.*, 2013, **42**, 7421-7435.

306 Q. Zhang, C. Weber, U. S. Schubert and R. Hoogenboom, *Mater. Horiz.*, 2017, **4**, 109-116.

307 S. Mura, J. Nicolas and P. Couvreur, *Nat. Mat.*, 2013, **12**, 991-1003.

308 D. Schmaljohann, *Adv. Drug Deliv. Rev.*, 2006, **58**, 1655-1670.

309 F. Yhaya, J. Lim, Y. Kim, M. Liang, A. M. Gregory and M. H. Stenzel, *Macromolecules*, 2011, **44**, 8433-8445.

310 L. Zhang, R. Guo, M. Yang, X. Jiang and B. Liu, *Adv. Mater.*, 2007, **19**, 2988-2992.

311 F. Hapiot, S. Menuel and E. Monflier, *ACS Catalysis*, 2013, **3**, 1006-1010.

312 L. Wang, H. Zou, Z. Dong, L. Zhou, J. Li, Q. Luo, J. Zhu, J. Xu and J. Liu, *Langmuir*, 2014, **30**, 4013-4018.

313 M. Kimura, M. Kato, T. Muto, K. Hanabusa and H. Shirai, *Macromolecules*, 2000, **33**, 1117-1119.

314 C. Koopmans and H. Ritter, *J. Am. Chem. Soc.*, 2007, **129**, 3502-3503.

315 K. Kataoka, H. Miyazaki, T. Okano and Y. Sakurai, *Macromolecules*, 1994, **27**, 1061-1062.

316 T. Liu and S. Liu, *Anal. Chem.*, 2011, **83**, 2775-2785.

317 M. Heskins and J. E. Guillet, *J. Macromol. Sci. Part A*, 1968, **2**, 1441-1455.

318 J.-F. Lutz, Ö. Akdemir and A. Hoth, *J. Am. Chem. Soc.*, 2006, **128**, 13046-13047.

319 D. Roy, W. L. A. Brooks and B. S. Sumerlin, *Chem. Soc. Rev.*, 2013, **42**, 7214-7243.

320 J. Seuring and S. Agarwal, *Macromol. Rapid Commun.*, 2012, **33**, 1898-1920.

321 V. Aseyev, H. Tenhu and F. M. Winnik, in *Self Organized Nanostructures of Amphiphilic Block Copolymers II*, eds. H. E. A. Müller and O. Borisov, Springer-Verlag Berlin Heidelberg, Berlin, Heidelberg, 2011, pp. 29-89.

322 Y.-J. Kim and Y. T. Matsunaga, *J. Mater. Chem. B*, 2017, **5**, 4307-4321.

323 A. K. Teotia, H. Sami and A. Kumar, in *Switchable and Responsive Surfaces and Materials for Biomedical Applications*, ed. Z. Zhang, Woodhead Publishing, Cambridge, 2015, pp. 3-43.

324 J. E. Betancourt and J. M. Rivera, *J. Am. Chem. Soc.*, 2009, **131**, 16666-16668.

325 J. E. Betancourt and J. M. Rivera, *Langmuir*, 2015, **31**, 2095-2103.

326 P. Wei, T. R. Cook, X. Yan, F. Huang and P. J. Stang, *J. Am. Chem. Soc.*, 2014, **136**, 15497-15500.

327 X. Li, C.-T. Poon, E. Y.-H. Hong, H.-L. Wong, A. K.-W. Chan, L. Wu and V. W.-W. Yam, *Soft Matter*, 2017, **13**, 8408-8418.

328 J. M. Fuller, K. R. Raghupathi, R. R. Ramireddy, A. V. Subrahmanyam, V. Yesilyurt and S. Thayumanavan, *J. Am. Chem. Soc.*, 2013, **135**, 8947-8954.

329 O. Munkhbat, M. Garzoni, K. R. Raghupathi, G. M. Pavan and S. Thayumanavan, *Langmuir*, 2016, **32**, 2874-2881.

330 T. Hirose, M. Irie and K. Matsuda, *Adv. Mater.*, 2008, **20**, 2137-2141.

331 K. R. Raghupathi, U. Sridhar, K. Byrne, K. Raghupathi and S. Thayumanavan, *J. Am. Chem. Soc.*, 2015, **137**, 5308-5311.

332 T. Ogoshi, K. Kida and T.-a. Yamagishi, *J. Am. Chem. Soc.*, 2012, **134**, 20146-20150.

333 L. Li, Y. Che, D. E. Gross, H. Huang, J. S. Moore and L. Zang, *ACS Macro Lett.*, 2012, **1**, 1335-1338.

334 Z. Huang, H. Lee, E. Lee, S.-K. Kang, J.-M. Nam and M. Lee, *Nat. Commun.*, 2011, **2**, 459.

335 K.-S. Moon, H.-J. Kim, E. Lee and M. Lee, *Angew. Chem. Int. Ed.*, 2007, **46**, 6807-6810.

336 S. Sengupta, D. Ebeling, S. Patwardhan, X. Zhang, H. von Berlepsch, C. Böttcher, V. Stepanenko, S. Uemura, C. Hentschel, H. Fuchs, F. C. Grozema, L. D. A. Siebbeles, A. R. Holzwarth, L. Chi and F. Würthner, *Angew. Chem. Int. Ed.*, 2012, **51**, 6378-6382.

337 F. Würthner, C. Thalacker, S. Diele and C. Tschierske, *Chem. Eur. J.*, 2001, **7**, 2245-2253.

338 R. Kjellander and E. Florin, *J. Chem. Soc., Faraday Trans. 1*, 1981, **77**, 2053-2077.

339 A. Maconnachie, P. Vasudevan and G. Allen, *Polymer*, 1978, **19**, 33-38.

340 Y. C. Bae, S. M. Lambert, D. S. Soane and J. M. Prausnitz, *Macromolecules*, 1991, **24**, 4403-4407.

341 T. Li, H. Tang and P. Wu, *Soft Matter*, 2015, **11**, 3046-3055.

342 F. Zeng, Z. Tong and H. Feng, *Polymer*, 1997, **38**, 5539-5544.

343 M. V. Deshmukh, A. A. Vaidya, M. G. Kulkarni, P. R. Rajamohanan and S. Ganapathy, *Polymer*, 2000, **41**, 7951-7960.

344 H. Kouřilová, J. Šťastná, L. Hanyková, Z. Sedláková and J. Spěváček, *Eur. Polym. J.*, 2010, **46**, 1299-1306.

345 F. Hua, X. Jiang and B. Zhao, *Macromolecules*, 2006, **39**, 3476-3479.

346 E. Lee, Y.-H. Jeong, J.-K. Kim and M. Lee, *Macromolecules*, 2007, **40**, 8355-8360.

347 P. P. N. Syamala and F. Würthner, *Chem. Eur. J.*, 2020, **26**, 8426-8434.

348 G. Bokias, D. Hourdet and I. Iliopoulos, *Macromolecules*, 2000, **33**, 2929-2935.

349 L. D. Taylor and L. D. Cerankowski, *J. Polym. Sci. Pol. Chem.*, 1975, **13**, 2551-2570.

350 L. M. Negrón, Y. Meléndez-Contés and J. M. Rivera, *J. Am. Chem. Soc.*, 2013, **135**, 3815-3817.

351 W. Li, A. Zhang and A. D. Schluter, *Chem. Commun.*, 2008, 5523-5525.

352 Y. Kwon, in *Handbook of Essential Pharmacokinetics, Pharmacodynamics and Drug Metabolism for Industrial Scientists*, Springer US, Boston, 2002, pp. 35-72.

353 A. K. Ghose and G. M. Crippen, *J. Comput. Chem.*, 1986, **7**, 565-577.

354 V. N. Viswanadhan, A. K. Ghose, G. R. Revankar and R. K. Robins, *J. Chem. Inf. Comput. Sci.*, 1989, **29**, 163-172.

355 N. Bodor and P. Buchwald, in *Retrometabolic Drug Design and Targeting*, John Wiley and Sons, New Jersey, pp. 9-38.

356 Calculator Plugins were used for logP calculation, Marvin 20.14, 2020 , ChemAxon (http://www.chemaxon.com).

357 T. Ishizone, A. Seki, M. Hagiwara, S. Han, H. Yokoyama, A. Oyane, A. Deffieux and S. Carlotti, *Macromolecules*, 2008, **41**, 2963-2967.

358 P. Kujawa, F. Segui, S. Shaban, C. Diab, Y. Okada, F. Tanaka and F. M. Winnik, *Macromolecules*, 2006, **39**, 341-348.

359 N. Schmid, A. P. Eichenberger, A. Choutko, S. Riniker, M. Winger, A. E. Mark and W. F. van Gunsteren, *Eur. Biophys. J.*, 2011, **40**, 843-856.

360 A. K. Malde, L. Zuo, M. Breeze, M. Stroet, D. Poger, P. C. Nair, C. Oostenbrink and A. E. Mark, *J. Chem. Theory Comput.*, 2011, **7**, 4026-4037.

361 A. Karpfen, C. H. Choi and M. Kertesz, *J. Phys. Chem. A*, 1997, **101**, 7426-7433.

362 M. J. Abraham, T. Murtola, R. Schulz, S. Páll, J. C. Smith, B. Hess and E. Lindahl, *SoftwareX*, 2015, **1-2**, 19-25.

363 J. J. P. Stewart, *J. Mol. Model.*, 2013, **19**, 1-32.

364 J. J. P. Stewart, *Stewart Computational Chemistry*, 2016, Colorado Springs, CO, USA. HTTP://OpenMOPAC.net.

365 A. Klamt and G. Schüürmann, *J. Chem. Soc., Perkin Trans. 2*, 1993, 799-805.

366 C.-Z. Dong, A. Ahamada-Himidi, S. Plocki, D. Aoun, M. Touaibia, N. Meddad-Bel Habich, J. Huet, C. Redeuilh, J.-E. Ombetta, J.-J. Godfroid, F. Massicot and F. Heymans, *Biorg. Med. Chem.*, 2005, **13**, 1989-2007.

367 J. Y. C. Lim and P. D. Beer, *Chem. Commun.*, 2015, **51**, 3686-3688.

368 O. Middel, W. Verboom and David N. Reinhoudt, *Eur. J. Org. Chem.*, 2002, **2002**, 2587-2597.

# Acknowledgments

First and foremost, I would like to express my benevolent gratitude to Prof. Dr. Frank Würthner for his inspiring guidance, constant encouragement, and motivation throughout my Ph.D. studies. I am greatly indebted to his relentless efforts in improving my research, for suggesting an exciting research problem and excellent infrastructure, which aided the work presented in this thesis. I am also grateful for the independence provided in molding my projects and opportunities to attend several national and international conferences.

My sincere gratitude is also due to Dr. Chantu R. Saha Möller for the immense knowledge and guidance provided in the writing of manuscripts and improving my projects in general. It has vastly enhanced my writing skills and attention to detail.

I am grateful to our collaboration partner, Prof. Dr. Stephan Gekle (University of Bayreuth), for performing MD simulations. These studies were our first clue towards the unique orientation of side chains in the rylene bisimide systems, which was a turning point for our understanding of the thermodynamic behavior of these dyes in water.

My special thanks to Dr. Bartolome Soberats, who has kept me motivated and inspired by our regular discussions and showed me the nuances of constructing a good paper. I am also grateful for critically reading several of my manuscripts and improving them to a great extent.

I thank Tim Schlossarek, Johannes Thein, and Dr. Bartolome Soberats for correcting various parts of this thesis and for the German translation of the summary.

I express my sincere gratitude to Dr. Vladimir Stepanenko for AFM measurements and very useful insights in our discussions. Furthermore, I thank Dr. Matthias Grüne, Patricia Altenberger, and Marvin Grüne for NMR measurements as well as Dr. Michael Büchner and Juliane Adelmann for mass spectrometry.

For helpful discussions and troubleshooting in computational studies, I am grateful to Dr. David Bialas, Niyas M. A. Salam, and Dr. Joachim Lindner. I express my gratitude to Dr. Soichiro Ogi, Dr. Vincenzo Grande, Dr. Wolfgang Wagner, and Markus Hecht for many helpful insights on supramolecular polymerization. Moreover, I would also like to thank several discussions with Dr. Daniel Görl, who first came across the entropically driven self-assembly of rylene bisimides and thus opened this field.

I would like to acknowledge Dr. Matthias Stolte, Priv.-Doz. Dr. Florian Beuerle, and Dr. David Schmidt for ensuring the smooth running of laboratories as well as the maintenance of several instruments, which made our work easier. Furthermore, I thank Joachim Bialas, Petra Seufert-Baumbach, Jennifer Begall, Johannes Thein, Lisa Otter, Anja Rausch, Olga Anhalt, Ann-Kathrin Lenz, Astrid Kudzus and Julius Albert for organizing the chemicals as well as keeping the labs running on a daily basis. Joachim, we are all grateful to you for the humor and joy you bought every day to the lab and lighting up many dull moments.

A special thanks to Christiana Toussaint, Eleonore Klaus, and Sarah Bullnheimer for the assistance with many administration tasks as well as helping with my initial days in Germany.

It was my great pleasure to work with my master's practical students, Benedikt Ritschel, Sandra Thürauf, André Muthig, and Daniel Volland. I am grateful for your synthetic support and many pleasant moments in the lab together.

I would also like to thank all the members of the Würthner group, the Beuerle group, the Nowak-Król group, as well as the former Fernández group for your continuous support during the last years. I owe a debt of gratitude to our 'Lunch Group', especially Gustavo, Agnieszka, Vincenzo, David, Kla, Ogi, Tomeu, Ayan, and many others who welcomed me with open arms and made my acclimatization in Würzburg much easier. I also thank Chia-An, Santosh, Roberto, Suvendu, Niyas, Pengzhong, and Anurag for our friendship and several moments outside the lab together.

Finally, I thank my family, especially my mother, for unconditional support, and my teachers, for believing in me. Megha and Anoop, you have continuously made sure that I am doing fine despite the distance of thousands of kilometers, with your constant calls and cards. I am indebted to have you in my life. Johannes, you had made immense sacrifices and been there through thick and thin in the last years and has kept me going when I was ready to throw in the towel. This would not have been possible without you.